

EVALUATING MACRO AND MICROSCOPIC ROCK DAMAGE FROM EXPLOSIONS AND THE EFFECTS ON SHEAR WAVE GENERATION

Randy Martin, et al.

**New England Research, Inc.
331 Olcott Drive, Suite L1
White River Junction, VT 05001**

30 June 2014

Final Report

APPROVED FOR PUBLIC RELEASE; DISTRIBUTION IS UNLIMITED.



**AIR FORCE RESEARCH LABORATORY
Space Vehicles Directorate
3550 Aberdeen Ave SE
AIR FORCE MATERIEL COMMAND
KIRTLAND AIR FORCE BASE, NM 87117-5776**

DTIC COPY

NOTICE AND SIGNATURE PAGE

Using Government drawings, specifications, or other data included in this document for any purpose other than Government procurement does not in any way obligate the U.S. Government. The fact that the Government formulated or supplied the drawings, specifications, or other data does not license the holder or any other person or corporation; or convey any rights or permission to manufacture, use, or sell any patented invention that may relate to them.

This report was cleared for public release by the 377 ABW Public Affairs Office and is available to the general public, including foreign nationals. Copies may be obtained from the Defense Technical Information Center (DTIC) (<http://www.dtic.mil>).

AFRL-RV-PS-TR-2014-0167 HAS BEEN REVIEWED AND IS APPROVED FOR PUBLICATION IN ACCORDANCE WITH ASSIGNED DISTRIBUTION STATEMENT.

//SIGNED//

Robert Raistrick
Project Manager, AFRL/RVBYE

//SIGNED//

Glenn M. Vaughan, Colonel, USAF
Chief, Battlespace Environment Division

This report is published in the interest of scientific and technical information exchange, and its publication does not constitute the Government's approval or disapproval of its ideas or findings.

REPORT DOCUMENTATION PAGE			Form Approved OMB No. 0704-0188	
Public reporting burden for this collection of information is estimated to average 1 hour per response, including the time for reviewing instructions, searching existing data sources, gathering and maintaining the data needed, and completing and reviewing this collection of information. Send comments regarding this burden estimate or any other aspect of this collection of information, including suggestions for reducing this burden to Department of Defense, Washington Headquarters Services, Directorate for Information Operations and Reports (0704-0188), 1215 Jefferson Davis Highway, Suite 1204, Arlington, VA 22202-4302. Respondents should be aware that notwithstanding any other provision of law, no person shall be subject to any penalty for failing to comply with a collection of information if it does not display a currently valid OMB control number. PLEASE DO NOT RETURN YOUR FORM TO THE ABOVE ADDRESS.				
1. REPORT DATE (DD-MM-YYYY) 30-06-2014		2. REPORT TYPE Final Report		3. DATES COVERED (From - To) 19 Apr 2010 to 23 Jun 2014
4. TITLE AND SUBTITLE Evaluating Macro and Microscopic Rock Damage from Explosions and the Effects on Shear Wave Generation		5a. CONTRACT NUMBER FA9453-10-C-0257		
		5b. GRANT NUMBER		
		5c. PROGRAM ELEMENT NUMBER 62601F		
6. AUTHOR(S) Randolph J. Martin, Peter Boyd Mark Leidig ¹ , Jessie Bonner ¹ , Anastasia Stroujkova ¹ , John Schuh ¹ , and James Lewkowicz ¹		5d. PROJECT NUMBER 1010		
		5e. TASK NUMBER PPM00000620		
		5f. WORK UNIT NUMBER EF004650		
7. PERFORMING ORGANIZATION NAME(S) AND ADDRESS(ES) New England Research, Inc. 331 Olcott Drive, Ste L1 White River Junction, VT 05001		¹ Weston Geophysical Corporation 181 Bedford Street, Suite 1 Lexington, MA 02420 8. PERFORMING ORGANIZATION REPORT NUMBER		
9. SPONSORING / MONITORING AGENCY NAME(S) AND ADDRESS(ES) Air Force Research Laboratory Space Vehicles Directorate 3550 Aberdeen Avenue SE Kirtland AFB, NM 87117-5776		10. SPONSOR/MONITOR'S ACRONYM(S) AFRL/RVBYE		
		11. SPONSOR/MONITOR'S REPORT NUMBER(S) AFRL-RV-PS-TR-2014-0167		
12. DISTRIBUTION / AVAILABILITY STATEMENT Approved for public release; distribution is unlimited. (377ABW-2014-0787 dtd 23 Sep 2014)				
13. SUPPLEMENTARY NOTES The views, opinions, and/or findings contained in this report are those of the author(s) and should not be construed as an official U.S. Air Force or U.S. Government policy or decision, unless so designated by other documentation.				
14. ABSTRACT <p>In July 2008, five small chemical explosions were detonated in low fracture density, homogeneous, yet transversely isotropic, granite in Barre, VT. The physical properties of the granite were measured before and after the explosions on cores recovered in the vicinity of each shot. The changes in the post-shot properties were used to quantify damage at the micro, meso, and macro scales. Near the emplacement, the rock was highly pulverized and granulated. Outward and above the emplacement level, the granite was characterized by high angle fractures parallel to the rift. This zone transitioned to a mostly intact matrix with few randomly oriented fractures out to the elastic region. At the microscale, damage was quantified by measuring the differences in ultrasonic wave speeds between the pre- and post-shot values on specimens of intact matrix rock. Near the working point, the P wave velocity decreased up to 12%. Damage at all scales was greatest above the emplacement level of the charge and parallel to the trend of the rift. The shapes of the zones of equal damage were non-spherical.</p> <p>Weston Geophysical Corp. and New England Research, Inc. conducted the field phase of the follow-up New England Damage Experiment (NEDE2) during June 2013 in the same granite quarry. A primary objective remained to identify possible source(s) of shear wave generation resulting from rock damage. We found that an increase in velocity of detonation results in increased seismic corner frequency and high frequency amplitudes and a slight decrease in the low-frequency amplitudes, although host rock water saturation affects this as well. The observed S wave radiation pattern is consistent with radiation due to opening of tensile fractures approximately parallel to the host rock rift direction. The presence of surface fractures for black powder and Composition B shots correlates with an increase in S/P amplitudes for these shots. The Heavy ANFO shot, which did not produce surface fracturing, has the second smallest S/P ratios, followed by the deep Heavy ANFO shot. In general, our results suggest a correlation between S/P amplitude ratios and surface fracturing resulting from the explosions (e.g. more fracturing causes increased S/P ratios). Travel time modeling of the shear phases is consistent with primary shear wave generation occurring at or near the source and not along the travel path.</p>				
15. SUBJECT TERMS Explosions, shear-wave generation, nuclear monitoring, rock damage, fracture decoupling				
16. SECURITY CLASSIFICATION OF:			17. LIMITATION OF ABSTRACT Unlimited	18. NUMBER OF PAGES 276
a. REPORT Unclassified	b. ABSTRACT Unclassified	c. THIS PAGE Unclassified		19a. NAME OF RESPONSIBLE PERSON Robert Raistrick
				19b. TELEPHONE NUMBER (include area code)

This page is intentionally left blank.

TABLE OF CONTENTS

LIST OF FIGURES	vii
LIST OF TABLES	xvii
1. SUMMARY	1
Introduction.....	1
NEDE1	1
NEDE2	2
2. NEW ENGLAND DAMAGE EXPERIMENT 2 (NEDE2)	5
Introduction.....	5
Objective	6
Location	6
Data Recording	11
Near-Source Array	11
Short Period Arrays.....	17
Video.....	20
Sensor Issues/Data Loss.....	21
Explosions.....	22
Shot Characteristics	22
Issues with Water in the Blast Holes	30
Velocity of Detonation.....	34
Surface Effects	34
Seismic Data Examples and Analyses	40
Spall	40
Waveform Examples.....	41
Peak Particle Velocities	44
Deep Versus Shallow Explosion Amplitude – Preliminary Results.....	51
Full Waveform Spectral Ratios – Preliminary Results	53
3. MOMENT TENSOR INVERSION FOR NEDE2 EXPLOSIONS.....	66
Abstract	66

Objectives	66
Research Accomplished.....	67
Inversion Method	67
Inversion Results.....	67
Discussion	72
Conclusions and Recommendations	77
4. SPECTRAL RATIO SOURCE CHARACTERIZATION	78
Introduction.....	78
Data Analysis	79
NEDE2 BP Shot 1 Phase Ratios	82
NEDE2 HANFO Shot 2 Phase Ratios	82
NEDE2 Comp B Shot 3 Phase Ratios.....	83
NEDE2 Deep HANFO Shot 4 Phase Ratios.....	83
NEDE2 HANFO Reshoot Shots 5 and 6 Phase Ratios.....	83
Comparison of NEDE and NEDE2 Phase Ratios	93
Discussion	96
5. NON-PARAMETRIC STUDIES OF SEISMIC SOURCES AND PROPAGATION EFFECTS FOR NEDE1 AND NEDE2 EXPLOSIONS.....	98
Abstract	98
Objectives	98
Research Accomplished.....	99
Experimental Data	99
Inversion for the Source and Propagation Effects	105
Results.....	105
Site/Propagation Transfer Functions.....	107
Effect of the VOD on P-Wave Spectra	108
Effect of the DOB	108
Effect of Fractures in the Emplacement Medium	111
Effect of Saturation	111
Effect of the Yield.....	113
Conclusions and Recommendations	113
6. MOMENT ESTIMATION FROM SHORT PERIOD SURFACE WAVES FROM THE NEDE2 EXPLOSIONS IN BARRE GRANITE	114

Abstract	114
Objectives	114
Research Accomplished.....	115
Model Development.....	115
Modeling the NEDE2 Explosions.....	122
Conclusions and Further Recommendations	134
7. EFFECT OF VELOCITY OF DETONATION OF EXPLOSIVES ON SEISMIC RADIATION	135
Abstract	135
Introduction.....	136
NEDE experiments	137
Seismic Data Analysis	139
Discussion	145
Conclusions.....	153
8. EXAMINING THE SHEAR WAVE SOURCE LOCATION THROUGH TRAVEL- TIME MODELING	154
Introduction.....	154
Observed Travel-Time Data	155
Theoretical Travel-Time Curves.....	163
Discussion	164
9. EFFECTS OF WATER SATURATION ON EXPLOSION SEISMIC COUPLING IN INTACT AND FRACTURED GRANITE.....	165
Abstract	165
Introduction.....	166
Experiment in water-saturated granite	166
Experiment in dry granite	175
Discussion	180
Conclusions.....	185
Water-saturated rock	185
Dry rock	185
APPENDIX 9-A. DESCRIPTION OF THE POROUS MEDIUM	187
10. FORWARD MODELING OF SEISMO-ACOUSTIC SIGNALS FROM EXPLOSIONS: NEDE2 EXAMPLES	189
Abstract	189

Objective	189
Research Completed.....	189
Overpressure Model Development.....	190
Seismic Model Development	192
Data and PPV/POP Analysis.....	196
Forward Modeling.....	198
Conclusions	202
11. NEAR-SOURCE ROCK DAMAGE FROM SINGLE-HOLE EXPLOSIONS TO SEISMIC WAVES.....	203
Abstract.	203
Objectives.....	204
Test Site Geology	205
Coreholes	206
Rock Properties	207
Damage Analysis	208
Summary and Conclusions.....	226
Experimental Studies on Barre Granite.....	226
Confined Compression to Failure.....	227
Elastic Anisotropy.....	230
Elastic Measurements: Static and Dynamic	234
Linear Compressibility.....	238
Permeability	241
Resistivity	244
REFERENCES	247
LIST OF SYMBOLS, ABBREVIATIONS, AND ACRONYMS	254

LIST OF FIGURES

Figure 1-1. Azimuthal variations of S/P amplitude ratios for: a) Shot 1, b) Shot 2, and c) Shot 3, and d) Shot 4.	4
Figure 2-1. Rheology surrounding an underground explosion (after Rodean (1971) and modified by Sammis for acoustic fluidization from Melosh, 1979).	7
Figure 2-2. Photograph of 3-5 m thick relatively unfractured sections of Barre granite.....	8
Figure 2-3. Geologic map (modified) from the Vermont Geological Survey.	9
Figure 2-4. Location of the test site north of the active Rock of Ages quarry.....	10
Figure 2-5. Test site stations (yellow triangles) and shots (red stars).....	14
Figure 2-6. Full near-source station network. (Google Earth Background)	15
Figure 2-7. Endevco accelerometers were grouted in place ~1 m from Shots 1-6.	16
Figure 2-8. NS15 Endevco accelerometer grouted and buried ~1 m from Shot 5.....	16
Figure 2-9. Plastic tub housing the RT130 recorder and battery.	17
Figure 2-10. Short period array stations (yellow triangles). (Google Earth Background)	19
Figure 2-11. Example of orienting to true north and leveling an L-4C 3D sensor before burial.	20
Figure 2-12. Camera view before trimming vegetation.....	21
Figure 2-13. Location of the shot points on the test site (Google Earth photo).....	24
Figure 2-14. Plywood and plastic tarp covering the drill holes to prevent mud and rain from entering the hole.....	25
Figure 2-15. Johnson Artesian drilling the holes and clearing the cuttings.....	25
Figure 2-16. Lowering a container filled with BP and the detonator to the bottom of the Shot 1 hole.....	26
Figure 2-17. Pouring the remainder of the BP into the hole.	27
Figure 2-18. Preparing a premeasured amount of HANFO for loading.	28
Figure 2-19. Initiation system of the HANFO charges including two 14 oz boosters, a blasting cap (inside the boosters), and shock tubing.	28
Figure 2-20. Determining the cast Comp B charges were larger than the ordered specifications and would not fit down the hole.	29
Figure 2-21. Building a makeshift Comp B explosive after the cast charges would not fit downhole.....	30
Figure 2-22. Generator and submersible pump in a drill hole.	31
Figure 2-23. Submersible pump being moved between holes.	32
Figure 2-24. Water pumped from a drill hole.	32

Figure 2-25. Fireball erupting from the Shot 3 surface fissure.....	33
Figure 2-26. Preparing stemming for loading Shot 4 hole as soon as pumping was completed. .	34
Figure 2-27. Digitized still images of the Shot 1 detonation.	35
Figure 2-28. Rough sketch of approximate fracture zone created by Shot 1.....	36
Figure 2-29. Largest cracks generated by Shot 1.....	37
Figure 2-30. Singed vegetation along the fracture network from Shot 3.....	38
Figure 2-31. Small cracks (shown by red ellipses) and burnt wiring and tubing (black arrows) generated by Shot 3.....	39
Figure 2-32. Near-source phenomenology for all six large shots recorded on accelerometers installed 1 m from the blast hole.....	40
Figure 2-33. Shot 1 to Shot 6 vertical components at NS09 (~0.5 km).....	41
Figure 2-34. Shot 1 to Shot 6 vertical components at R03 (~6 km).	42
Figure 2-35. Shot 1 to Shot 6 radial components at R03 (~6 km).	42
Figure 2-36. Shot 1 to Shot 6 transverse components at R03 (~6 km).	43
Figure 2-37. Shot 2 vertical components along the SE array (3-24 km).	44
Figure 2-38. Shot 1 composite waveform PPV.	46
Figure 2-39. Shot 2 composite waveform PPV.	47
Figure 2-40. Shot 3 composite waveform PPV.	47
Figure 2-41. Shot 4 composite waveform PPV.	48
Figure 2-42. Shot 5 composite waveform PPV.	48
Figure 2-43. Shot 6 composite waveform PPV.	49
Figure 2-44. Shot 7 composite waveform PPV.	49
Figure 2-45. Shot 8 composite waveform PPV.	50
Figure 2-46. Shot 9 composite waveform PPV.	50
Figure 2-47. Near-source accelerograms for a) Shot 2 and b) Shot 4.....	52
Figure 2-48. Seismic records for Shot 2 and Shot 4 recorded at a) Station NS08 and b) NS09...	53
Figure 2-49. Seismic records for Shot 2 and Shot 4 recorded at a) Station R02 and b) R10 for filter pass bands of 1-10 Hz (upper plots) and 10-100 Hz (lower plots).	53
Figure 2-50. Shot 2 and Shot 1 waveforms on ring network.	55
Figure 2-51. Spectral ratios for Shot 2 (HANFO; 150 lbs) / Shot 1 (Black Powder; 150 lbs).	56
Figure 2-52. Shot 2 and Shot 3 waveforms on ring network.	57
Figure 2-53. Spectral ratios for Shot 2 (HANFO; 150.0 lbs) / Shot 3 (Comp B; 161.2 lbs).	58
Figure 2-54. Shot 2 and Shot 4 waveforms on ring network.	58

Figure 2-55. Spectral ratios for Shot 2 (HANFO; 150.0 lbs) / Shot 4 (Deep HANFO; 151.1 lbs).	59
Figure 2-56. Shot 2 and Shot 5 waveforms on ring network.	60
Figure 2-57. Spectral ratios for Shot 2 (HANFO; 150.0 lbs) / Shot 5 (HANFO reshoot of NEDE1 HANFO; 150.0 lbs).	61
Figure 2-58. Shot 2 and Shot 6 waveforms on ring network.	62
Figure 2-59. Spectral ratios for Shot 2 (HANFO; 150.0 lbs) / Shot 6 (HANFO reshoot of NEDE1 Comp B; 150.0 lbs).	63
Figure 2-60. Shot 5 and Shot 6 waveforms on ring network.	64
Figure 2-61. Spectral ratios for Shot 5 (HANFO reshoot of NEDE1 HANFO; 150.0 lbs) / Shot 6 (HANFO reshoot of NEDE1 HANFO; 150.0 lbs).	65
Figure 3-1. The near-source stations (triangles) installed around the test site at the Rock of Ages Quarry in Barre, VT. b) Enlarged view of the testing area showing the explosions (stars).	67
Figure 3-2. Comparison between the data (blue) and the Green's functions (red) for Shot 1: a) Station NS02, b) Station NS15, c) Station NS03, and d) Station NS08.	68
Figure 3-3. RMS errors for the moment tensor components as a function of frequency: a) Shot 1, b) Shot 2, c) Shot 3, and d) Shot 4.	69
Figure 3-4. Moment rate tensor components for: a) Shot 1, b) Shot 2, c) Shot 3, and d) Shot 4.	70
Figure 3-5. Near-source accelerograms for two pairs of reciprocal ray trajectories...	72
Figure 3-6. a) Near-source accelerograms for Shot 2 recorded by NS11, NS14, NS15, and NS16; b) Shot 1, 3, 4, and 6 recorded by NS15 located near Shot 5.	74
Figure 3-7. Azimuthal variations of P-wave amplitude ratios between: a) Shot 1 and Shot 4, b) Shot 2 and Shot 4, and c) Shot 3 and Shot 4.	75
Figure 3-8. Vertical (blue) and transverse (green) component seismograms for Shots 1-4 recorded at: a) Station R06, and b) Station R01.	76
Figure 3-9. Azimuthal variations of S/P amplitude ratios for: a) Shot 1, b) Shot 2, and c) Shot 3, and d) Shot 4.	77
Figure 4-1. Hodograms of P (top row), S (middle row), and Rg (bottom row) windows used to confirm isolation of proper phase.	79
Figure 4-2. 3-D hodograms of P (top left), S (top right), and Rg (bottom) windows used to confirm isolation of proper phase.	80
Figure 4-3. Vertical component PSD of P phase window at station SE02 for Shots 1-5.	81
Figure 4-4. Vertical component PSD of S phase window at station SE02 for Shots 1-5.	81
Figure 4-5. Vertical component PSD of Rg phase window at station SE02 for Shots 1-5.	82
Figure 4-6. Vertical component waveform (top) from Shot 1 at station SE02. PSD of the P, S, and Rg phases (bottom left) and phase spectral ratios (bottom right). Min. resolved freq. 6 Hz.	84

Figure 4-7. Vertical component waveform (top) from Shot 1 at station SE07. PSD of the P, S, and Rg phases (bottom left) and phase spectral ratios (bottom right). Min. resolved freq. 2.2 Hz.	85
Figure 4-8. Vertical component waveform (top) from Shot 2 at station SE02. PSD of the P, S, and Rg phases (bottom left) and phase spectral ratios (bottom right). Min. resolved freq. 6.5 Hz.	86
Figure 4-9. Vertical component waveform (top) from Shot 2 at station SE07. PSD of the P, S, and Rg phases (bottom left) and phase spectral ratios (bottom right). Min. resolved freq. 2.4 Hz.	87
Figure 4-10. Vertical component waveform (top) from Shot 3 at station SE02. PSD of the P, S, and Rg phases (bottom left) and phase spectral ratios (bottom right). Min. resolved freq. 5.7 Hz.	88
Figure 4-11. Vertical component waveform (top) from Shot 3 at station SE07. PSD of the P, S, and Rg phases (bottom left) and phase spectral ratios (bottom right). Min. resolved freq. 2.1 Hz.	89
Figure 4-12. Vertical component waveform (top) from Shot 4 at station SE02. PSD of the P, S, and Rg phases (bottom left) and phase spectral ratios (bottom right). Min. resolved freq. 6.3 Hz.	90
Figure 4-13. Vertical component waveform (top) from Shot 4 at station SE07. PSD of the P, S, and Rg phases (bottom left) and phase spectral ratios (bottom right). Min. resolved freq. 1.9 Hz.	91
Figure 4-14. Vertical component waveform (top) from Shot 5 at station SE02. PSD of the P, S, and Rg phases (bottom left) and phase spectral ratios (bottom right). Min. resolved freq. 7.2 Hz.	91
Figure 4-15. Vertical component waveform (top) from Shot 5 at station SE07. PSD of the P, S, and Rg phases (bottom left) and phase spectral ratios (bottom right). Min. resolved freq. 1.8 Hz.	92
Figure 4-16. Vertical component waveform (top) from Shot 6 at station SE02. PSD of the P, S, and Rg phases (bottom left) and phase spectral ratios (bottom right). Min. resolved freq. 6.8 Hz.	92
Figure 4-17. Vertical component waveform (top) from Shot 6 at station SE07. PSD of the P, S, and Rg phases (bottom left) and phase spectral ratios (bottom right). Min. resolved freq. 1.9 Hz.	93
Figure 4-18. Vertical component waveform (top) from the NEDE1 BP Shot 1 at station SE02. PSD of the P, S, and Rg phases (bottom left) and phase spectral ratios (bottom right). Min. resolved freq. 6 Hz.	94
Figure 4-19. Vertical component waveform (top) from the NEDE1 HANFO Shot 4 at station SE02. PSD of the P, S, and Rg phases (bottom left) and phase spectral ratios (bottom right). Min. resolved freq. 6.2 Hz.	95

Figure 4-20. Vertical component waveform (top) from the NEDE1 Comp B Shot 5 at station SE02. PSD of the P, S, and Rg phases (bottom left) and phase spectral ratios (bottom right). Min. resolved freq. 6.5 Hz.	96
Figure 5-1. (a) The local network around the test site at the Rock of Ages Quarry located in Barre, VT..	101
Figure 5-2. Waveforms recorded 3 km from the sources (Station SE01) for the explosions of (a) NEDE1 experiment, (b) NEDE2 experiment. P-wave spectra for (c) NEDE1 explosions shown in (a); (d) NEDE2 explosions shown in (b).	102
Figure 5-3. Waveforms recorded 6 km from the sources (Station SE02) for the explosions of (a) NEDE1 experiment, (b) NEDE2 experiment. P-wave spectra for (c) NEDE1 explosions shown in (a); (d) NEDE2 explosions shown in (b).	103
Figure 5-4. Spectral amplitudes (vertical components) of the pre-event records (noise) at stations recording both NEDE1 and NEDE2 experiments: (a) R01/NE02, (b) SE01, (c) R06/SE02, (d) SE03, (e) SE04, and (f) SE05..	104
Figure 5-5. Comparison between recovered source spectra obtained using different subsets of the data..	107
Figure 5-6. Comparison between recovered transfer functions obtained using only NEDE1 data (green lines), only NEDE2 data (blue data) and combined dataset (cyan lines) for stations that were operational during both experiments: (a) Station NE02; (b) SE01; (c) SE02; (d) SE03; (e) SE04; and (f) SE05.	109
Figure 5-7. a) Source spectra for the explosions with different VOD for NEDE2 experiment (equal TNT equivalent yield). b) Source spectra for the explosions with different VOD for NEDE1 experiment (equal mass of explosives, different TNT equivalent yield). c) Comparison of the source spectra for the event with different DOB. d) Comparison of the spectra between the explosions in intact and fractured rocks for the NEDE2 experiment. e) Effect of the explosion yield on the spectra for NEDE1 explosions. f) Differences between NEDE1 and NEDE2 explosions possibly due to pore water content.	110
Figure 5-8. a) Comparison of the spectra predicted using the MM71 model and the near-source data recorded between 300-500 m from the sources for the explosions with different VOD. b) Comparison of the spectra predicted using the MM71 model and the near-source data for the explosions with different DOB.	111
Figure 5-9. Low-frequency spectral amplitude plotted as a function of TNT equivalent yield for NEDE1 and NEDE2 explosions..	112
Figure 6-1. Location of 4.5 Hz geophones (NEDE1) used to estimate the velocity and attenuation structure of the upper crust near Barre, VT.	116
Figure 6-2. Spectral amplitudes for Rg recorded on the a) SE and b) NE profiles shown in Figure 6-1..	117
Figure 6-3. Regressions of spectral amplitudes at 2 Hz for Rg recorded on the a) SE and b) NE profiles.	118
Figure 6-4. Attenuation coefficients as a function of frequency for Rg recorded on the a) SE and b) NE profiles shown in Figure 6-1.	119

Figure 6-5. Q estimates as a function of frequency for Rg recorded on the a) SE and b) NE profiles..	119
Figure 6-6. Observed a) group velocity dispersion and b) attenuation coefficients compared to predictions based on a joint inversion for shear wave velocity and attenuation structure.....	120
Figure 6-7. a) Shear wave velocity and b) Q structures (black) from joint inversion of Rg velocity and attenuation gammas compared to the starting models (red).....	122
Figure 6-8. Map showing a ring of azimuthal sensors at approximately 6 km from the granite quarry test site.....	125
Figure 6-9. A comparison of the synthetic Rg (black) using the Mo estimates in Table 6-3 to observed data (red) from four ring stations (Figure 6-8) that recorded the NEDE2 Shots 1-4 (a,b,c, and d respectively) filtered between 0.5-5 Hz.	126
Figure 6-10. Observed versus theoretical spectral amplitudes for NEDE1 a) Shot 1, b) Shot 2, c) Shot 3, and d) Shot 4.....	127
Figure 6-11. Spectral ratios for Rg for the ring network stations.	128
Figure 6-12. Varying the Mo estimates to provide a range of possible moments to bound the observed data.	129
Figure 6-13. A comparison of the predicted source spectra for the NEDE2 Shots 1-4 using DJ91 (solid) and MM71 (dashed).	130
Figure 6-14. a) Synthetic waveforms produced using the Patton (2012) source model for a K=2.6. b) Spectral amplitudes of the synthetics in a).....	132
Figure 6-15. A comparison of the synthetic Rg (black) using the Patton (2012) explosion and damage source model to observed data (red) from four ring stations (Figure 6-8) that recorded the NEDE2 Shots 1-4 (a,b,c, and d respectively).	133
Figure 6-16. Observed spectral amplitudes for NEDE2 a) Shot 1, b) Shot 2, c) Shot 3, and d) Shot 4 compared to synthetic estimates using the Patton (2012) explosion plus damage model..	134
Figure 7-1. (a) The 6 km circle network around the test site at the Rock of Ages Quarry located in Barre, VT. (b) Enlarged view of intermediate range stations. (c) Enlarged view of the testing area showing the near-field accelerometers (triangles) and the explosions (stars).....	141
Figure 7-2. Near-source accelerometer data for: (a) Shot 1, (b) Shot 2, (c) Shot 3, and (d) Shot 4.	142
Figure 7-3. (a) Vertical component of the displacement seismograms recorded by Station R03 (at a distance of approximately 5.5 km) for Shot 1 (top panel), Shot 2 (middle panel) and Shot 3 (bottom panel); (b) spectral amplitudes for the traces in (a); (c) spectral ratios between Shot 2 / Shot 1 (grey line) and Shot 3 /Shot 2 (black line).....	143
Figure 7-4. (a) Displacement spectra for BP Shot 1 (dotted gray line), HANFO Shot 2 (dashed line) and Comp B Shot 3 (solid gray line) averaged over the intermediate distance instruments (NS07, NS08, NS09); (b) displacement spectra for shallow HANFO Shot 2 (dashed black line) and deep HANFO Shot 4 (dashed gray line) averaged over the same group of instruments as in (a); (c) displacement spectra for BP Shot 1, HANFO Shot 2 and Comp B Shot 3 averaged over	

the circular (6 km radius) network; and (d) displacement spectra for shallow HANFO Shot 2 and deep HANFO Shot 4 averaged over the same group of instruments as in (c).	144
Figure 7-5. (a) Comparison between two Comp B explosions from the NEDE1 (83 kg TNT equivalent, top panel) and the NEDE2 (73 kg TNT equivalent, bottom panel).	145
Figure 7-6. Displacement seismograms recorded at Station R06 located approximately 6 km from the test bed.....	146
Figure 7-7. Azimuthal variations of P-wave amplitude ratios between: a) Shot 1 and Shot 4, b) Shot 2 and Shot 4, and c) Shot 3 and Shot 4.....	151
Figure 7-8. Azimuthal variations of S/P amplitude ratios for: a) Shot 1, b) Shot 2, and c) Shot 3, and d) Shot 4..	152
Figure 7-9. (a) Theoretical radiation pattern for P (solid line) and S-waves (dashed line) resulting from an opening of a vertical tensile fracture with N30°E strike. Also shown is the direction of the opening fracture and the angle θ . (b) Theoretical S/P amplitude ratio for the fracture described in (a).....	153
Figure 8-1. Shot 1 P (black) and S (blue) wave travel-time data and least-squares regression line fits..	156
Figure 8-2. Shot 2 P (black) and S (blue) wave travel-time data and least-squares regression line fits..	157
Figure 8-3. Shot 3 P (black) and S (blue) wave travel-time data and least-squares regression line fits..	158
Figure 8-4. Shot 4 P (black) and S (blue) wave travel-time data and least-squares regression line fits..	159
Figure 8-5. Shot 5 P (black) and S (blue) wave travel-time data and least-squares regression line fits.	160
Figure 8-6. Shot 6 P (black) and S (blue) wave travel-time data and least-squares regression line fits..	161
Figure 8-7. Composite P (black) and S (blue) wave travel-time data and least-squares regression line fits..	162
Figure 8-8. Layer over half-space velocity model determined from P and S travel time data near the NEDE2 test site.....	164
Figure 9-1. (a) The near-source network located on Spruce Ridge, New Hampshire. The open triangles show the station locations for the Phase II experiment.....	169
Figure 9-2. Seismic tomography results (Phase I) showing <i>P</i> -velocity (a) before and (b) after FD1 explosion along the SE-NW borehole cross-section (Figure 9-1b).	171
Figure 9-3. Seismic tomography results (Phase II) showing the changes in <i>P</i> -velocity (in percent) after FD11 and FD21 explosions along the SE-NW borehole cross-section (Figure 9-1c).....	172
Figure 9-4. Examples of the vertical component waveforms from the co-located explosions conducted in NH recorded approximately 600 m from the sources.	173

Figure 9-5. (a) FD2 and FD3 spectra computed for the intermediate range network stations shown in Figure 9-1a.	174
Figure 9-6. a) Pre- and post-shot <i>P</i> -wave velocities measured from the cores.....	176
Figure 9-7. (a) The 6 km circle network around the NEDE2 test site at the Rock of Ages Quarry located in Barre, VT.....	177
Figure 9-8. Waveform comparison between the NEDE2 virgin and fractured rock explosions conducted in Barre, VT recorded by Station NS09.	179
Figure 9-9. (a) NEDE2-2 and NEDE2-5 spectra computed for the 6 km circle stations shown in Figure 9-4a.	180
Figure 9-10. Schematic configuration of the repeat shot with respect to the damage zone created by the first shot of similar size.....	182
Figure 9-11. MM71 model predictions for intact rock (solid line, Model A), fractured rock (dash-dot line, Model B) and the “hybrid” model (dashed line) with fractured rock inside the elastic radius and intact rock outside the elastic radius.....	183
Figure 9-12. Comparison of the theoretical spectral ratios predicted using MM71 model between explosions in intact and “porous” media and the data.	184
Figure 10-1. Blast suppression factors (S_z) versus scaled heights-of-burst (sHOB) for peak overpressures from HUMBLE REDWOOD data (circles).....	192
Figure 10-2. Peak overpressure estimates for 1-ton explosion detonated on the a) surface and b) fully-coupled using the ANSI (blue), BOOM (green) and Perkins and Jackson (red) models. .	193
Figure 10-3. Amplitude reduction for seismic waves recorded from the ten 539 kg explosions conducted in alluvium during the HR I & II experiments (black circles) as a function of scaled height of burst (sHOB). Also shown are two explosions from the HRIII experiment in limestone.	195
Figure 10-4. PPV relationships for a 1-ton a) surface explosion b) fully-coupled explosion using the soft rock coupling curve shown in Figure 10-3.	196
Figure 10-5. Map showing the locations of seismic stations (red) and seismo-acoustic stations (blue) used in this study..	197
Figure 10-6. Vertical-component recordings for Shots 1-6 of NEDE2 from the 6 km station R06SE02.	198
Figure 10-7. Infrasound recordings for Shots 1-6 of NEDE2 from the 0.35 km NS06 (a) and the 0.6 km (b) NS10 stations.	199
Figure 10-8. Predicted a) PPV and b) POP (red lines) for Shot 1 compared to observed data (black circles).....	200
Figure 10-9. Predicted a) PPV and b) POP for Shot 2 compared to observed data.....	200
Figure 10-10. Predicted a) PPV and b) POP for Shot 3 compared to observed data.....	201
Figure 10-11. Predicted a) PPV and b) POP for Shot 4 compared to observed data.....	201
Figure 10-12. Predicted a) PPV and b) POP for Shot 5 compared to observed data.....	202

Figure 10-13. Predicted a) PPV and b) POP for Shot 6 compared to observed data.....	202
Figure 11-1. Pervasive rift microfabric due to microscale fractures, in Barre Granite..	205
Figure 11-2. Photomicrograph of Barre Granite thin section taken at a depth of 46.5 ft (14.2 m) in the CH-1 core.....	206
Figure 11-3. Locations of shotholes and coreholes (Green – pre-shot and Blue – post-shot) at the NEDE site..	207
Figure 11-4. Compressional wave velocity measured as a function of orientation in the Barre granite..	209
Figure 11-5. Pre-Shot #2 fast (parallel to the rift) and slow (perpendicular to the rift) compressional wave velocities as a function of depth at corehole CH-2.	210
Figure 11-6. Example of compressional wave velocity change as a function of confining stress.	211
Figure 11-7. Characteristics of the explosives used at the test site.....	212
Figure 11-8. Schematic cross section at Shot #4 showing the distribution of damage at all scales.	214
Figure 11-9. Examples of damage regions outlined in Figure 11-8.	216
Figure 11-10. A section of core from CH-10 recovered from a depth of 38 feet exhibits fracturing in the plane of the rift.	217
Figure 11-11. The effect of differential axial stress on shear wave velocity in a Barre granite specimen loaded to failure in confined compression.	218
Figure 11-12. Corehole CH-4 P- and S-Wave velocity profiles at Shot #5 (COMP-B).....	219
Figure 11-13. Pre-Shot (CH-1) and Post-Shot (CH-3) permeability and resistivity results at Shot #2 (ANFO).	220
Figure 11-14. Comparison between microscale damage, as evidenced by compressional wave slowing at high explosive Shot #5 (COMP-B), vs no microscale damage evidenced at low VOD Shot #1 (Blackpowder).	221
Figure 11-15. Cross section, based on detailed vertical velocity profiles of the coreholes at Shot #4, are drawn parallel to the rift.	222
Figure 11-16. Cross sections, as in Figure 11-14, but drawn with vertical and lateral scales equal.	223
Figure 11-17. The coreholes analyzed to define the damage geometry are shown in the cross section. Microcrack damage profiles for a 122.7 kg ANFO shot in Barre, VT.....	224
Figure 11-18. Plan view of the damage contours for a 122.7 kg ANFO shot in Barre, VT.	225
Figure 11-19. A sample jacketed with copper showing the position of the strain gages and the transverse velocity transducers.	227
Figure 11-20. An instrumented sample assembly rests on the base plug of a NER AutoLab 1500.	228

Figure 11-21. Data for a confined compression test on an oriented sample of Barre granite. ...	229
Figure 11-22. Polarized shear wave velocities are plotted as a function of differential stress for the confined compression experiment shown in Figure 11-4	230
Figure 11-23. Reference coordinate system for a transversely isotropic rock.....	231
Figure 11-24. Schematic for one compressional and two polarized shear waves propagating parallel to the 3 axis in a transversely isotropic rock.....	232
Figure 11-25. The two Young's moduli and three Poisson's ratios computed from the stiffness coefficients are shown with respect to layering in a transversely isotropic rock.....	233
Figure 11-26. Compressional and shear wave velocities are plotted as a function of pressure. Three oriented samples were tested to obtain these data.	235
Figure 11-27. Five elastic stiffnesses for a transversely isotropic sample of Barre granite are plotted as a function of pressure.	236
Figure 11-28. Young's moduli parallel and normal to the rift and the bulk modulus are plotted as a function of pressure.....	237
Figure 11-29. Poisson's ratios for the transversely isotropic Barre granite are plotted as a function of pressure.....	238
Figure 11-30. A Barre granite core that has been partitioned every 5 degrees in order to determine the fast and slow direction.....	239
Figure 11-31. Strains are measured in the principal strain directions for a sample of Barre granite..	240
Figure 11-32. The static bulk moduli computed from the linear compressibility data presented in Figure 11-31 is plotted as a function of confining pressure.....	241
Figure 11-33. Schematic diagram of a typical AutoLab permeability system.	242
Figure 11-34. Diagram illustrating the physical model used to model transient permeability data	243
Figure 11-35. Permeability is shown as a function of effective pressure for two oriented specimens from the same depth.	244
Figure 11-36. Formation factor is shown as a function of effective pressure for two oriented specimens from the same depth.	246

LIST OF TABLES

Table 2-1. Near-Source Sensors.	12
Table 2-2. Near-Source Recording Parameters.	13
Table 2-3. Short Period Array Stations.	18
Table 2-4. Short Period Array Recording Parameters.	18
Table 2-5. Camera Locations.	20
Table 2-6. Origin Characteristics for NEDE2 Shots.	23
Table 2-7. Explosive Characteristics for NEDE2 Shots.	23
Table 2-8. TNT Equivalency Factors.	24
Table 2-9. Comparison of NEDE1 and NEDE2 PPV.	51
Table 3-1. Velocity Model Used to Calculate the Green's Functions.	68
Table 3-2. Moment Tensor Inversion Results.	71
Table 3-3. Summary of the Explosion Characteristics.	74
Table 4-1. Explosive Characteristics for NEDE2 Shots.	79
Table 5-1. Characteristics for the NEDE Explosions	100
Table 6-1. Shot Information for the 2013 NEDE2 Experiment (Shots 1-4).	115
Table 6-2. Velocity and Attenuation Model for Barre, VT region.	121
Table 6-3. DJ91 Parameters for NEDE2 Shots 1-4.	124
Table 7-1. Explosive Characteristics for NEDE2 Shots.	138
Table 7-2. Explosion Energy Estimates.	147
Table 9-1. Explosion characteristics.	168
Table 9-2. Rock properties from laboratory measurements.	168
Table 10-1. Origin, yield, and weather information for the NEDE2 explosions in this study. ..	190
Table 10-2. Percent Error for Predicted and Observed Data	203
Table 11-1. Bulk Properties of Barre Granite.	208

ACKNOWLEDGMENTS

We wish to thank the Air Force Research Laboratory for funding the experiment under contract AFRL-FA9453-10-C-0257. Special thanks goes to Don Murray and Rock of Ages Corp. for allowing us to return and impose on their operations. Tim Rath (Maxam NA) provided invaluable explosive knowledge and helped successfully conduct the blasts. Aaron Ferris and Peter Hubbard (WGC) provided tireless field support and risked life and limb. Noel Barstow and the IRIS PASSCAL team once again loaned us equipment on a last minute request to allow us to collect the necessary data. Dan Kleinert of the National Center for Physical Acoustics loaned two infrasound sensors to the project. We appreciate the helpful Vermont residents who let us dig in their yard to install seismometers on their property. The inversion code was written by David Yang (Yang, 1997). We thank Howard Patton for discussing various aspects of his source model with us. We thank Michael Pasyanos, Sean Ford, and William Walter for assistance in estimating the DJ91 source spectra. We thank Igor Morozov of University of Saskatchewan for fruitful discussions.

1. SUMMARY

INTRODUCTION

Explosions generate S waves (*Lg*) that can be used as stable estimators of yield for nuclear explosion test sites in different emplacement media and under variable confinement conditions and tectonic stresses. The Nuclear Explosion Monitoring (NEM) research community has no unifying model for S wave generation from explosions. Instead, there are only theories on the mechanisms for S wave generation from explosions. Proposed explanations for the *Lg* phase include *pS* conversions at the free surface (Xie and Lay, 1994) and *Rg* generated by a compensated linear-vector dipole source (CLVD; Gupta *et al.*, 1997; Patton and Taylor, 1995; Stevens *et al.*, 2003a; Patton *et al.*, 2005) that is scattered (Myers *et al.*, 1999) into *S* and/or *Lg* along the propagation path due to topography (Myers, 2007) and/or geology heterogeneity (Lay and Xie, 2007). Modeling by Sammis (2003) has postulated that crack nucleation and growth can generate significant S waves in the far-field. To date, it has been difficult to separate each mechanism in the available NEM datasets in order to quantify their relative effects on S wave generation.

Two of the proposed mechanisms for S wave generation involve secondary processes related to the damage and deformations caused by the explosions. First, outside the cavity radius, there is a “shell” of fragmented rock. Sammis (2002) theoretically showed that the integrated effect of the nucleation and growth of the fractures in this shell can generate secondary seismic waves as large as the P waves from the explosion itself.

The second proposed method for S wave generation from late term damage seems consistent with the Compensated Linear Vector Dipole (CLVD) source, which is an elastodynamic equivalent of a conical source. In this case, it is an inverted cone of damaged rock with apex at the detonation point (Patton *et al.*, 2005). Media within the cone deforms and fails as a result of tensile stresses caused by the downgoing shock wave reflected off the free surface. Spallation is an obvious example of such failure. Driven block motions at depth, as envisioned by Masse (1981), is another example, which may have greater significance for seismic wave generation.

NEDE1

Weston Geophysical Corp., New England Research, Inc., and several geotechnical consultants conducted the New England Damage Experiment (NEDE Phase 1; NEDE1) in central Vermont during July 2008. A series of five explosions with yields between 61 and 122 kg and three types of explosives (black powder (BP), ammonium nitrate and fuel oil with emulsion (heavy ANFO; HANFO), and Composition B (Comp B)) were detonated in homogeneous low fracture density granite. The goal of the experiment was to generate different amounts/types of rock damage around the source by using explosives with different velocities of detonation (VOD), ranging

from 0.5 to 8.1 km/sec, and then relate the shear wave generation to the amount of damage. Increased VOD causes increased borehole pressures, which exceed the rock's compressive strength, and results in more extensive fracturing of the source rock. This zone of highly fractured rock may prevent the explosive gases from driving long fractures. In contrast, slower VOD explosives generate fewer fractures around the borehole, but the explosive gases are able to enter the cracks and drive long fractures. Surface observation of the test site confirmed this as few radial fractures were found for the fast VOD explosive, multiple small cracks were seen for the middle VOD explosive, and large fractures with surface displacement were found for the slowest VOD explosive.

NEDE2

A few questions were raised during the analysis of the NEDE1 data and a follow-up experiment (NEDE Phase 2; NEDE2) was planned to address these questions. The experimental field phase of the NEDE2 was conducted during June 2013. The experiment was carried out in the same granite quarry near Barre, VT as the original NEDE1. Approximately 40 sensors were deployed to record the blasts. The primary objective remained to identify possible source(s) of shear wave generation resulting from rock damage during explosions. Instead of using equal weights of each explosive, NEDE2 utilized equivalent TNT yields (~68 kg) of each explosive so that the blasts would release similar amounts of energy. The NEDE2 also detonated a deep shot to reduce effects of the free surface and reshoots (i.e. detonate an explosion in the damage zone of a previous blast) to examine fracture decoupling and driven fracture effects. In addition to reoccupying sensor sites from a NEDE1 linear array to a distance of 21 km, a ring of sensors was installed at 6 km distance to measure azimuthal radiation effects.

This report provides a detailed description of the NEDE2 field experiment (Chapter 2) followed by analyses of the resulting data. We analyzed the relationships between the VOD of explosives and seismic wave radiation for small chemical explosions (Chapter 7). The Comp B shots produced larger P wave amplitudes than equivalent yield (W in kg of TNT equivalent) HANFO and BP shots. The BP shot had the lowest amplitude, despite being the same TNT equivalent yield. Analysis of the source spectra (Chapters 4 and 7) revealed that the BP shot has the lowest corner frequency and steeper high frequency roll off than the HANFO and Comp B shots. These observations indicate that the increase in the VOD shifts the seismic energy toward higher frequencies and may reduce low frequency radiation. High frequency deficiency in the far-field spectra for the BP shot can in part be explained by the slower burn rate resulting in longer source impulse duration. Increase in low-frequency seismic energy for the Comp B shot in comparison with the HANFO shot is likely caused by the presence of water in the shot borehole. The NEDE1 Comp B shots, conducted in dry boreholes, had reduced low frequency amplitude compared to the HANFO shots as well as the NEDE2 Comp B shot.

The estimated total seismic energy radiated by the BP shot is lower than the energy radiated by the HANFO and Comp B shots. The seismic efficiency (Chapter 7) for the BP shot is only 0.35%, while it is 2.2% for the HANFO shot, and almost 3% for the Comp B shot. The measured seismic efficiencies for HANFO and Comp B are consistent with the estimate of approximately

3.7% made by Haskell (1967) for granitic rocks, while the seismic efficiency for the BP is significantly lower.

The observed S wave radiation pattern is consistent with the opening of tensile fractures approximately parallel to the host rock rift direction (Chapter 7). Opening of the rift-parallel fractures is also confirmed by core analysis (e.g. Martin, *et al.*, 2011b). The presence of surface fractures from the BP and Comp B shots correlates with the increase in S/P amplitude ratios for these shots (Figure 1-1). The HANFO shot, which did not produce surface fracturing, has the second smallest S/P ratios, followed by the deep HANFO shot. Analysis of S/P amplitude ratios suggests that the S waves for the shallow HANFO shot consist of approximately 54% scattered waves and 46% radiated by the tensile fractures. For the Comp B shot, the scattered S waves account for 48% of the total amplitude, while radiated S waves constitute 52%. Comparison between the observed and model predicted S/P ratios for the BP shot indicates that opening of the tensile fractures can account for almost the entire far-field radiation. This observation suggests that the majority of the energy produced from a slow velocity of detonation can be redirected into the opening of fractures along zones of pre-existing weakness, which can explain significant differences in the spectral content compared to the HANFO and Comp B shots. Low seismic radiation efficiency of the tensile fracturing can explain the low amplitudes for the BP explosion.

Moment tensor solutions for the NEDE2 shots show dominant diagonal elements (Chapter 3); however, we observe significant off-diagonal components indicating non-isotropic motions. The BP shot produced the smallest seismic moment, which is further confirmed by a reduction in high frequency energy compared to the HANFO and Comp B shots.

Modeling the seismic moment (Chapter 6) shows that the Denny and Johnson (DJ91) moments produced synthetic data that fit within the scatter of the observed Rg spectral amplitudes above 3 Hz; however, below 3 Hz, the synthetic spectra predict more Rg energy than observed from the explosions. Mueller-Murphy (MM71) moments produce synthetic Rg spectral amplitudes too large to match the observed data. The best fit to the observed data results when using the Patton (2012a, 2012b) late-time damage source model, which is tied to the DJ91 theoretical moment, with an added damage component modeled by a CLVD moment tensor. The Patton model results in synthetic data that fit with the scatter of the observed data at all frequencies, with the exception of the deeply buried shot.

Two NEDE2 explosions were conducted in the damage zones from NEDE1 explosions (reshoots). Shooting in the fractured emplacement medium leads to decreased seismic amplitudes (Chapters 4 and 5). The decrease is more pronounced in the high frequency part of the spectra, particularly if the explosions are conducted in water-saturated rocks.

The deep HANFO shot produced reduced P amplitudes below 10 Hz and reduced S and Rg amplitudes at most frequencies compared to the shallow HANFO shot. The greater confining

pressure for the deep shot likely resulted in reduced fracture generation, which could be responsible for the lessened low frequency and shear energy (Chapter 5). A comparison of a larger NEDE1 HANFO shot to a smaller NEDE2 HANFO shot at similar depths indicated smaller P/S and P/Rg ratios for the larger shot, while the P amplitudes remained similar. These results suggest increased rock damage results in larger shear and Rg phases (Chapter 4).

In general, our results suggest a correlation between S/P amplitude ratios and explosion driven surface fracturing (e.g. more fracturing causes increased S/P ratios). Travel time modeling of the shear phases (Chapter 8) is consistent with primary shear wave generation occurring at or near the source and not along the travel path.

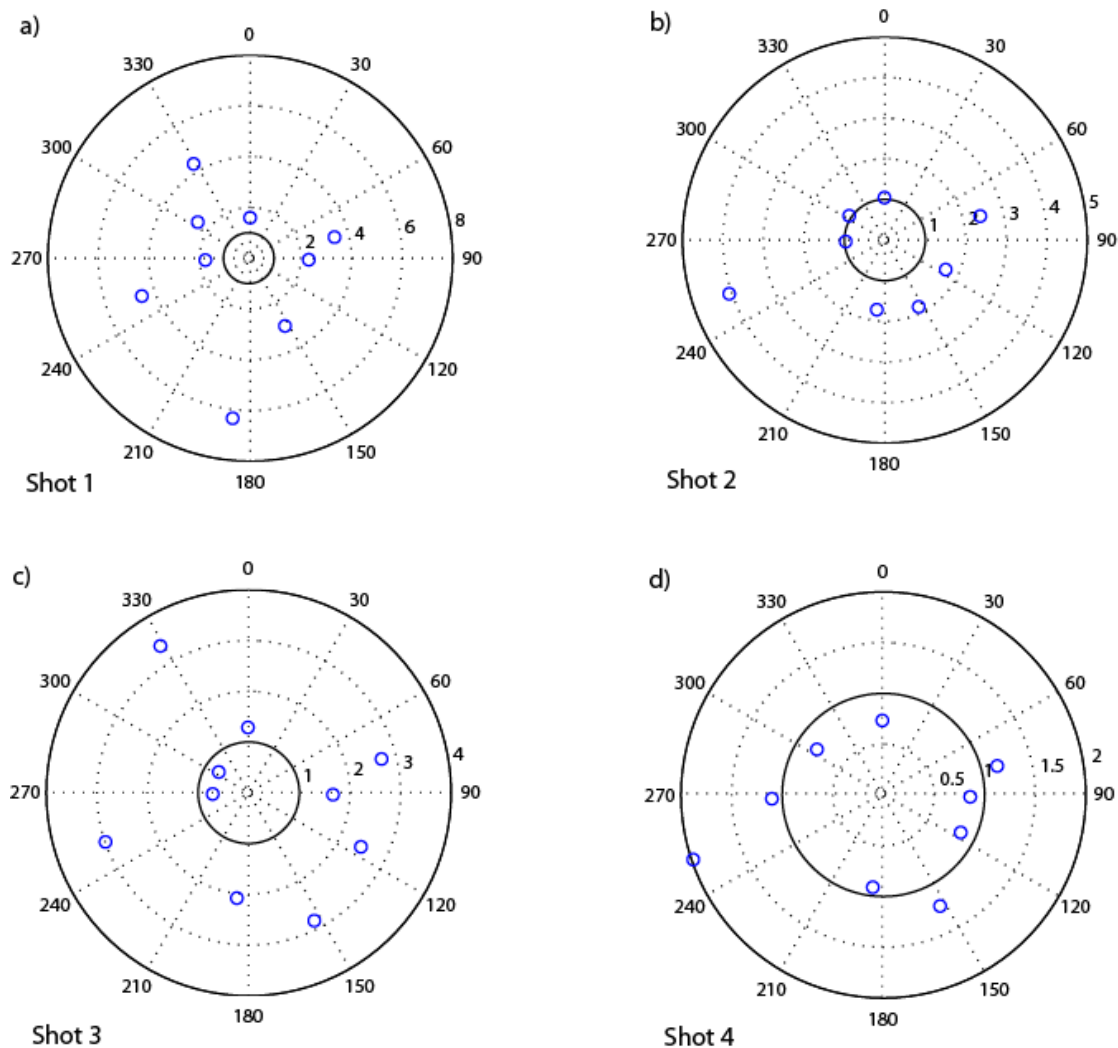


Figure 1-1. Azimuthal variations of S/P amplitude ratios for: a) Shot 1, b) Shot 2, and c) Shot 3, and d) Shot 4. Vertical component was used to measure P-wave amplitudes, while S-wave amplitudes were measured on the transverse component.

2. NEW ENGLAND DAMAGE EXPERIMENT 2 (NEDE2)

INTRODUCTION

WGC and NER conducted the experimental field phase of the follow-up New England Damage Experiment (Phase 2; NEDE2) during June 2013. The experiment was conducted in the same granite quarry near Barre, VT as the NEDE1. The goals of this experiment were to address questions created by the first experiment in July 2008 and to test new theories that were proposed from the original dataset. A primary objective remained to identify possible source(s) of shear wave generation resulting from rock damage during explosions.

The velocity of explosive detonation (VOD), resulting borehole pressures, and loading rates (Stroujkova *et al.*, 2012) have been shown to influence the amount of damage from an explosion¹. A faster VOD generates higher pressures that crush the rock into a powder, which inhibits the explosive gasses from driving fractures during the crack forming processes. We detonated various types of explosives with significantly different VOD so we could alter the quantity of damage from each source. During the first experiment, we detonated equal weights of the different types of explosives. Since the explosives have differing energy densities and burn rates, the explosions released different amounts of energy. In the follow-up experiment, we controlled the amount of each explosive so that the explosive charges represented similar TNT equivalent yields.

In addition to examining the result of damage effects immediately surrounding the blast, a deeper shot was conducted to test the theory that shear waves can be generated by spallation and permanent ground deformation. This test was also conducted to test new theories concerning the effects that reduced damage for deeper explosions have on surface wave generation (Patton, 2012a, 2012b). Two additional shots were conducted in the damage zones created during the NEDE1. These shots provided additional data for (and were paid for) by the Fracture Decouple Experiment, a DTRA-funded experiment to quantify amplitude reduction caused by shooting in the damage zone of a previous explosion.

Seismic sensors were installed specifically to record this experiment, and we occupied many of the same sites as in NEDE1 when possible. Additionally, we deployed a circular network to examine source radiation pattern effects based on lessons learned from the first NEDE experiment. This section of the final report documents the field project and the data collected.

¹ <http://www.johnex.com.au/index.php?section=105> (last accessed in July 2008).

OBJECTIVE

Recent advances in explosion source theory indicate that the damage that occurs near an explosion is a prominent source of *S*-wave energy. The Ashby and Sammis (1990) model for crack nucleation and growth predicts *S*-wave generation in the far field (Figure 2-1; Sammis, 2002). Modeling by Patton *et al.* (2005) and Stevens *et al.* (2003b) have shown the importance of the cone of damage above a source, modeled by a compensated linear vector dipole (CLVD), in generating *R_g* in the near field and *S* (*L_g*) in the far field, respectively. The phenomenology in the CLVD regime includes block motions, crack damage, spallation, and permanent deformation. The NEDE2 was conducted to collect improved data for testing these theories and answering questions regarding shear wave generation mechanism(s).

Two additional explosions were conducted in conjunction with the Fracture Decouple Experiment. Explosions were conducted in the damage zones created by the two 270 lb explosions from the NEDE1 experiment and provided additional data on fracture decoupling.

LOCATION

The NEDE2 was conducted in the Barre granite, a homogenous hard rock with low fracture density (Figure 2-2), to allow study of the damage zones and fractures created by a fully confined and contained explosion. Figure 2-3 shows a general geologic map of Vermont with a black box showing the location of the Barre granite. The geology of Vermont is an extension of the Appalachian Mountains with structural trends that generally run in a north to northeast orientation. The Barre granite is a felsic intrusion into Silurian to Devonian age rocks of the Connecticut Valley-Gaspe Basin caused by melting due to closing of a basin and collision of continental landmasses (Doolan, 1996). Significant reshaping of the land occurred under thick ice sheets.

The fine-grained Barre grey granite has been quarried for over 200 years as a monument stone due its low fracture density and homogeneous composition. While coring the granite for our test applications in NEDE1, the driller often had to snap the core from the bottom of the hole due to a lack of naturally occurring fractures. A site near the active quarry pit was chosen for the blasts (Figure 2-4). The upper 50 feet of fractured and weathered granite had been stripped off at this site, which allowed us to be closer in depth to the relatively unfractured, monument-quality Barre granite.

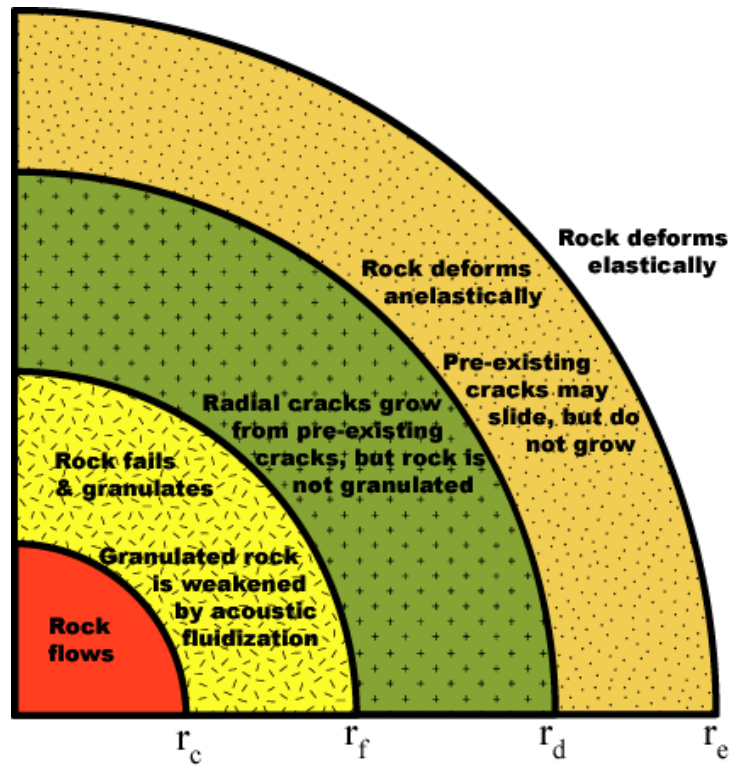


Figure 2-1. Rheology surrounding an underground explosion (after Rodean (1971) and modified by Sammis for acoustic fluidization from Melosh, 1979).



Figure 2-2. Photograph of 3-5 m thick relatively unfractured sections of Barre granite. The test site was located behind this granite ledge.

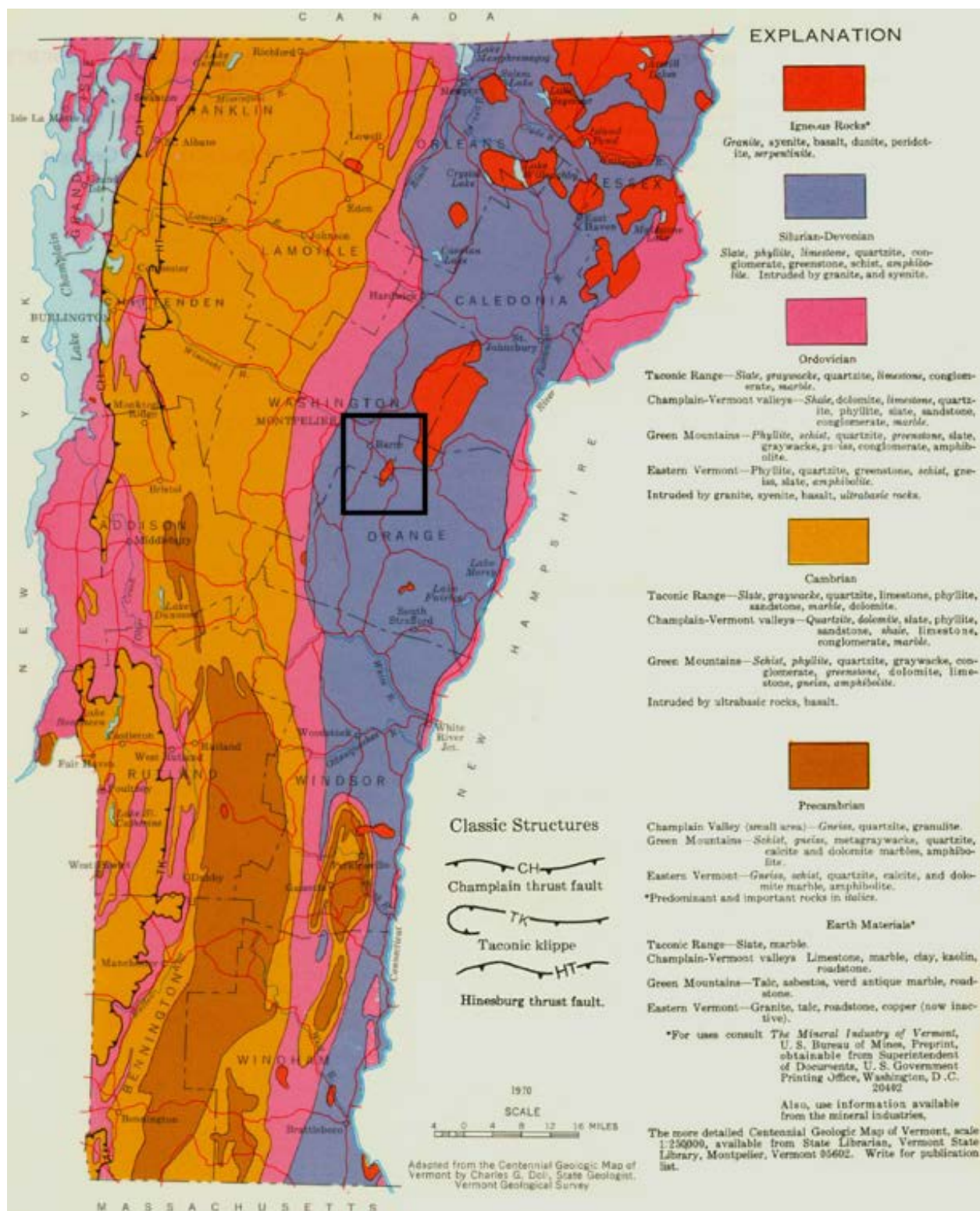


Figure 2-3. Geologic map (modified) from the Vermont Geological Survey. The black box highlights Barre, VT and the Barre granite igneous intrusion to the southeast. Source: <http://www.anr.state.vt.us/DEC/GEO/images/geo5.JPG>



Figure 2-4. Location of the test site north of the active Rock of Ages quarry.

DATA RECORDING

The NEDE2 explosions were recorded on over 36 seismic instruments, including seismometers, accelerometers, acoustic sensors, and high-definition video cameras. The seismic instrumentation was deployed at distances of less than 1 m to 24 km from the explosions. We recovered >97% of the seismic data. The seismic systems were deployed as part of three networks including the near-source network at distances less than 1 km, a ring at ~6 km distance with ~30° spacing, and a linear array extending 24 km to the SE of the quarry with 3 km spacing.

Near-Source Array

The near-source network was composed of 16 sites using 100 g Endevco accelerometers, 4 g TerraTech accelerometers, a REFTEK 131A-02/BH accelerometer, Sercel L-4C 3D seismometers, and NCPA (Univ. of Mississippi) acoustic sensors. Table 2-1 lists the locations and instrumentation deployed for the near-source array. Figure 2-5 shows the locations of the test bed sensors and the shot locations. The remainder of the near-source stations can be seen in Figure 2-6.

Endevco accelerometers were grouted in place (Figure 2-7 & Figure 2-8) ~1 m from the blast hole for Shots 1-6 (NS11-NS16). We were short one digitizer so NS14 had the recorder through 18:00 UTC 6/22/2013. After this, the recorder was moved to NS13 for the remaining two shots (Shot 3 & Calibration 3).

TerraTech accelerometers were buried around the test site to provide additional data for moment tensor analysis (NS01-NS05). A borehole was drilled next to NS01 and the REFTEK borehole accelerometer was installed at ~29 m depth (NSBH).

NS06 consisted of a buried L-4C 3D and surface NCPA acoustic sensor and was installed close to the nearest residence to provide verification that vibration and noise limits were not exceeded. L-4C 3D seismometers were buried at NS07-NS10 and provided a close-in linear array from 300-600 m. NS10 recorded an NCPA acoustic sensor on channels 4-6.

All three-component surface sensors were oriented to true north. Data were recorded at 1000 sps on REFTEK RT130 or RT130S digitizers for all stations. More recording parameters can be found in Table 2-2. The DAS and GPS clock were placed in a plastic tub. One or more 17 Ah AGM battery powered each station. Figure 2-9 shows an example of the plastic tub with recording equipment.

Table 2-1. Near-Source Sensors.

Station	Latitude (°; WGS84)	Longitude (°; WGS84)	Elev (m)	Depth (m)	DAS	DAS Serial	Sensor 1	Sensor 2	GPS Clock
NS01	44.15813	-72.47812	510	0.2	RT130S	B9D5	TerraTech 7	131A-02/BH 79	11382
NSBH	44.15813	-72.47812	516	29.4					
NS02	44.15827	-72.47858	530	0.2	RT130	AE6B	TerraTech 4		???
NS03	44.15737	-72.47933	495	0.2	RT130S	B9D7	TerraTech 9		11452
NS04	44.15635	-72.47737	493	0.2	RT130S	B973	TerraTech 3		11507
NS05	44.15635	-72.47905	493	0.2	RT130S	B9C9	TerraTech 1		11509
NS06	44.15708	-72.47377	455	0.5	RT130S	B9DB	L-4C 3D 70	NCPA 106	11296
NS07	44.15710	-72.48185	493	0.5	RT130S	B9C1	L-4C 3D 63		11302
NS08	44.15700	-72.48303	474	0.5	RT130	9E4B	L-4C 3D 61		11293
NS09	44.15693	-72.48428	470	0.5	RT130	9E42	L-4C 3D 66		11383
NS10	44.15668	-72.48553	462	0.5	RT130S	B9CB	L-4C 3D 62	NCPA 143	11285
NS11	44.15794	-72.47843	502	0	RT130S	B9D2	Endevco 2		11381
NS12	44.15797	-72.47791	503	0	RT130	9E18	Endevco 15		11475
NS13	44.15776	-72.47816	501	0	RT130S	B9C7	Endevco 7	WITS	11463
NS14	44.15770	-72.47795	501	0	RT130S	B9C7	Endevco 9		11463
NS15	44.15751	-72.47803	501	0	RT130S	B9CA	Endevco 4		11524
NS16	44.15753	-72.47765	501	0	RT130	9D8F	Endevco 6		11510

Table 2-2. Near-Source Recording Parameters.

Parameter	Value
Digitizer	REFTEK RT130S REFTEK RT130
Gain	1
Sample Rate	1000
Record Mode	Continuous
Data Format	Steim 2

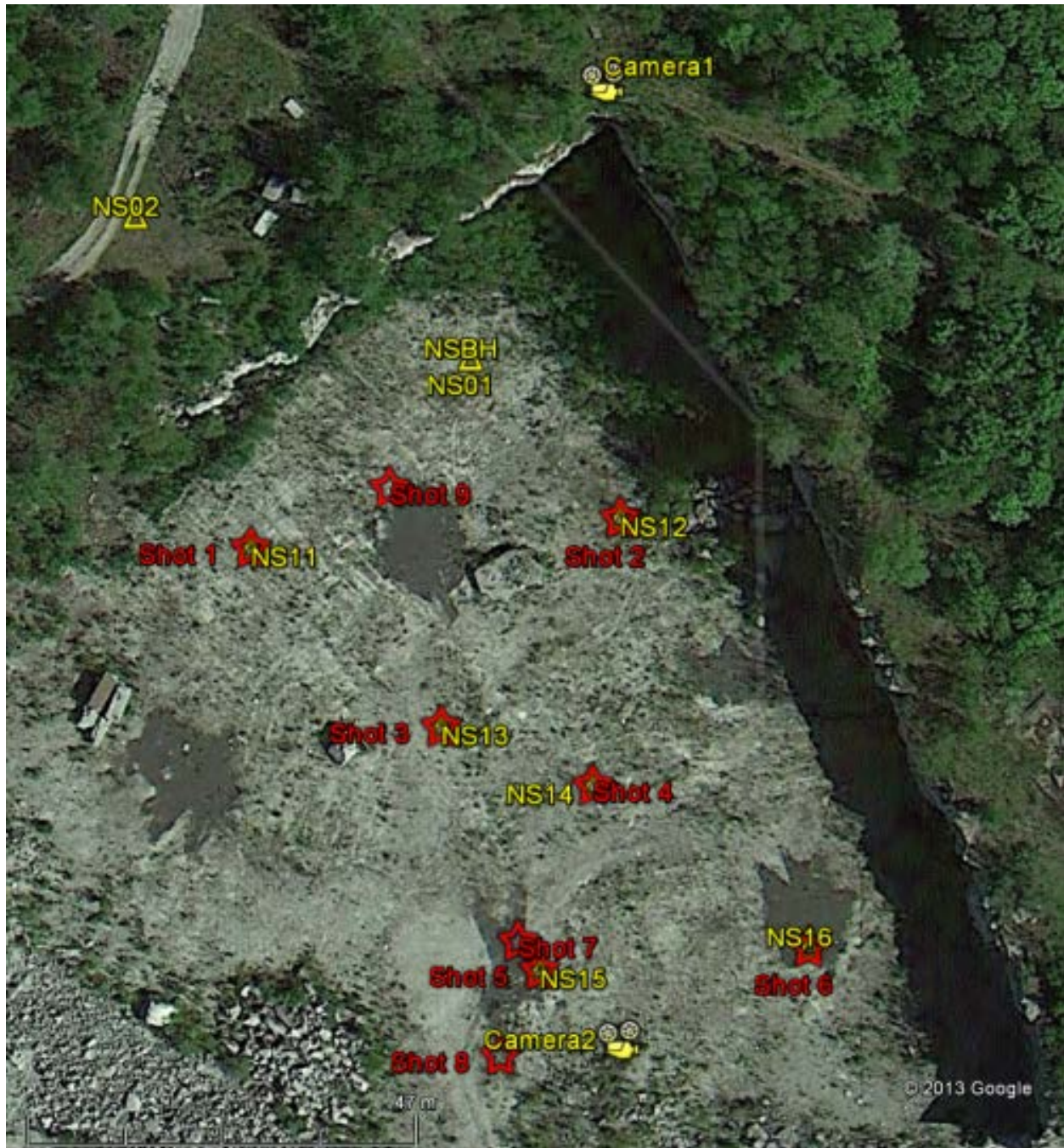


Figure 2-5. Test site stations (yellow triangles) and shots (red stars). NS11-NS16 were installed ~1 m from the blast borehole and the symbols are obscured by the red stars. NS13 and NS14 split time with the same DAS. NS14 recorded all shots except Shot 3 and Calibration 3, which NS13 recorded. The camera locations are shown overlooking the test site. (Google Earth Background)



Figure 2-6. Full near-source station network. (Google Earth Background)



Figure 2-7. Endevco accelerometers were grouted in place ~1 m from Shots 1-6.



Figure 2-8. NS15 Endevco accelerometer grouted and buried ~1 m from Shot 5.



Figure 2-9. Plastic tub housing the RT130 recorder and battery.

Short Period Arrays

Two short period arrays were installed at local distances. The first was a ring of 12 seismometers installed at a radius of 6 km from the test site. The sensors were spaced $\sim 30^\circ$ apart azimuthally. The second array consisted of seven seismometers (an eighth site was also part of the ring) deployed in a linear array to a distance of 24 km with an interstation spacing of ~ 3 km. We attempted to utilize the same sites occupied during the NEDE1 experiment to remove site effect variations; however, this was not always possible due to property permissions. Figure 2-10 shows the locations and Table 2-3 lists the station details. These systems were recording continuously at 500 sps. More recording information can be found in Table 2-4.

Stations R01-R12 and SE01-SE04 utilized PASSCAL BIHO boxes (quick deploy boxes) with 2 Hz L-22 seismometers. Stations SE05-SE08 used 1 Hz L-4C 3D seismometers with plastic tubs. Either 45 or 78 Ah AGM batteries in combination with solar panels powered the stations.

The sensors were placed in shallow holes, oriented to truth north, leveled, and loosely covered with soil (Figure 2-11). The soil was generally an organic rich dense soil, but sometimes had large amounts of decaying plant matter that left the site somewhat “spongy”. No solid bedrock was found at the sites within a foot of the surface. Therefore, it is expected that site responses will have some variation.

Table 2-3. Short Period Array Stations.

Station	Latitude (°; WGS84)	Longitude (°; WGS84)	Elev (m)	Depth (m)	DAS	DAS Serial	Sensor	GPS Clock
SE01	44.13357	-72.46658	521	0.5	RT130	92F3	L-22 222L	???
SE03	44.08342	-72.42962	467	0.5	RT130	983D	L-22 238L	1869
SE04	44.05868	-72.39523	597	0.5	RT130	943F	L-22 953L	1208
SE05	44.03678	-72.39517	544	0.5	RT130	9E4F	L-4C 3D 65	11511
SE06	44.01757	-72.37782	507	0.5	RT130	9D63	L-4C 3D 69	10906
SE07	43.99570	-72.36603	513	0.5	RT130	9E17	L-4C 3D 64	11284
SE08	43.96445	-72.33678	462	0.5	RT130	9DAA	L-4C 3D 68	11513
R01	44.21172	-72.47897	337	0.5	RT130	9805	L-22 1488	1309
R02	44.20173	-72.42900	502	0.5	RT130	947C	L-22 975L	3185
R03	44.16988	-72.41126	438	0.5	RT130	92E8	L-22 725L	550
R04	44.15655	-72.40298	490	0.5	RT130	9804	L-22 506L	1088
R05	44.13411	-72.40986	417	0.5	RT130	929A	L-22 ???	???
R06/SE02	44.10950	-72.44365	477	0.5	RT130	9442	L-22 1503L	1705
R07	44.09792	-72.48762	553	0.5	RT130	984D	L-22 740L	789
R08	44.10972	-72.52071	383	0.5	RT130	92C3	L-22 954L	1309
R09	44.14112	-72.54592	327	0.5	RT130	92A6	L-22 462L	2608
R10	44.15577	-72.55312	387	0.5	RT130	9245	L-22 ???	1084
R11	44.19044	-72.54471	357	0.5	RT130	984E	L-22 963L	1720
R12	44.20353	-72.51665	220	0.5	RT130	9144	L-22 ???	3249

Table 2-4. Short Period Array Recording Parameters.

Parameter	Value
Digitizer	REFTEK RT130
Gain	32
Sample Rate	500
Record Mode	Continuous
Data Format	Steim 2

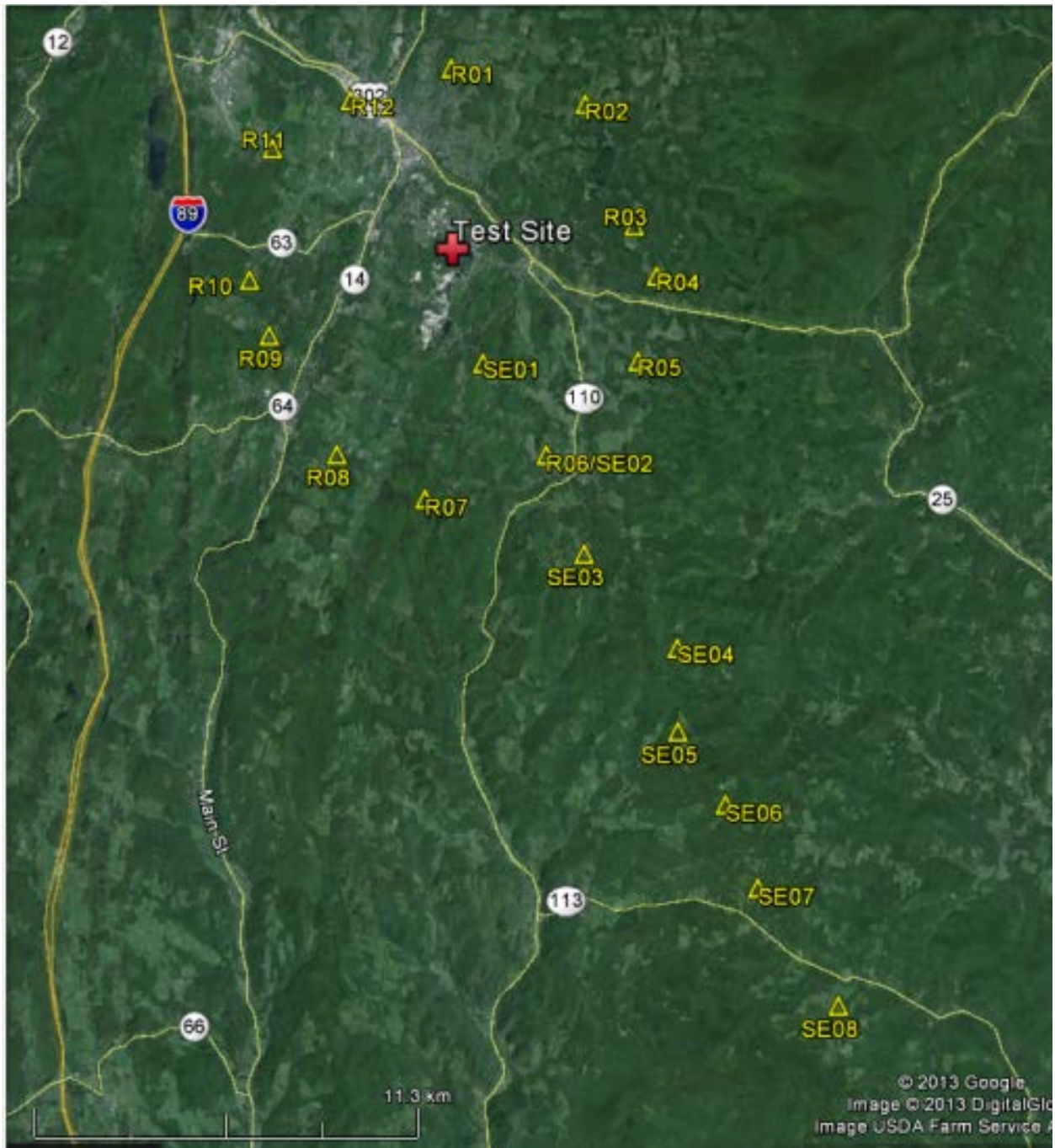


Figure 2-10. Short period array stations (yellow triangles). (Google Earth Background)



Figure 2-11. Example of orienting to true north and leveling an L-4C 3D sensor before burial.

Video

A Sony HDR-CX220 video camera recorded all of the explosions in order to study the surface disturbance. The video was recorded in Full HD format (1920x1080 60p) at 59.94 frames/second. Figure 2-12 shows the camera view of the test site prior to trimming vegetation out of the way. A second personal hand held video camera placed on a tripod was also used. The locations of the cameras are listed in Table 2-5 and plotted in Figure 2-5.

Table 2-5. Camera Locations.

Station	Latitude	Longitude	Elev (m)	Notes
Camera1	44.15839	-72.47794	526	Recorded all shots – Hi-Def Camera
Camera2	44.15741	-72.47792	501	Recorded some shots



Figure 2-12. Camera view before trimming vegetation.

Sensor Issues/Data Loss

The NSBH signal on channels 1 and 3 is weak because of faulty wiring inside the REFTEK sensor.

NS07 originally had 1 GB memory cards in an RT130S. The DAS stopped recording after filling the memory but before dumping to disk. We discovered that the RT130S cannot use 1 GB cards. Fortunately, the problem was found prior to the second day so we only lost the first day of shots.

The R08 RT130 at locked up during the night at ~01:00 UTC between the two days of shots. We lost the second day of shots.

The memory card at R10 was corrupt, but the data was recovered and no shots were lost.

Shot 9 at NS13 was lost after the data cable was melted by a fire associated with Shot 3.

EXPLOSIONS

Shot Characteristics

Nine explosions were detonated at the test site on 21-22 June 2013 (Table 2-6 and Figure 2-13) and their charge characteristics are provided in Table 2-7.

The shot locations were measured by placing a hand held GPS unit on a board covering the shot hole (Figure 2-14) and allowed to average for at least 10 minutes. Horizontal accuracy is approximately 3 m while vertical GPS accuracy is likely 5-10 m. Shot time was measured with the Weston Inexpensive Timing System (WITS), which measures the detonation of the explosive booster (detonator for the black powder shot). Timing accuracy for the WITS recorded shots is 2 milliseconds. WITS was not recorded for Shots 7 and 8 so the time was approximated with the surface accelerometer (NS15) and the estimated travel time from the WITS recorded Shot 5. Timing accuracy for these two shots is 10 milliseconds.

The shot holes were originally drilled (Figure 2-15) to varying depths so that Shots 1-3 would have the same Scaled Depth of Burial (SDOB), but drill cuttings and mud settled back into some of the holes skewing the planned hole depths.

The primary goal of this experiment was to examine how damage affects shear wave generation. One way to vary damage is to use explosives with dramatically different velocity of detonation (VOD). As done with the NEDE1 experiment, this experiment used black powder (BP), ANFO/Emulsion (Heavy ANFO; HANFO), and Composition B (Comp B).

The NEDE1 experiment used the same weight of each explosive. For this experiment, a 150 lb (68 kg) TNT equivalent amount of each explosive was used.

Table 2-8 lists the TNT equivalency factors for BP, HANFO, and Comp B. The weight of the 14 oz boosters, primarily composed of Comp B, were included in the charge weight calculations.

Table 2-6. Origin Characteristics for NEDE2 Shots.

Shot #	Latitude (°;WGS84)	Longitude (°;WGS84)	Elev (m)	Date (UTC)	Julian Date (UTC)	Time (UTC)	Description	Shot Order	WITS
1	44.15794	-72.47843	507	6/21/2013	172	20:22:10.701	Black powder virgin rock	1	✓
2	44.15797	-72.47791	509	6/22/2013	173	17:29:09.320	Heavy ANFO virgin rock	7	✓
3	44.15776	-72.47816	508	6/22/2013	173	18:15:33.492	Comp B (boosters) virgin rock	8	✓
4	44.15770	-72.47795	511	6/22/2013	173	14:46:42.734	Heavy ANFO Deep shot	6	✓
5	44.15751	-72.47803	507	6/21/2013	172	21:42:36.444	Reshoot of previous Heavy ANFO	5	✓
6	44.15753	-72.47765	511	6/21/2013	172	20:51:33.925	Reshoot of previous Comp B	2	✓
7	44.15754	-72.47806	514	6/21/2013	172	21:26:22.428	Comp B booster calibration	4	
8	44.15742	-72.47809	513	6/21/2013	172	21:13:54.476	Comp B booster calibration	3	
9	44.15800	-72.47823	508	6/22/2013	173	18:41:36.135	Comp B booster calibration	9	✓

Table 2-7. Explosive Characteristics for NEDE2 Shots.

Shot	Explosive 1	Explosive 2	Weight of explosive 1 (lbs)	Weight of explosive 2 (lbs)	TNT Equivalent Yield (lbs)	Charge bottom (m)	Charge center (m)	SDOB TNT Equiv (m/kt ^(1/3))	Hole Diameter (cm)
1	Black powder	N/A	250.0	0.0	150.0	14.20	12.89	305.7	22.2
2	Heavy ANFO	Booster	184.5	1.8	150.0	14.25	13.50	320.1	22.2
3	Comp B	Emulsion	100.7	31.6	161.2	13.36	12.32	285.2	22.2
4	Heavy ANFO	Booster	184.5	2.6	151.1	29.79	29.03	686.7	22.2
5	Heavy ANFO	Booster	184.5	1.8	150.0	14.02	13.31	315.6	22.2
6	Heavy ANFO	Booster	184.5	1.8	150.0	13.51	12.80	303.6	22.2
7	Booster	N/A	1.8	N/A	2.4	14.02	13.94	1319.1	10.2
8	Booster	N/A	1.8	N/A	2.4	10.67	10.59	1002.0	5.1
9	Booster	N/A	1.8	N/A	2.4	14.02	13.94	1319.1	5.1

Table 2-8. TNT Equivalency Factors.

Explosive	TNT Equivalency
Black Powder	0.6
Heavy ANFO	0.8
Composition B	1.35



Figure 2-13. Location of the shot points on the test site (Google Earth photo).



Figure 2-14. Plywood and plastic tarp covering the drill holes to prevent mud and rain from entering the hole. *GPS locations were made directly over the hole.*



Figure 2-15. Johnson Artesian drilling the holes and clearing the cuttings.

BP (Figure 2-16 and Figure 2-17) is traditionally used for firearms and fireworks because its slow burn rate produces gases that can propel a bullet but not damage the barrel. It has a low brisance, the rate at which an explosive reaches maximum pressure, which means it generates relatively fewer fractures in the rock around the explosive source. The fractures generated will be longer due to the escape of the explosive gasses. Occasionally, it is used to break monument stone, such as granite, without damaging the stone itself due to properties of gas expansion along pre-existing cracks.



Figure 2-16. Lowering a container filled with BP and the detonator to the bottom of the Shot 1 hole. *This container was used to ensure the detonator was in contact with the BP. The VOD and WITS cables are taped to the outside.*



Figure 2-17. Pouring the remainder of the BP into the hole.

HANFO (Figure 2-18) is the primary blasting agent used in the mining industry due to its stability, low cost, easy production, as well as optimum blast effects for rock fracturing. ANFO is considered a high explosive when properly confined and especially when mixed with an emulsion. We use the phrase “Heavy ANFO” to describe the 50:50 ANFO:Emulsion mix used for the NEDE2. The HANFO was detonated with two or three 14 oz boosters and a blasting cap (Figure 2-19).



Figure 2-18. Preparing a premeasured amount of HANFO for loading.

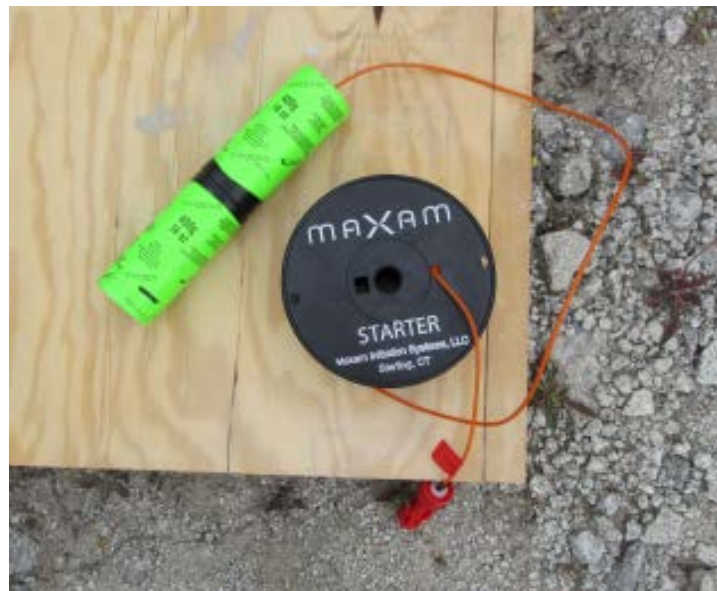


Figure 2-19. Initiation system of the HANFO charges including two 14 oz boosters, a blasting cap (inside the boosters), and shock tubing.

Comp B (Figure 2-20) is a military grade explosive composed of 60% RDX and 40% TNT (possibly up to 1% desensitizing wax). It is primarily used in military applications such as

munitions. Comp B is a shapeable charge and the high VOD of this explosive allowed it to be used in the first nuclear weapons.



Figure 2-20. Determining the cast Comp B charges were larger than the ordered specifications and would not fit down the hole.

The Comp B charges were cast specifically to fit our boreholes by Energetic Systems with a requirement that the charges should not be larger than 8" in diameter so they could easily fit in 8¾" holes with the tubing, wiring, and straps attached. Unfortunately, the charges were cast too large in diameter (Figure 2-20) and we could not use the cast Comp B charges. We improvised by building a column of boosters, which are primarily composed of Comp B, to simulate a cast charge (Figure 2-21). The charge was composed of 304 5.3 oz boosters. A small amount of emulsion was poured in the hole prior to loading the Comp B charge to increase explosive coupling to the borehole (Table 2-7).

Table 2-6 lists the total depth of the boreholes and the centroid depths of the explosive column. Stemming consisted of granite flour from drilling, a blast plug designed to lock into the borehole walls, and ½" gravel. The boreholes had an 8.75" to 9" diameter. A many-ton grout box was placed on the stemmed Shot 1 hole to ensure the stemming was not ejected (Figure 2-27).



Figure 2-21. Building a makeshift Comp B explosive after the cast charges would not fit downhole.

Issues with Water in the Blast Holes

During the NEDE1 experiment, water was not an issue at this test site as all drill holes were dry. This region experienced 28 straight days of precipitation prior to drilling the holes for the NEDE2 experiment. The result was that all holes were completed with at least some water. The amount of water ranged from a few inches in the Shot 1 hole to 27 m of water in the 33 m borehole sensor hole.

Water posed two fundamental problems for the experiment. The goal of the experiment was to create fractures of different types and lengths to examine seismic phase generation differences. Water in the holes improves the energy coupling but also causing fractures to be enhanced similar to hydraulic fracturing in the energy industry. The second issue with water relates to explosive loading and performance. Black powder will not burn when wet and although the HANFO is water resistant, pockets of water may become trapped inside the explosive column and reduce its performance.

To mitigate the water issues, a pump system was rented to drain the fracture systems and dry the holes. Since each hole had a different hydraulic head, it was believed the water was trapped in

isolated fracture systems and pumping had a chance of removing the water. A generator powered pump (Figure 2-22) was lowered into each hole (Figure 2-23) and the water pumped out (Figure 2-24).



Figure 2-22. Generator and submersible pump in a drill hole.



Figure 2-23. Submersible pump being moved between holes.



Figure 2-24. Water pumped from a drill hole.

All shot holes were completely evacuated of water except Shot 3 and Shot 4. After pumping shot hole 3, we could hear water flowing back into the hole and knew this would be the most difficult hole to dry. Since it would hold the Comp B charge, flowing water would not be an issue and we pumped as much water as we could from the hole. Ultimately, the hole was loaded with water at 7.6 m depth. This shot should not have resulted in surface cracking based on our modeling and previous experience, but a ~21 m fracture running approximately N/S was created on the surface. The video shows a series of fireballs erupting from the fracture (Figure 2-25) and igniting a digitizer enclosure close to the fracture almost a minute after the shot. It is likely that a water-filled fracture network was hydraulically fractured and extended to the surface.

Shot 4, the deep HANFO shot, was drilled to 30.6 m and had water standing at ~12 m depth when we arrived. After pumping the hole multiple times, the majority of the water was removed, but a small trickle could be heard entering the hole. A final pumping was performed followed immediately by loading the booster and HANFO (Figure 2-26). It is not known how much water was in the hole at detonation time, but it was likely at least a few feet. The water-filled fracture was higher in the hole so it is not believed that the water affected the detonation other than increasing the coupling to the borehole walls.



Figure 2-25. Fireball erupting from the Shot 3 surface fissure.



Figure 2-26. Preparing stemming for loading Shot 4 hole as soon as pumping was completed.

Velocity of Detonation

The velocity of detonation (VOD) was measured using a MREL HandiTrap II. A resistance wire is taped to the booster and lowered down the hole. As the explosives burn up the borehole, the resistance wire is melted and the recorder measures the decreasing resistance at 1 million samples per second. The resistance was then converted to distance and a velocity calculated. Further analysis of the VOD data may yield some information, but the VOD recorders appear not to have recorded properly.

Surface Effects

A Sony Full HD video camera (Figure 2-5 & Figure 2-12) recorded each explosion with 1920x1080p resolution at ~60 frames per second. The video data show the surface processes that occurred during the explosion so that secondary effects of the source can be modeled.

All shots generated spall, but no shots produced cratering, retarc, or flyrock. Shots 1 and 3 lost some containment through surface fracturing. Shots 5 and 6 lost minimal containment through nearby boreholes drilled for tomography or core logging in NEDE1. This loss of containment will affect the amount of gas available for driving fractures in the granite and will have to be taken into account during analyses, primarily of secondary seismic phases.

Shot 1 generated significant surface fracturing to the west of the shot hole and still video images are shown in Figure 2-27. A rough schematic of the fracture zone is shown in Figure 2-28 and a photo of the largest crack set generated by Shot 1 is shown in Figure 2-29. These cracks did not show vertical displacement. The surface sediments were simply disturbed by the escaping gas. The fracture set migrated from S of the shot hole to the NW. A large many-ton grout bucket was placed directly on the blast hole to prevent stemming ejection (Figure 2-27).

The Comp B Shot 3 did not behave as expected. Based on the NEDE1 experiment and theoretical predictions, the black powder and the HANFO shots had the best chance of surface fractures due to the large gas volumes generated. The Comp B shot should not have fractured the surface, yet a 21 m fracture system was found running nearly N/S about 6 m east of the shot hole. This fracture system emitted at least three fireballs based on videography (Figure 2-25), but likely released intense heat along the entire fracture as the vegetation was singed (Figure 2-30). Figure 2-31 shows the melted detonation tubing and charred Endevco data cable next to cracks from which fire was emitted.



Figure 2-27. Digitized still images of the Shot 1 detonation. *The fractures propagated from S of the shot to the NW.*

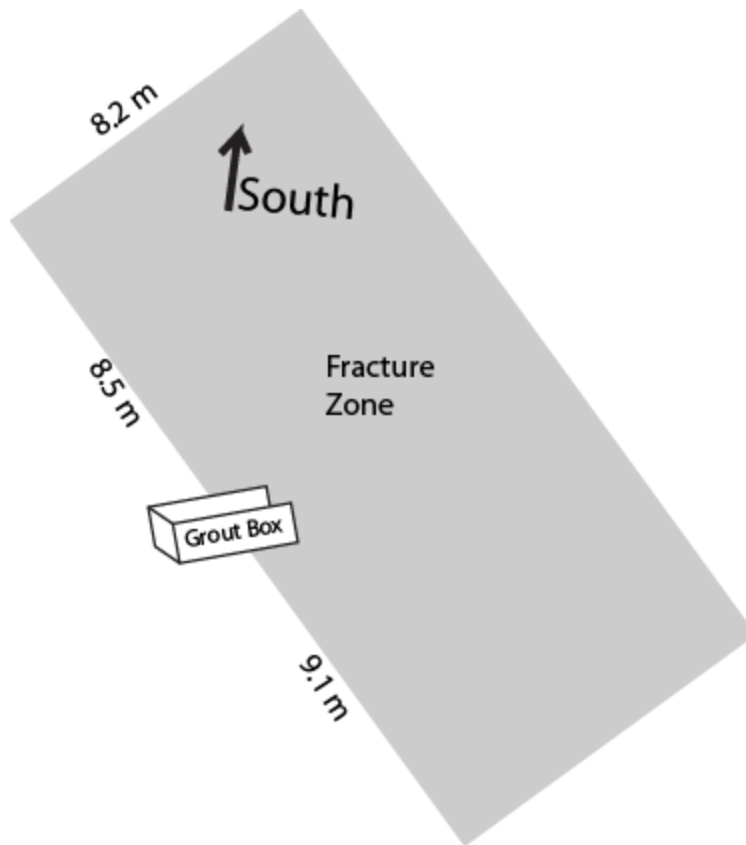


Figure 2-28. Rough sketch of approximate fracture zone created by Shot 1.



Figure 2-29. Largest cracks generated by Shot 1.



Figure 2-30. Singed vegetation along the fracture network from Shot 3.



Figure 2-31. Small cracks (shown by red ellipses) and burnt wiring and tubing (black arrows) generated by Shot 3. *Toe of boot shown for scale.*

SEISMIC DATA EXAMPLES AND ANALYSES

In this section, we present examples of the waveforms collected during the experiment and initial analyses.

Spall

Below are a few examples of the near-source data recordings. In Figure 2-32, the vertical spall from all six large non-calibration shots is recorded on the accelerometer installed 1 m from the blast hole. A classic near-source accelerometer record should show an impulsive shock wave arrival, a brief period of -1 g spall, and then a small spike(s) from the slap down(s). This series of events, with some complexity, can be seen from all shots. Shot 1 has a long duration, smaller amplitude shock wave arrival possibly caused by the slow “burning” of the explosives column instead of an instantaneous detonation. Shot 2 produced the largest recorded force of 75 g. Shots 3 & 6 also produced surface forces in excess of 30 g. As expected the double depth shot produced the smallest shock with only 2.7 g at the surface.

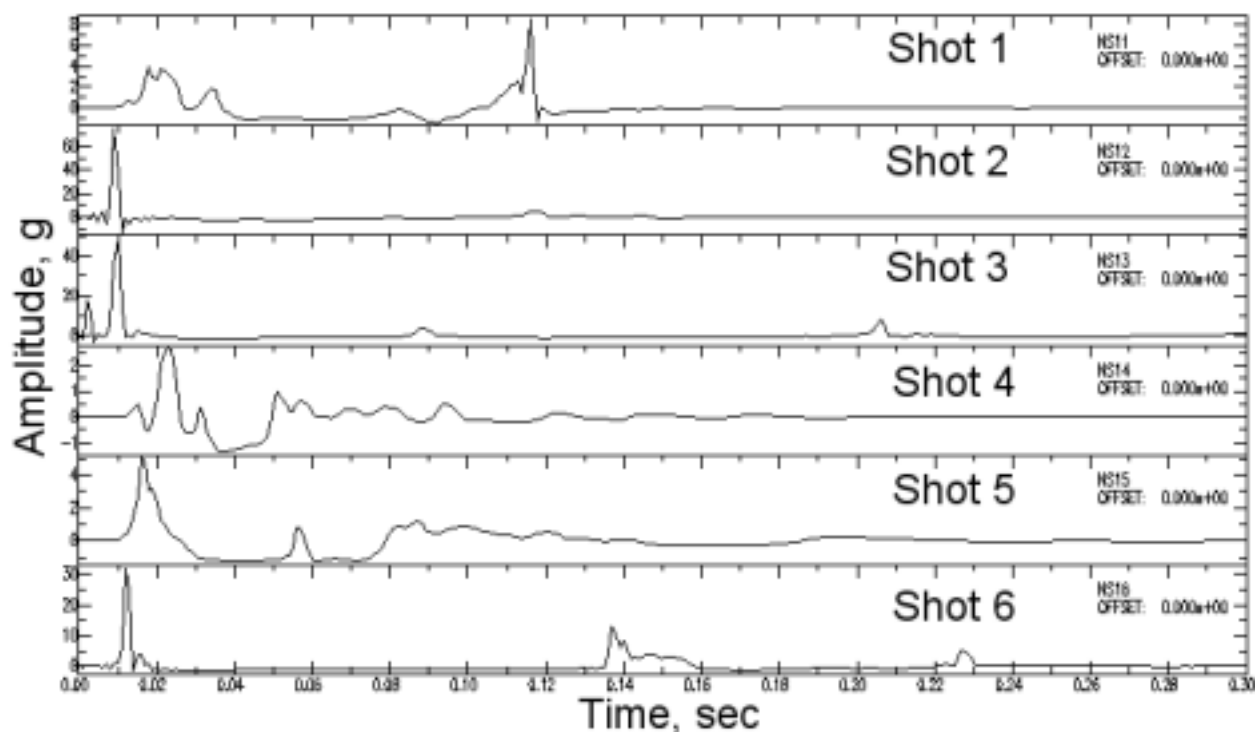


Figure 2-32. Near-source phenomenology for all six large shots recorded on accelerometers installed 1 m from the blast hole. *These data are not plotted on the same amplitude scales in order to better show the characteristics of the initial shock wave, the -1 g spall, and the spall slapdown(s).*

Waveform Examples

In Figure 2-33 through Figure 2-36, we present examples of the waveforms for the 6 large shots recorded on the near-source and radial networks. Figure 2-37 provides a record section of the Shot 2 data for the SE array.

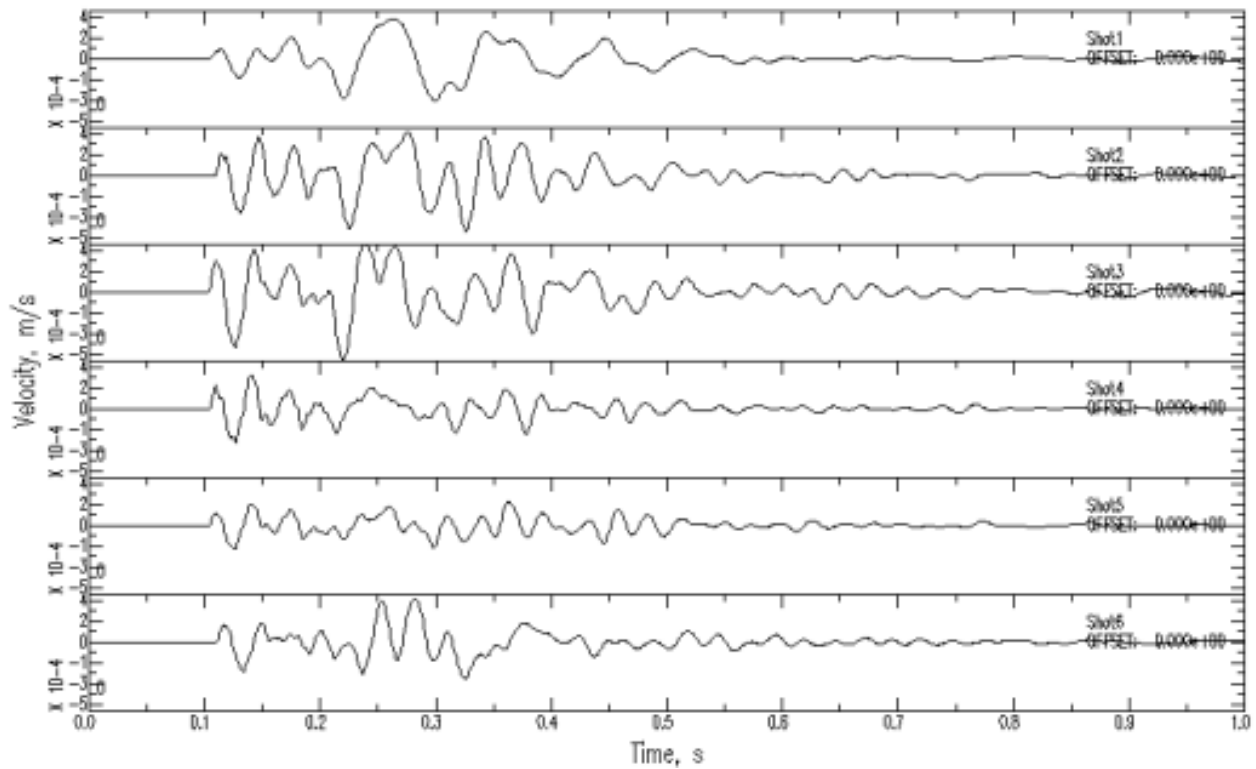


Figure 2-33. Shot 1 to Shot 6 vertical components at NS09 (~0.5 km).

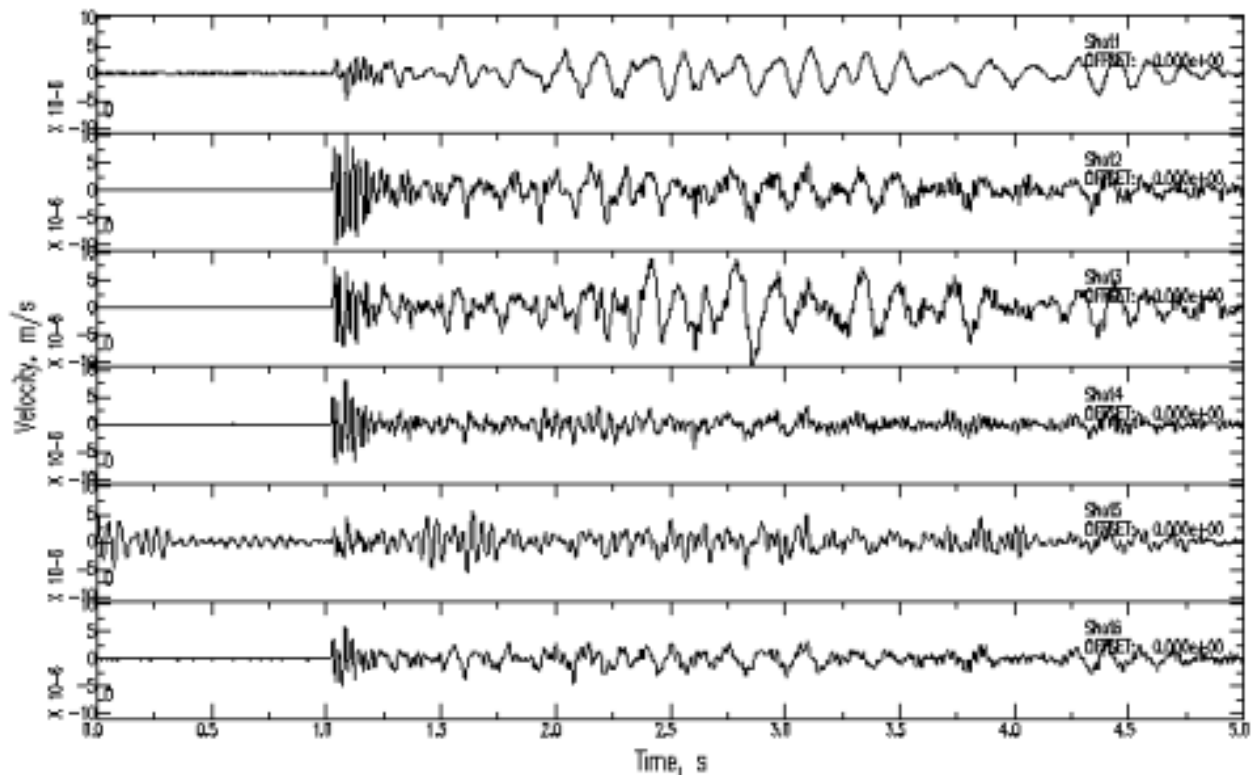


Figure 2-34. Shot 1 to Shot 6 vertical components at R03 (~6 km).

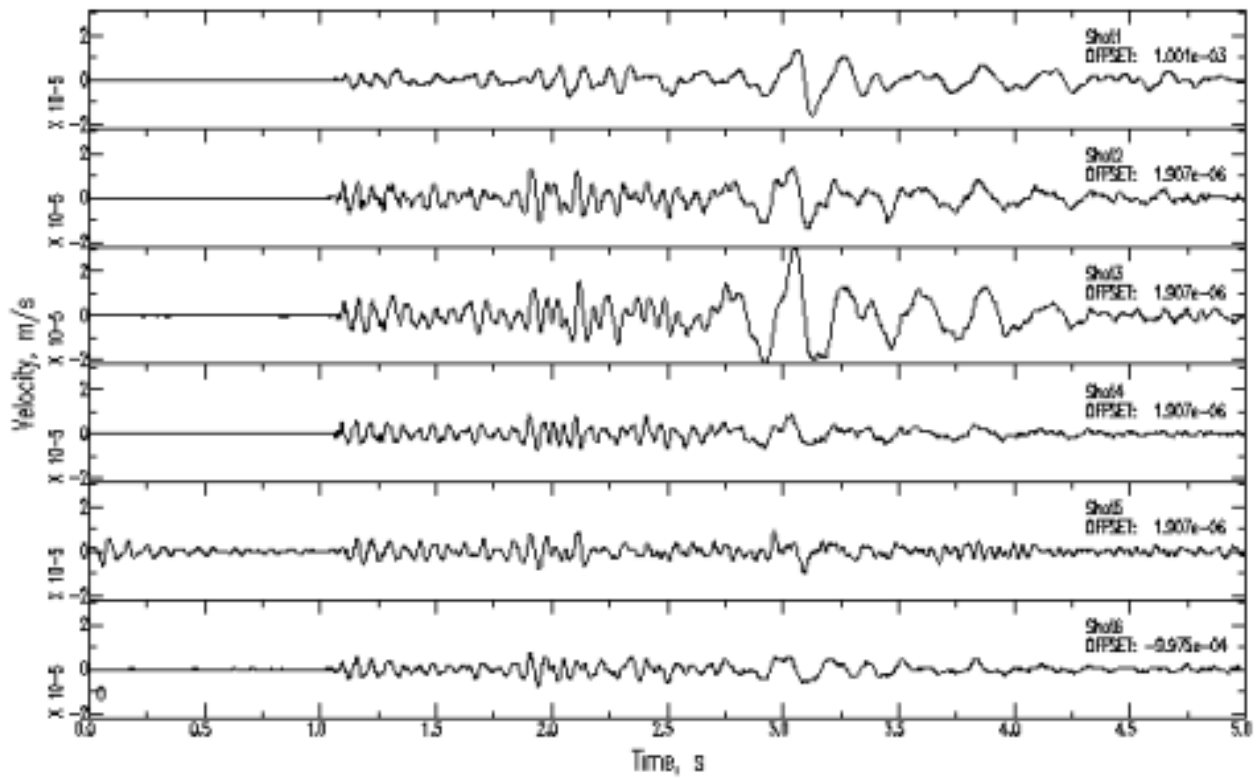


Figure 2-35. Shot 1 to Shot 6 radial components at R03 (~6 km).

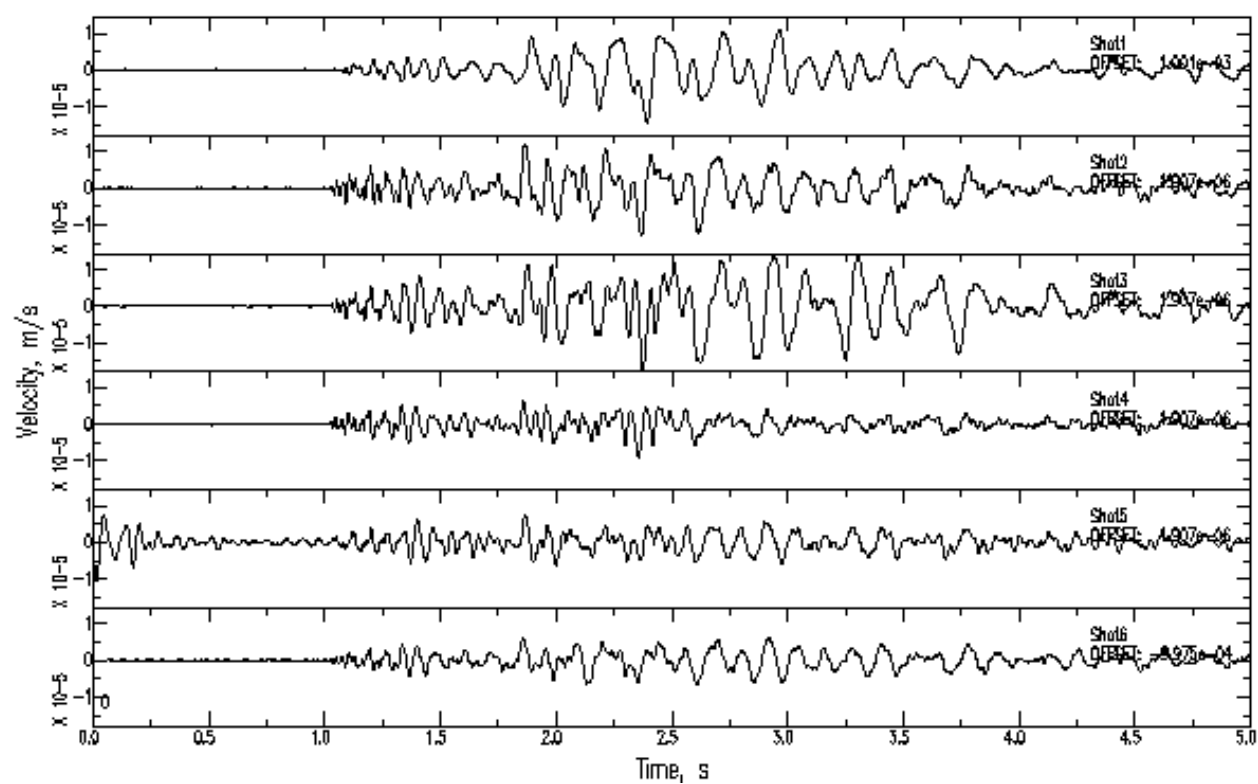


Figure 2-36. Shot 1 to Shot 6 transverse components at R03 (~6 km).

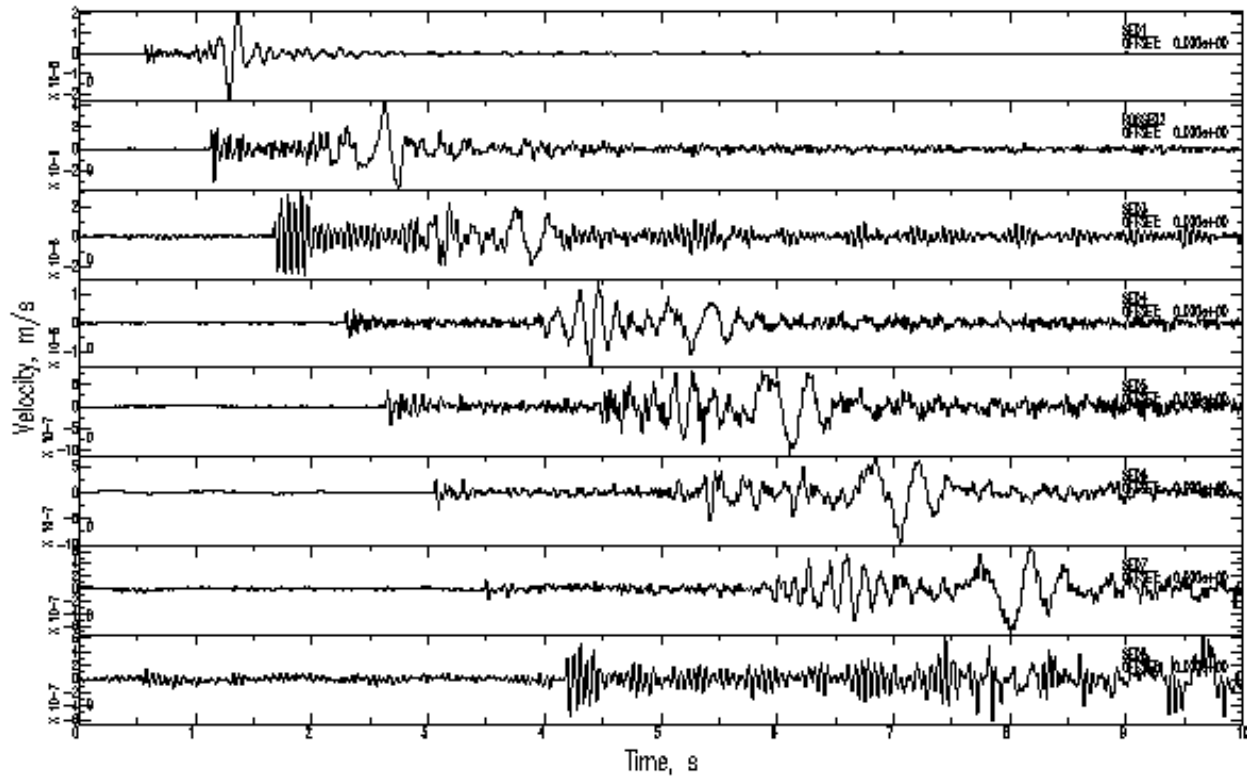


Figure 2-37. Shot 2 vertical components along the SE array (3-24 km).

Peak Particle Velocities

Peak particle velocity is often used by the mining industry to quantify the vibrations from their blasting operations in order to ensure they do not damage local residences or businesses. PPV can also provide a comparison of seismic amplitudes generated by various shots. PPV were computed using the vector summation technique (Leidig *et al.*, 2010) for the full waveform between 0 and 10 seconds after the origin time. Data contaminated by cultural or background noise were removed from the analysis.

The PPV with distance from a blast can be approximated using a power law equation:

$$PPV = K \times SD^A \quad (2-1)$$

where K and A are site constants. K is a function of the amount of energy transmitted to the source rock from the explosion. A is an attenuation term for the source rock. SD is scaled distance of the form:

$$SD = \frac{D}{\sqrt[3]{W}} \quad (2-2)$$

where D is distance (meters or feet), W is explosive charge weight (kg or lbs), and ε is either 2 or 3 for square root or cube root, respectively, depending on the charge dimensions and distance to the explosion.

A similar, but more thorough analysis was conducted for the NEDE1 shots (Leidig *et al.*, 2010) and the best-fit curve for NEDE1 Shot 4 was used as a comparison to the NEDE2 shots. Figure 2-38 through Figure 2-46 plot the observed PPV, best-fit power law equation, and the NEDE1 Shot 4 power law equation. Table 2-9 lists the best-fit PPV power law equations for the five NEDE1 and nine NEDE2 explosions.

In both experiments, the black powder shots produced seismic PPV $\sim 1/2$ those from the HANFO and Comp B shots (Figure 2-38). The most likely explanation is that the black powder deflagrates instead of detonating. The long duration burn results in a more gradual energy release, with reduced corner frequency and reduced PPV.

The HANFO shot amplitudes from the NEDE1 were slightly larger than the Comp B amplitudes, but that trend did not hold for the NEDE2 explosions (Figure 2-39 and Figure 2-40). For the NEDE2 explosions, the local distance (3-24 km) PPV were very similar but the near-source (<1 km) PPV were somewhat larger for the Comp B shot. It is not clear what caused this difference, but observations of surface fracturing indicate the NEDE2 Comp B shot did not behave like the NEDE1 Comp B shots. It is believed that the water filled borehole and fracture system increased the seismic coupling and resulting rock damage compared to explosions in dry rock.

The deep HANFO (Shot 4; Figure 2-41) PPV were significantly smaller at the near-source stations than the shallow HANFO (Shot 2) PPV but the PPV were similar at the local distances. The exponent for the Shot 4 best-fit equation is smaller than for the other large yield shots. The reason for the reduced seismic amplitude attenuation is not known but may be related to the shot depth. Body waves attenuate more slowly with distance than surface waves. Therefore, the PPV for this shot may represent the body wave energy at a wider range of distances, while the PPV for the other shots may be more affected by the surface waves. Further analyses are needed to understand whether this effect is related to body versus surface waves.

The PPV from the reshoot of the NEDE1 Comp B (Shot 6; Figure 2-43) were slightly larger than the PPV from the reshoot of the NEDE1 HANFO (Shot 5; Figure 2-42). A hypothesis of this experiment is that HANFO will create more rock damage than Comp B. The comparison of these two shots would support that theory and the results of the Fracture Decoupling Experiment as increased rock damage will result in reduced seismic coupling and lower PPV.

The PPV of the calibration shots attenuate much more quickly with distance as seen by the smaller A values. The shots have less reliable data due to their small size, so there is more

uncertainty in the results but all three shots show a consistent trend. Shot 7 (Figure 2-44) and Shot 9 (Figure 2-46) have A values between -1.84 and -1.94, while the PPV for Shot 8 (Figure 2-45) attenuate very rapidly and have an A value of -2.12. The calibration shots were significantly overburied (SDOB 1000-1300) and likely did not generate much surface wave energy. Instead of decreased attenuation with distance like Shot 4, these shots had a much higher corner frequency and the high frequency energy likely attenuated much more quickly resulting in smaller A values.

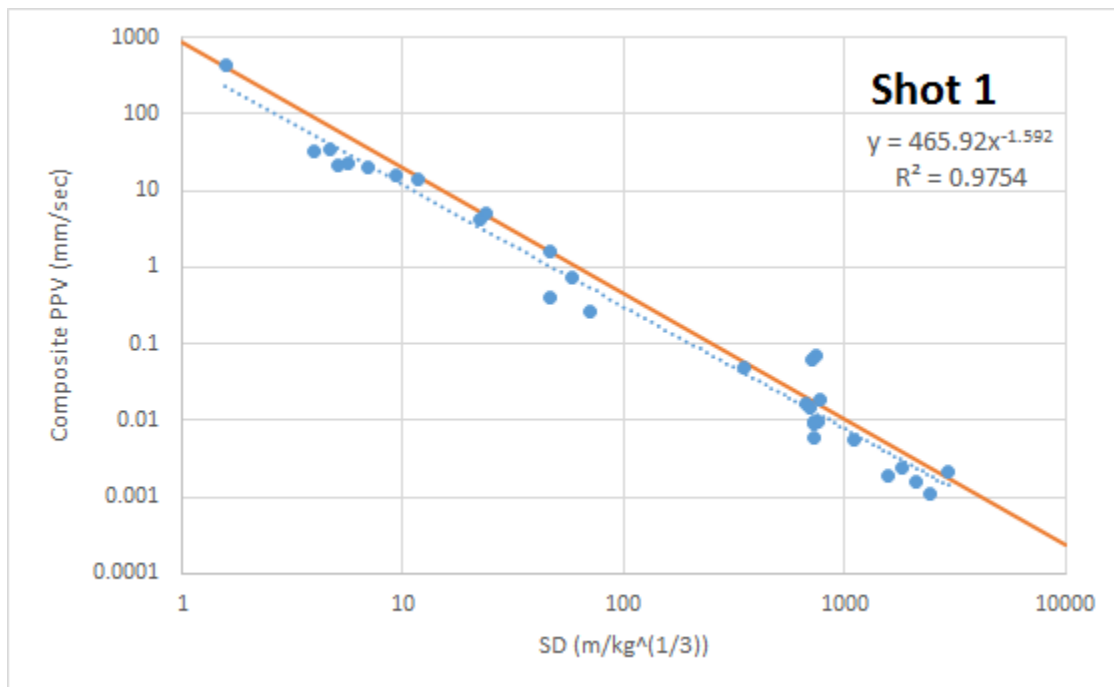


Figure 2-38. Shot 1 composite waveform PPV. *The blue dots represent PPV recordings with scaled distance, the dashed blue line is the best fit to these data (shown by the equations and correlation coefficients below the Shot label), and the red line is predicted based on the NEDEI results.*

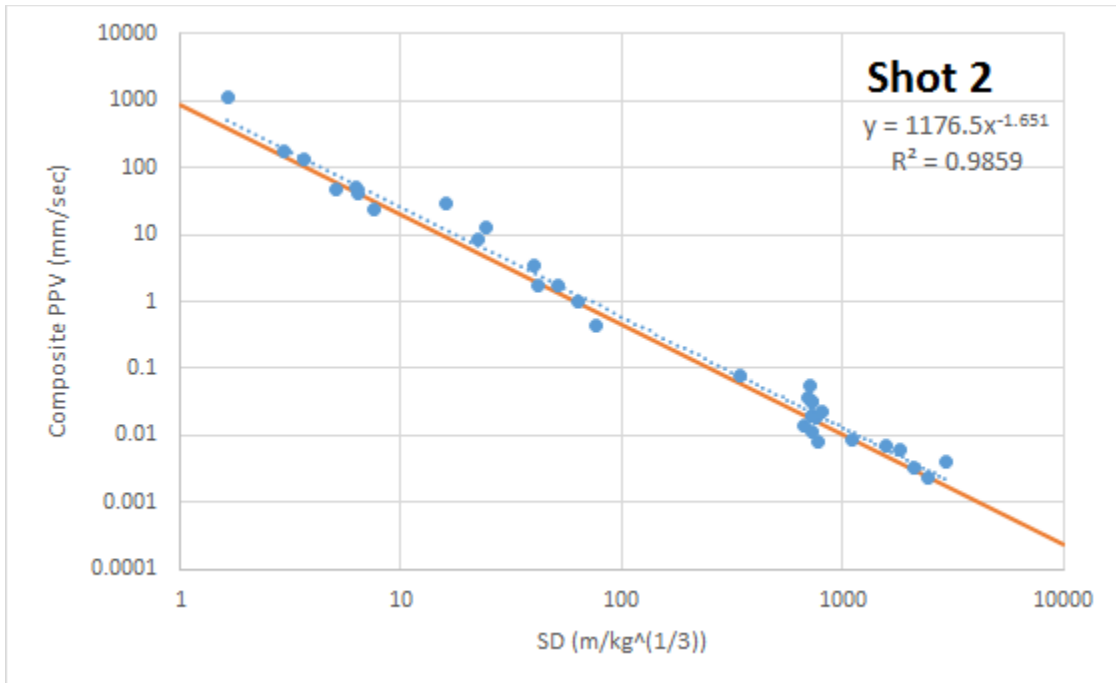


Figure 2-39. Shot 2 composite waveform PPV.

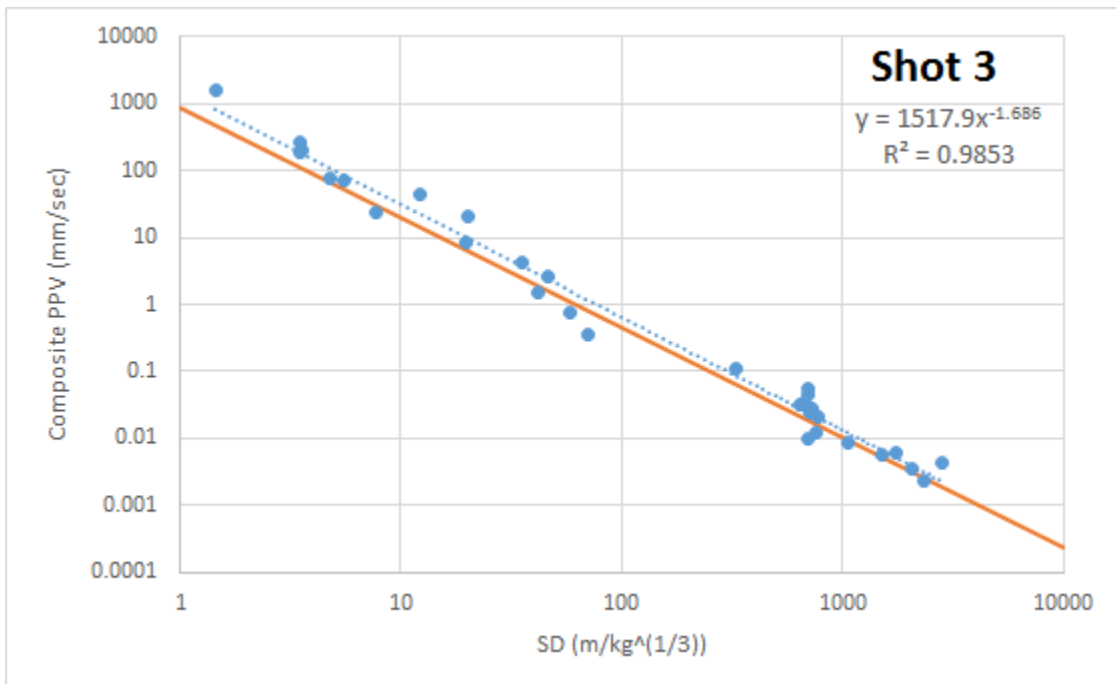


Figure 2-40. Shot 3 composite waveform PPV.

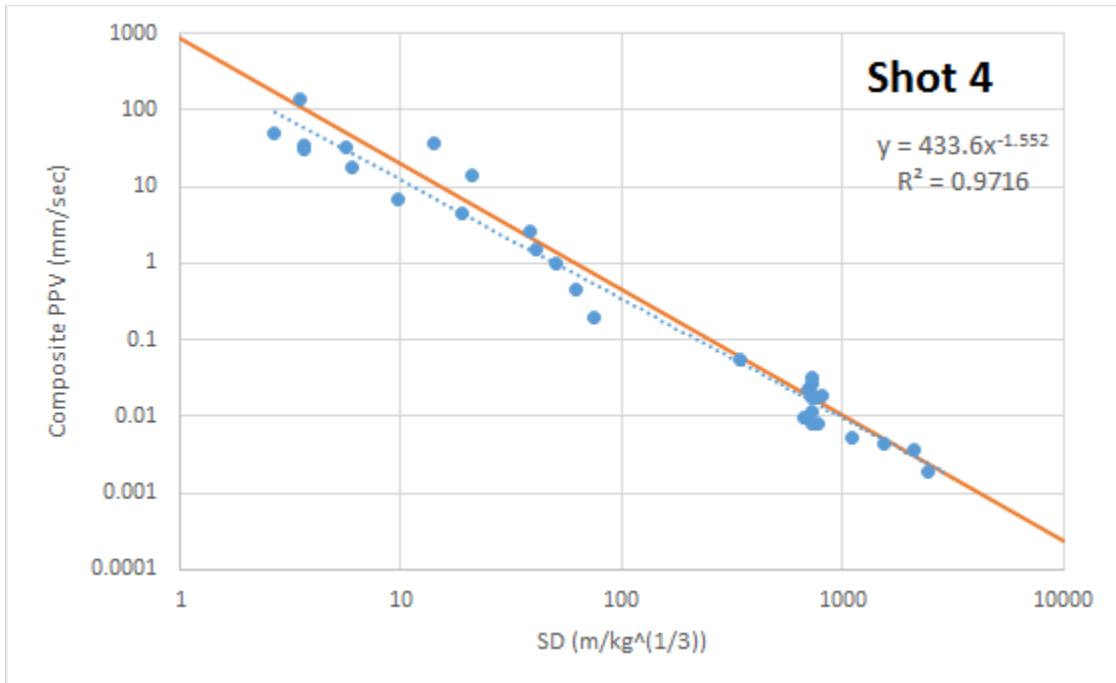


Figure 2-41. Shot 4 composite waveform PPV.

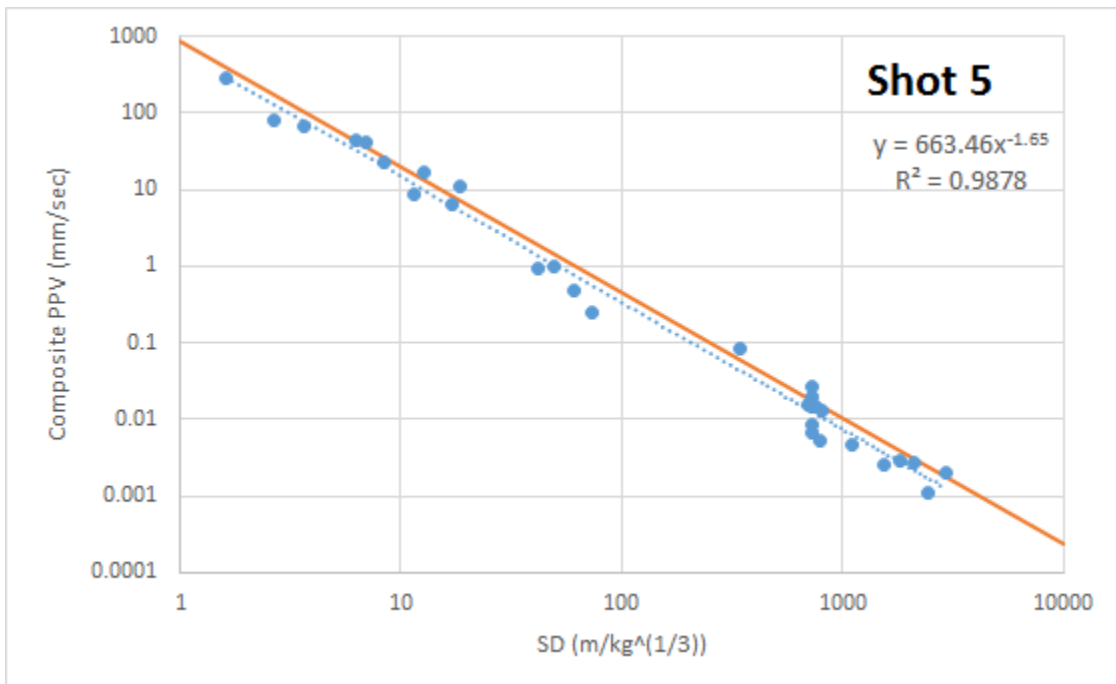


Figure 2-42. Shot 5 composite waveform PPV.

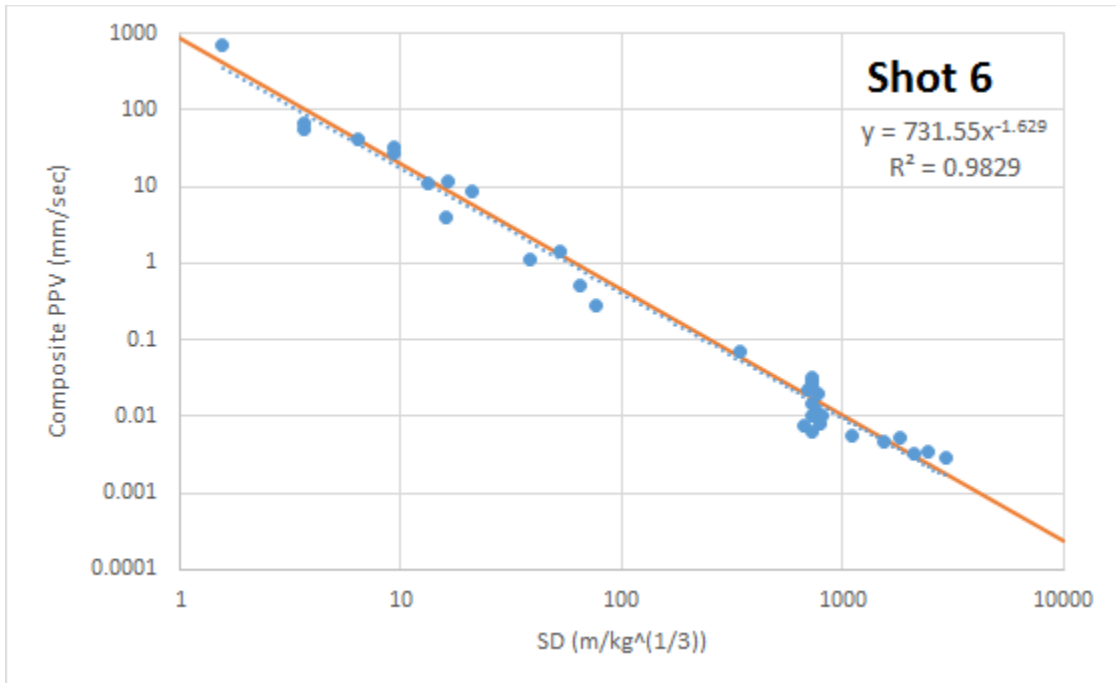


Figure 2-43. Shot 6 composite waveform PPV.

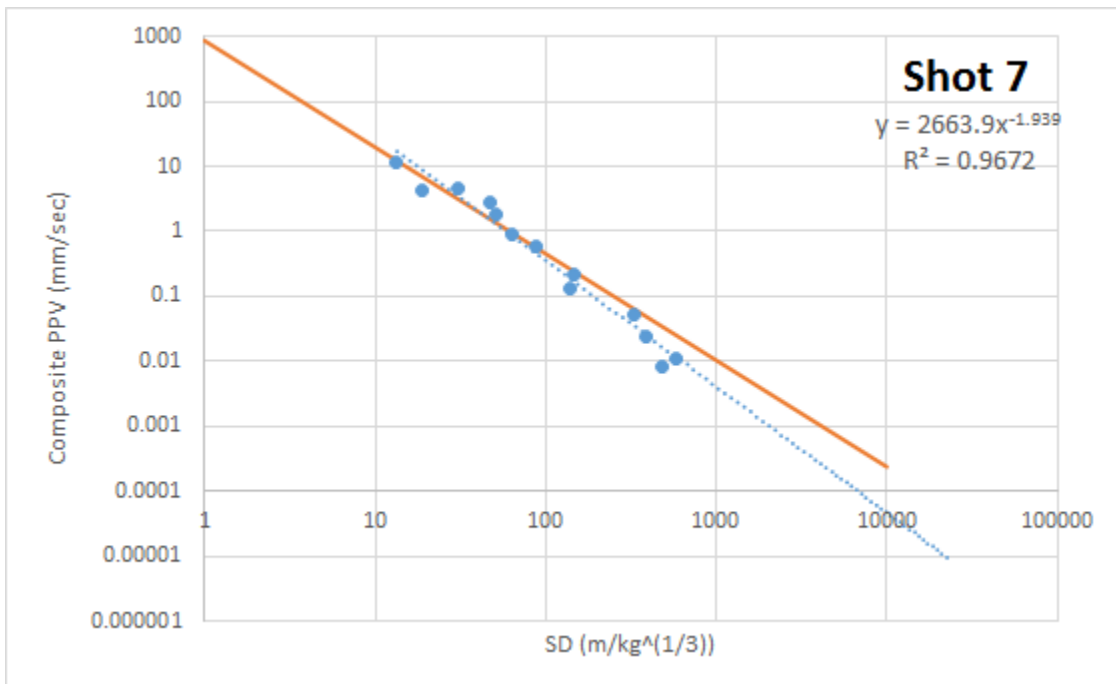


Figure 2-44. Shot 7 composite waveform PPV.

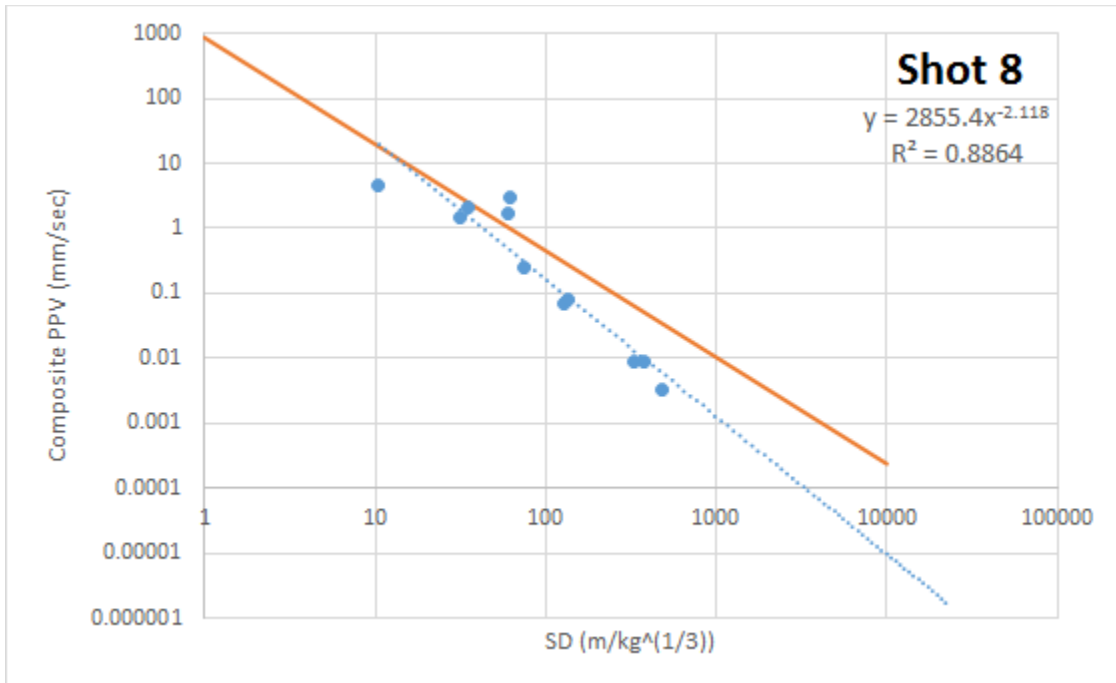


Figure 2-45. Shot 8 composite waveform PPV.

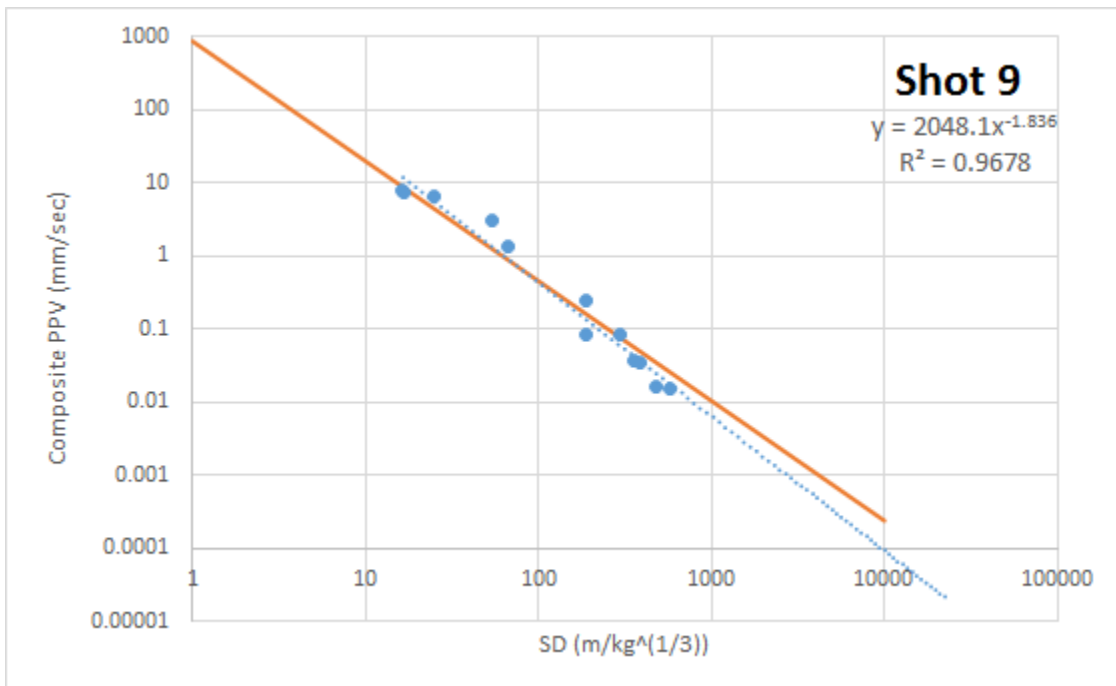


Figure 2-46. Shot 9 composite waveform PPV.

Table 2-9. Comparison of NEDE1 and NEDE2 PPV.

Shot	Explosive	Best-Fit PPV Equation
NEDE1 Shot 1	BP	$378 \cdot SD^{-1.60}$
NEDE1 Shot 2	HANFO	$1049 \cdot SD^{-1.62}$
NEDE1 Shot 3	Comp B	$956 \cdot SD^{-1.59}$
NEDE1 Shot 4	HANFO	$863 \cdot SD^{-1.64}$
NEDE1 Shot 5	Comp B	$725 \cdot SD^{-1.59}$
NEDE2 Shot 1	BP	$466 \cdot SD^{-1.59}$
NEDE2 Shot 2	HANFO	$1177 \cdot SD^{-1.65}$
NEDE2 Shot 3	Comp B	$1518 \cdot SD^{-1.69}$
NEDE2 Shot 4	HANFO	$434 \cdot SD^{-1.55}$
NEDE2 Shot 5	HANFO	$663 \cdot SD^{-1.65}$
NEDE2 Shot 6	HANFO	$732 \cdot SD^{-1.63}$
NEDE2 Shot 7	Comp B	$2664 \cdot SD^{-1.94}$
NEDE2 Shot 8	Comp B	$2855 \cdot SD^{-2.12}$
NEDE2 Shot 9	Comp B	$2048 \cdot SD^{-1.84}$

Deep Versus Shallow Explosion Amplitude – Preliminary Results

Shallow explosions produce significant damage in the source region, including spallation, which is thought to be responsible for S-wave radiation by the source. In addition to spallation, permanent ground deformation resulting from shallow explosions indicates material dilation in the source region. Increasing the depth of burial ensures that spallation and associated damage mechanisms are suppressed. Measurements of the rock properties from the cores extracted near the NEDE explosions conducted in the NEDE1 have demonstrated that these explosions indeed produced significant material damage in the source region (e.g. Stroujkova *et al.*, 2012). Near-source accelerograms indicate significant spallation for all NEDE shots.

Examining the dependence of S-wave generation for explosions with different scaled depth of burials (sDOB) was one of the main objectives of recent Source Physics Experiments in Nevada (SPE-N, e.g. Brunish *et al.*, 2011). Patton (2012a) compared the observed waveforms from SPE-N-1 explosion (sDOB = $1266 \text{ m/kt}^{1/3}$ using TNT equivalency) with synthetic waveforms and showed that observed phase shifts in high frequency Rg cannot be explained with an isotropic source model. The upcoming SPE-N-4 test in Nevada designed to test this hypothesis will be conducted at sDOB of $2532 \text{ m/kt}^{1/3}$.

The expected differences between the shallow and deep sources include smaller Rg amplitude for the deeper shot, and the phase shift between the shallow and the deep shots. NEDE2 Shot 2 (designated shallow source) and Shot 4 (deep source) had sDOBs of $285 \text{ m/kt}^{1/3}$ and $687 \text{ m/kt}^{1/3}$ respectively. Thus, NEDE2 explosions have significantly smaller sDOB than SPE-N shots. Figure 2-47 shows a comparison between Shots 2 and 4 recorded by near-source accelerometers located at the surface within 1 meter from the shot holes. The deep shot waveform at the surface shows that the station appears to be very close to the linear zone. While the slanted distance between the source centroid and the receiver increase by approximately a factor of 2.2 for the deep shot, the amplitude of the shallow shot is greater by more than an order of magnitude. The spall dwell time is also significantly reduced for the deep shot. Comparison of the far-field traces between Shots 2 and 4 is shown in Figure 2-48 and Figure 2-49. Traces recorded at several hundred meters from the source (Figure 2-48) show that Rg amplitudes for the deep shot are reduced by approximately factor of 2, while P wave amplitudes exhibit much less significant reduction. Rg amplitudes are affected by depth and focal mechanism, therefore modeling is needed to determine whether the observed amplitude reduction can be explained by the depth difference alone. There is slight phase advancement (approximately 6 ms) observed for Shot 4 compared to Shot 2; however Shot 4 was located approximately 6 m closer to the recorder.

Figure 2-49 shows Shots 2 and 4 recorded at approximately 6 km distance from the source at different azimuths. The surface wave phase advancement is less apparent at this distance. Filtering the waveforms in two different pass-bands (1-10 Hz and 10-100 Hz) shows that Shot 2 amplitudes at low frequencies exceed Shot 4 amplitudes. At higher frequencies, the amplitudes for both shots are approximately equal. The increase in low frequency amplitudes for the shallow shot may be related to spall effects.

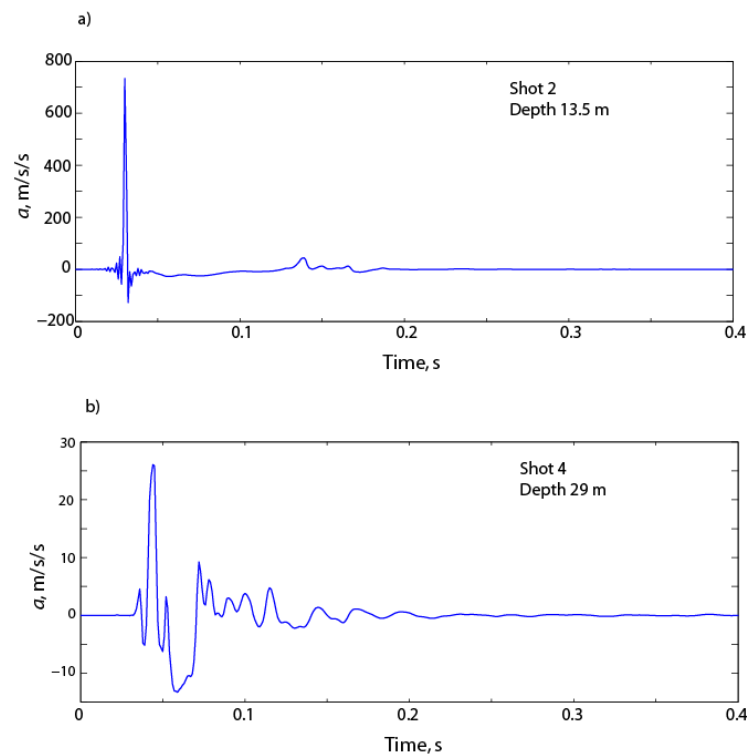


Figure 2-47. Near-source accelerograms for a) Shot 2 and b) Shot 4.

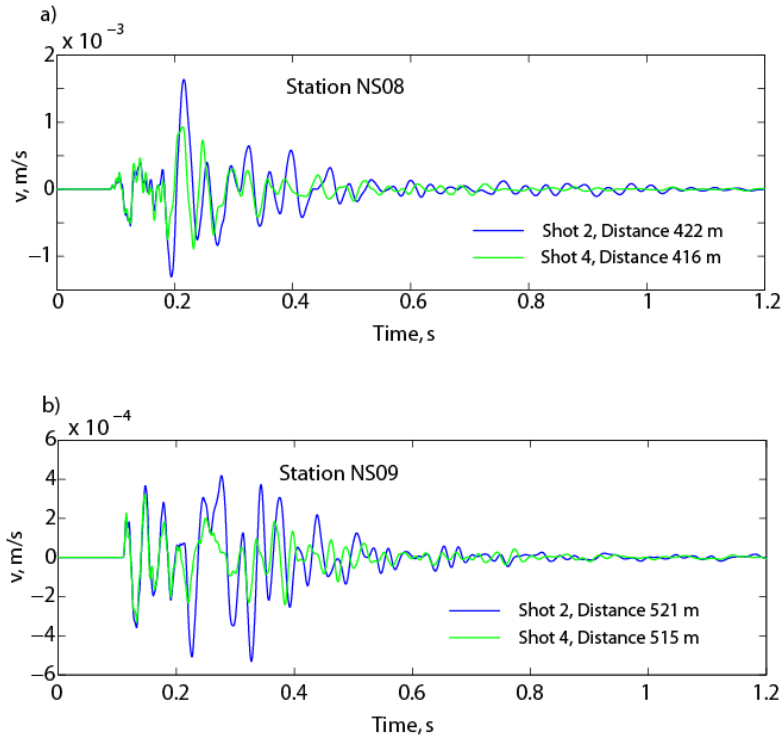


Figure 2-48. Seismic records for Shot 2 and Shot 4 recorded at a) Station NS08 and b) NS09.

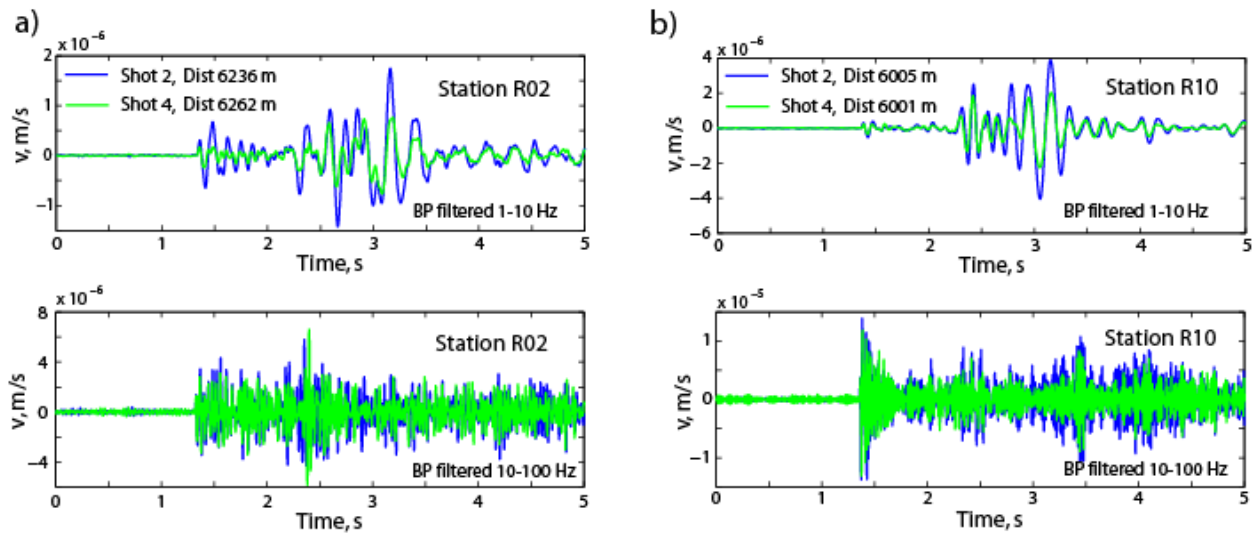


Figure 2-49. Seismic records for Shot 2 and Shot 4 recorded at a) Station R02 and b) R10 for filter pass bands of 1-10 Hz (upper plots) and 10-100 Hz (lower plots).

Full Waveform Spectral Ratios – Preliminary Results

Spectral ratio estimates were produced for the NEDE2 primary shots with yields of ~150 lbs TNT equivalent using the ~6 km ring array. Some noisy waveforms were not used leaving at least 10 of the 12 stations for each comparison. The windows shown in the following waveform

plots were used to estimate the spectra, thus the spectral ratios are for the entire waveform plus some pre-event noise and coda. This length of window was needed to extract adequate resolution of the surface waves below approximately 5 Hz. In most of the comparisons, HANFO Shot 2 (150 lbs TNT equivalent in virgin granite) was used as the reference waveform.

Some of the initial observations of these spectral ratios include:

- The Black Powder Shot 1 behaved similarly to the NEDE1 BP shot in that it has a lower corner frequency (~ 10 Hz) and does not generate high frequency body waves (Figure 2-50 and Figure 2-51). However, it has surface waves of similar amplitude as the HANFO and Comp B shots.
- The HANFO (Shot 2) and Comp B (Shot 3) shots in virgin rock appear to have the same body wave amplitudes above 10 Hz (Figure 2-52 and Figure 2-53). The most obvious differences appear to be in the surface waves (< 10 Hz) where the Comp B shot produced as much as 3x larger amplitudes than the HANFO shot, which was not observed in the NEDE1. There appears to be some azimuthal trend to these amplitudes with larger Comp B surface waves to the north and east than to the south and west. This will be a focus of continued studies when we isolate the Rg at these stations. The effect of the water on fracture generation is unclear for the new Comp B shot, as it is obvious from the post-blast observations that the new Comp B shot produced significant surface fracturing (not observed for the NEDE1 shots).
- The significantly overburied HANFO Shot 4 ($687 \text{ m/kt}^{1/3}$) produces smaller amplitudes than the shallower buried HANFO Shot 2 ($320 \text{ m/kt}^{1/3}$) at frequencies less than 20 Hz (Figure 2-54 and Figure 2-55).
- Shots 5 and 6 were 150 lb HANFO re-shoots in the NEDE1 damage zones for HANFO and Comp B, respectively. When compared to the Shot 2 150 lb HANFO shot in virgin, undamaged granite, Shots 5 and 6 are smaller at most frequencies (Figure 2-56, Figure 2-57, Figure 2-58, and Figure 2-59). The largest difference is again in the surface waves, where Shot 2 has as much as 7x larger surface waves than Shot 5 (HANFO reshoot).
- Shot 6 (reshoot in the Comp B damage zone) has larger amplitudes than Shot 5 (reshoot in the HANFO damage zone) (Figure 2-60 and Figure 2-61). If the NEDE1 Comp B shot produced less fractures than the HANFO shot, these new observations would support fracture decoupling.

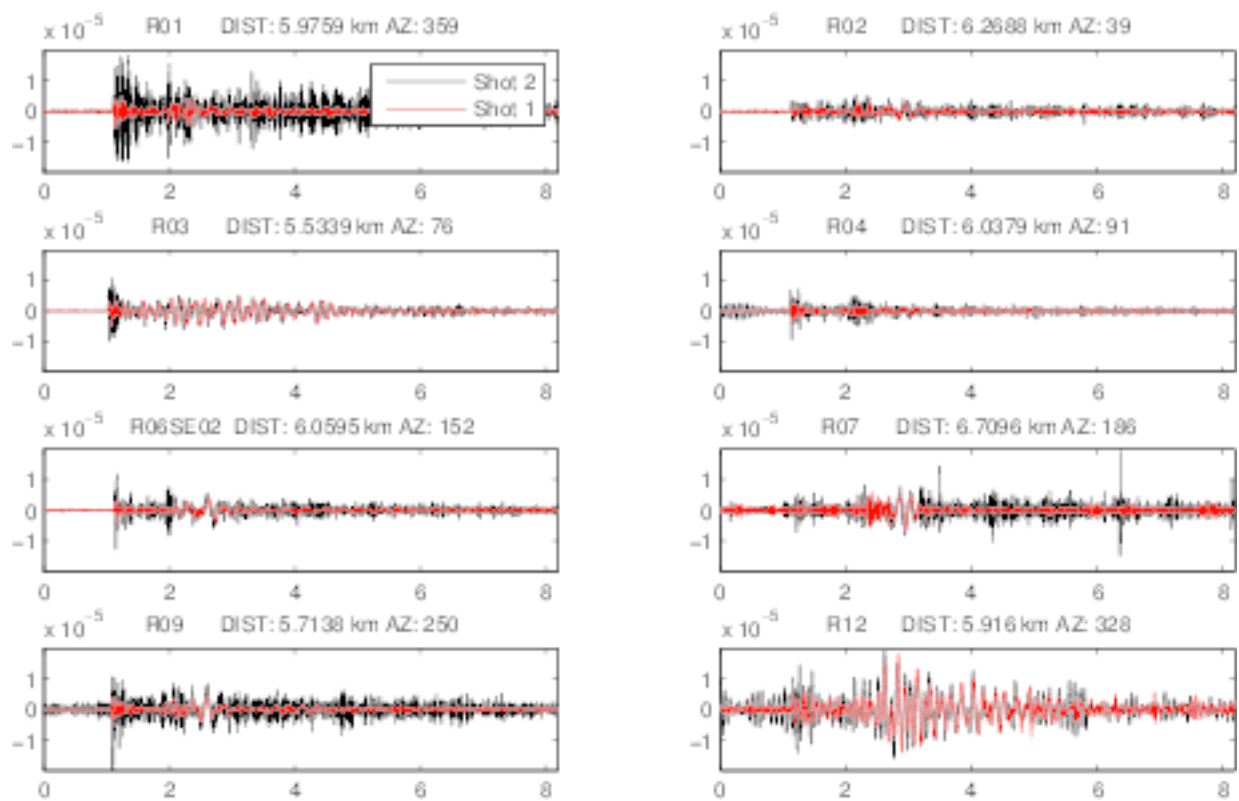


Figure 2-50. Shot 2 and Shot 1 waveforms on ring network.

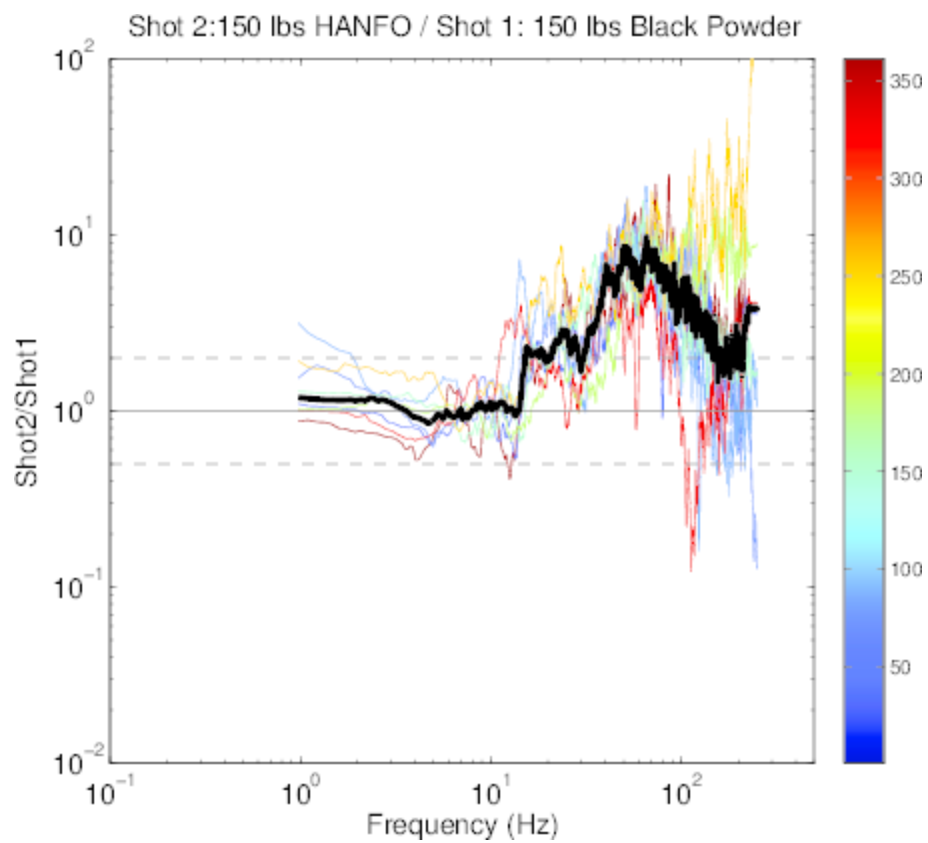


Figure 2-51. Spectral ratios for Shot 2 (HANFO; 150 lbs) / Shot 1 (Black Powder; 150 lbs).

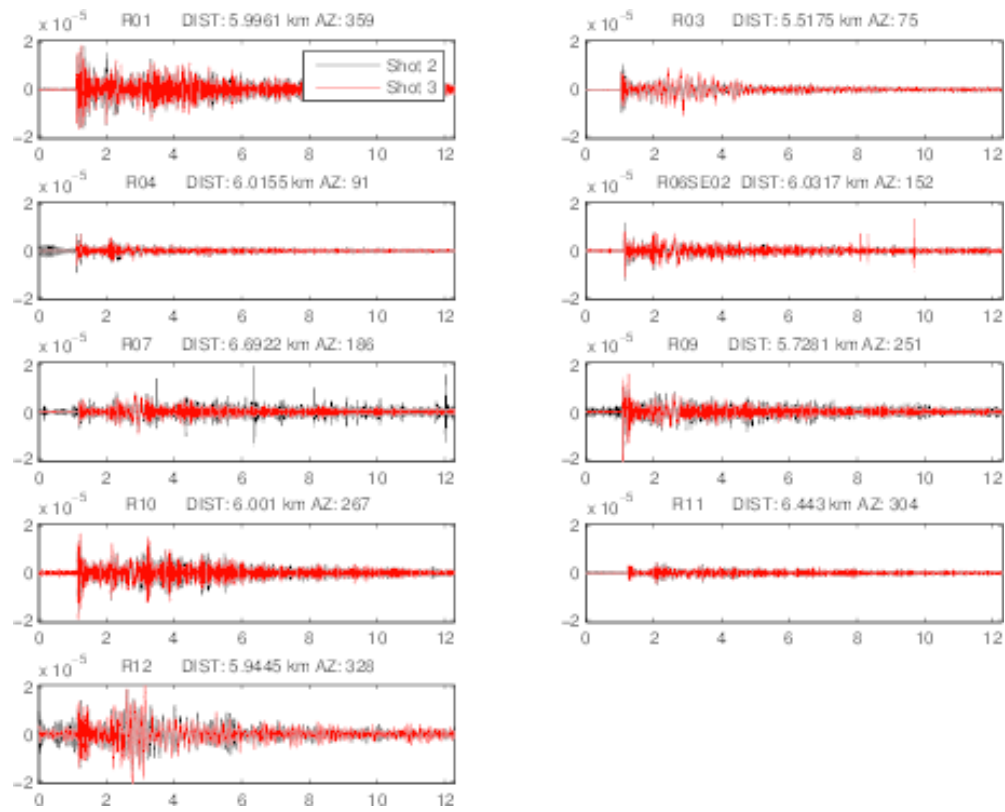


Figure 2-52. Shot 2 and Shot 3 waveforms on ring network.

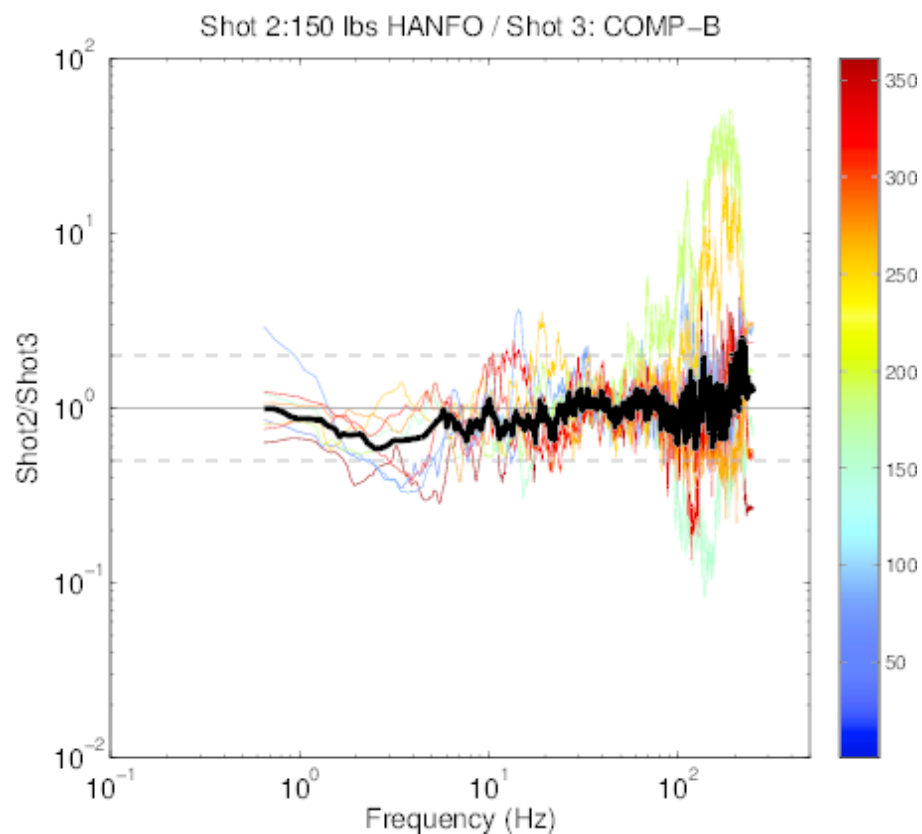


Figure 2-53. Spectral ratios for Shot 2 (HANFO; 150.0 lbs) / Shot 3 (Comp B; 161.2 lbs).

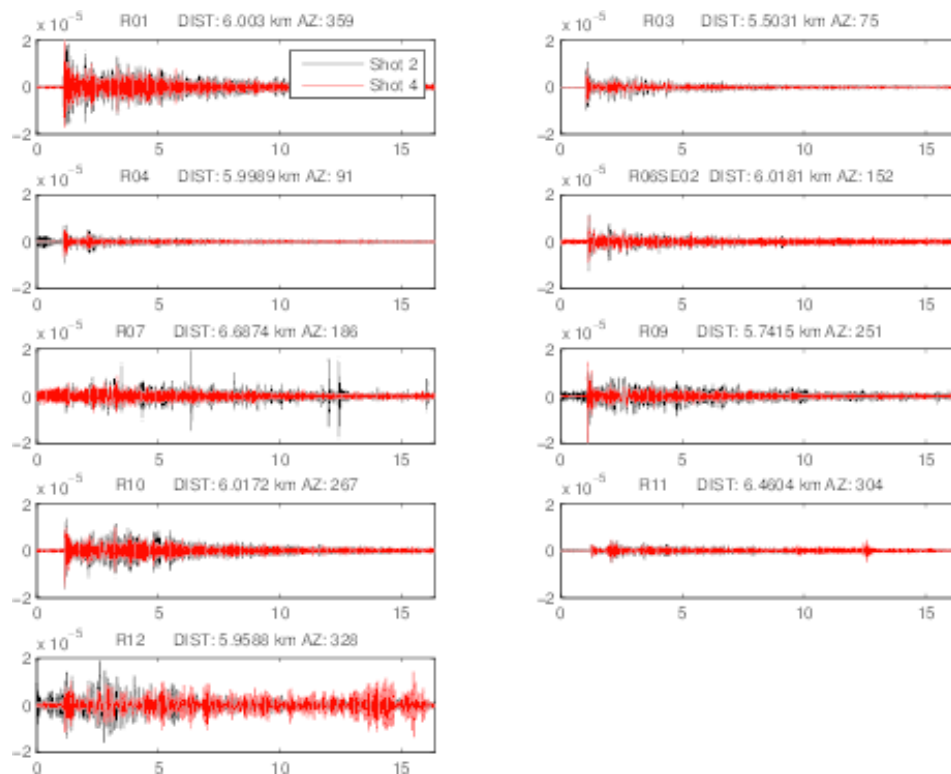


Figure 2-54. Shot 2 and Shot 4 waveforms on ring network.

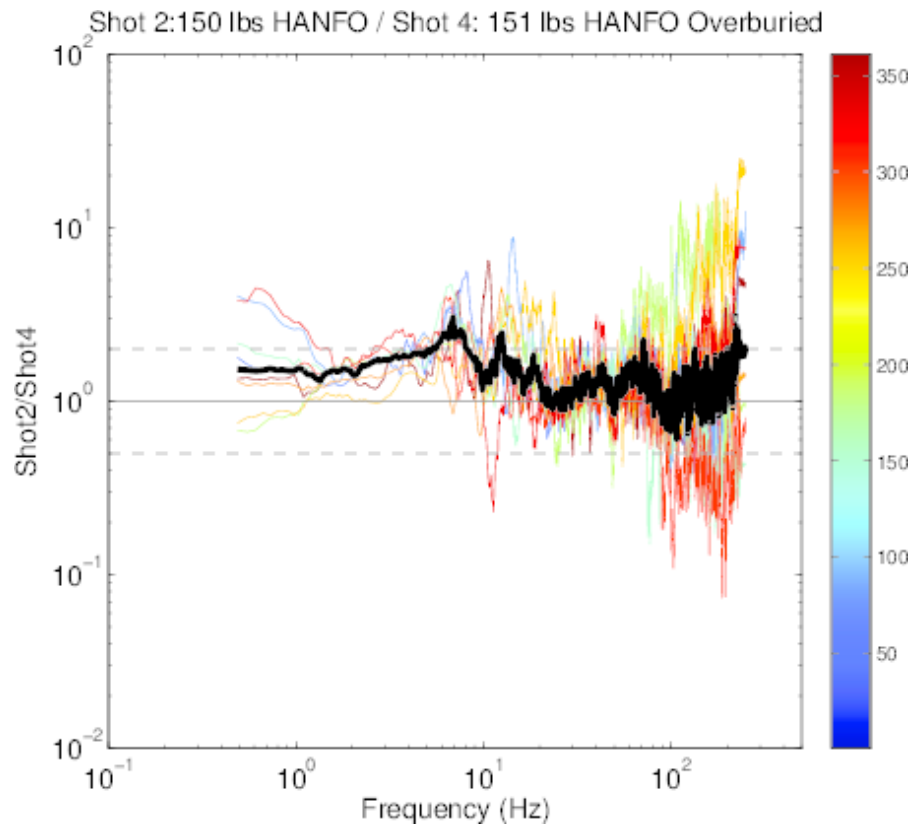


Figure 2-55. Spectral ratios for Shot 2 (HANFO; 150.0 lbs) / Shot 4 (Deep HANFO; 151.1 lbs).

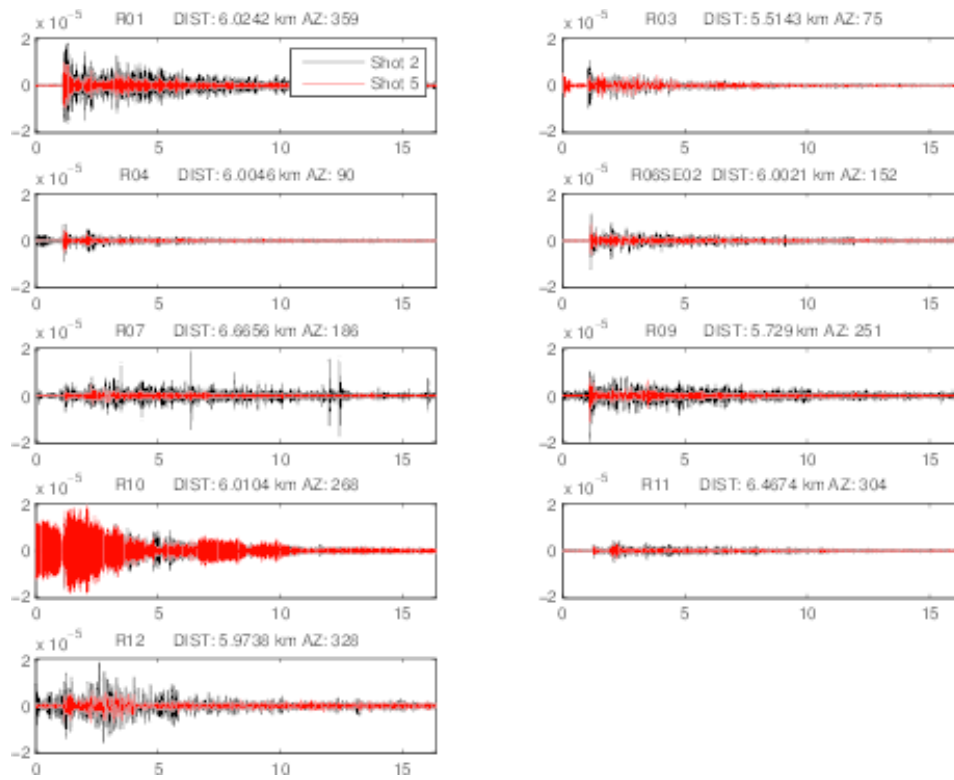


Figure 2-56. Shot 2 and Shot 5 waveforms on ring network.

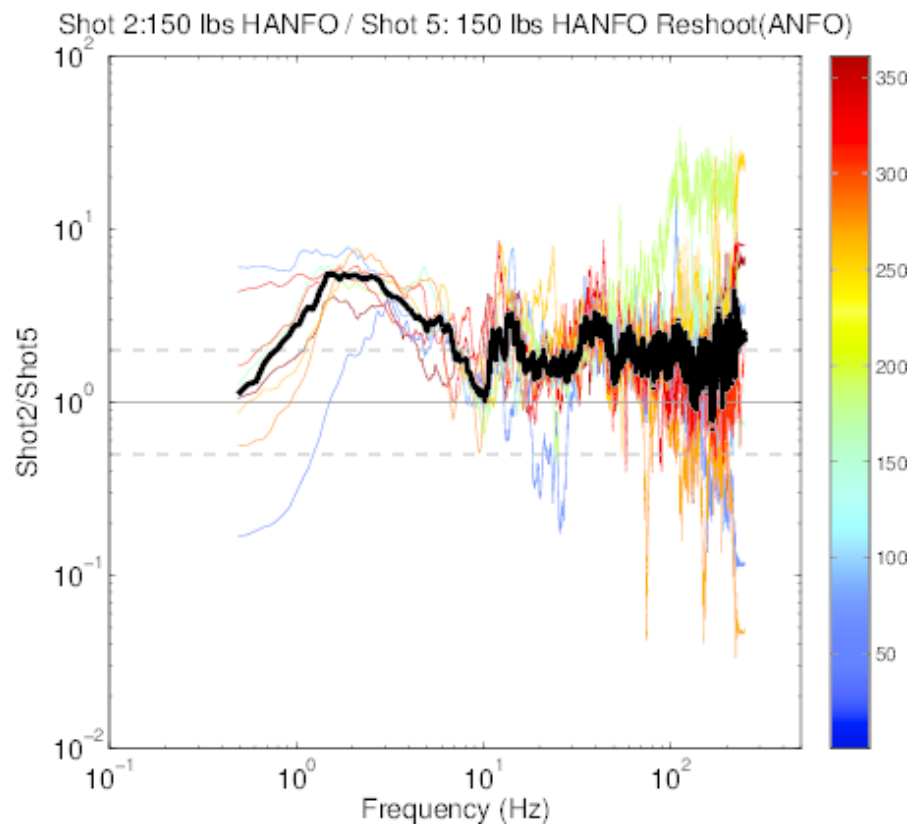


Figure 2-57. Spectral ratios for Shot 2 (HANFO; 150.0 lbs) / Shot 5 (HANFO reshoot of NEDE1 HANFO; 150.0 lbs).

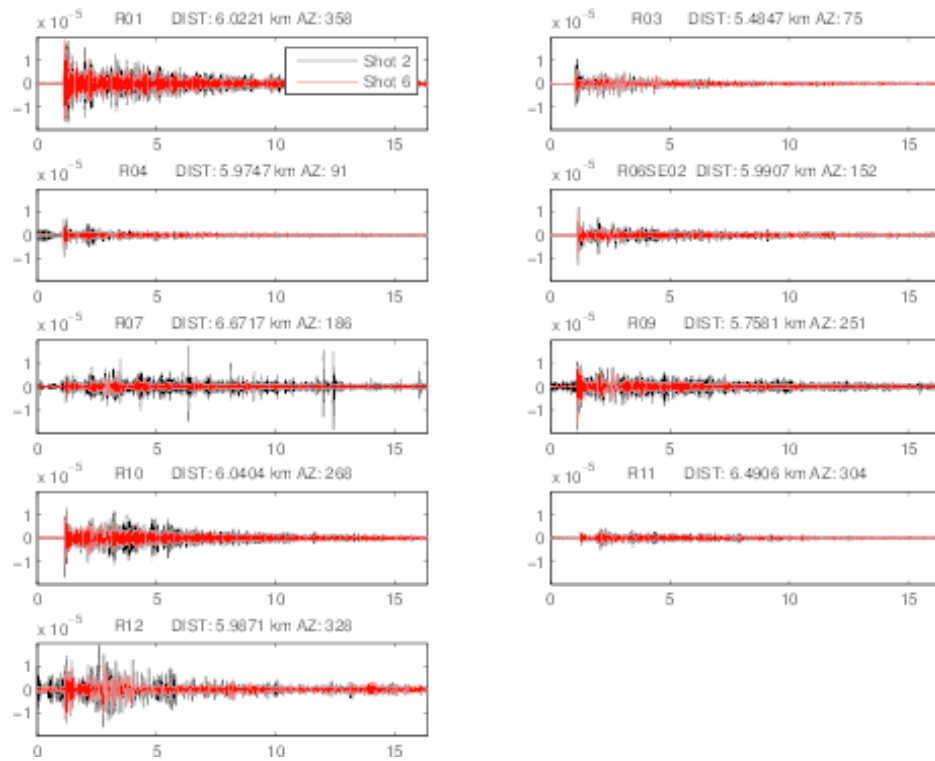


Figure 2-58. Shot 2 and Shot 6 waveforms on ring network.

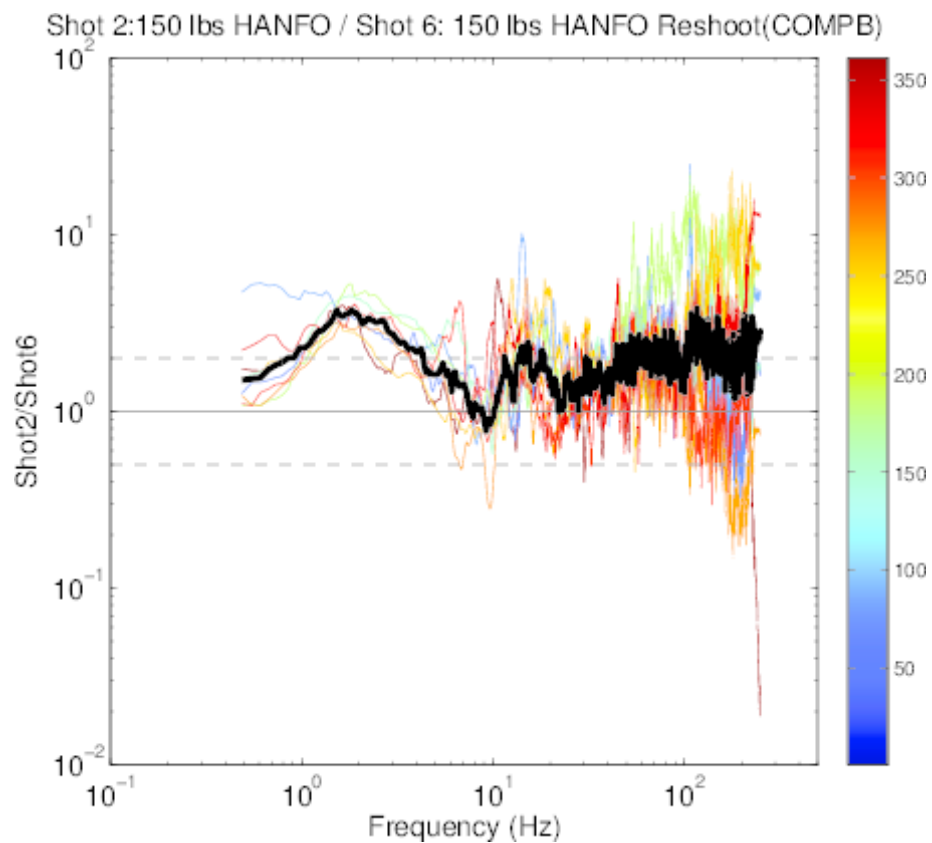


Figure 2-59. Spectral ratios for Shot 2 (HANFO; 150.0 lbs) / Shot 6 (HANFO reshoot of NEDE1 Comp B; 150.0 lbs).

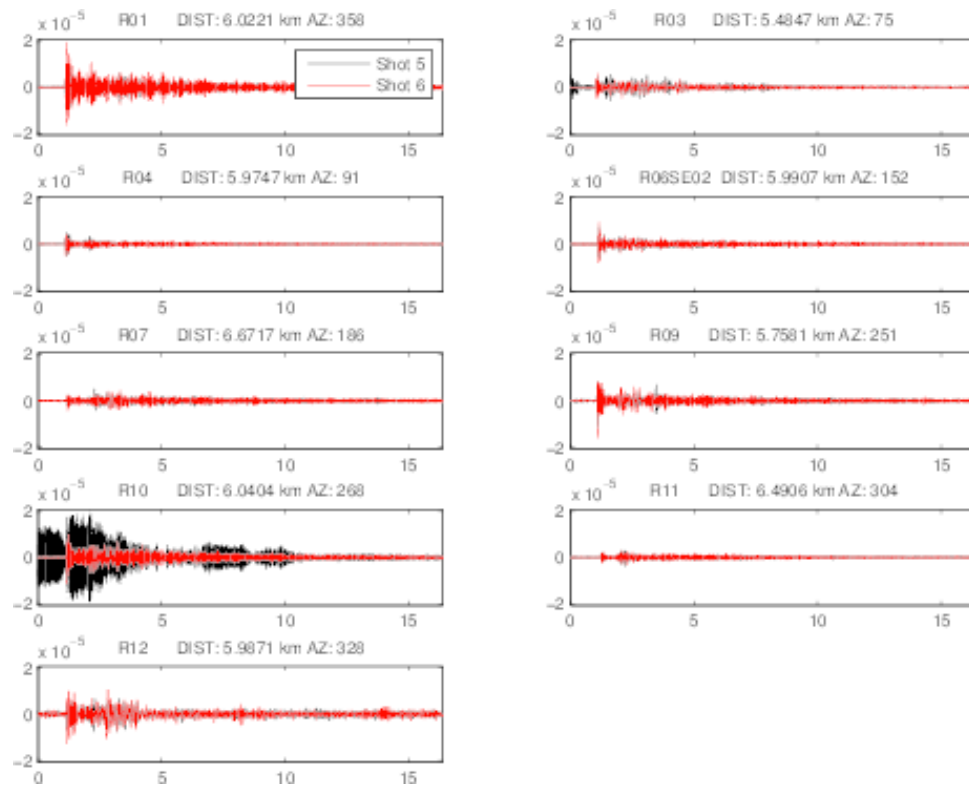


Figure 2-60. Shot 5 and Shot 6 waveforms on ring network.

Shot 5:150 lbs HANFO Reshoot(ANFO) / Shot 6: 150 lbs HANFO Reshoot(COMP)

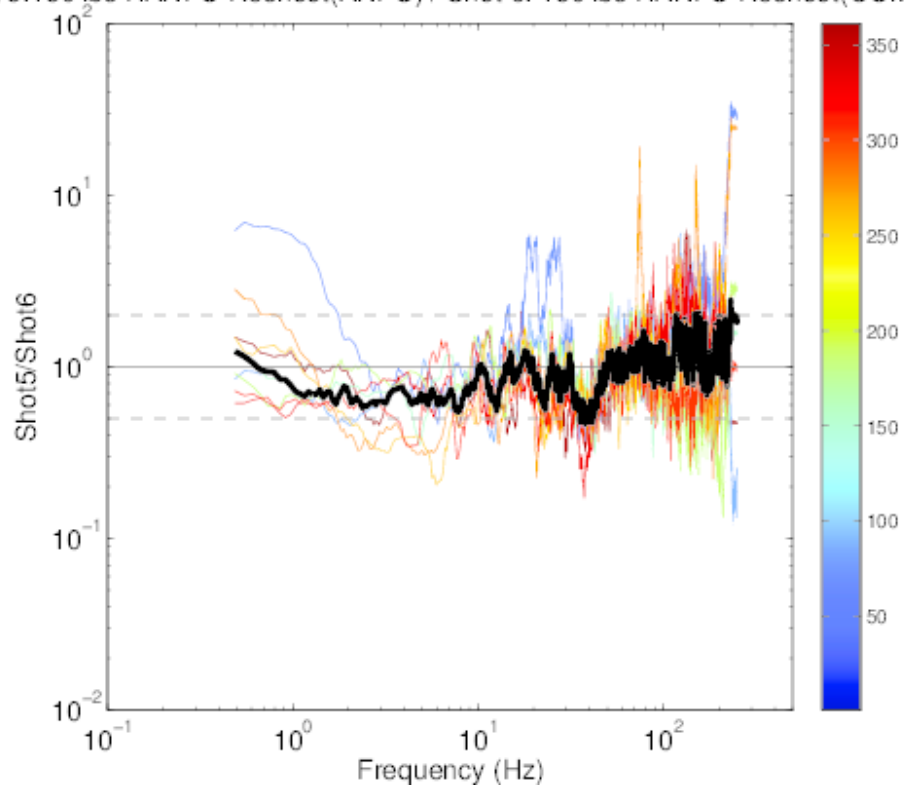


Figure 2-61. Spectral ratios for Shot 5 (HANFO reshoot of NEDE1 HANFO; 150.0 lbs) / Shot 6 (HANFO reshoot of NEDE1 HANFO; 150.0 lbs).

3. MOMENT TENSOR INVERSION FOR NEDE2 EXPLOSIONS

ABSTRACT

The New England Damage Experiment Phase 2 (NEDE2) was conducted in a granite quarry located near Barre, Vermont during the summer of 2013. The objective of the experiment was to investigate shear wave generation by small explosions in homogenous granite conducted using different explosives (black powder, HANFO and Comp B). In addition, a deeper HANFO explosion was detonated to study the effect of depth on seismic radiation.

In this study, we calculated the time-dependent moment tensors for four of the explosions conducted as a part of the experiment. The moment tensor inversion was performed using the methodology developed in Stump and Johnson (1977). Only the near-source stations (distances between 30 and 500 m) were used to perform the inversion. The shallow ANFO shot has the lowest isotropic component (64% isotropic) among all shots, while the black powder shot has the highest (82% isotropic). The deep ANFO shot has significantly higher isotropic component (80% isotropic) than the shallow ANFO shot (64% isotropic). The shallow ANFO shot produced a first arrival with a negative polarity at one of the near-source stations, which was in agreement with the smallest isotropic component for that shot. It is possible that the polarity reversal was due to block movement at the test site.

We did not find significant correlation between the moment tensor isotropic component and the surface fracturing or the P-wave radiation pattern. This may be explained by poor resolution of the moment tensor components due to the velocity model complexities, including strong anisotropy. A correlation was observed between the surface fracturing and the S/P amplitude ratios. The largest S/P ratios were observed for the black powder shot, which produced surface fracturing. The HANFO shot, which did not produce surface fracturing, has the second smallest S/P ratios, followed by the deep HANFO shot. These results show that long fractures may be responsible for the shear wave generation.

OBJECTIVES

The objective of this study was to calculate moment tensors of the explosions conducted using explosives with different velocity of detonation (VOD). Comparison between the moment tensors obtained using the near-source instrument with the far field seismic radiation (both P and S waves) and the fractures generated by explosions may shed light on the mechanisms of the explosion source anisotropy and shear wave radiation.

RESEARCH ACCOMPLISHED

Inversion Method

The moment tensor inversion was performed using a methodology developed in Stump and Johnson (1977) and implemented as an inversion code by Xiaoning (David) Yang (1997). The inverse problem in the frequency domain is formulated as a system of the linear equations:

$$\mathbf{u} = \mathbf{G}\mathbf{M} \quad (3-1)$$

where the vector \mathbf{u} is composed of measured spectra, \mathbf{G} represents Green's functions in the frequency domain, and \mathbf{M} is a vector made up of the components of the unknown moment tensor (M_{xx} , M_{xy} , M_{xz} , M_{yy} , M_{yz} , M_{zz}). The Green's functions are computed using wavenumber integration (CPS 3.30, Herrmann, 2002). The system of the equations is solved using the Singular Value Decomposition (SVD) method. The components of the moment tensor are calculated for each frequency producing source spectra. The results are then converted to the time domain to produce source-time functions for each component.

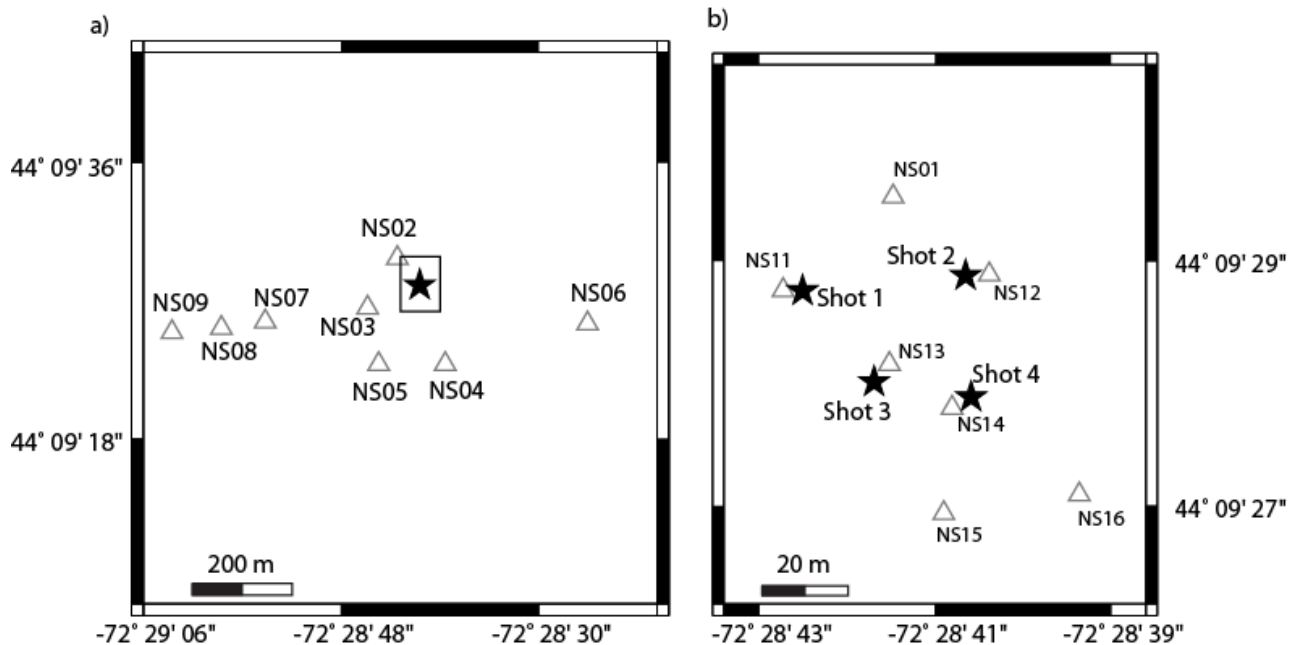


Figure 3-1. The near-source stations (triangles) installed around the test site at the Rock of Ages Quarry in Barre, VT. b) Enlarged view of the testing area showing the explosions (stars).

Inversion Results

To perform the moment tensor inversion, we used near-source stations located between 30 m and ~500 m (NS01-NS16) shown in Figure 3-1. Stations located across the quarry (NS04 and NS06) were not used due to considerable site and propagation effects. The traces recorded less than 30

m from the sources were eliminated from the inversion due to non-linear effects from the explosions. Overall between 8 and 10 stations were available for inversion for each explosion.

Table 3-1. Velocity Model Used to Calculate the Green's Functions.

Layer thickness, m	V_p , m/s	V_s , m/s	ρ , kg/m ³
3	4100	1900	2100
3	4200	2000	2200
3	4300	2100	2300
3	4400	2200	2400
3	4450	2300	2500
200	4500	2400	2600
Half-space	4550	2500	2600

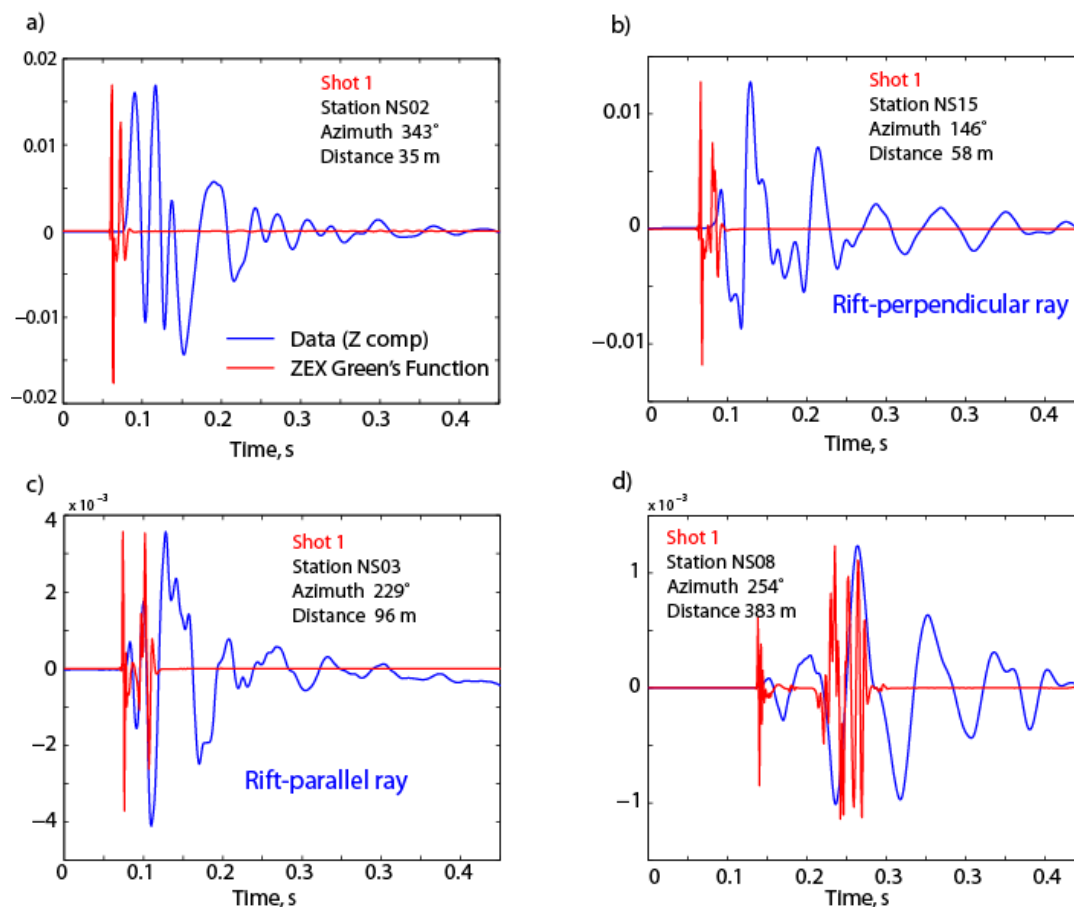


Figure 3-2. Comparison between the data (blue) and the Green's functions (red) for Shot 1: a) Station NS02, b) Station NS15, c) Station NS03, and d) Station NS08.

Prior to the inversion, the accelerometer data were corrected for the instrument response and converted to velocity. The Green's functions were calculated using the velocity model in Table 3-1 developed using laboratory measurements and refraction data. Figure 3-2 shows the comparison between the data converted to velocity (vertical components) and the Green's function (vertical component of the isotropic source ZEX). The travel times match fairly well between the data and the synthetics for ranges >100 m and for rift-parallel ray trajectories (Figure 3-2c-d). The model is too fast for the rift-perpendicular rays (Figure 3-2a-b). The observed traces were manually aligned with the Green's functions before the inversion.

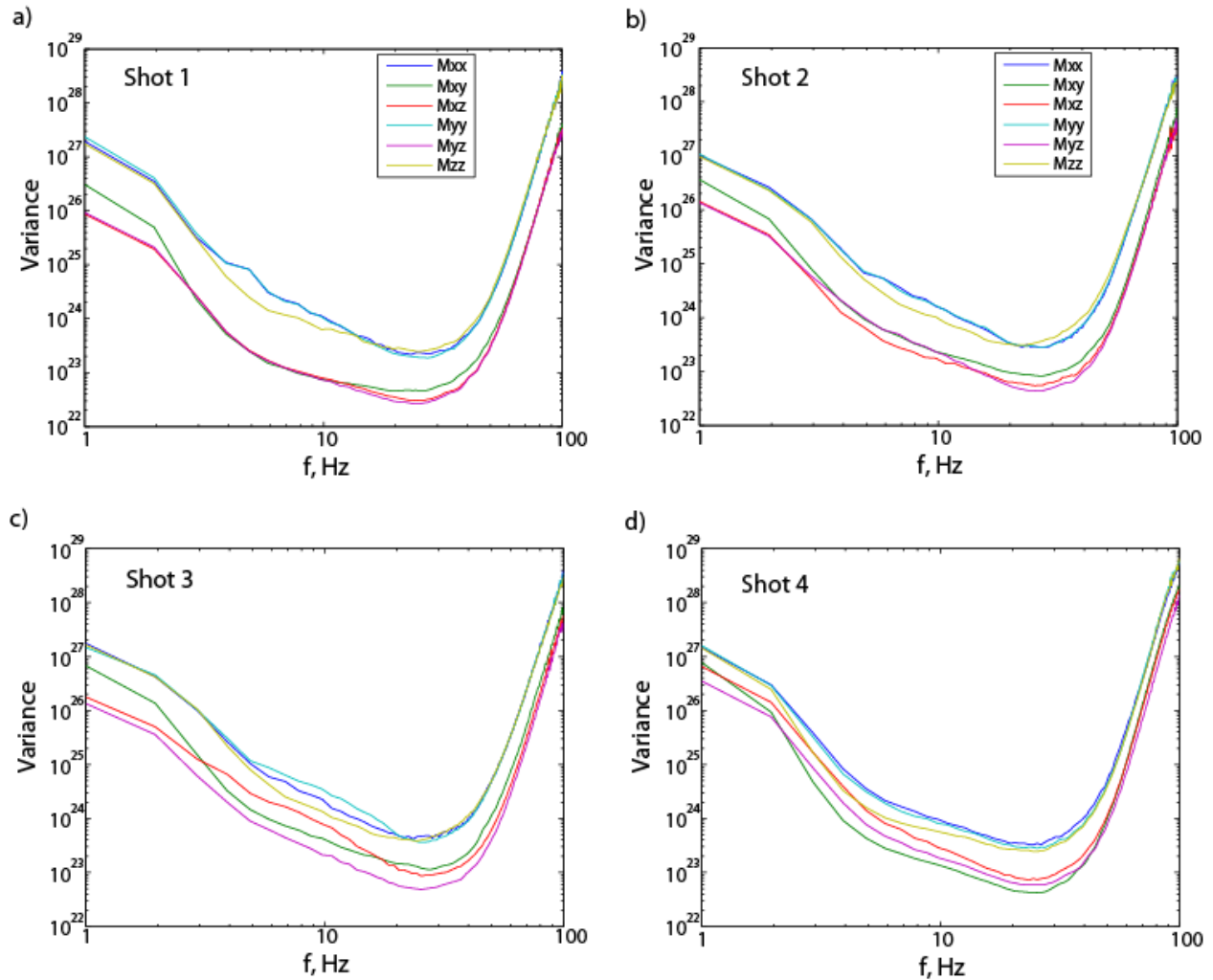


Figure 3-3. RMS errors for the moment tensor components as a function of frequency: a) Shot1, b) Shot 2, c) Shot 3, and d) Shot 4.

The inversion was performed using singular value decomposition (SVD) in the frequency domain. The time dependent source moment tensors were recovered using the inverse Fourier transform. The inversion produced both high-frequency and low-frequency artifacts in the time-

dependent moment-rate tensor components. According to Yang (1999), the high-frequency noise is due to imperfect alignment of the data and the Green's functions. The low-frequency artifacts are due to differences between the model and actual medium (Green's function discrepancies). Figure 3-3 shows the variance reduction for different moment tensor components for Shots 1-4. A significant variance drop is achieved in the frequency range between 5-50 Hz. The artifacts are more prominent outside this range. To minimize the effect of the artifacts the time-domain moment tensors were bandpass-filtered between 10 Hz and 50 Hz.

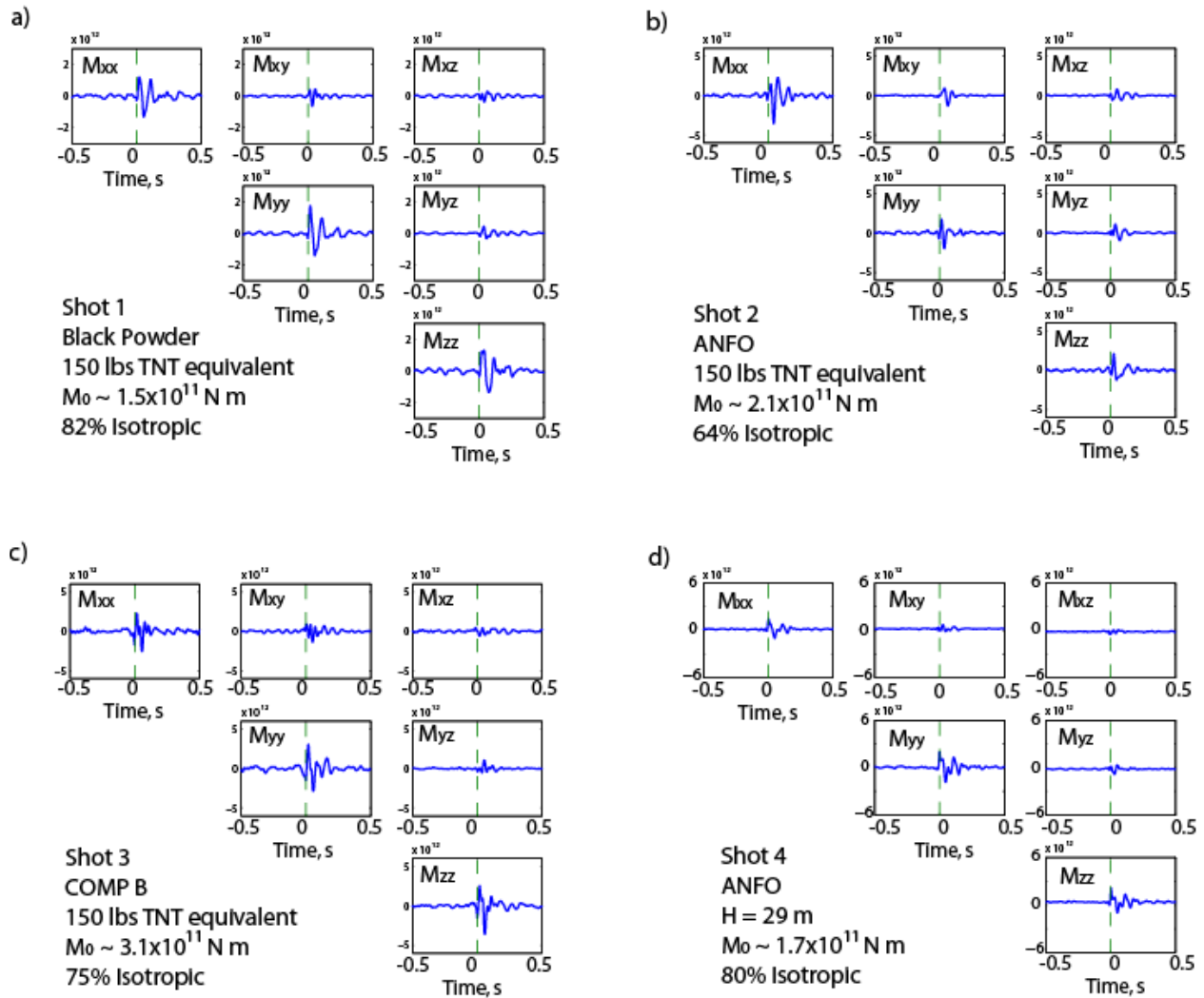


Figure 3-4. Moment rate tensor components for: a) Shot 1, b) Shot 2, c) Shot 3, and d) Shot 4.

Filtered time-domain moment tensor results for Shots 1-4 are presented in Figure 3-4. Table 3-2 lists the component of the moment tensor estimated for time with the largest sum of the diagonal elements $t = t|_{\max(\text{tr}(M))}$. The moment tensor is dominated by the diagonal components for all

explosions, however for Shots 2 and 3 the off-diagonal elements reach 40% of the total moment M_0 estimated as:

$$M_0 = \frac{1}{3} \sum M_{ii} = \frac{1}{3} \text{tr}(M) . \quad (3-2)$$

Moment tensors calculated for small shallow chemical explosions often have M_{zz} as the dominant moment tensor component (e.g. Yang and Bonner, 2009). This can be explained by addition of a vertical dipole due to spall and/or upward material movement due to dilatancy (e.g. Patton and Taylor, 2008). In our case, however, only Shot 3 has M_{zz} exceeding the horizontal components. Shots 1 and 4 have dominant M_{yy} , while Shot 2 has dominant M_{xx} .

While all of the explosions have the same yields, their moments are variable because of the differences in the explosives and in the emplacement conditions. The moment M_0 for the black powder shot is about 25% less than the HANFO shot and about 50% less than the Comp B shot. The black powder shot has the highest isotropic component (82%). The shallow HANFO shot has the lowest isotropic component (64%).

The moment M_0 for the deep HANFO shot is 81% of M_0 for the shallow HANFO shot. The deep shot has significantly higher isotropic component than the shallow shot. This result is expected, because in the absence of pre-stress, the source asymmetry is largely caused by the interaction with the free surface.

Table 3-2. Moment Tensor Inversion Results.

Shot #	M_{xx} $\times 10^{11}$ N×m	M_{xy} $\times 10^{11}$ N×m	M_{xz} $\times 10^{11}$ N×m	M_{yy} $\times 10^{11}$ N×m	M_{yz} $\times 10^{11}$ N×m	M_{zz} $\times 10^{11}$ N×m	M_0 $\times 10^{11}$ N×m	% <i>iso</i>
1	1.2095	0.3224	0.0111	1.8324	0.0510	1.2955	1.4558	82
2	3.6001	-0.3036	-0.8874	1.4632	-0.0095	1.3707	2.1447	64
3	2.6698	0.7708	0.3894	2.9726	-0.8630	3.7485	3.1303	75
4	1.3366	-0.0529	-0.2224	2.1367	0.3721	1.6836	1.7190	80

DISCUSSION

The results of the source mechanism study for different explosive types are somewhat unexpected. The hypothesis behind the experiment was that the macro-fractures created by the explosions are the main source of the explosion source anisotropy and consequently determine the amplitudes of the shear waves. The slower explosives tend to drive longer fractures, while the faster explosives pulverize the material adjacent to the charge. This was confirmed for the explosions conducted during the NEDE1 experiment (e.g. Martin *et al.*, 2011a; Stroujkova *et al.*, 2012). The black powder and HANFO explosions produced surface fractures, while Comp B explosions did not. The situation changed for the NEDE2. The black powder shot produced surface fracturing, but so did the Comp B shot, while the HANFO shot did not. The difference can be attributed to the presence of water in the Comp B shot borehole since water evaporation during explosions increases pressure in the shot borehole and drives longer fractures.

The percentage of the isotropic component does not appear to correlate with the surface fracturing. The black powder shot has the highest isotropic component while producing surface fractures. The HANFO shot on the other hand has the lowest isotropic component without visible surface fractures. Another peculiar feature of the HANFO shot is a negative polarity observed at one of the near-source station (NS15). Figure 3-6 shows a comparison between two pairs of waveforms travelling nearly reciprocal paths shown in Figure 3-1. The polarity for Shot 2 recorded by NS15 is flipped, and the amplitude is significantly reduced compared to Shot 5 recorded at NS12. The polarity for Shot 2 recorded at NS16 is directed upward. Notice that the waveforms for Shot 5 and 6 recorded by NS12 are very similar, while Shot 2 waveforms traveling along the reciprocal paths are different. Figure 3-6a shows that other near-source recordings for Shot 2 have positive polarities. The other stations located at similar azimuth and different distances from Shot 2 recorded positive P polarity. Other shots recorded by Station NS15 have positive polarities, however their P amplitudes are reduced. It is possible that the negative polarity was caused by a movement/rotation of large rock mass at the test site. In any case, this observation supports the lowest isotropic moment tensor for Shot 2.

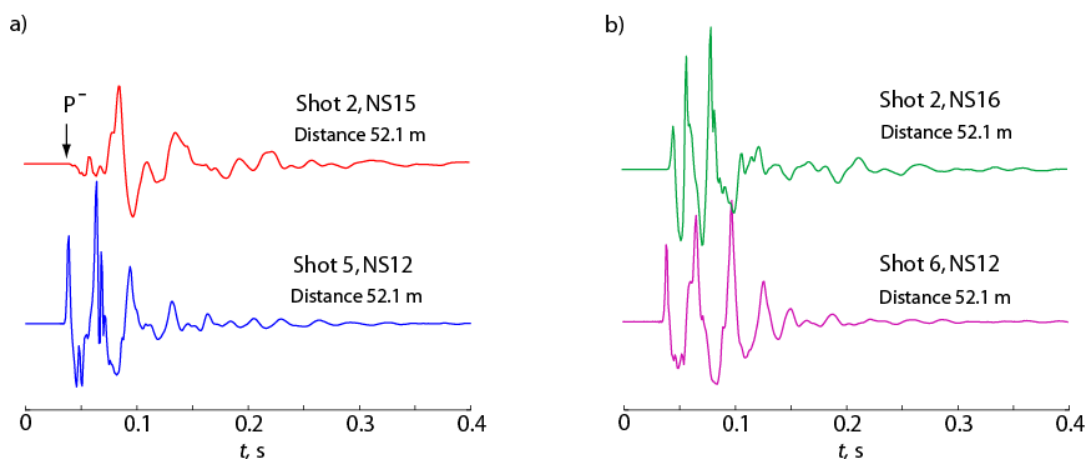


Figure 3-5. Near-source accelerograms for two pairs of reciprocal ray trajectories. a) Shot 2 recorded by NS15 located near Shot 5, and Shot 5 recorded by NS12 located near Shot 2; b) Shot 2 recorded by NS16 located near Shot 6, and Shot 6 recorded by NS12 located near Shot 2. All distances between sources and receivers are approximately 52.1 m.

P-wave radiation pattern is also a good indicator of the source symmetry. Unfortunately, P-wave amplitudes are affected by the strong anisotropy and topography around the test site (e.g. Stroujkova *et al.*, 2012). To correct for the propagation effects we used P-wave amplitude ratios for the circular array stations to examine source symmetry. Figure 3-7 shows the azimuthal plots of the amplitude ratios between Shots 1, 2, and 3 and Shot 4. Shot 4 was chosen as a reference shot because it was the deepest shot with relatively high estimated isotropic component, for which the surface effects should be the smallest. The waveforms were filtered between 10 and 50 Hz in order to be compared with the moment tensor results. The amplitude ratios for Shot 1 show significant differences in different directions (Figure 3-7a), even though the moment tensor for Shot 1 has the highest isotropic component. This complex azimuthal pattern in P-wave amplitudes may be caused by considerable differences in spectral content between Shots 1 and 4. However filtering both signals below 10 Hz does not reduce azimuthal differences. The amplitude ratios for Shot 2 are close to 1 in all directions except ENE, where it reaches approximately 1.5. For Shot 3 the ratios are close to 1 in all directions except WNW, where they reach approximately 1.8. The P-wave amplitude ratios are more homogeneous for Shots 2 and 3 (64-75% isotropic component) than for Shot 1 (82% isotropic component).

Another important metric of seismic source anisotropy is the ratio between S and P wave amplitudes. Figure 3-8 shows the seismic records for Shots 1-4 recorded at Station R06 (Figure 2-10; Figure 3-8a) and Station R01 (Figure 2-10; Figure 3-8b). We notice that there is considerable amount of energy observed on the transverse component. The P-wave amplitude of the transverse component starts small and then increases as time progresses, which can be attributed to scattering. The relative S-wave amplitudes are significantly higher for Shots 1 and 3 than for Shot 4. This cannot be a result of scattering or P-S conversion; therefore, at least some of the energy arriving as S-wave originates at the source.

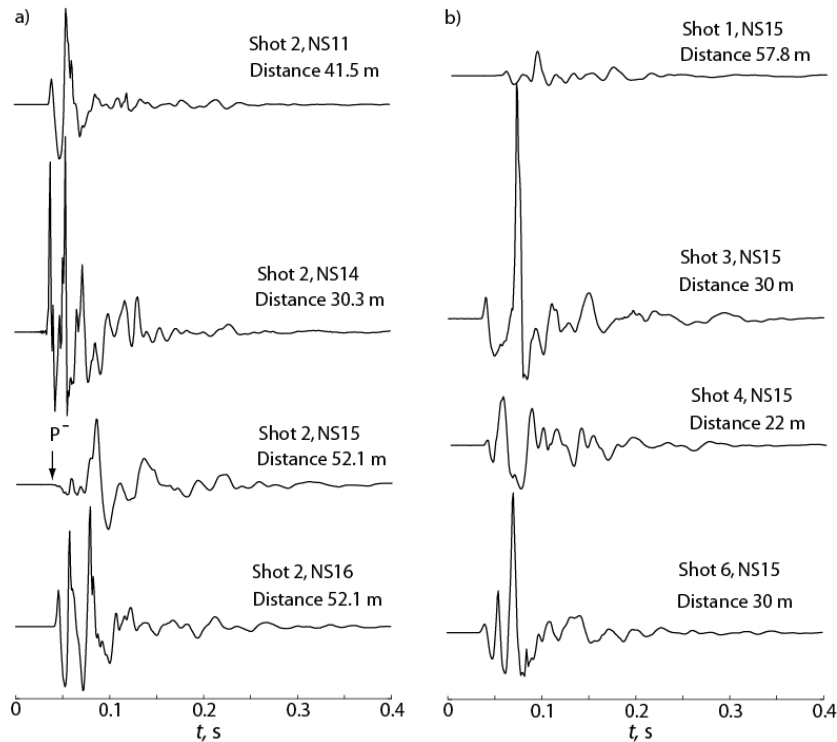


Figure 3-6. a) Near-source accelerograms for Shot 2 recorded by NS11, NS14, NS15, and NS16; b) Shot 1, 3, 4, and 6 recorded by NS15 located near Shot 5. The vertical scale is the same for all waveforms.

Figure 3-9 shows the S/P ratios as a function of azimuth for Shots 1-4 calculated using the stations of the circular array (Figure 2-10). Table 3-3 shows the mean S/P ratios for the explosions and their standard deviations (column 4). The ratios for Shot 1 are greater than one for all stations and have a mean value of 3.31. They appear to be randomly distributed and have the largest variance. The ratios for Shot 3 are also random with the mean value close to 2, while the ratios for Shot 2 are close to 1 in the NW quadrant and close to 2 in the SE quadrant. There is an old deep water-filled quarry located to the SE from the test site, suggesting that larger S/P ratios in that direction may be caused by P-S scattering. The ratios for Shot 4 are close to 1. Thus, the lowest P/S ratios are observed for the deep shot, which was expected. According to Table 3-3, the larger S/P ratios correlate with surface fracturing, while there is no correlation with the estimated moment tensors.

Table 3-3. Summary of the Explosion Characteristics.

Shot	MT isotropic component (%)	Surface fracturing	Mean S/P ratio
1	82	Yes	3.31±1.53
2	65	No	1.85±1.02
3	70	Yes	2.08±0.95
4	80	No	1.07±0.38

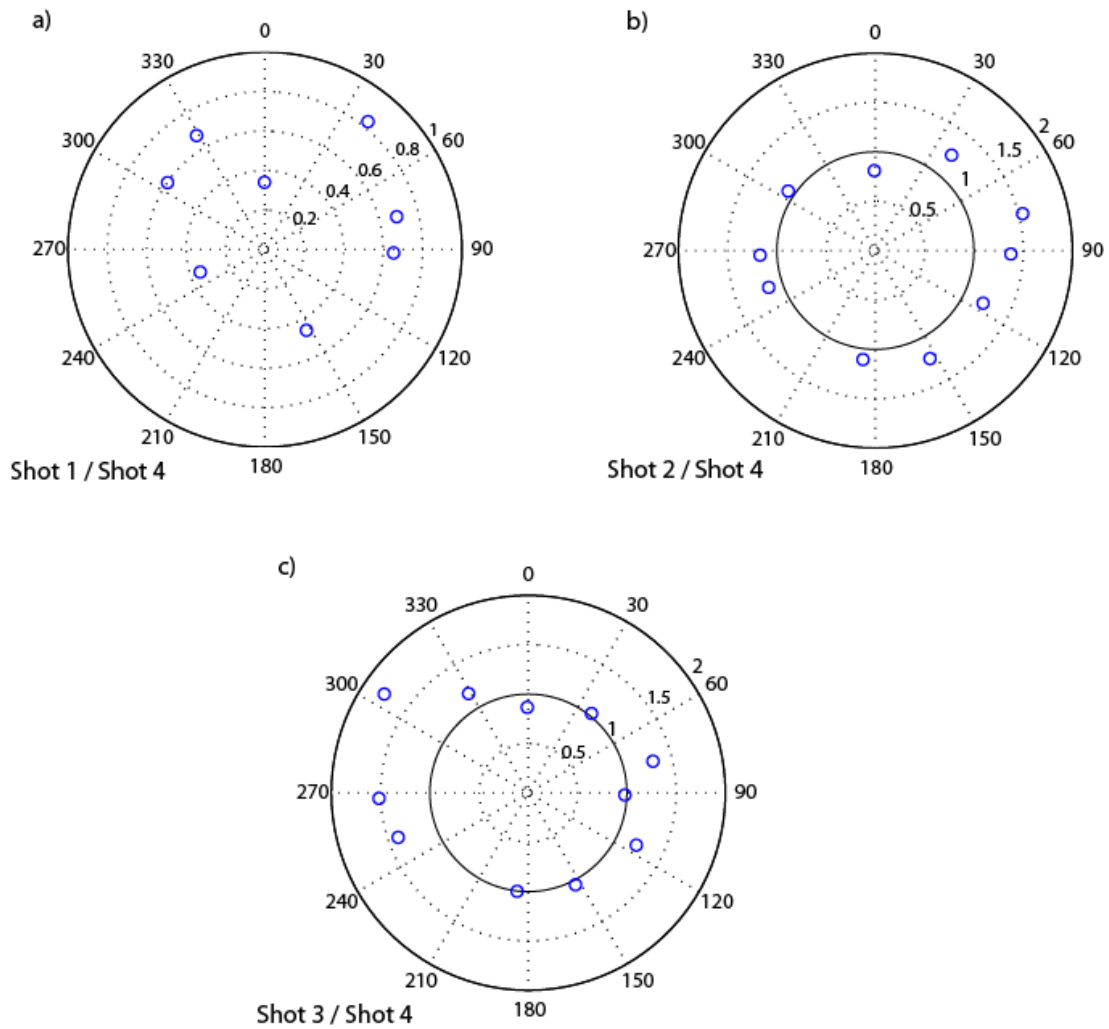


Figure 3-7. Azimuthal variations of P-wave amplitude ratios between: a) Shot 1 and Shot 4, b) Shot 2 and Shot 4, and c) Shot 3 and Shot 4.

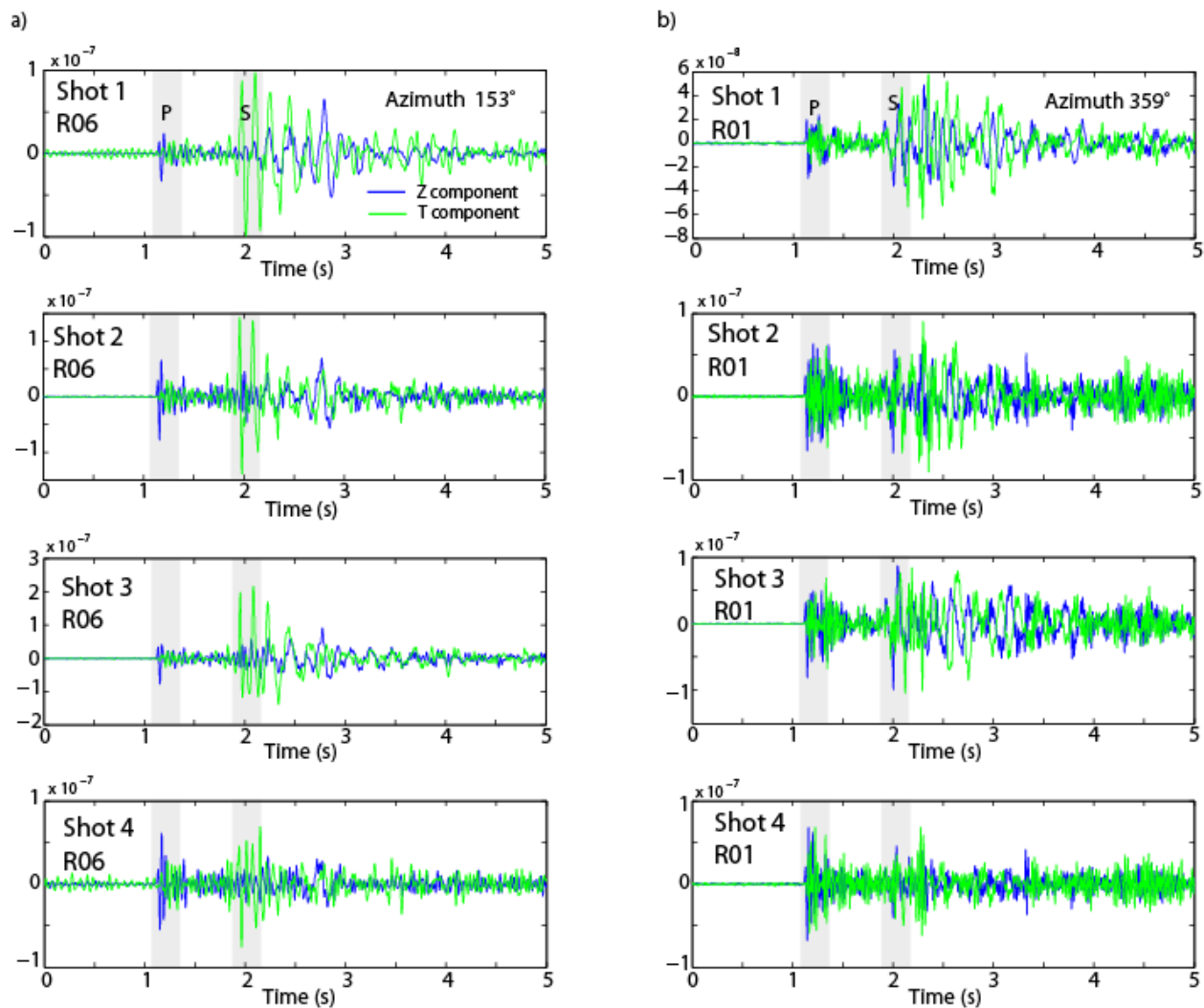


Figure 3-8. Vertical (blue) and transverse (green) component seismograms for Shots 1-4 recorded at: a) Station R06, and b) Station R01. Both stations are located at approximately 6 km distance from the sources.

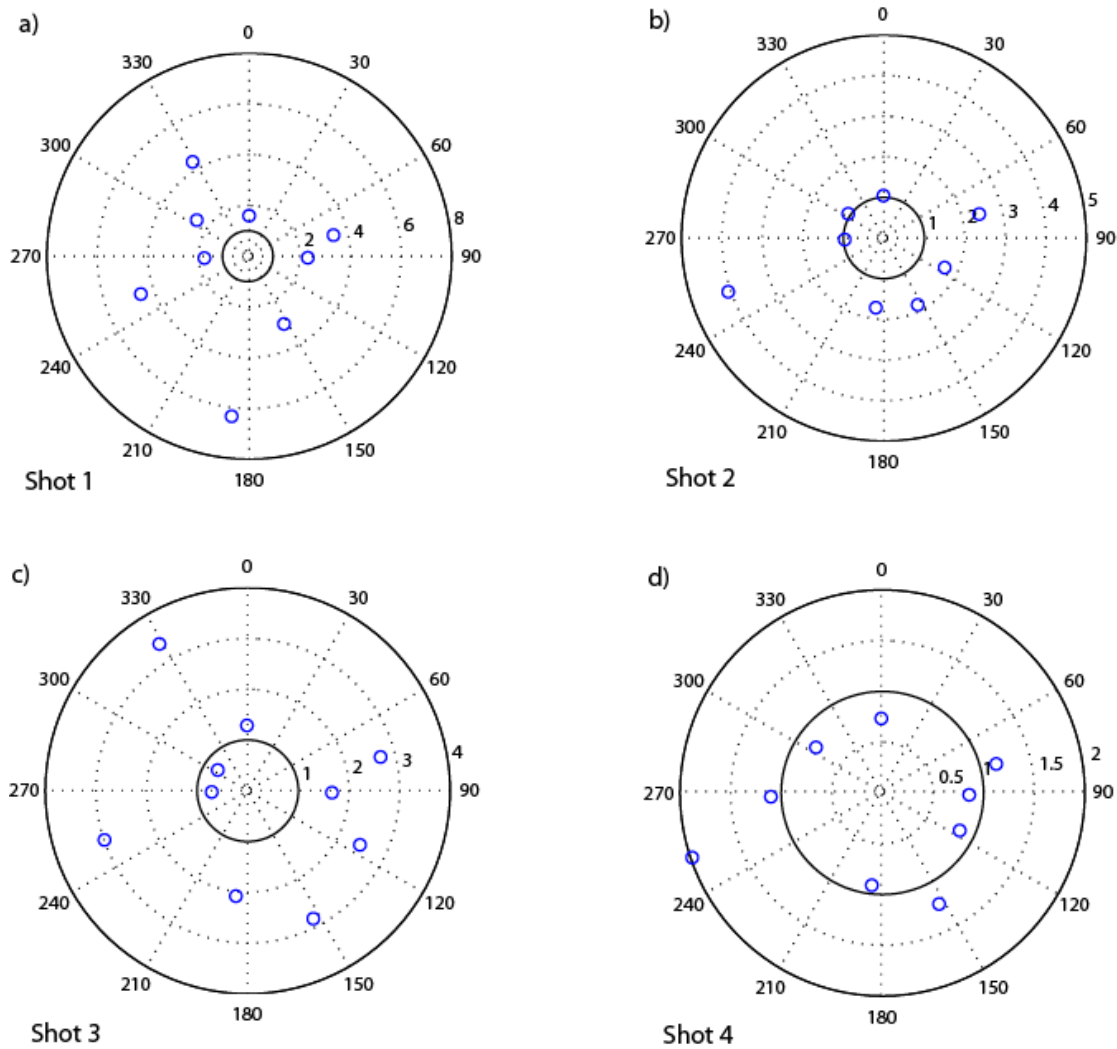


Figure 3-9. Azimuthal variations of S/P amplitude ratios for: a) Shot 1, b) Shot 2, and c) Shot 3, and d) Shot 4. Vertical component was used to measure P-wave amplitudes, while S-wave amplitudes were measured on the transverse component. The waveforms were bandpass filtered between 10 and 50 Hz for consistency with the moment tensors.

CONCLUSIONS AND RECOMMENDATIONS

We estimated the moment tensor solutions for four explosions conducted in the Rock of Ages quarry in Barre, VT during NEDE2. The main goal of this study was to find correlations between the seismic source anisotropy and the VOD of the explosives.

The diagonal elements are dominant in the moment tensor solutions; however, Shots 2 and 3 have significant off-diagonal components. The isotropic component varies between 64% for the

shallow HANFO shot (Shot 2) and 82% for the black powder shot (Shot 1). The deep HANFO shot has significantly higher isotropic component (80% isotropic) than the shallow HANFO shot (64% isotropic).

Even though all explosions had approximately equal TNT yields, the explosive moments are different. The moment M_0 for the black powder shot is about 25% less than the HANFO shot and about 50% less than the Comp B shot.. The moment M_0 for the deep shot is approximately 81% of M_0 for the shallow shot. Shot 2 produced a negative polarity at one of the near-source stations which was in agreement with the smallest isotropic component for that shot.

Our results show no significant correlation between the surface fracturing and the moment tensor isotropic component. The moment tensors may have poor resolution at high frequencies due to complexities in the seismic velocity including strong vertical anisotropy. We also did not observe any correlation between the P-wave radiation pattern and the moment tensor isotropic component. There is however a strong correlation between the surface fracturing and the S/P amplitude ratios. In our experiments, the surface fracturing was related to either slow VOD or presence of water in the shot borehole. The largest S/P ratios were observed for the black powder shot. The HANFO shot, which did not produce surface fracturing, has the second smallest S/P ratios, followed by the deep HANFO shot. These results show that long fractures may be responsible for the complex shear wave generation.

4. SPECTRAL RATIO SOURCE CHARACTERIZATION

INTRODUCTION

The primary objective of the New England Damage Experiment (NEDE Phases I and 2) is to understand phase generation and propagation, particularly for shear waves, from explosion sources. One of the theories for shear wave generation is that rock damage from the explosion creates small fractures that each contribute a small amount of shear energy to the radiated signal. To test this hypothesis we conducted explosions using three types of blasting materials including black powder (BP), ammonium nitrate/emulsion (HANFO), and Composition B (Comp B).

These three materials have disparate velocities of detonation (VOD) and produce dramatically different volumes of gas. BP deflagrates, e.g. burns, instead of detonating, unless under high confining pressures. The variations in VOD (Leidig *et al.*, 2010) and gas production result in significantly different amounts and types of rock damage around the explosion. If rock damage is a source of shear waves or other phases, we should observe variations in the phases from the different explosions. Table 4-1 details the explosives used and additional information can be found in Chapter 2.

Table 4-1. Explosive Characteristics for NEDE2 Shots.

Shot	Explosive 1	Explosive 2	Weight of explosive 1 (lbs)	Weight of explosive 2 (lbs)	TNT Equivalent Yield (lbs)	Charge bottom (m)	Charge center (m)	SDOB TNT Equiv (m/kt ^{1/3})	Hole Diameter (cm)
1	Black powder	N/A	250.0	0.0	150.0	14.20	12.89	305.7	22.2
2	Heavy ANFO	Booster	184.5	1.8	150.0	14.25	13.50	320.1	22.2
3	Comp B	Emulsion	100.7	31.6	161.2	13.36	12.32	285.2	22.2
4	Heavy ANFO	Booster	184.5	2.6	151.1	29.79	29.03	686.7	22.2
5	Heavy ANFO	Booster	184.5	1.8	150.0	14.02	13.31	315.6	22.2
6	Heavy ANFO	Booster	184.5	1.8	150.0	13.51	12.80	303.6	22.2

DATA ANALYSIS

In order to remove the effects of sensor emplacement conditions and slightly different travel paths and distances between shots, spectral ratios were examined for each shot. The P, S, and Rg phases and noise samples were isolated with windows of equal lengths. Power Spectral Densities (PSD) were then calculated for each window (Figure 4-3 through Figure 4-14). To ensure the proper phase was isolated in each window, hodograms were produced for each event. The P phase window should consist of little transverse motion, while the S window should be primarily transverse motion. The Rg phase should exhibit retrograde elliptical motion. Example hodograms are shown for Shot 2 at station SE02 in 2-D (Figure 4-1) and 3-D (Figure 4-2).

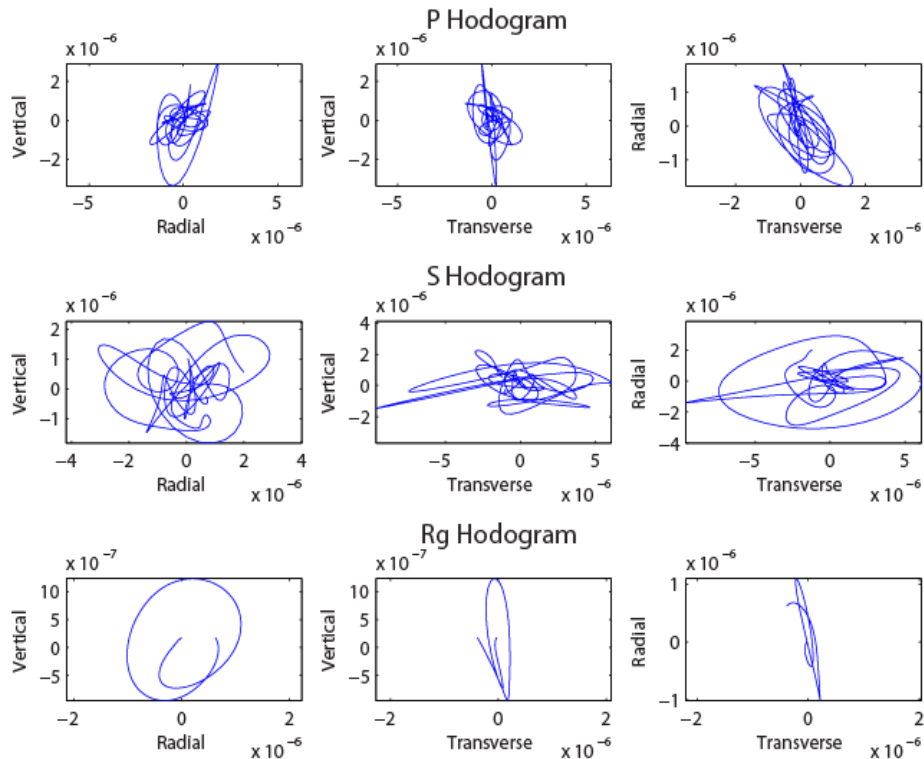


Figure 4-1. Hodograms of P (top row), S (middle row), and Rg (bottom row) windows used to confirm isolation of proper phase.

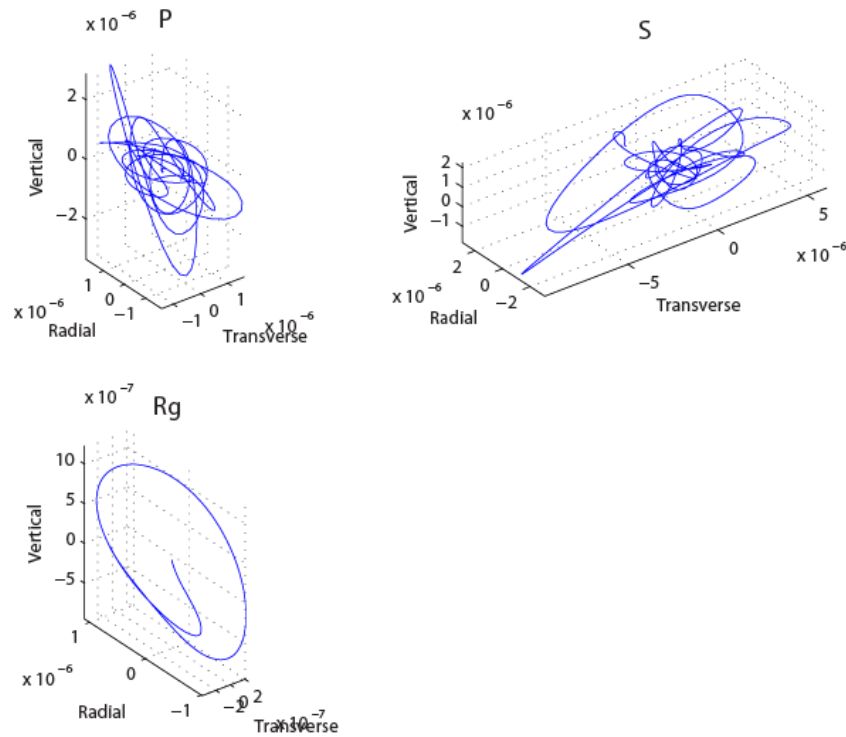


Figure 4-2. 3-D hodograms of P (top left), S (top right), and Rg (bottom) windows used to confirm isolation of proper phase. *P* motion primarily on vertical and radial components, *S* motion primarily on the transverse component, and *Rg* motion shows retrograde elliptical motion on the vertical and radial components.

Figure 4-3 through Figure 4-5 plot the P, S, and Rg PSD for Shots 1-5 at station SE02 (6 km). These plots will be discussed in the following sections. To simplify the plots visually, Shot 6 is not shown.

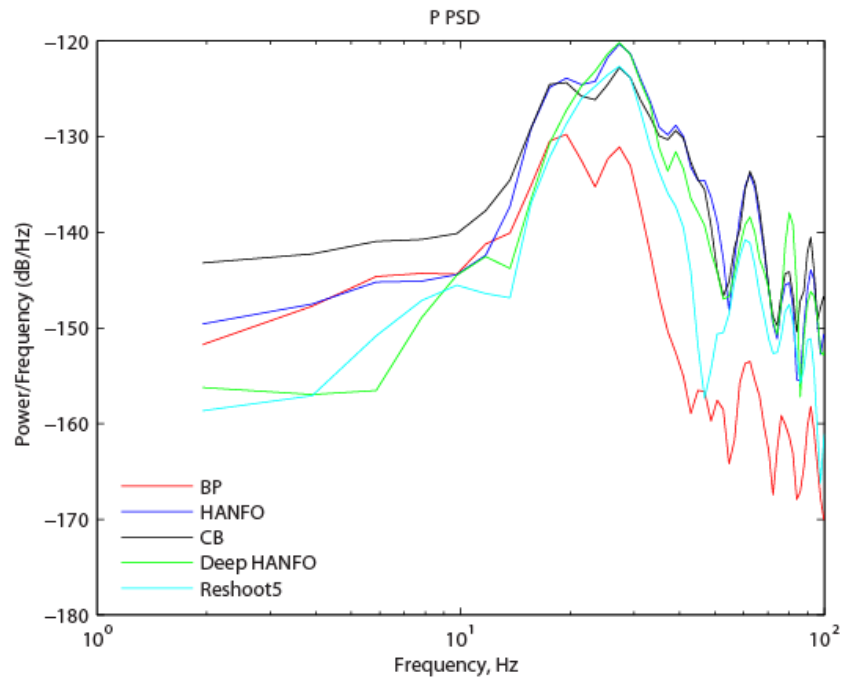


Figure 4-3. Vertical component PSD of P phase window at station SE02 for Shots 1-5.

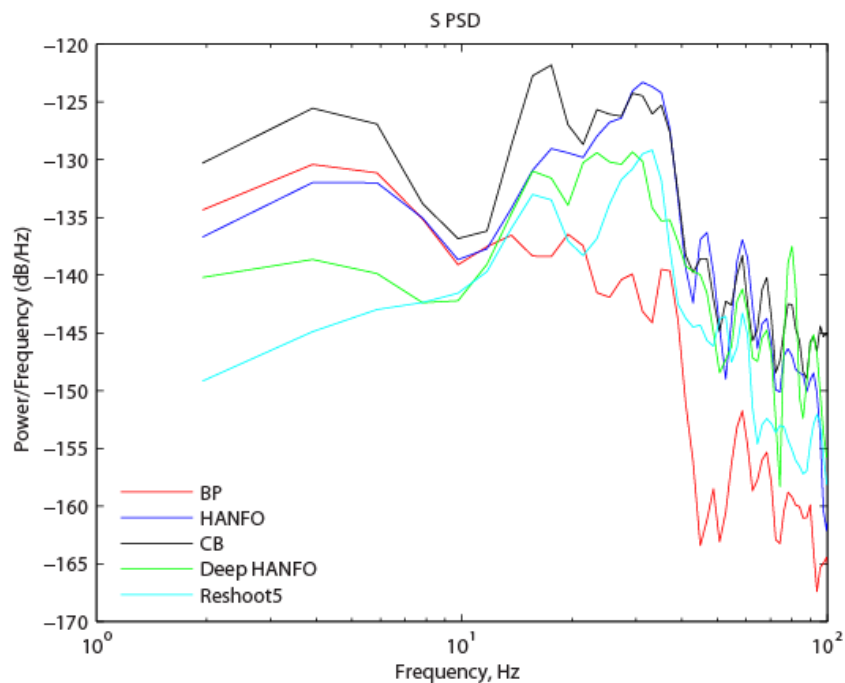


Figure 4-4. Vertical component PSD of S phase window at station SE02 for Shots 1-5.

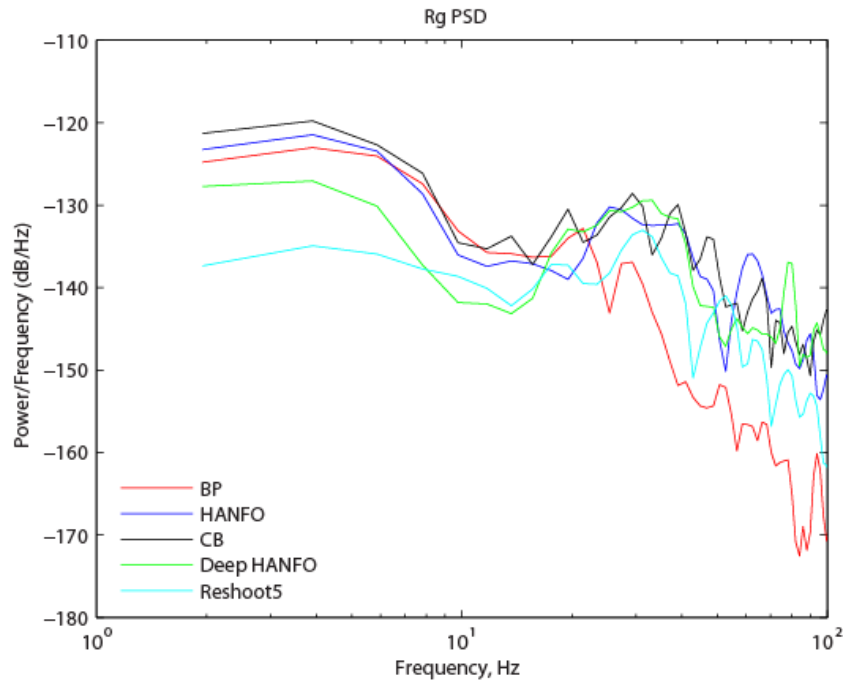


Figure 4-5. Vertical component PSD of Rg phase window at station SE02 for Shots 1-5.

NEDE2 BP Shot 1 Phase Ratios

Figure 4-6 plots the vertical component spectral analysis for BP Shot 1 at station SE02 (6 km). The vertical component waveform is shown with the phase windows marked by the colored vertical lines. Due to the short event to station distance, narrow phase windows are required to isolate the various phases and results in only resolving the PSD at higher frequencies. In this case, only data above 6 Hz should be trusted. Below ~15 Hz, the S and Rg phases have at least 10 times more energy than the P wave, but between 15 and 30 Hz, the P wave amplitudes are up to 10 times larger. The Rg window is likely composed of mainly P and S coda in this frequency range though. Above 30 Hz, the ratios vacillate around one as the signal amplitude decreases above the explosion corner frequency. The BP shot generated P and S energy up to 20 dB less than the HANFO or Comp B shots above 10 Hz. Below 10 Hz, the BP P and S energy matches the HANFO P and S energy. The BP Rg PSD is very similar to the HANFO Rg PSD.

At station SE07 (21 km), the S and Rg phases are larger than the P phase at all frequencies (Figure 4-7). Above 30 Hz, the signal decays to the background noise level. The shear waves at this station are well formed, while the P wave is relatively small. At both distances, these phases exhibit similar frequency spectral peaks.

NEDE2 HANFO Shot 2 Phase Ratios

HANFO Shot 2 displays similar spectral characteristics to Shot 1 except the P/Rg ratio is larger than the P/S ratio at 6 km distance between 15 and 30 Hz. This difference appears to be primarily related to larger P and S wave amplitudes from the HANFO shot, rather than smaller amplitudes

in the Rg window (Figure 4-3 through Figure 4-5). The shear wave PSD of the HANFO shot is up to 20 dB larger than the BP shot (Figure 4-4). Below ~15 Hz, the S and Rg energy is greater than the P energy. At 21 km (Figure 4-9), the P amplitudes are smaller relative to the S and Rg amplitudes and the ratios generally do not exceed a value of one at any frequency.

NEDE2 Comp B Shot 3 Phase Ratios

The waveform and spectra from the Comp B Shot 3 (Figure 4-10 and Figure 4-11) look very similar to the HANFO Shot 2. At 6 km, the P/S ratio is less than one at frequencies below 20 Hz and does not exceed a value of two until 40 Hz. This is caused by a combination of reduced P amplitudes between 20-40 Hz and increased S amplitudes below 25 Hz compared to the HANFO shot (Figure 4-3 and Figure 4-4). This observation differs from the expected result, but there were issues with Shot 3 that will be addressed in the discussion section. The Comp B and HANFO shots generated similar energy at all frequencies in the Rg window.

At 21 km distance, the P/S and P/Rg ratios remain at or below one at all frequencies just as with the BP and HANFO shots. This suggests that the travel path to SE07 either attenuates the P energy or converts P energy to S and Rg energy.

NEDE2 Deep HANFO Shot 4 Phase Ratios

In comparison to the shallower HANFO Shot 2, the deep HANFO Shot 4 produced slightly smaller amplitude P waves at most frequencies, particularly below 10 Hz, and up to 8 dB reduced amplitudes for S waves below 40 Hz (Figure 4-3, Figure 4-4, Figure 4-12). The over buried nature of this shot possibly reduced rock damage and the ability to generate shear waves. This observation would support the theory of rock damage being at least partially responsible for shear waves from explosions. It is also likely that the depth reduced the CLVD source and block motions. The Rg energy from the deep shot was ~5 dB less than for the shallow shot.

At the 21 km station, these effects are not as apparent (Figure 4-13). The amplitudes of all phases are reduced for the deep shot relative to the shallow shot, but just as with the other shots, the P/S and P/Rg ratios do not consistently reach a value of one.

NEDE2 HANFO Reshoot Shots 5 and 6 Phase Ratios

Shots 5 and 6 of the NEDE2 experiment were conducted in the damage zones from previous explosions conducted in the NEDE1 experiment. These shots were conducted as part of a DTRA project on amplitude biases from fracture decoupling and show significant differences from the traditional virgin rock explosions. All three phases exhibit a 2 dB to 10 dB amplitude reduction compared to the shallow virgin rock HANFO shot. The P waveform amplitude is larger than either the S or Rg phases, with both of the latter being poorly formed at 6 km (Figure 4-14 and Figure 4-16).

When the energy reaches SE07, the P wave is only slightly larger than the background noise (Figure 4-15 and Figure 4-17). The signals lack a well-defined Rg phase but the P/Rg ratio is still significantly less than one below 30 Hz.

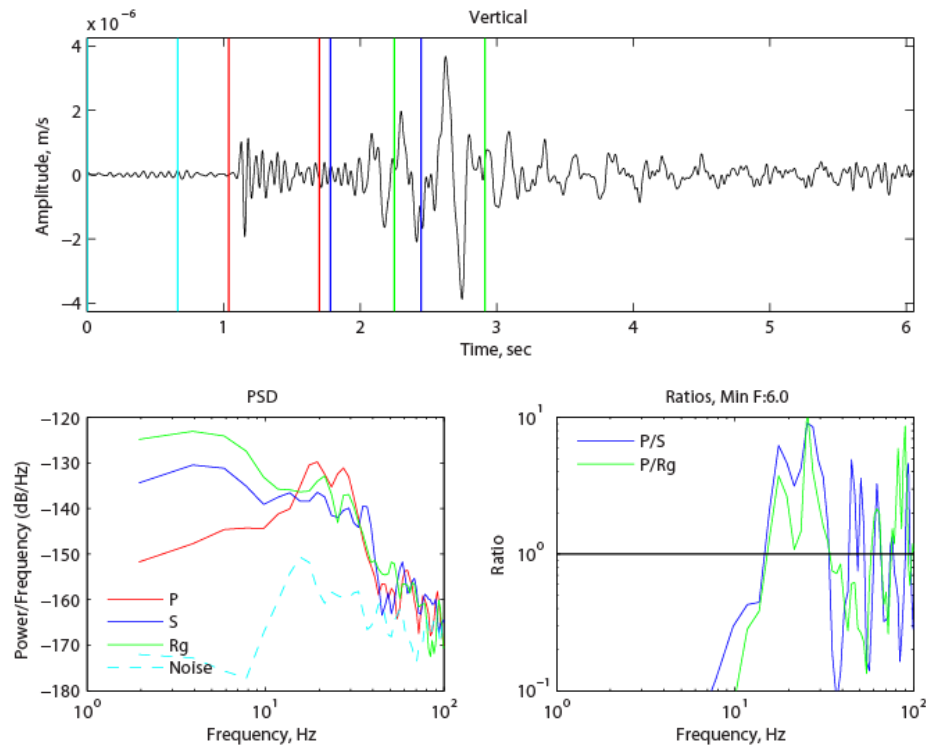


Figure 4-6. Vertical component waveform (top) from Shot 1 at station SE02. PSD of the P, S, and Rg phases (bottom left) and phase spectral ratios (bottom right). Min. resolved freq. 6 Hz.

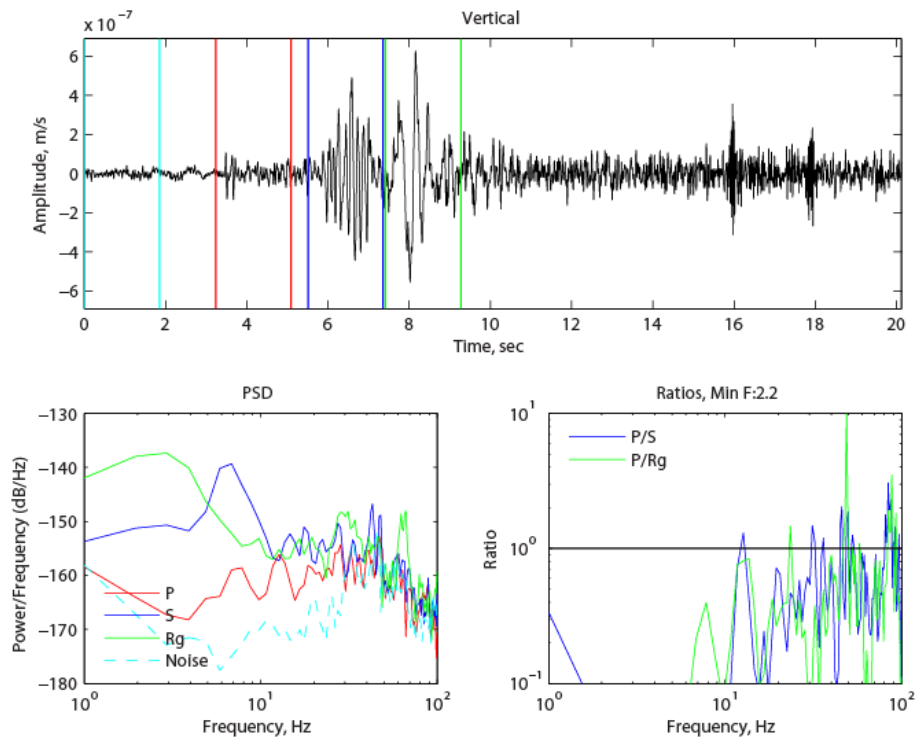


Figure 4-7. Vertical component waveform (top) from Shot 1 at station SE07. PSD of the P, S, and Rg phases (bottom left) and phase spectral ratios (bottom right). Min. resolved freq. 2.2 Hz.

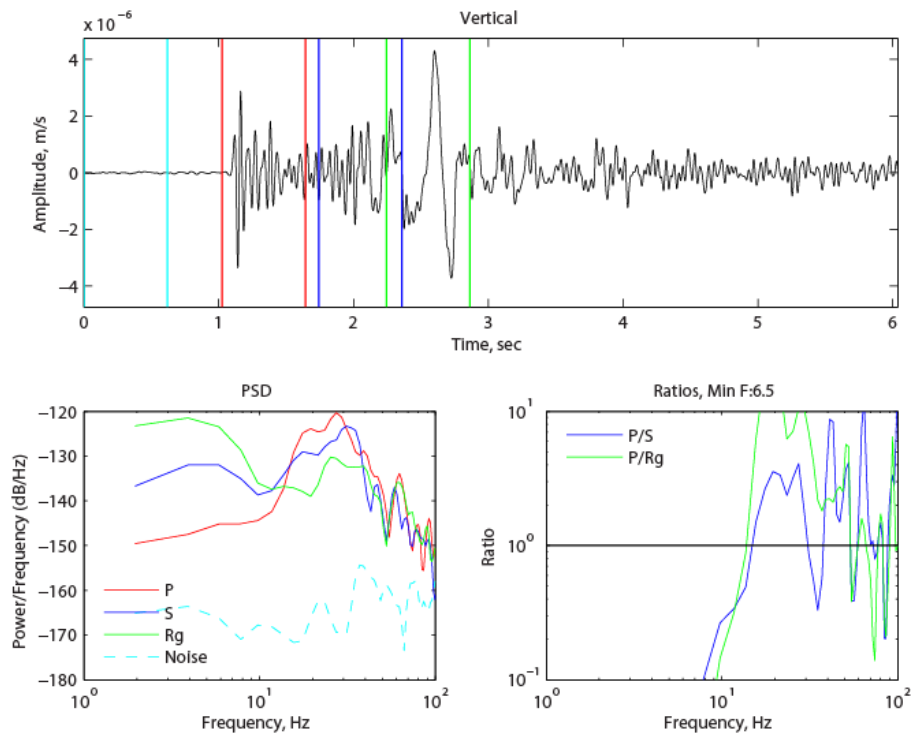


Figure 4-8. Vertical component waveform (top) from Shot 2 at station SE02. PSD of the P, S, and Rg phases (bottom left) and phase spectral ratios (bottom right). Min. resolved freq. 6.5 Hz.

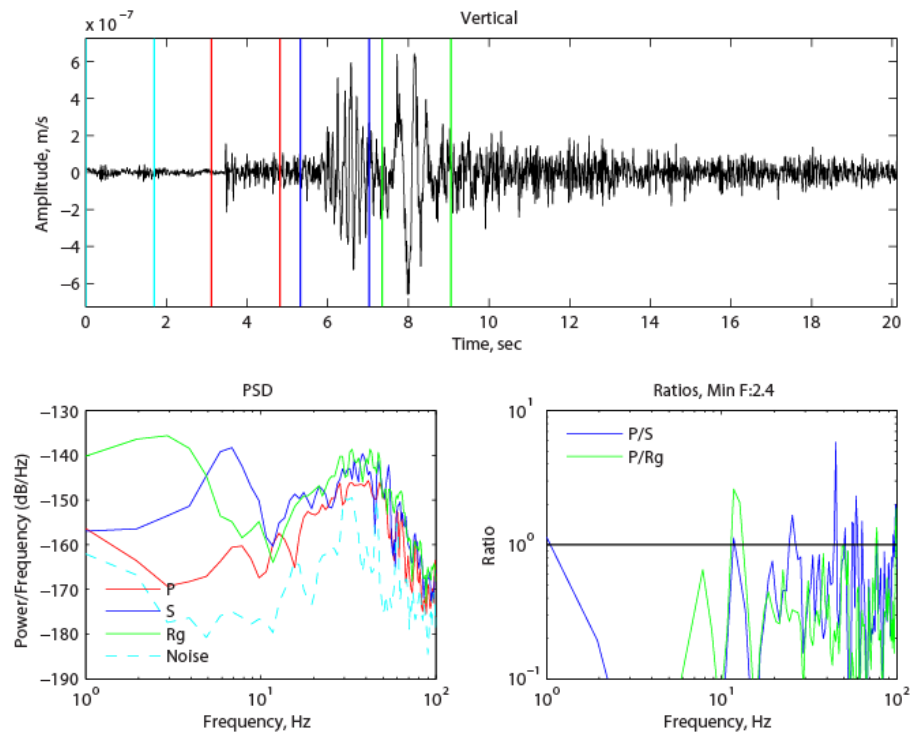


Figure 4-9. Vertical component waveform (top) from Shot 2 at station SE07. PSD of the P, S, and Rg phases (bottom left) and phase spectral ratios (bottom right). Min. resolved freq. 2.4 Hz.

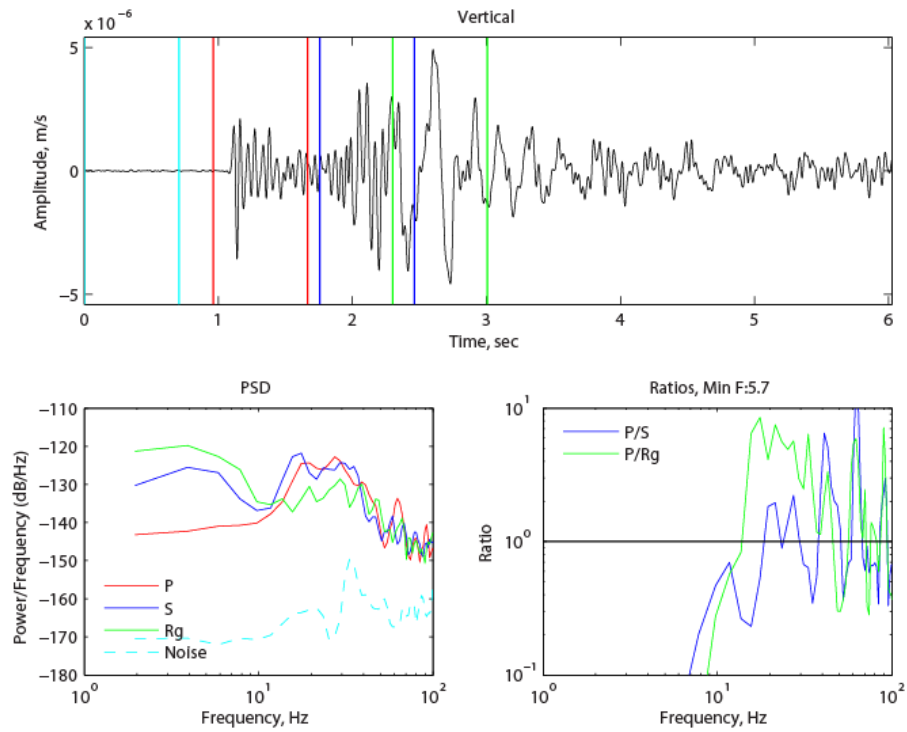


Figure 4-10. Vertical component waveform (top) from Shot 3 at station SE02. PSD of the P, S, and Rg phases (bottom left) and phase spectral ratios (bottom right). Min. resolved freq. 5.7 Hz.

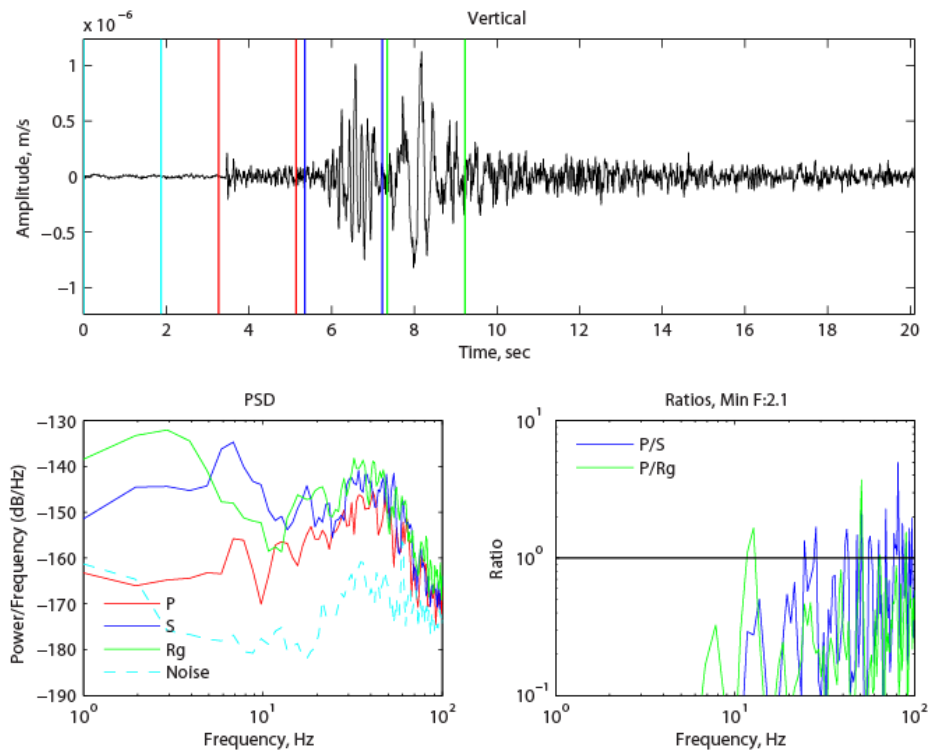


Figure 4-11. Vertical component waveform (top) from Shot 3 at station SE07. PSD of the P, S, and Rg phases (bottom left) and phase spectral ratios (bottom right). Min. resolved freq. 2.1 Hz.

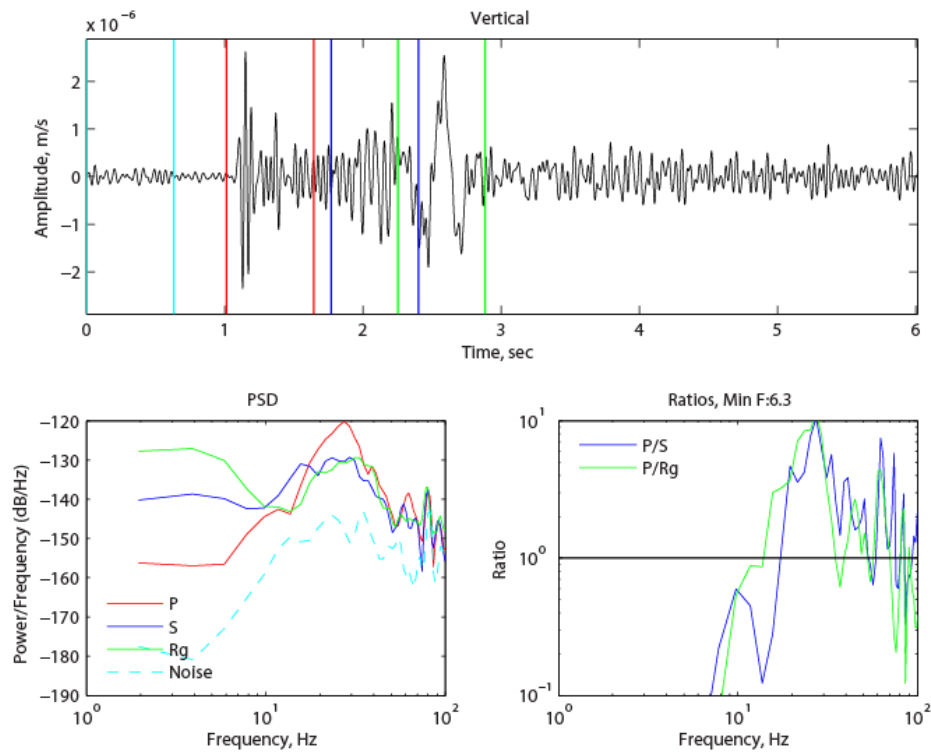


Figure 4-12. Vertical component waveform (top) from Shot 4 at station SE02. PSD of the P, S, and Rg phases (bottom left) and phase spectral ratios (bottom right). Min. resolved freq. 6.3 Hz.

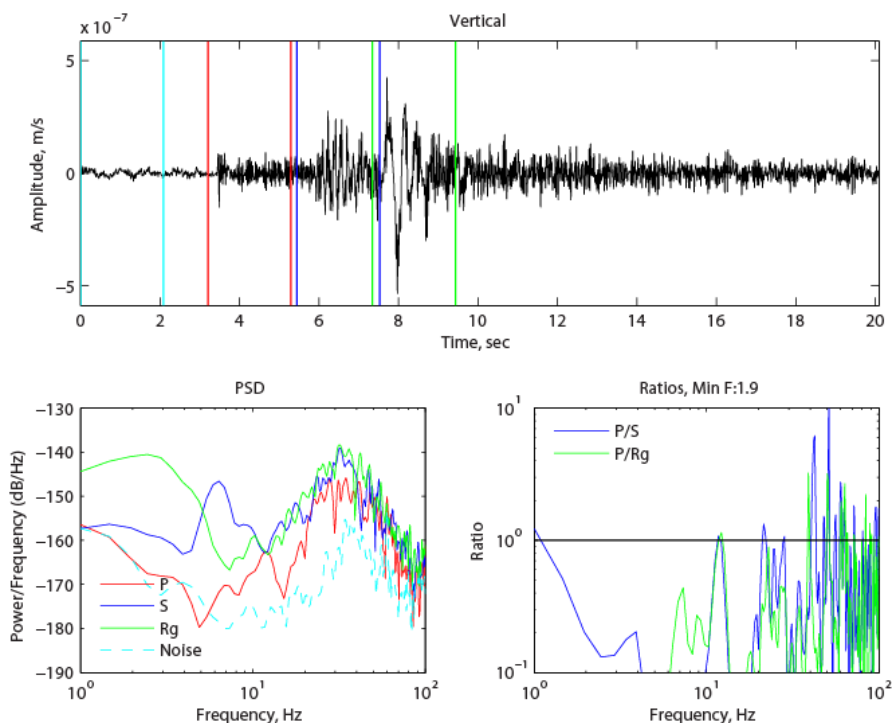


Figure 4-13. Vertical component waveform (top) from Shot 4 at station SE07. PSD of the P, S, and Rg phases (bottom left) and phase spectral ratios (bottom right). Min. resolved freq. 1.9 Hz.

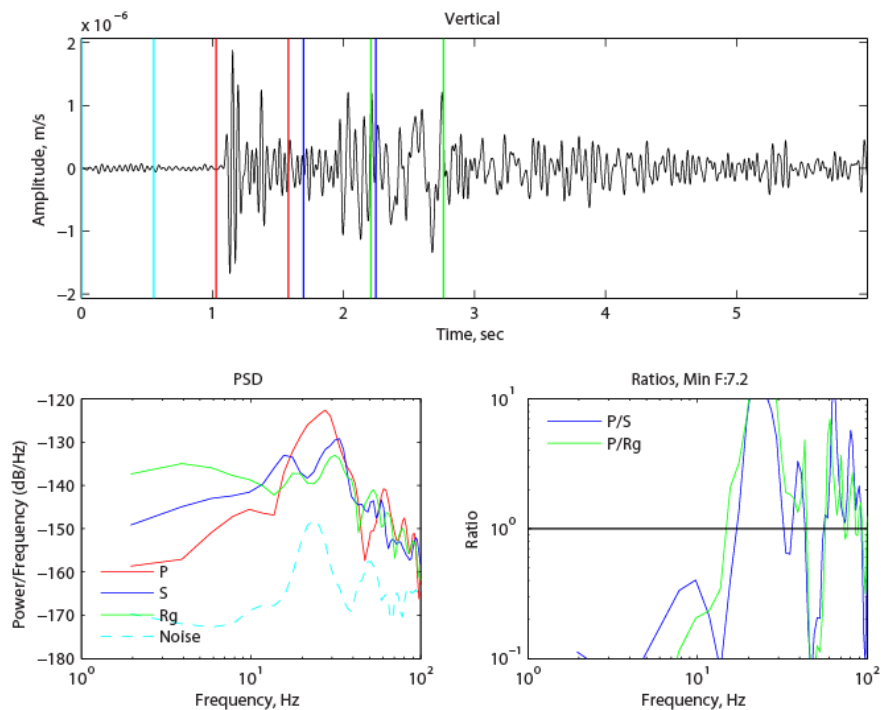


Figure 4-14. Vertical component waveform (top) from Shot 5 at station SE02. PSD of the P, S, and Rg phases (bottom left) and phase spectral ratios (bottom right). Min. resolved freq. 7.2 Hz.

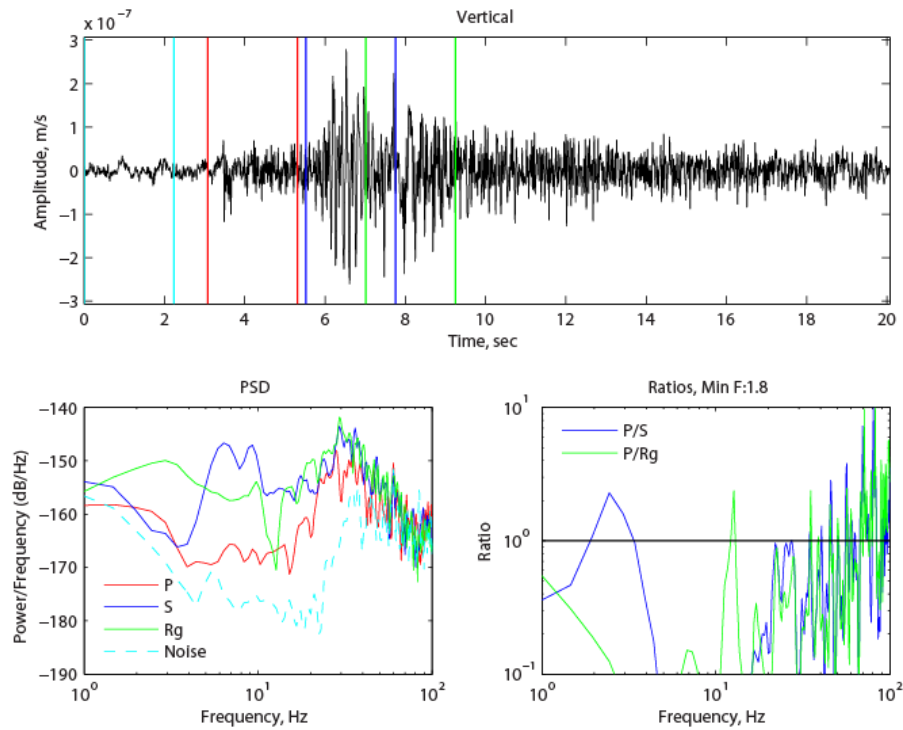


Figure 4-15. Vertical component waveform (top) from Shot 5 at station SE07. PSD of the P, S, and Rg phases (bottom left) and phase spectral ratios (bottom right). Min. resolved freq. 1.8 Hz.

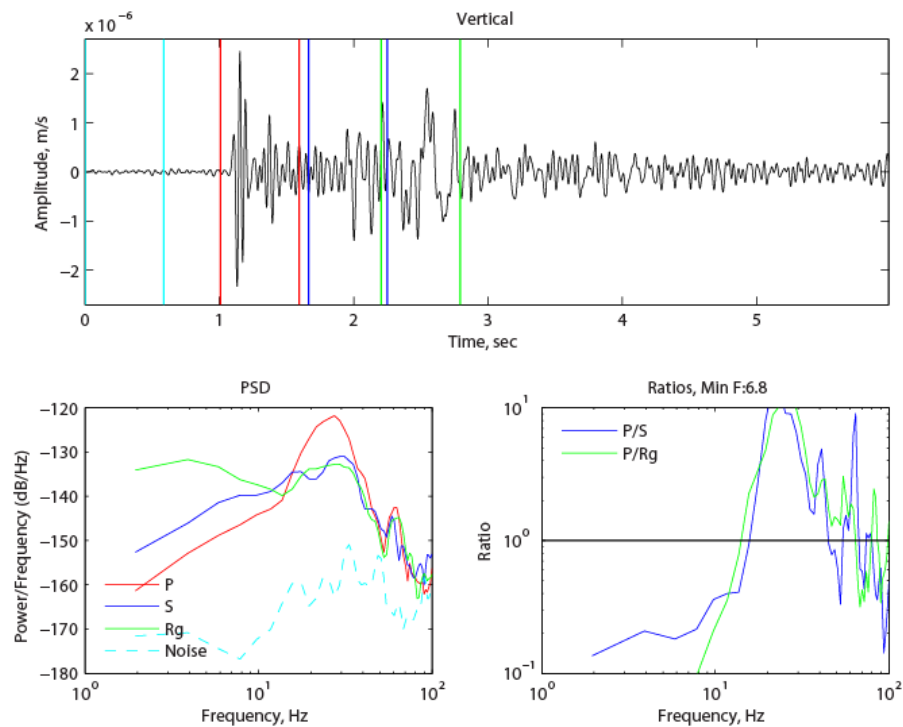


Figure 4-16. Vertical component waveform (top) from Shot 6 at station SE02. PSD of the P, S, and Rg phases (bottom left) and phase spectral ratios (bottom right). Min. resolved freq. 6.8 Hz.

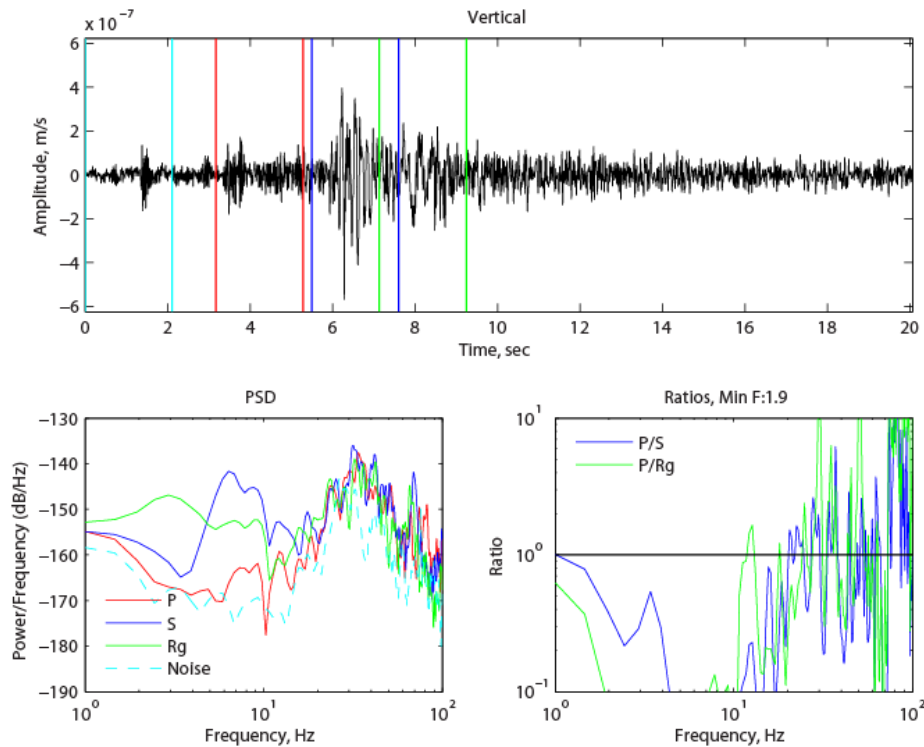


Figure 4-17. Vertical component waveform (top) from Shot 6 at station SE07. PSD of the P, S, and Rg phases (bottom left) and phase spectral ratios (bottom right). Min. resolved freq. 1.9 Hz.

Comparison of NEDE and NEDE2 Phase Ratios

Shots 1 from the NEDE1 and NEDE2 were both BP shots with the latter shot having almost twice the amount of explosive. Figure 4-18 plots the waveform and spectra from the original NEDE1 explosion. The amplitude of the P, S, and Rg phase amplitudes are about 2 times larger for the NEDE2 shot, but the P/S and P/Rg ratios are similar for the two shots.

The larger NEDE1 Shot 4 HANFO (Figure 4-19) produced larger S and Rg amplitudes than the smaller NEDE2 Shot 2 HANFO (Figure 4-8), while the P amplitudes are similar. The P/S and P/Rg ratios cross a value of one near 12 Hz for NEDE2 Shot 2, but the crossing point was close to 20 Hz for NEDE1 Shot 4. These differences are subtle, but suggest a larger shot at a similar depth of burial produces more shear and Rg energy.

The P/S and P/Rg issues mentioned earlier for the NEDE2 Comp B Shot 3 are highlighted when comparing with the NEDE1 Comp B Shot 5 (Figure 4-20). The NEDE1 Comp B shot had a larger P wave with respect to the S and Rg phases and the P/S and P/Rg ratios were above one from ~10-50 Hz. These results indicate the NEDE2 Comp B shot generated relatively more S and Rg energy relative to the P energy. The issues with the NEDE2 Comp B shot will be discussed in the next section.

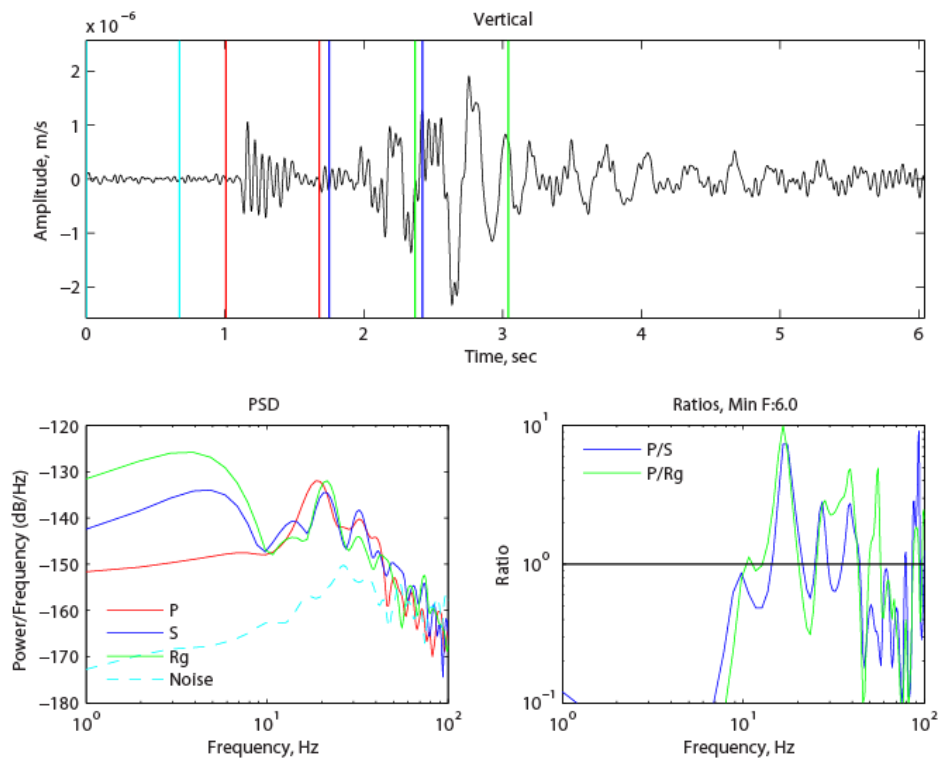


Figure 4-18. Vertical component waveform (top) from the NEDE1 BP Shot 1 at station SE02. PSD of the P, S, and Rg phases (bottom left) and phase spectral ratios (bottom right). Min. resolved freq. 6 Hz.

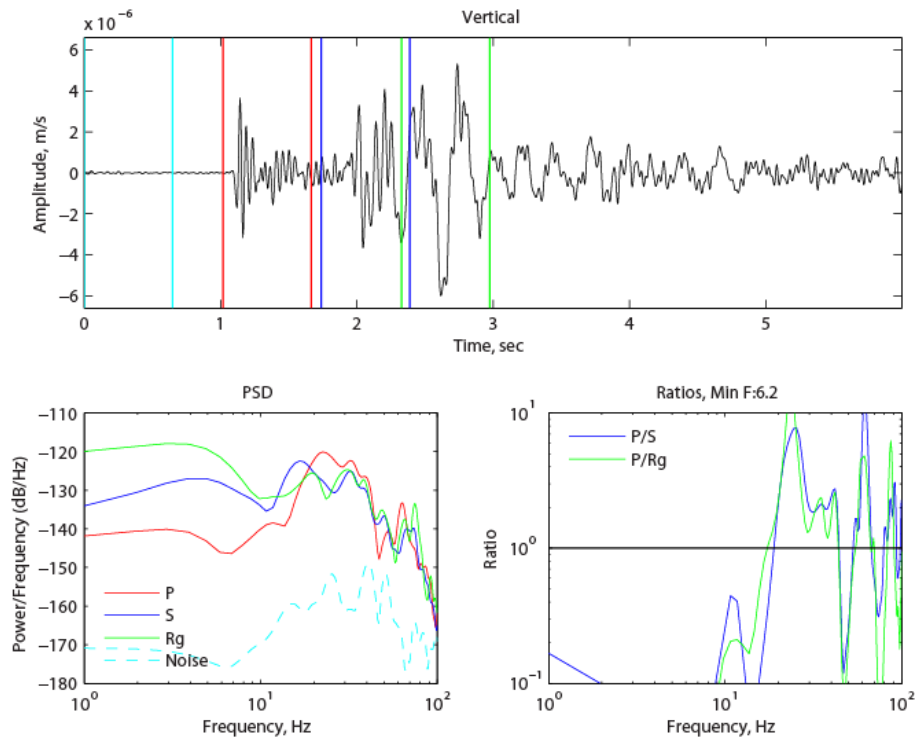


Figure 4-19. Vertical component waveform (top) from the NEDE1 HANFO Shot 4 at station SE02. PSD of the P, S, and Rg phases (bottom left) and phase spectral ratios (bottom right). Min. resolved freq. 6.2 Hz.

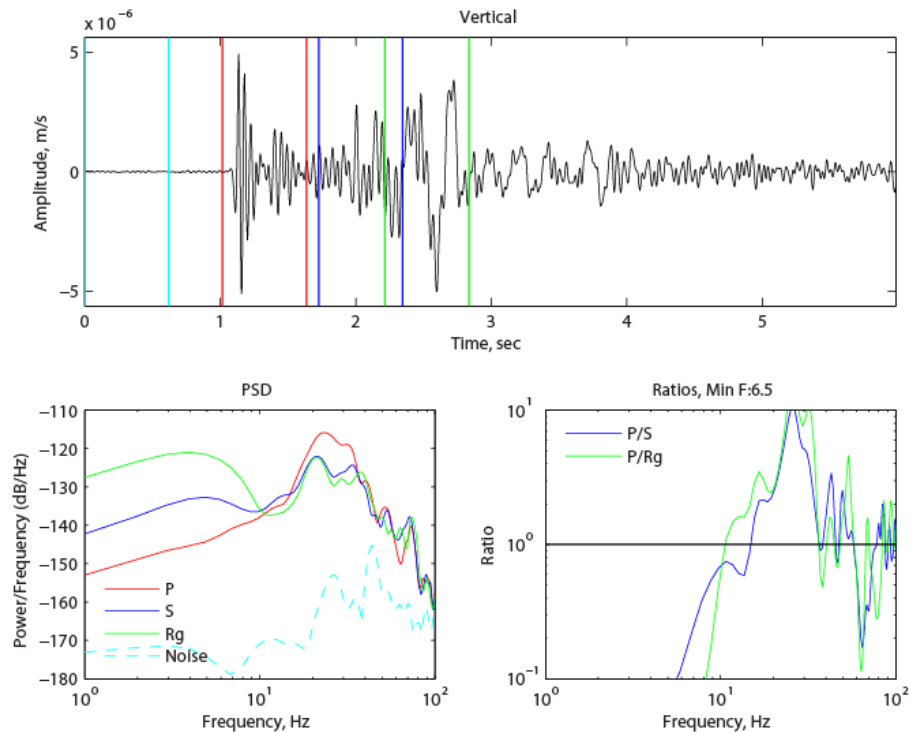


Figure 4-20. Vertical component waveform (top) from the NEDE1 Comp B Shot 5 at station SE02. PSD of the P, S, and Rg phases (bottom left) and phase spectral ratios (bottom right). Min. resolved freq. 6.5 Hz.

DISCUSSION

It is important to acknowledge an issue with the NEDE2 Comp B shot. All shots were intended to detonate above the water table in dry holes, but this was not possible for the NEDE2 Comp B shot. Most of the NEDE2 holes contained water shortly after drilling but were able to be pumped and dried prior to loading. The Comp B hole continuously recharged even after a day of pumping. In the NEDE1, the Comp B charges did not produce any surface fracturing like the BP and HANFO blasts. This was the expected result and is due to the fast loading rates in the borehole and reduced gas generation of Comp B. The Comp B did not drive long fractures like the BP and HANFO. In the NEDE2 shot, the water in the borehole and fracture system acted like a hydraulic ram extending the existing fracture network. The result was a 20+ m long fracture on the surface that emitted three fireballs. The damage from the NEDE2 Comp B shot potentially behaved more like a BP shot with water, instead of explosive gas, extending the fractures.

The primary goal of the New England Damage Experiment series is to understand shear wave generation from explosion sources. A number of key observations were made examining the NEDE2 shots (equal TNT yields) and comparing them to the NEDE1 shots (equal explosive weight):

- As observed during both experiments, BP is deficient in energy > 20 Hz.

- HANFO produced larger P and S amplitudes than BP > 12 Hz.
- The P, S, Rg spectra exhibit spectral peaks at similar frequencies.
- At the 6 km station, $P > S$ and Rg above 10 Hz; at the 21 km station, $P < S$ and R at all frequencies; which indicates greater P attenuation or significant phase conversion to S/Rg along travel path.
- Contradictory to expectations and NEDE1 data, NEDE2 P/S ratio on the vertical component was smallest for Comp B.
- Issues with the NEDE2 Comp B shot resulted in increased P amplitude < 12 Hz and increased S amplitude < 25 Hz compared to HANFO.
- The deep HANFO shot has reduced P amplitude < 10 Hz, and reduced S and Rg amplitudes at most frequencies compared to the shallow HANFO shot.
- Reshoot amplitudes reduced for all phases at all frequencies compared to virgin rock HANFO shot.
- Rg window amplitudes similar for BP, HANFO, and Comp B shots <20 Hz.
- The larger NEDE1 Shot 4 produced larger S and Rg phases, but similar P energy to the smaller NEDE2 Shot 2.
- The NEDE2 Comp B shot produced larger S and Rg amplitudes relative to P amplitudes than the NEDE1 Shot 5 Comp B.

These observations suggest that BP produces similar amounts of seismic energy at frequencies less than 20 Hz when a TNT equivalent quantity is used. This is likely the result of deflagration (burning) of the BP not producing a sharp, high frequency signal. The BP shot produced large quantities of gas and caused extensive fracturing of the sub- and near-surface rock. The equal or reduced seismic amplitudes of the BP shot suggest that long gas driven fractures are not the primary source of shear waves from explosions.

In contrast, the Comp B shot presumably produced a hydraulically driven 20+ m long fracture and produced significantly more shear energy than the other shots. P energy was also increased for the Comp B shot, and Stroujkova *et al.* (submitted 2013; Chapter 9 of this report) has shown that explosions in water saturated rock result in improved seismic coupling. Therefore, it is uncertain whether the long surface fracture or the increased seismic coupling is responsible for the increased shear energy. The reshoots produced reduced amplitudes for all phases at all frequencies due to diminished seismic coupling. In either case, these results suggest shear wave energy is generated at or in the damage zone of the shot.

The reduction in P/S ratio from 6 to 21 km may indicate that travel path causes either increased P waves attenuation or P energy conversion into shear energy. Further P/S ratio analysis needs to be done as a function of distance along the linear array to resolve this question.

Postulated theories regarding shear wave generation from explosions include late term damage modeled with a CLVD source and block motions. The deep HANFO shot, which is expected to have a higher corner frequency, resulted in reduced P wave amplitudes below 10 Hz and reduced S and Rg amplitudes at all frequencies. The larger yield NEDE1 Shot 4 produced larger S and Rg amplitudes than the similar depth, but smaller, NEDE2 Shot 2, while the P phases had similar amplitudes. This limited data is not enough data to draw a firm conclusion, but the results do not discredit these theories as possible shear wave sources.

5. NON-PARAMETRIC STUDIES OF SEISMIC SOURCES AND PROPAGATION EFFECTS FOR NEDE1 AND NEDE2 EXPLOSIONS

ABSTRACT

The New England Damage Experiment (NEDE) was conducted in Barre, VT, in order to evaluate the effect of the velocity of detonation (VOD) of explosives on seismic radiation. Complexities in geology and topography significantly affected the spectra of the local data. In order to separate the source signature from propagation effects we applied a non-parametric inversion method proposed by Andrews (1986). This technique allows estimation of both propagation/site and source effects simultaneously by solving a linear system of equations. The main advantage of this method is that it does not require a priori knowledge of the medium along the source – station path.

Application of the technique to 11 NEDE explosions conducted using different explosives and emplacement conditions has shown that: a) an increase in VOD results in an increase in corner frequency and high-frequency amplitudes and a slight decrease in the low-frequency amplitudes, b) an increase in the depth of burial causes decreased low-frequency amplitudes, c) fracturing of the emplacement medium leads to decreased seismic amplitudes over the entire frequency range. The methodology can be further evaluated and then transferred to explosions conducted at nuclear test sites using explosions with known yield and other source parameters.

OBJECTIVES

Monitoring nuclear explosions is commonly performed at regional or teleseismic distances, thus the spectra of the recorded seismic waves are significantly affected by the propagation. The effects of geology and structure along the propagation path add significant complexities to the P-wave spectra and change the source signature, while attenuation and scattering may potentially change the high-frequency roll-off of the spectra. Removing propagation effects is particularly important for explosion monitoring, because explosion sources radiate significant energy at high frequencies, which are strongly affected by local site conditions, such as complex surface geology and irregular topography. Accurate removal of the propagation and site effects for each explosion-station path requires knowledge of numerous medium parameters (including velocity and attenuation models), which are often poorly quantified.

To avoid the need to parameterize the medium to remove the propagation effects we used a non-parametric inversion method proposed by Andrews (1986). This technique estimates both the site and source effects simultaneously by solving a linear system of equations. It has been used and further developed by numerous authors to study site effects and earthquake spectra (e.g., Castro *et al.* 1990; Boatwright *et al.* 1991; Hartzell 1992). The main benefit of this approach is that it does not rely on knowledge of the medium properties between the source and the receiver.

To study explosion source spectra we used data from the recent New England Damage Experiment conducted by Weston Geophysical in Barre, VT (e.g. Stroujkova *et al.*, 2012). The explosions were conducted using three types of explosives with different velocities of detonation (VOD): Black Powder, Ammonium Nitrate Fuel Oil/Emulsion (HANFO), and Composition B (Comp B). The main objective of the experiment was to study differences in seismic wave generation between different types of explosives, and to determine the mechanism responsible for these differences. One of the HANFO explosions was detonated at greater depth to study the effects of the depth of burial (DOB). In addition, two of the explosions were conducted in fracture zones created by earlier explosions. Thus, this unique dataset contains explosions with different characteristics conducted within a small area. This ensures that the propagation paths from each of these explosions to the monitoring stations are very similar and the effects of propagation can be factored out using the inversion procedure.

RESEARCH ACCOMPLISHED

Experimental Data

The New England Damage Experiment (NEDE) was conducted in a granite quarry located near Barre, Vermont. The first part of the experiment (NEDE1) was conducted in July of 2008 (Leidig, 2010; Stroujkova *et al.*, 2012). The second field campaign (NEDE2) took place in June of 2013. The main purpose of the experiment was to study shear wave generation due to explosives with different velocities of detonation (VOD). The explosives used in this study have different densities, burn rates and different energy content per unit mass. The explosive with the slowest VOD that was used in the experiments was black powder, which burns without forming a detonation wave (deflagration). On the other hand, the high explosives such as HANFO and Comp B develop detonation waves.

Table 5-1 shows some characteristics of NEDE explosions. Five explosions were detonated during NEDE1: three 61 kg explosions (Shot S1-1 – black powder, Shot S1-2 – HANFO, and Shot S1-3 – Comp B), and two 122 kg explosions (Shot S1-4 – HANFO and Shot S1-5 – Comp B). Equal weights of the different types of explosives were detonated. The velocity of detonation was measured for four out of five explosions. The Black Powder burned with the slowest burning rate of 0.49 km/s. The ANFO/Emulsion explosion detonated with a VOD of 5.06 – 5.26 km/s, and Comp B explosives have the highest VOD between all three explosives of (8.31 km/s). Sensor locations are shown in Figure 5-1.

During the NEDE2 field experiment, six explosions with almost the same TNT-equivalent yield were detonated. Shots S2-1, S2-2, and S2-3 were detonated using different explosive types. Shot

S2-4 (HANFO) was overburied compared to Shot S2-2, which had the same yield and explosive type. Shots S2-5 and S2-6 were conducted in fracture zones left by previous explosions conducted during NEDE1 experiment (S1-4 and S1-5 respectively).

Examples of the waveforms and spectra for the explosions are shown in Figure 5-2 and Figure 5-3. Figure 5-2 shows the data recorded at Station SE01, located approximately 3 km from the sources, for NEDE1 (Figure 5-2 a,c) and NEDE2 (Figure 5-2 b,d). The spectra for BP explosions are deficient in high frequencies. Their P-wave amplitudes are lower than the amplitudes for HANFO and Comp B explosions, while their surface wave amplitudes are comparable to those. All the NEDE explosions (Figure 5-2 b,d) had nearly the same TNT-equivalent yields; however their amplitudes were significantly different. Shots 2-1, 2-2, and 2-3 were detonated using different explosive types. The overburied explosion (Shot 2-4) and the fracture zone explosion (Shot 2-5) have smaller amplitudes. Despite the differences in the amplitudes, the waveforms are very similar. Traces recorded by Station SE02 located approximately 6 km from the sources show similar characteristics (Figure 5-3).

Table 5-1. Characteristics for the NEDE Explosions

Shot #	Explosive	Weight of explosive (kg)	TNT Equivalent Yield (kg)*	Borehole diameter (cm)	Charge center depth (m)	sDOB (m/kt ^{1/3})	Charge length (m)
NEDE1							
S1-1	Black powder	60.8	36.5	22.2	8.3	250.2	1.65
S1-2	HANFO	61.5	49.2	22.2	11.3	308.4	1.15
S1-3	Comp B	61.7	83.3	22.2	11.3	258.7	0.94
S1-4	HANFO	122.4	97.9	22.2	12.9	279.9	2.29
S1-5	Comp B	122.6	165.5	22.2	12.7	231.3	1.87
NEDE2							
S2-1	Black powder	113.5	68.1	22.2	12.89	305.7	2.62
S2-2	HANFO	83.8	68.1	22.2	13.50	320.1	1.5
S2-3	Comp B	45.7	73.2	22.2	12.32	285.2	2.08
S2-4	HANFO (deep)	83.8	68.4	22.2	29.03	686.7	1.5
S2-5	HANFO (reshoot)	83.8	68.1	22.2	13.50	320.1	1.5
S2-6	HANFO (reshoot)	83.8	68.1	22.2	13.50	320.1	1.5

*The TNT equivalency conversion factors are: Black Powder/TNT – 0.6, HANFO/TNT - 0.8, Comp B/TNT - 1.35

Explosion spectra recorded at the same station also show similar peaks caused by the propagation and site effects, such as reflections, refractions and layer reverberations (Figure 5-2 c-d and Figure 5-3 c-d). Notice systematic differences in the site effects between NEDE1 and NEDE2 events, expressed as differences in spectral peaks between the experiments. While the dominant frequencies of the peaks stay nearly the same, the widths and the amplitudes appear to be different between NEDE1 and NEDE2. This may be caused by changes in the instrument or the source coupling due to rainfall prior to the experiment in 2013.

To determine whether the changes were caused by the site responses, we plotted spectra of the pre-event noise for the stations operational during both years. Figure 5-4 shows that there was no systematic difference in the pre-event spectra; therefore the reason for the changes in the event spectra between NEDE1 and NEDE2 is not clear.

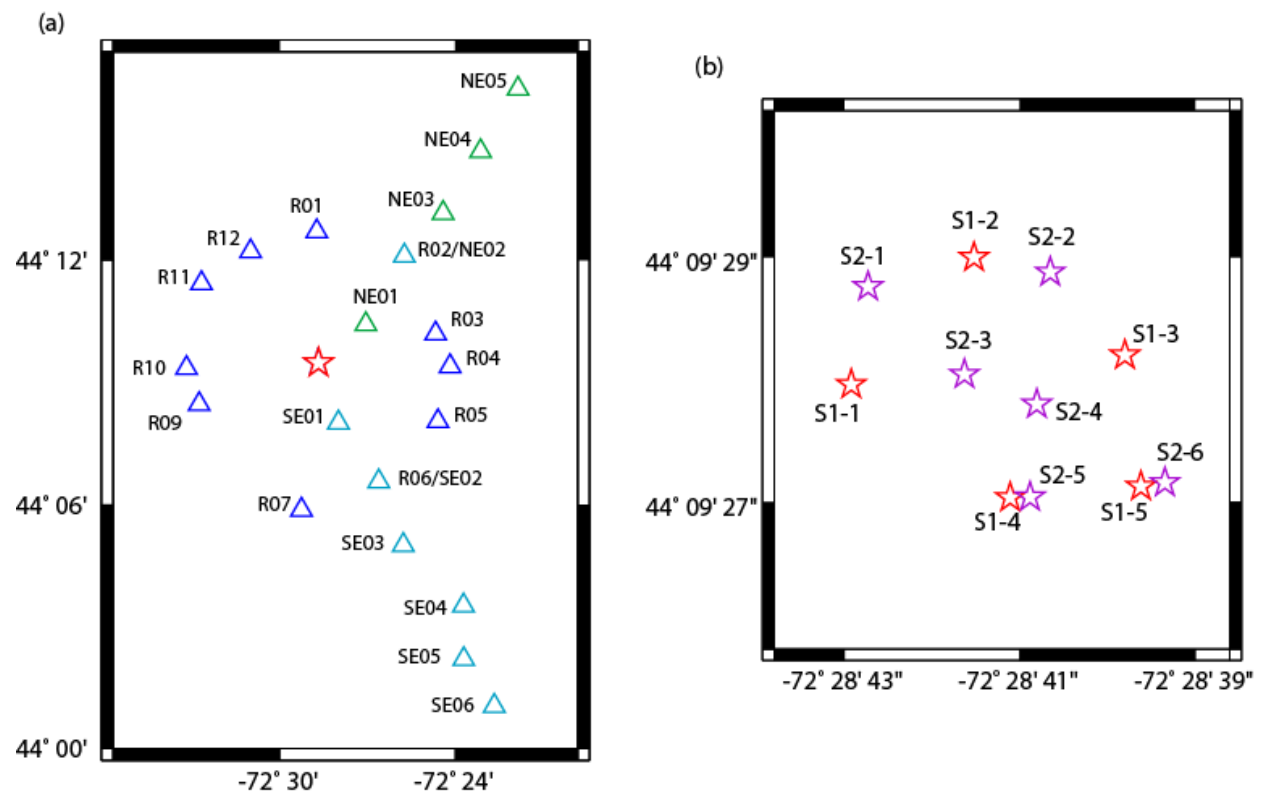


Figure 5-1. (a) The local network around the test site at the Rock of Ages Quarry located in Barre, VT. Green triangles show stations that were only installed for NEDE1, blue triangles show stations operating during NEDE2 only, and stations shown in cyan were operational for both NEDE1 and NEDE2. (b) Enlarged view of the testing area showing the explosions (stars). Red and purple stars show the locations of the explosions conducted during the NEDE1 and NEDE2 field campaigns, respectively.

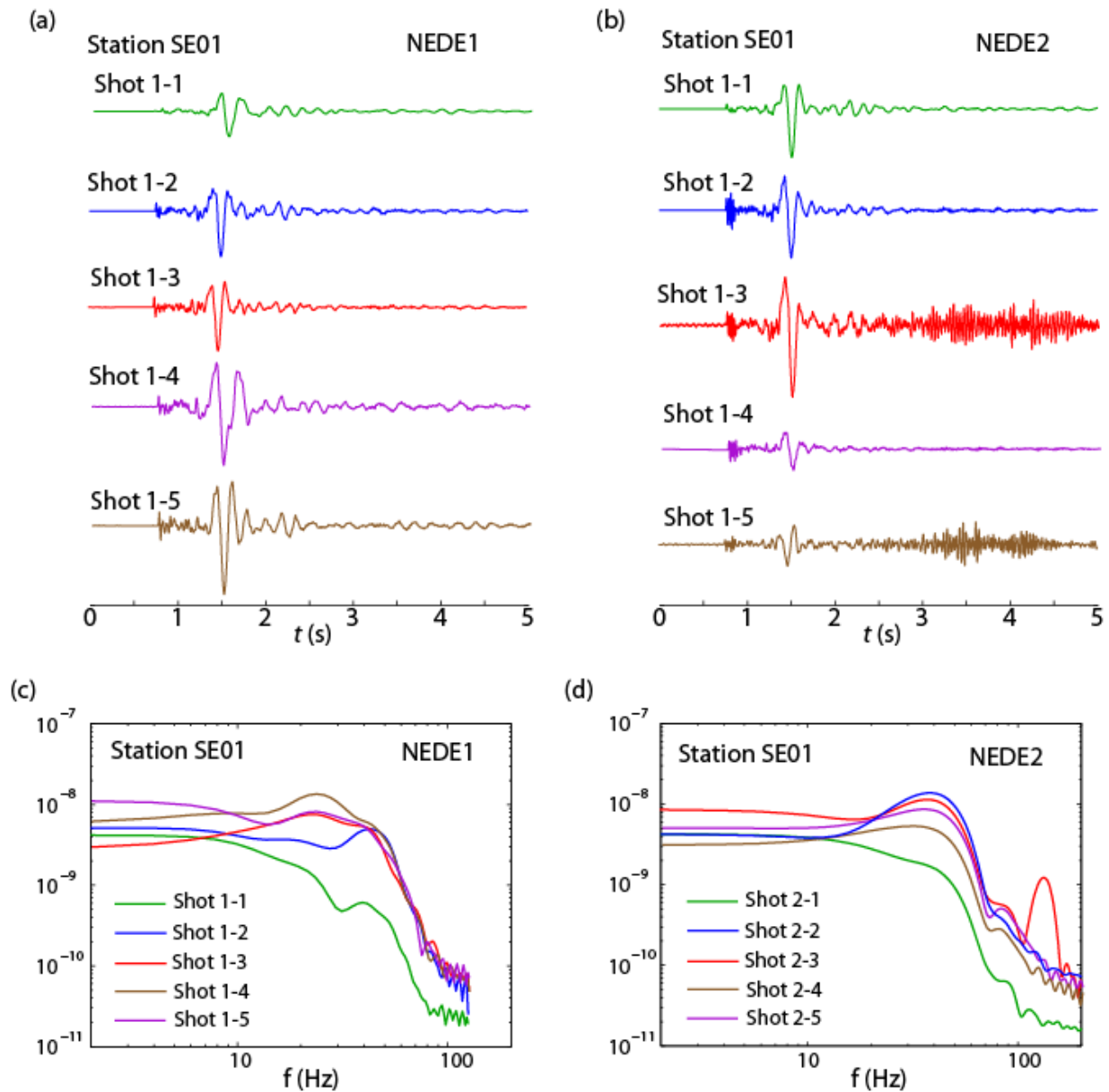


Figure 5-2. Waveforms recorded 3 km from the sources (Station SE01) for the explosions of (a) NEDE1 experiment, (b) NEDE2 experiment. P-wave spectra for (c) NEDE1 explosions shown in (a); (d) NEDE2 explosions shown in (b).

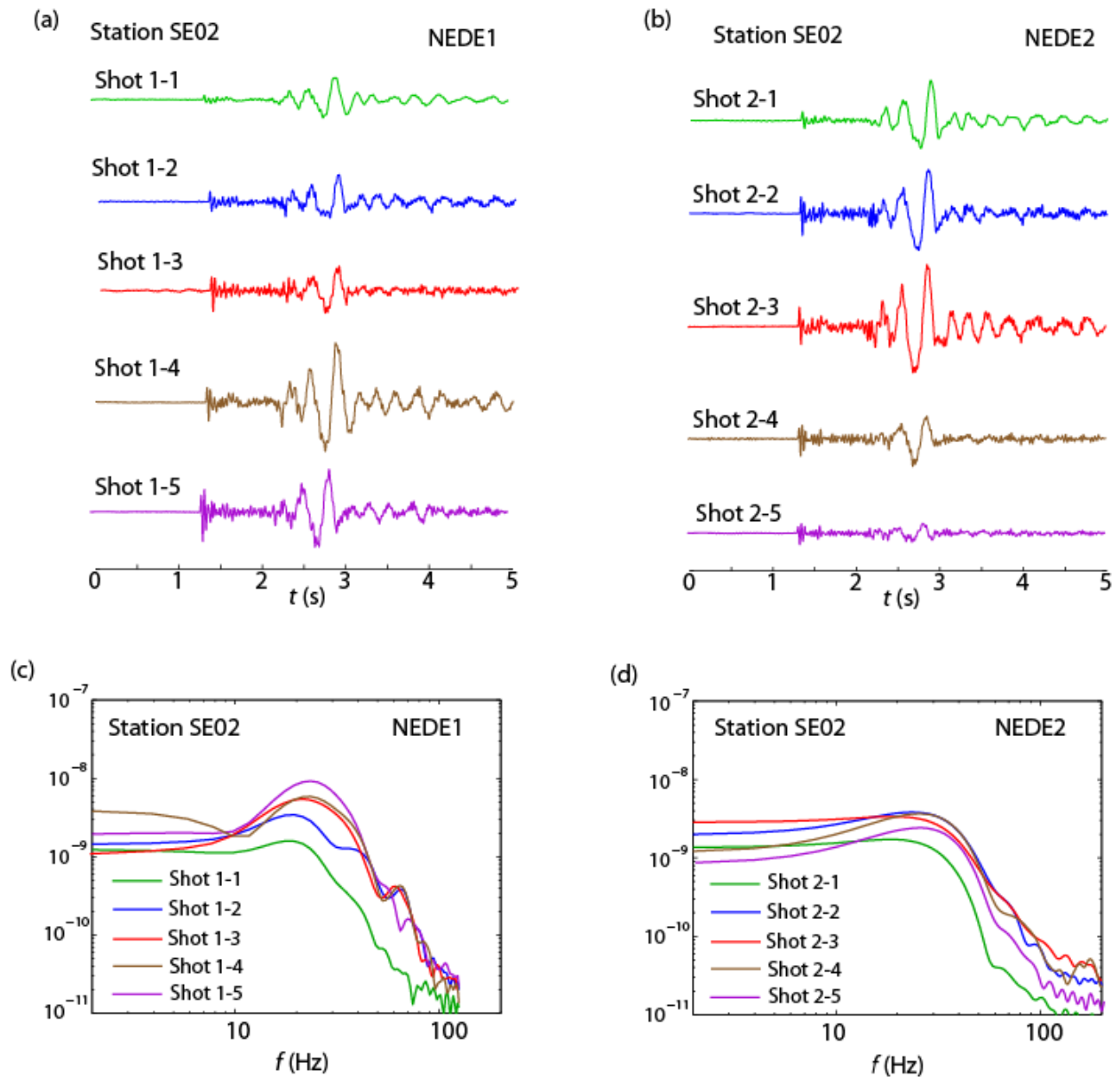


Figure 5-3. Waveforms recorded 6 km from the sources (Station SE02) for the explosions of (a) NEDE1 experiment, (b) NEDE2 experiment. P-wave spectra for (c) NEDE1 explosions shown in (a); (d) NEDE2 explosions shown in (b).

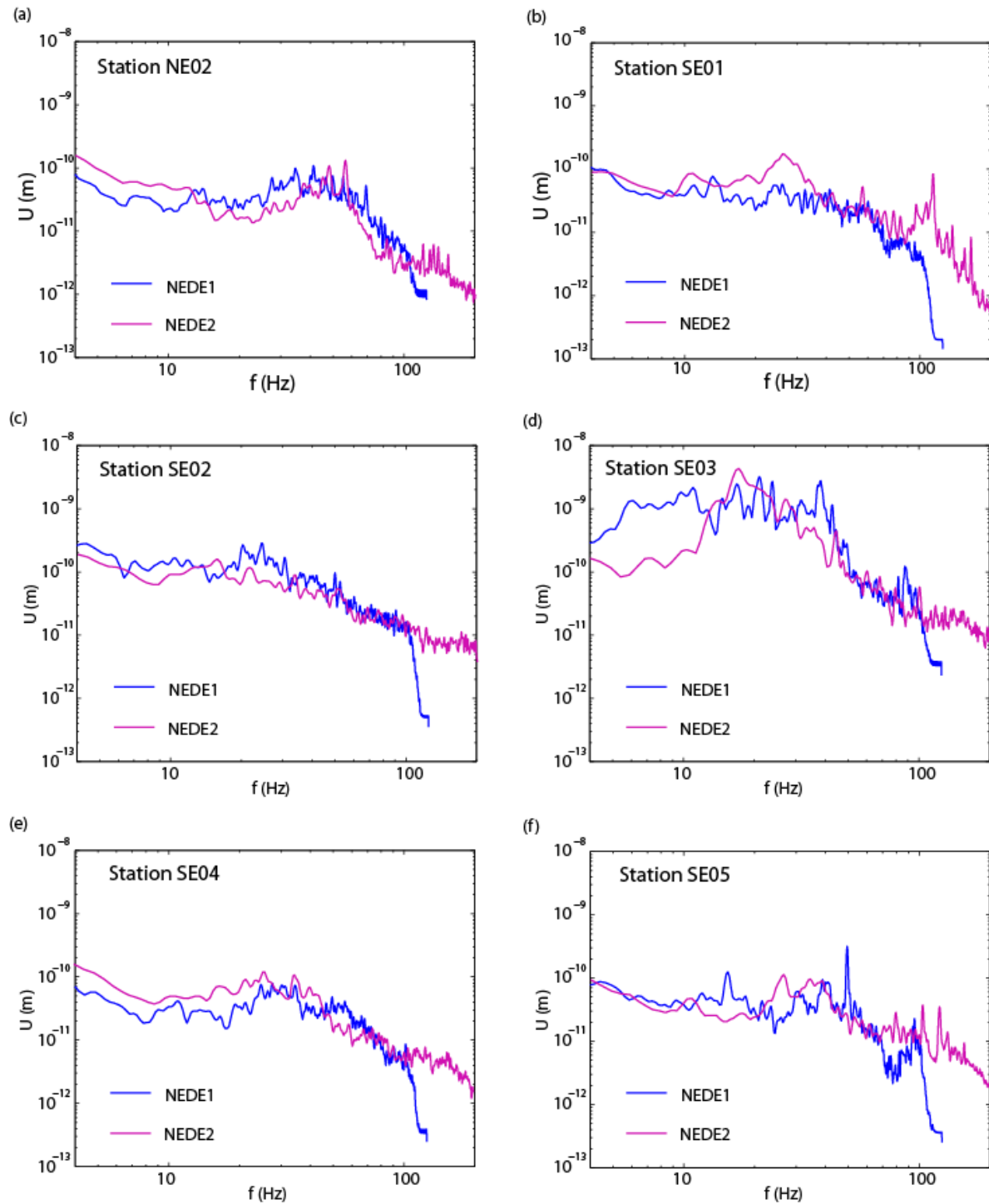


Figure 5-4. Spectral amplitudes (vertical components) of the pre-event records (noise) at stations recording both NEDE1 and NEDE2 experiments: (a) R01/NE02, (b) SE01, (c) R06/SE02, (d) SE03, (e) SE04, and (f) SE05. The noise spectra were averaged for all events of each experiment. The blue lines show the spectra for NEDE1 experiment, purple lines for NEDE2 experiment.

Inversion for the Source and Propagation Effects

While the spectral stacking shows that site effects dominate earthquake signals, it does not give much information about the source. To separate the source and the propagation effects we use the technique first developed by Andrews (1986), who formulated a generalized inverse problem to simultaneously invert the data of events recorded by several stations. The k^{th} spectrum $R_k(f)$ radiated by an event i observed at a given station j is assumed to be a convolution of an explosion source term $E_{i(k)}(f)$ with a propagation term $P_{j(k)}(f)$ and a site term $S_{j(k)}(f)$. In the frequency domain:

$$R_k(f) = E_{i(k)}(f) \cdot P_{j(k)}(f) \cdot S_{j(k)}(f) = E_{i(k)}(f) \cdot T_{j(k)}(f) \quad (5-1)$$

Given that the explosions are located at close proximity to one another, the propagation and the site terms can be combined into a single transfer function term $T_{j(k)}(f)$. After taking the logarithm of each side, we obtain a linear set of equations of the form,

$$\log(R_k) = \log(E_{i(k)}) + \log(T_{j(k)}) \quad (5-2)$$

When written in matrix notation, this equation takes the form

$$R = IJ \cdot \bar{x}, \quad (5-3)$$

where IJ is an $m \times n$ selection matrix of zeroes and ones. The number of rows (m) corresponds to the total number of seismic traces used for the inversion. The number of columns (n) corresponds to the number of unknowns, which is equal to the number of events plus number of stations. The solution vector $\bar{x}(f)$ to this linear system yields both a site effect spectrum for each station and a source spectrum for each event. The system of equations is solved separately for each frequency.

The system of equations still contains an undetermined degree of freedom regarding the absolute amplitude of the site effect. The event spectra can be divided by any factor or function and the station spectra multiplied by the same, and still give the same result (Andrews, 1986). For an ideal station on hard rock, the mean site amplification factor should equal one. Three small calibration explosions were conducted as a part of NEDE2 experiment. However, they were detonated very close to previous explosions in old boreholes intended for a tomography study in NEDE1. As a result, their amplitudes were too small and could not be used at local distances.

RESULTS

Applying the inversion method to the explosions, we simultaneously obtained the source spectra and the site responses for the events of both NEDE1 and NEDE2. Unfortunately, only several stations stayed the same for both experiments. In order to be able to compare the shots for both experiments we ran three separate inversions: 1) using five events from NEDE1 and stations

from the SE and NE profiles (shown with green and cyan triangles in Figure 5-1a; 2) using 6 events from NEDE2 and stations of the SE profile and a circular array (shown with blue and cyan triangles); and 3) a combined solution using all 11 events and all stations shown in Figure 5-1a. Figure 5-5 shows the comparison between the source spectra recovered using the single-datasets (NEDE1 or NEDE2 only) vs. in the combined inversion (both NEDE1 and NEDE2). Notice that the recovered spectra are similar, however there are some differences increasing toward lower frequencies. This may be caused by using instruments with different natural frequencies near 1-2 Hz for these stations. The results are discussed in more detail in the following sections.

As shown in Figure 5-5, the amplitudes of all explosions increased towards the low frequency limit for the combined dataset inversion, however their relative amplitudes with respect to one another did not change significantly. Therefore the results can be used to compare NEDE1 and NEDE2 shots.

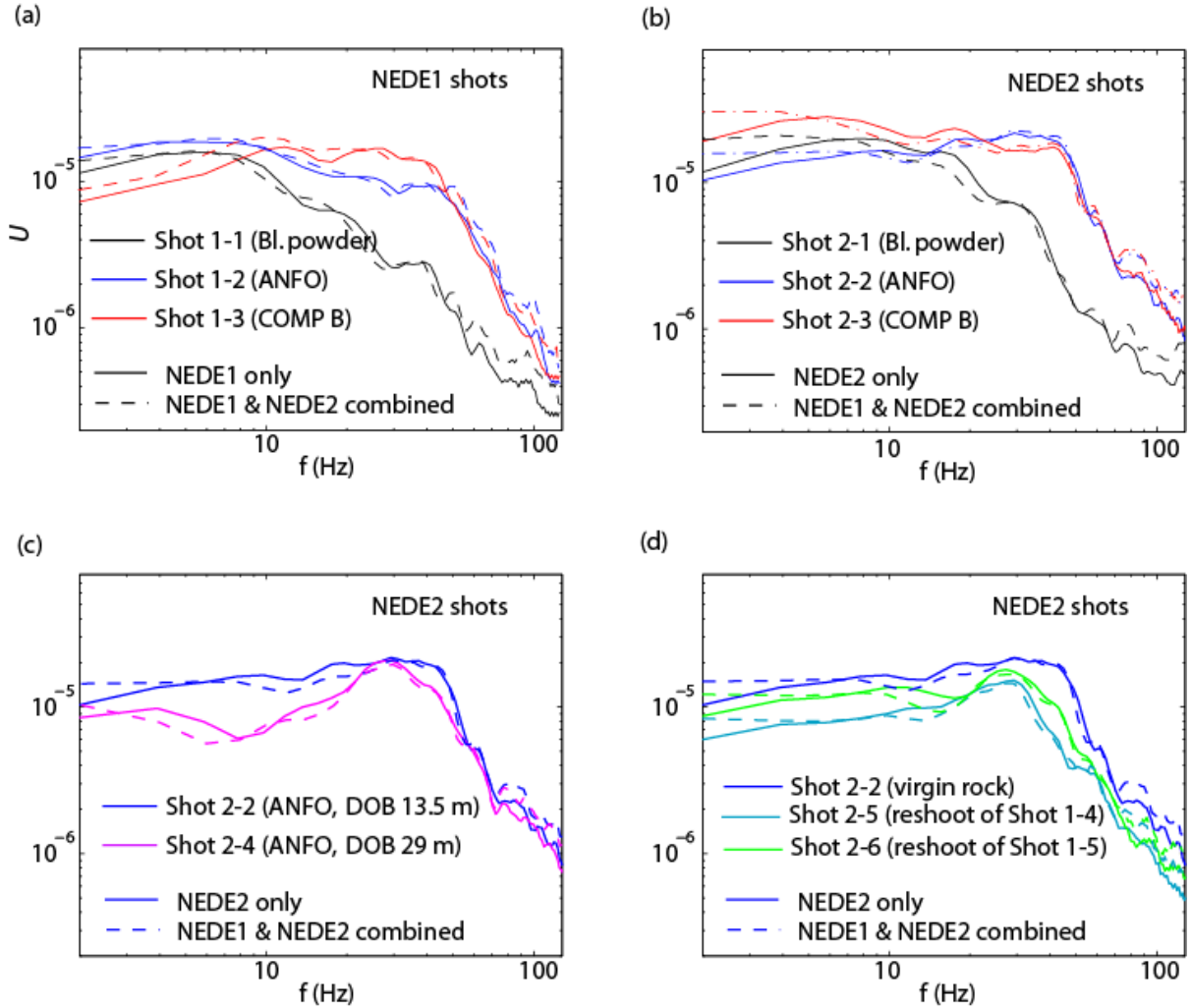


Figure 5-5. Comparison between recovered source spectra obtained using different subsets of the data. (a) *NEDE1* shots *S1-1*, *S1-2*, and *S1-3* data recovered using *NEDE1* data only (solid lines) and combined dataset (*NEDE1* and *NEDE2*) shown with dashed lines; (b) *NEDE2* shots *S2-1*, *S2-2*, and *S2-3* data recovered using *NEDE2* data only (solid lines) and combined dataset (dashed lines); (c) *NEDE2* shots *S2-2* and *S2-4*; (d) *NEDE2* shots *S2-2*, *S2-5*, and *S2-6*.

Site/Propagation Transfer Functions

Figure 5-6 shows the inversion results for three sets of events and stations as was previously mentioned. The recovered transfer functions show significant differences between the different inversion runs for some stations (e.g. NE02, SE05). For other stations, the differences are mainly in the absolute amplitudes, which are related to the extra degree of freedom mentioned in the method description.

The resolved transfer functions (Figure 5-6) show station-specific spectral peaks, mainly between 10 and 100 Hz. The transfer function for Station SE01 shows an amplification peak around 40 Hz, similar to the feature observed in the event spectra (Figure 5-2 c-d). Similarly, the transfer function for Station SE02 has a peak between 20-30 Hz, also observed in the event spectra (Figure 5-3 c-d). This comparison shows that this method can separate the site/propagation effects from the source spectra.

Effect of the VOD on P-Wave Spectra

Studying the effect of VOD on seismic radiation was the main objective of this project. Figure 5-7 a-b shows the spectra recovered for the NEDE1 and NEDE2 experiments. As we expected by analyzing the event spectra, the HANFO and Comp B shots have higher corner frequencies than the black powder shots for both experiments. In addition, the high-frequency roll off is higher for the black powder shot. The relationships between the HANFO and Comp B shots, however, are different between NEDE1 and NEDE2. NEDE1 shots were conducted in dry conditions, and the Comp B charge was factory-made. On the other hand, the NEDE2 Comp B shot was conducted in a water-filled borehole. In addition, the charge was made using multiple Comp B boosters with gaps between them filled with HANFO. This charge configuration reduced the charge density. Thus, the VOD for this explosion may have been lower than for NEDE1. For NEDE1 shots, the spectral amplitudes of the Comp B shot are lower than the amplitudes of the HANFO shot in the low-frequency limit and higher around the corner frequency. For NEDE2 shots, the situation is reversed: the Comp B shot amplitudes are higher in the low-frequency limit and lower close to the corner frequency. The increase in low-frequency amplitude for the NEDE2 Comp B shot may be caused by “water boost” (e.g. Butkovich, 1971), the effect related to water evaporation during an explosion at pressures above 5 GPa.

Effect of the DOB

Shallow explosions produce significant damage in the source region, including permanent ground deformation resulting in material dilation in the source region. Figure 5-7c shows a comparison of the P-wave spectra between Shot 2-2 ($sDOB = 320 \text{ m/kt}^{1/3}$) and Shot 2-4 ($sDOB = 687 \text{ m/kt}^{1/3}$). The low frequency amplitudes for the deeper shot are reduced with respect to the shallow source amplitudes. The high frequency amplitudes are almost the same between the two shots. The MM71 source model (Mueller and Murphy, 1971) predicts the high-frequency amplitudes for the deeper source to exceed the amplitudes for the shallow source (Figure 5-8b), which is not observed in the data.

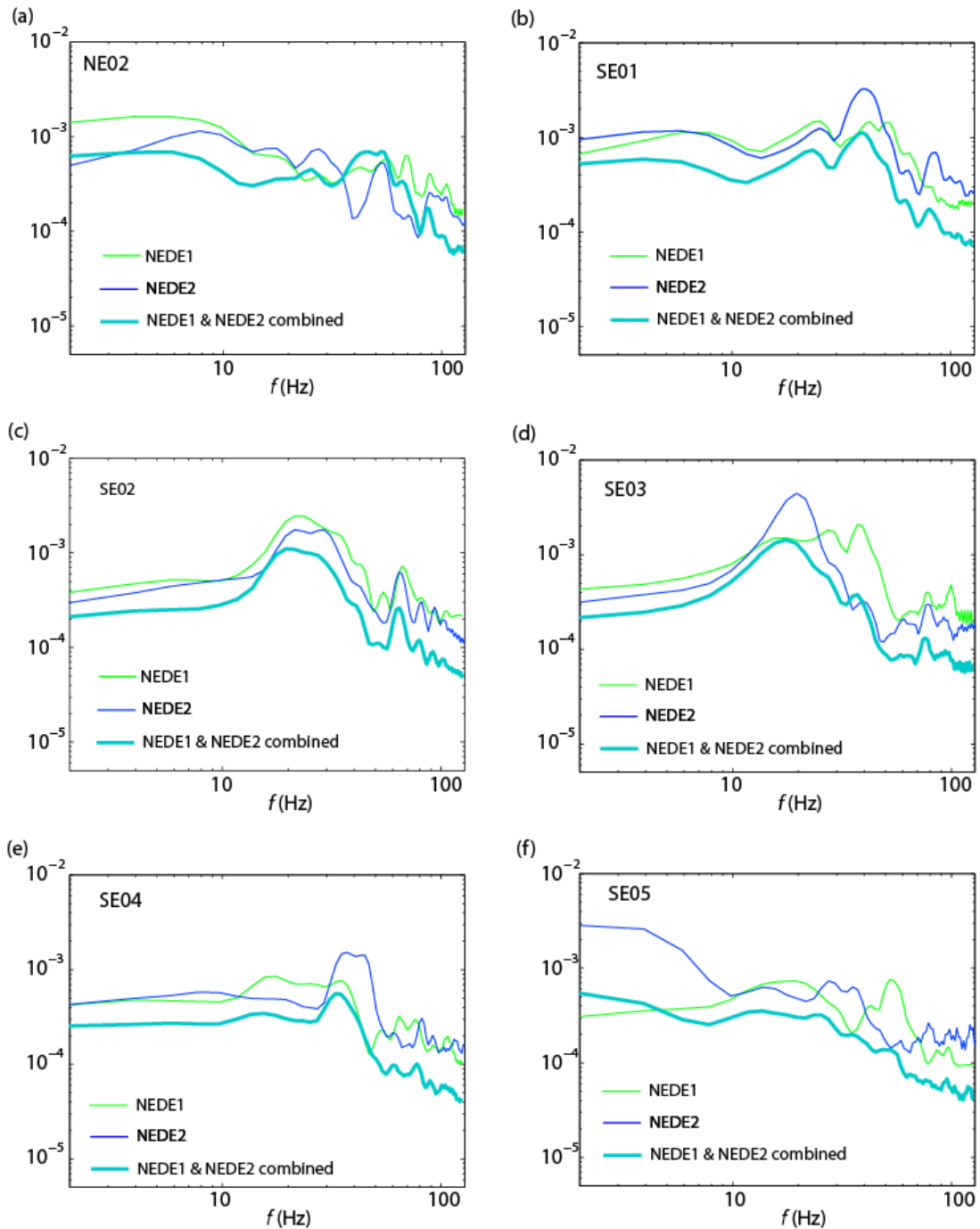


Figure 5-6. Comparison between recovered transfer functions obtained using only NEDE1 data (green lines), only NEDE2 data (blue data) and combined dataset (cyan lines) for stations that were operational during both experiments: (a) Station NE02; (b) SE01; (c) SE02; (d) SE03; (e) SE04; and (f) SE05.

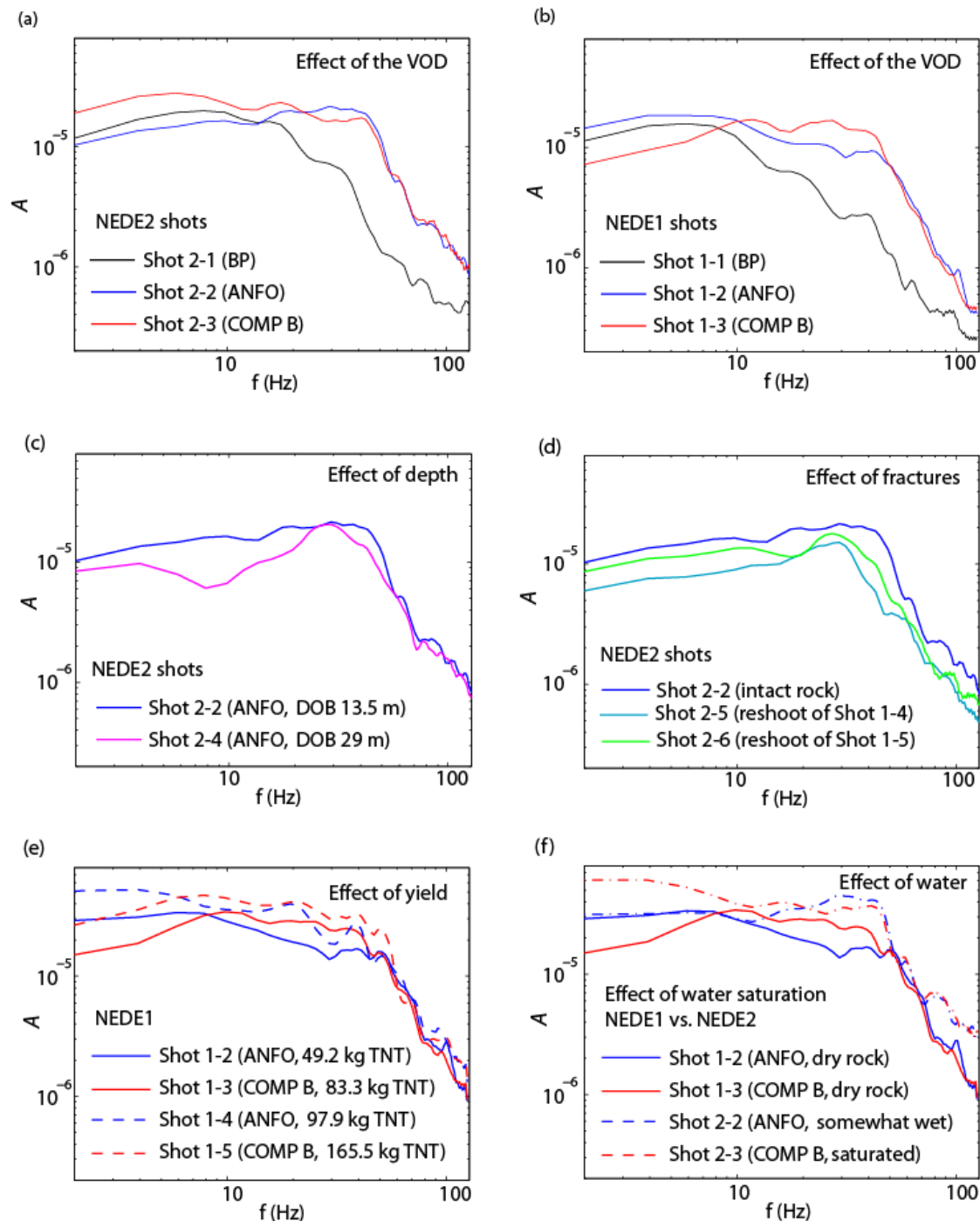


Figure 5-7. a) Source spectra for the explosions with different VOD for NEDE2 experiment (equal TNT equivalent yield). b) Source spectra for the explosions with different VOD for NEDE1 experiment (equal mass of explosives, different TNT equivalent yield). c) Comparison of the source spectra for the event with different DOB. d) Comparison of the spectra between the explosions in intact and fractured rocks for the NEDE2 experiment. e) Effect of the explosion yield on the spectra for NEDE1 explosions. f) Differences between NEDE1 and NEDE2 explosions possibly due to pore water content.

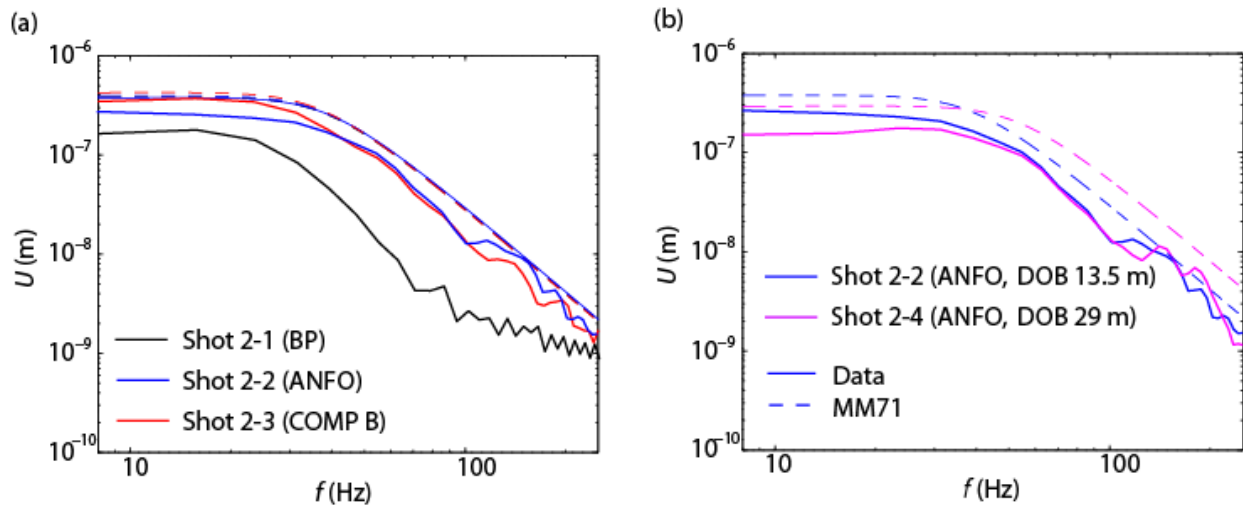


Figure 5-8. a) Comparison of the spectra predicted using the MM71 model and the near-source data recorded between 300-500 m from the sources for the explosions with different VOD. b) Comparison of the spectra predicted using the MM71 model and the near-source data for the explosions with different DOB. Dashed lines show the model prediction, while solid lines show the observed spectra.

Effect of Fractures in the Emplacement Medium

Shots 2-5 and 2-6 were reshoots of Shots S1-4 (122 kg TNT equivalent HANFO) and S1-5 (122 kg TNT equivalent Comp B), respectively. Shot 2-2, detonated in undamaged granite, was used as a control (virgin rock) shot.

To quantify damage produced by explosions, an extensive coring program was completed before and after the NEDE1 shots (e.g. Stroujkova *et al.*, 2013; Martin *et al.*, 2011b). The explosion-induced fracturing caused significant impact on physical rock properties, including acoustic velocity reductions on the order of 20% over a 5 m interval surrounding the working point (e.g. Martin *et al.*, 2011b). The repeat shots were conducted within 1 m of the working points of the NEDE1 explosions, and therefore the emplacement conditions were affected by the previous explosions.

The spectral amplitudes for the fractured rock shots are reduced at all frequencies compared to the intact rock shot (Figure 5-7d). Note however, the NEDE2 shots were conducted in relatively dry conditions. The fractured rock explosion spectra in water-saturated rocks (e.g. Fracture Decoupling Experiment in New Hampshire) have different characteristics with predominant amplitude reduction at higher frequencies and subsequent corner frequency reduction (e.g. Stroujkova *et al.*, 2013).

Effect of Saturation

The NEDE1 experiment was conducted in extremely dry conditions. During the NEDE2 experiment, weeks of rainfall preceded the experiment. Water at the test site was confined to a

series of sub-horizontal joints. Some of the shot holes were dry, while others had water before the experiment. Water was pumped/drained out of all shot holes, except S2-3 (Comp B shot) and S2-4 (deep HANFO shot). Thus, some of the differences between NEDE1 and NEDE2 explosions could be explained by the presence of water.

It was already mentioned that S2-3 (Comp B) had greater amplitudes at lower frequencies than S2-2 (HANFO), while the relationship between HANFO and Comp B was reversed for NEDE1. Figure 5-7f shows a comparison between shots S1-2 (HANFO, 49 kg TNT equiv.), S1-3 (Comp B, 83 kg TNT equiv.), S2-2 (HANFO, 68 kg TNT equiv.), and S2-3 (Comp B, 73 kg TNT equiv.). The smaller shot S1-2 has similar low-frequency amplitudes and lower high-frequency amplitudes than the larger S2-2 shot. Shot S2-2 was conducted in a dry borehole; however the site had more fluids overall during the NEDE2. On the other hand, the yield for S2-3 was slightly smaller than S1-3, however the low frequency amplitude for S2-3 exceeds the amplitude of S1-3 by a factor of 3.6. In addition, the Shot S2-3's low-frequency amplitude exceeds that of a much larger explosion (S1-5) by a factor of 2 (e.g. Figure 5-8). Such an increase in low frequencies could be caused by the presence of water in the S2-3 borehole. On the other hand, it could be due to the lower charge density, which may have lowered the VOD for S2-3. Unfortunately, the VOD measurements for NEDE2 are not available to resolve this issue. Overall, the effect of water saturation on P-waves is inconclusive.

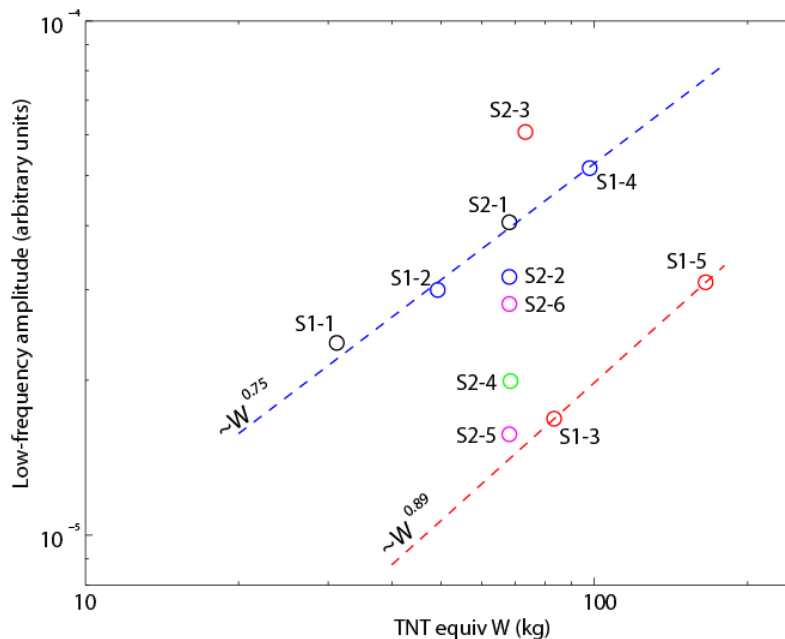


Figure 5-9. Low-frequency spectral amplitude plotted as a function of TNT equivalent yield for NEDE1 and NEDE2 explosions. The dashed lines show the yield exponents for HANFO and BP event (blue line) and Comp B events (red line). Only NEDE1 events S1-3 and S1-5 were used to estimate the linear fit. For BP and HANFO only events S1-1, S1-2, S1-4, and S2-1 were used.

Effect of the Yield

Two of the NEDE1 explosions (S1-4 and S1-5) had twice the yields of the smaller explosions (S1-2 and S1-3). Figure 5-7e shows the source spectra for these explosions. The spectral ratios are close to 2 in the low-frequency limit, and decrease to 1 above 50 Hz.

To summarize the effect of yield on the explosion amplitude, we plotted the low-frequency amplitude ($f = 1.9$ Hz) as a function of the TNT equivalent yield for NEDE1 and NEDE2 explosions. This comparison was possible because the results of the combined inversion were used. Since no reference station or event were used to constrain the inversion, the amplitudes are estimated in some arbitrary units. However, their relative magnitudes with respect to one another are expected to be approximately correct. Figure 5-9 shows the amplitudes plotted as a function of yield in logarithmic coordinates. Interestingly, both BP explosions and NEDE1 HANFO explosions follow virtually the same trend. We estimated the linear fit for these four explosions and for two NEDE1 Comp B explosions. The yield exponents are $\sim W^{0.75}$ for the HANFO+BP shots ($\sim W^{0.70}$ if S2-2 is added to the regression) and $\sim W^{0.89}$ for the Comp B shots. NEDE2 HANFO shot S2-2 is slightly below the line for HANFO explosions. NEDE2 Comp B (S2-3) amplitude is substantially above the linear fit estimated for other Comp B shots.

CONCLUSIONS AND RECOMMENDATIONS

We applied a non-parametric inversion proposed by Andrews (1986) to local records of small chemical explosions conducted during NEDE experiments in Barre, VT. Using this technique, we simultaneously estimated both the site and source effects by solving a linear system of equations. The main objective of this study was to separate the changes to the explosion spectra due to differences in VOD, explosion depth, yield, and emplacement conditions.

To summarize, the results of the inversion show that:

- Increase in velocity of detonation (VOD) results in increase in corner frequency and high-frequency amplitudes and a slight decrease in the low-frequency amplitudes. Since nuclear explosions have even faster energy release than conventional explosives, the experiments with different VOD may shed light on the differences between nuclear and chemical sources.
- An increase in DOB causes a decrease in low-frequency amplitudes.
- Emplacement in a previously fractured medium leads to decreased seismic amplitudes. The decrease is more pronounced in the high frequency part of the spectra, particularly if the explosions are conducted in water-saturated rocks.
- Water saturation in the emplacement medium may increase the low-frequency amplitudes; however, these results are inconclusive and require more research.
- Based on our limited data, the low-frequency amplitudes are proportional to $W^{0.75}$ for the HANFO+BP shots and to $W^{0.89}$ for the Comp B shots. Larger numbers of data points are needed to verify the yield exponents.

Using small calibration explosions would be very helpful to improve performance of this method. Unfortunately, the calibration explosions conducted as a part of the NEDE2 experiment were conducted very close to previous explosions. Consequently, their amplitudes were too small and could not be used at local distances.

The methodology can be further developed using small chemical explosions and then transferred to explosions conducted at nuclear test sites using explosions with known yield and other source parameters. Subsequently, the methodology can be applied to denied test sites, such as Punggye-ri Nuclear Test Site in DPRK.

6. MOMENT ESTIMATION FROM SHORT PERIOD SURFACE WAVES FROM THE NEDE2 EXPLOSIONS IN BARRE GRANITE

ABSTRACT

We have estimated the seismic moments for explosions conducted during the 2013 New England Damage Experiment Phase 2 (NEDE2) using the Denny and Johnson (DJ91, 1991), Mueller and Murphy (MM71; 1971), and the Patton (2012b) explosion source models. We generated Green's functions for a newly developed velocity and attenuation model for the upper crust in the study region. We convolved the synthetics with moments estimated from the source models and compared to observed short-period surface waves (Rg) recorded at local distances. The results show that the DJ91 moments produced synthetic data that matched the observed Rg spectral amplitudes above 3 Hz; however, below 3 Hz, the synthetic spectra predict more Rg energy than observed from the explosions. MM71 moments produce synthetic Rg spectral amplitudes too large to match the observed data. The best match to the observed data results when using the Patton *et al.* (2008) source model, which is tied to the DJ91 theoretical moment, with an added damage component modeled by a CLVD moment tensor. The CLVD source reduces the synthetic Rg amplitudes in the 1-3 Hz band and more closely matches the observed data.

OBJECTIVES

Determining the absolute moment of small explosions is a challenging task. The objective of this study is to estimate the moments for the 2013 New England Damage Experiment Phase 2 (NEDE2) Shots 1-4 using short-period, fundamental mode surface waves (Rg). The NEDE was a two-phase explosion experiment conducted in 2008 (NEDE1) and 2013 (NEDE2). For the details on the NEDE1, the reader is referred to Leidig *et al.*, 2010 and Stroujkova *et al.*, 2012. For NEDE2, nine explosions were detonated at a granite quarry near Barre, VT and recorded on a network of accelerometers and seismometers (Chapter 2). Shots 1-4 (Table 6-1) are the focus of this study and represent explosions of different explosive weights (45.7-113.5 kg) but similar

TNT-equivalent yields (68-73 kg TNT equivalent) in undamaged granite using different explosive types, including black powder (Shot 1), heavy Ammonium Nitrate Fuel Oil (HANFO; Shot 2 and 4), and Composition B (Shot 3). Shots 1-3 had similar depths (12-14 m) while Shot 4 was significantly overburied at 29 m. The other NEDE2 shots were either 0.5 kg calibration explosions (Shots 7-9) or re-shoots in the damage zones of NEDE1 tests (Shots 5-6). We do not study Shots 5-9 in this chapter. In the following sections, we develop a velocity and attenuation model for the upper crust, examine theoretical moments for the explosions using different source models, and then compare the models to observed data.

RESEARCH ACCOMPLISHED

Model Development

In order to model short period surface waves from the NEDE2 explosions, we need a velocity and attenuation model for the upper crust near Barre, VT. Instead of using the NEDE2 data to generate this model, we used data collected during NEDE1 to study Rg propagation in Barre Granite and nearby metamorphic rocks. We used surface wave group velocity and spectral amplitude data from two approximately linear profiles of 4.5 Hz geophones deployed at distances between 2 and 30 km to the NE and SE of the explosion test site (Figure 6-1). For this study, we used recordings of the NEDE1 Shot 4 (122 kg HANFO) because it was the largest explosion with the best SNR. Stations beyond 20 km had variable SNR (some good, some poor) and were not used in the analysis. The geophone data were corrected for the instrument response prior to the analysis.

Table 6-1. Shot Information for the 2013 NEDE2 Experiment (Shots 1-4).

Shot	Latitude (WGS84)	Longitude (WGS84)	Elev (m)	Date (UTC)	Time (UTC)	Explosive	TNT Equivalent Yield (kg)	Center of charge (m)
1	44.15794	-72.47843	507.2	6/21/13	20:22:10.701	BP	68	12.9
2	44.15797	-72.47791	509.0	6/22/13	17:29:09.320	HANFO	68	13.5
3	44.15776	-72.47816	508.1	6/22/13	18:15:33.492	Comp B	73	12.3
4	44.15770	-72.47795	511.5	6/22/13	14:46:42.734	HANFO	68.4	29.0



Figure 6-1. Location of 4.5 Hz geophones (NEDE1) used to estimate the velocity and attenuation structure of the upper crust near Barre, VT. *The source (NEDE1 Shot 4) was located in the granite quarry and was the detonation of 122 kg of HANFO explosives, fully tamped. Map Source: Google Earth.*

Attenuation Model. To determine the attenuation coefficient for short period, fundamental mode Rayleigh waves (Rg), we have analyzed the decay of spectral amplitudes of Rg with distance. Spectral amplitudes were extracted (Figure 6-2) from complex waveforms using Multiple Filter Analyses (MFA; Herrmann, 2010). The method we employed to estimate the attenuation coefficient for Rg is based on Patton *et al.* (2005) wherein Rg amplitudes are assumed to spread geometrically as \sqrt{x} , where x is epicentral distance in km. The spectral amplitudes (A_0) can be corrected for attenuation and geometric spreading by:

$$A_0 = A\sqrt{x}e^{\gamma x} \quad (6-1)$$

where A is the spectral amplitude measured at a station and γ is the attenuation coefficient. After correcting for geometric spreading, A' , taking the natural logarithm of Equation 6-1 and solving for A' :

$$\ln A' = S - \gamma x. \quad (6-2)$$

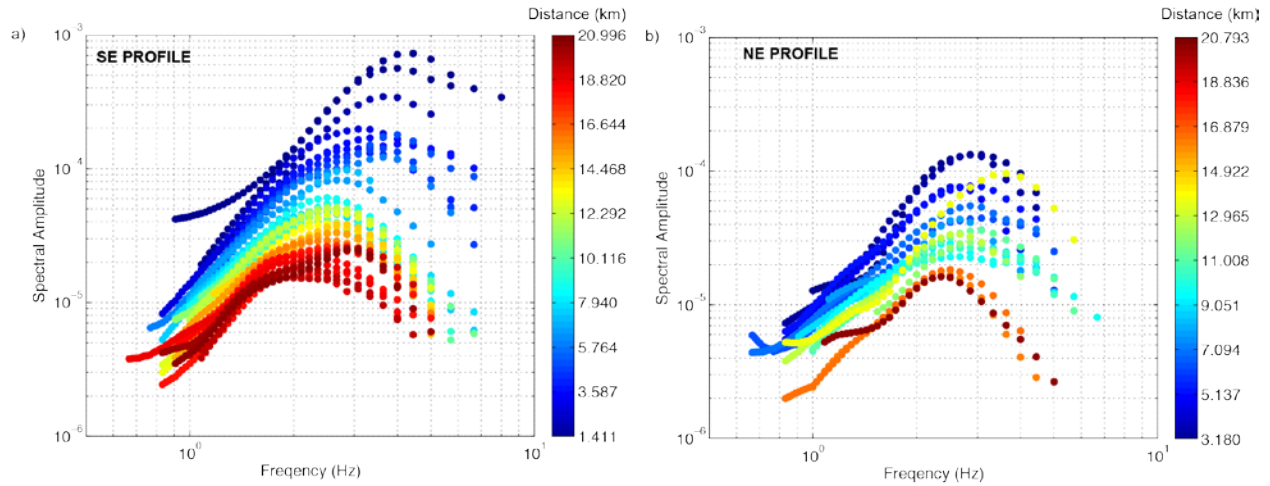


Figure 6-2. Spectral amplitudes for Rg recorded on the a) SE and b) NE profiles shown in Figure 6-1. The Rg were isolated using MFA of the vertical component waveforms. The color scale represents different stations and distances.

S is a source term that should be included to correct for the effects of radiation pattern or using several explosions that have different moments to estimate γ . Many assume the effects of radiation pattern are negligible for explosions, however, we have previously observed possible radiation patterns from these NEDE1 explosions (Stroujkova *et al.*, 2012). Thus, we use data from approximately linear profiles from a single explosion so that $\ln A_0$ can be ignored when estimating γ . Regressions of $\ln A$ versus distance, x , (Figure 6-3) are used to estimate γ at each period for which we have Rg spectral amplitude data (Figure 6-4). In addition to the spectral

amplitudes, the MFA also provides the group velocity, U , at each period. We use the attenuation coefficients and group velocities at each period T to convert to $Q_{Rg}(f)$ as shown in Figure 6-5. The results for both profiles agree and suggest that Q_{Rg} ranges between 40 and 70 for these paths. There seems to be some frequency dependence for the SE profile with Q becoming larger with increasing period; however, when the estimated error is considered, it is hard to make a case for a power law frequency dependence on these profiles. When both the SE and NE profile data were combined into a single dataset, the resulting Q model did not change significantly, but the error bars increased. R_g amplitudes to the NE seem to be slightly smaller than the SE amplitudes, again suggesting possible azimuthal radiation patterns effects in the NEDE1 Shot 4.

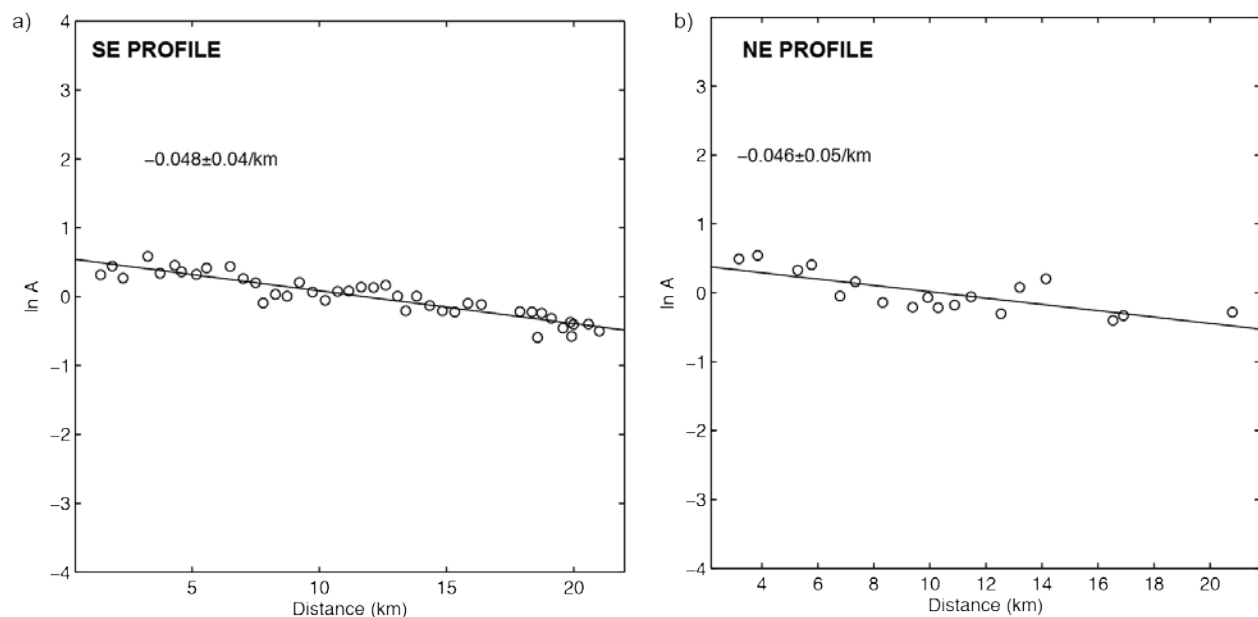


Figure 6-3. Regressions of spectral amplitudes at 2 Hz for R_g recorded on the a) SE and b) NE profiles. Shown in each subplot is the attenuation coefficient in /km and an estimate of the regression error.

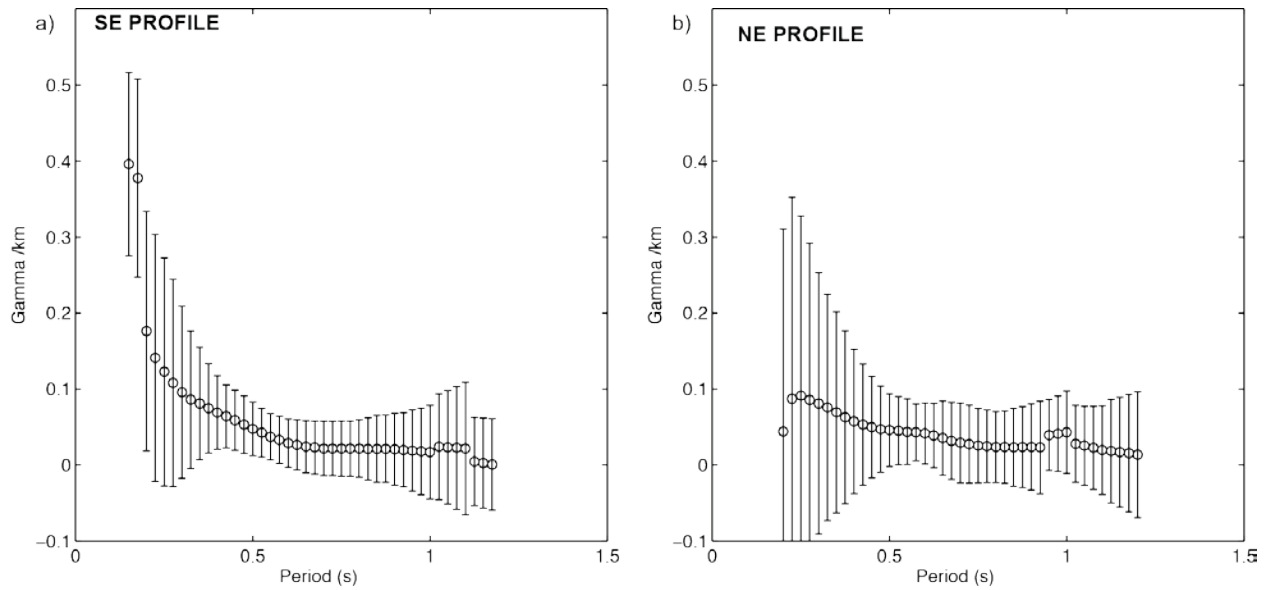


Figure 6-4. Attenuation coefficients as a function of frequency for Rg recorded on the a) SE and b) NE profiles shown in Figure 6-1.

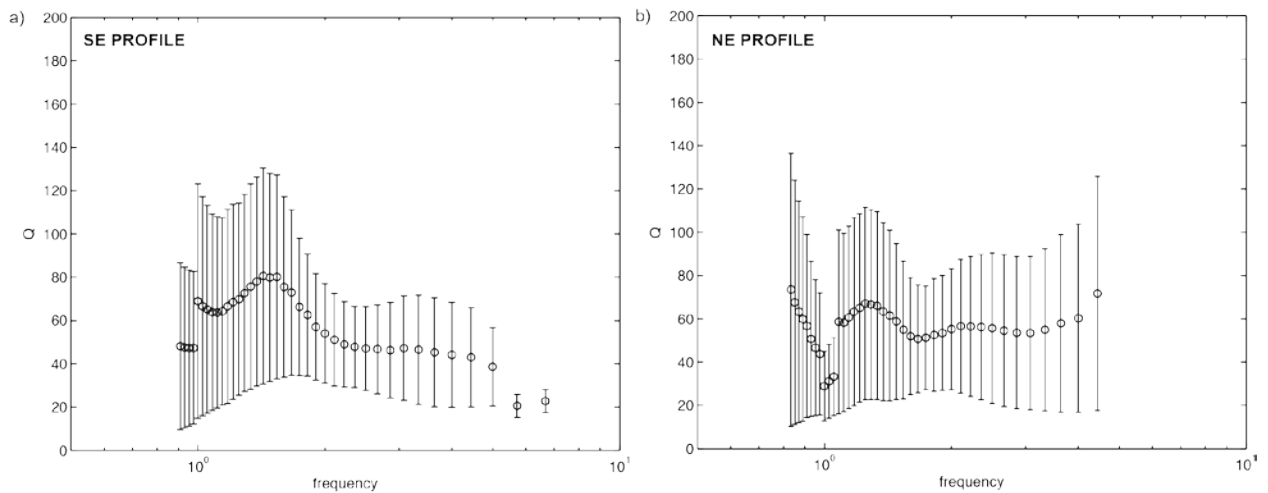


Figure 6-5. Q estimates as a function of frequency for Rg recorded on the a) SE and b) NE profiles. Error estimates are based on the regression error in the gamma coefficients as well as scatter in the Rg group velocity dispersion curves.

Velocity Model. To develop the velocity model, we performed a joint inversion of group velocity dispersion measurements (Figure 6-6a) and the observed attenuation coefficients (Figure 6-4). We focused on the SE profile data because the surface waves appear better developed due to fewer spectral holes in the MFA, and have less error in the attenuation coefficient analysis.

The final dispersion curve (Figure 6-6a) used in the inversion represents an average of the dispersion curves for the SE stations shown in Figure 6-1 with ± 1 standard deviation shown.

For the inversion, we used a starting model that had been initially developed by Stroujkova (2010). In their model, New England Research (NER) measured the velocities in the upper 20 m using cores from several boreholes (Peter Boyd, pers. com. 2009). The measurements show a gradual velocity increase from approximately 4.0 km/s at the surface to 4.4 km/s at a depth of approximately 20 meters. The velocity below 20 m was found by examining the travel times of the first arrivals on the SE and NE geophone profiles. The apparent P-wave velocity for these data was 4.9 km/s. They used a V_p/V_s ratio of 1.8 to obtain a shear-wave velocity of 2.72 km/s. They could not pinpoint where the velocity changes from 4.4 km/s to 4.9 km/s. We tried starting models that varied this depth from 50 to 500 m and most of the inversions seemed to prefer a gradual increase in velocity and not a sharp discontinuity.

The best-fitting velocity and Q models are shown in Figure 6-7, while the fit between the observed velocity and attenuation data to the predicted estimates are shown in Figure 6-6. The shear-wave velocity model gradually increases from 2.4 km/s at the surface to >3 km/s at 800 m. The Q model ranges from 10 at the surface to >100 at 800 m, although there is little resolution in the R_g at this depth. These inverted values are in agreement with the estimates from the regression-based analysis (Figure 6-5). The distinct discontinuity at 260 m in the Q model does not appear to correlate with any velocity contrast and may be an artifact of the damping used in the inversion. It is important to remember that these structures are non-unique, as we found many similar models that could fit the data within the observed error. Also, these models represent the path-averaged structure between 1-20 km from the source and may not capture small-scale structure, lateral variations, or structural discontinuities (e.g., granite/metamorphic rock contact). The final inverted model is tabulated in Table 6-2. The velocity and Q models are similar to structures developed in Massachusetts and Connecticut by Saikia *et al.* (1990).

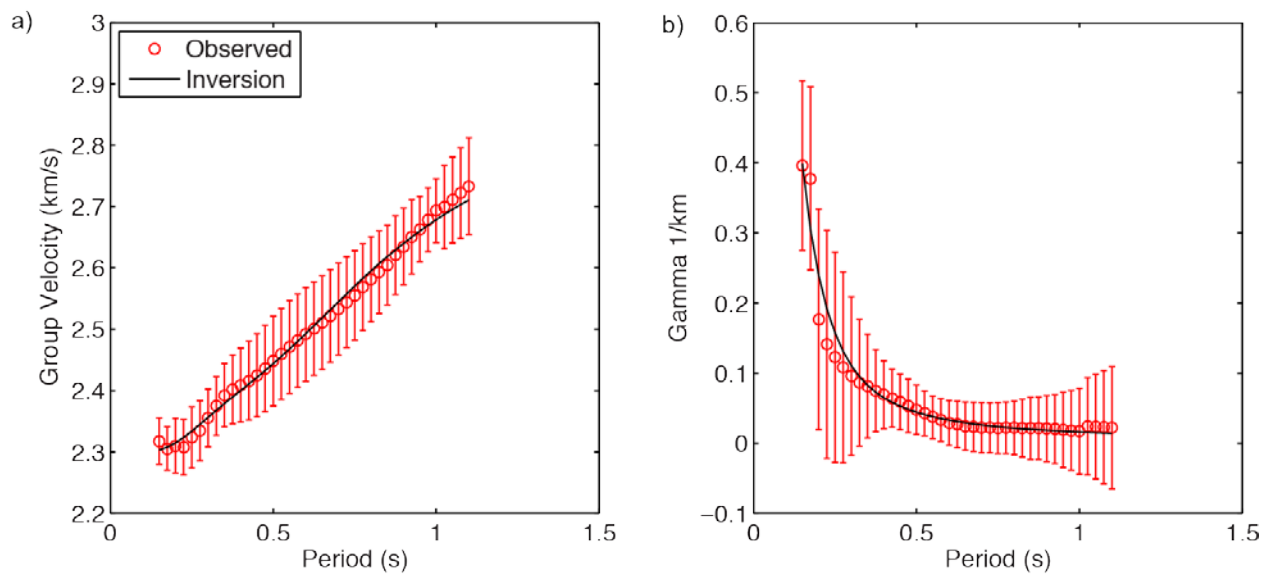


Figure 6-6. Observed a) group velocity dispersion and b) attenuation coefficients compared to predictions based on a joint inversion for shear wave velocity and attenuation structure.

Table 6-2. Velocity and Attenuation Model for Barre, VT region.

H(KM)	VP(KM/S)	VS(KM/S)	RHO(GM/CC)	QS
0.01	4.000	2.369	2.45	14
0.05	4.695	2.603	2.43	14
0.05	4.569	2.539	2.41	14
0.05	4.850	2.687	2.47	23
0.05	4.756	2.642	2.45	28
0.05	4.852	2.699	2.47	38
0.05	5.019	2.789	2.50	85
0.05	5.136	2.850	2.53	79
0.05	5.155	2.859	2.53	65
0.05	5.091	2.827	2.52	63
0.2	5.288	2.959	2.56	114
0.2	5.410	3.025	2.58	101
0.2	5.677	3.162	2.64	110
0	5.738	3.199	2.65	91

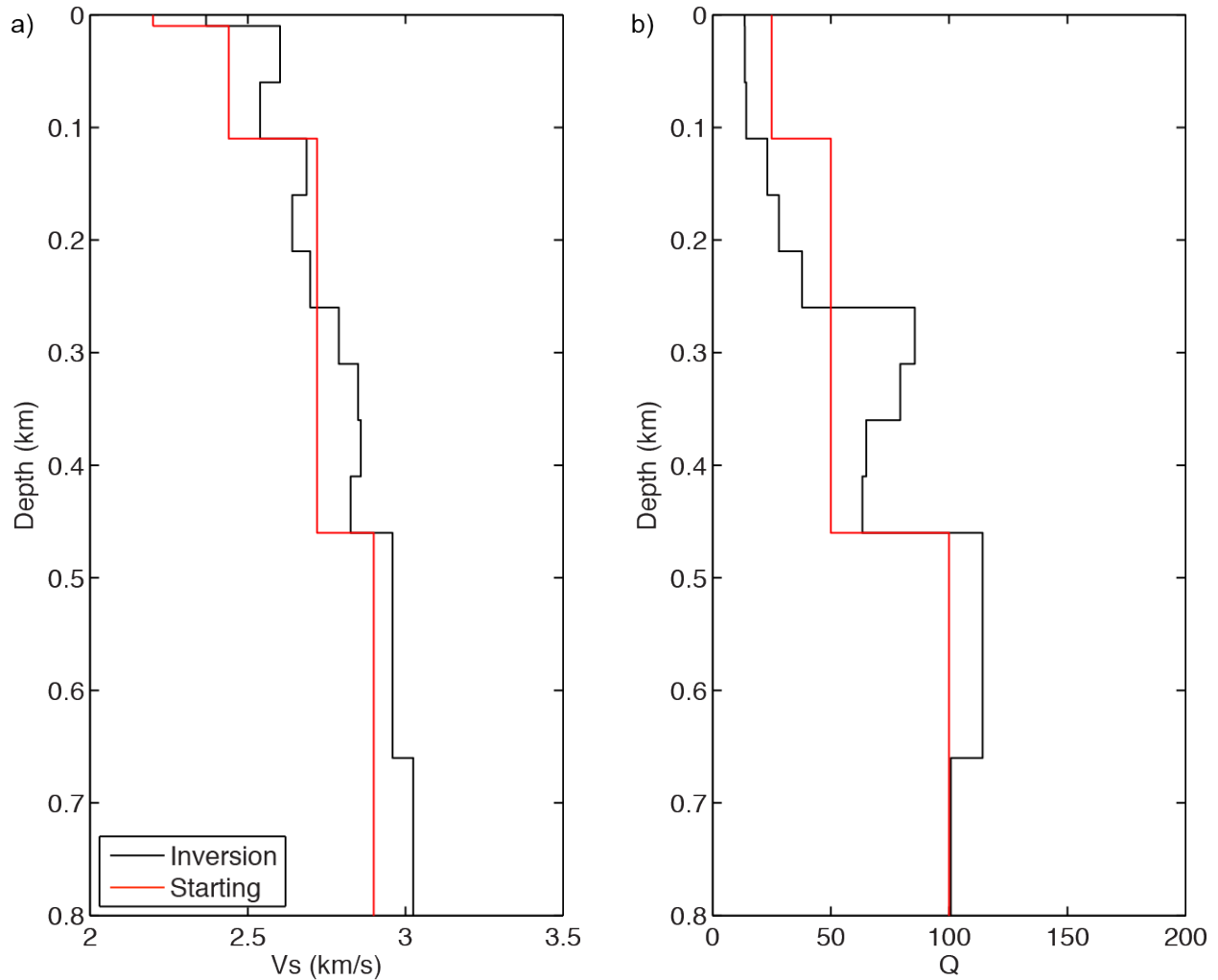


Figure 6-7. a) Shear wave velocity and b) Q structures (black) from joint inversion of Rg velocity and attenuation gammas compared to the starting models (red).

Modeling the NEDE2 Explosions

We generated synthetic surface wave seismograms for Shots 1-4 of the NEDE explosions using a simple procedure. Modal summation codes (Herrmann, 2010) were used to generate Green's functions for the model shown in Table 6-2. For the final step, an explosion moment was estimated and applied to the Green's functions in order to scale the seismogram amplitudes appropriately. Three explosion source models available for moment estimation include Denny and Johnson (1991; DJ91), Muller and Murphy (1971; MM71), and Patton (2012b).

DJ91 Model. DJ91 relate theoretical moments, M_t , predicted for a spherical source with observed moments, M_o , for a dataset of nuclear and small chemical explosions. DJ91 defined the observed explosion moment, M_o , as:

$$M_o \text{ (N-m)} = \frac{1}{311} M_t P_o^{0.3490} 10^{-0.0269GP} \quad (6-3)$$

where GP is gas porosity in percent, $P_o = \rho gh$ with density ρ in units of kg/m^3 , g is 9.8 m/s^2 , and h is depth in meters. The theoretical moment, M_t , for a spherical explosion is defined as:

$$M_t = \frac{4}{3} \pi \rho V_p^2 R_c^3 \quad (6-4)$$

where V_p is in m/s , and

$$R_c = \frac{1.47 \times 10^4 W^{\frac{1}{3}}}{V_s^{0.3848} P_o^{0.2625} 10^{0.0025GP}} \quad (6-5)$$

where V_s is in m/s and W is yield in kilotons.

Table 6-3 shows the parameters used to estimate M_o for Shots 1-4. The velocities were taken from the Stoujkova *et al.* (2010) estimates. We do not have an estimate of the gas porosity but it is low due to relatively few fractures and was assigned as 1%. The yields and depths of the shots were used to estimate DJ91 M_o of $6.52 \cdot 10^{10} \text{ N-m}$, $6.39 \cdot 10^{10} \text{ N-m}$, and $7.14 \cdot 10^{10} \text{ N-m}$ for NEDE2 Shots 1-3, respectively. The significantly over-buried Shot 4 has a reduced moment of $4.60 \cdot 10^{10} \text{ N-m}$ due to the increased depth of the event. We did not multiply the chemical explosion yield by a factor of 2 (Denny *et al.*, 1997) for reasons discussed in Bonner *et al.* (2013) and Ford and Walter (2013). We also present the M_t estimates for DJ91 in Table 6-3. Patton and Taylor (2008) believes that M_t should be the moment that is combined with damage effects to model explosions, and we explore this possibility in a later section of this chapter. The estimated DJ91 M_o moments were applied as an isotropic moment tensor to the Green's functions, and synthetic seismograms were generated in units of velocity (m/s). We focus our modeling of the NEDE2 explosions on a circular ring of sensors deployed at $\sim 6 \text{ km}$ from the blast (Figure 6-8) to better understand the effects of source anisotropy on moment estimation.

Table 6-3. DJ91 Parameters for NEDE2 Shots 1-4.

	Shot 1	Shot 2	Shot 3	Shot 4
V_p (km/s)	4.2			
V_s (km/s)	2.3			
Density (g/cm ³)	2.4			
Gas Porosity (%)	1			
Yield (kg)	68.1	68.1	73.2	68.4
Depth (m)	12.9	13.5	12.3	29
DJ91 Mt	$2.63 \cdot 10^{11}$	$2.54 \cdot 10^{11}$	$2.93 \cdot 10^{11}$	$1.40 \cdot 10^{11}$
DJ91 Mo	$6.52 \cdot 10^{10}$	$6.39 \cdot 10^{10}$	$7.14 \cdot 10^{10}$	$4.60 \cdot 10^{10}$

Synthetic Waveforms. The synthetic Rg for the moments (Table 6-3) and upper crustal model (Table 6-2) are shown in Figure 6-9 compared to observed data recorded on every third station (R3, R6, R9, and R12) of the ring network (Figure 6-8). The synthetic and observed data are filtered between 0.5-5 Hz using a 2nd order, zero-phase Butterworth band pass filter. It is clear from these comparisons that the velocity model developed from the NEDE1 data could be tweaked to provide a better fit between the observed and synthetic data. A quick analysis of the observed dispersion curves at 6 km show stations in the NE quadrant have slower group velocities at frequencies above 5 Hz than we considered for the synthetics. It is also evident in these figures that a single model would not fit all of these waveforms, as we observe variable waveform features and arrival times at different stations. However, the current model developed using NEDE1 data, provides a satisfactory fit to the arrival times of the Rg at these stations. More importantly, the moments and attenuation models used to generate the synthetics are producing Rg amplitudes that are within a factor of 3 or better of the observed amplitudes in this bandwidth.

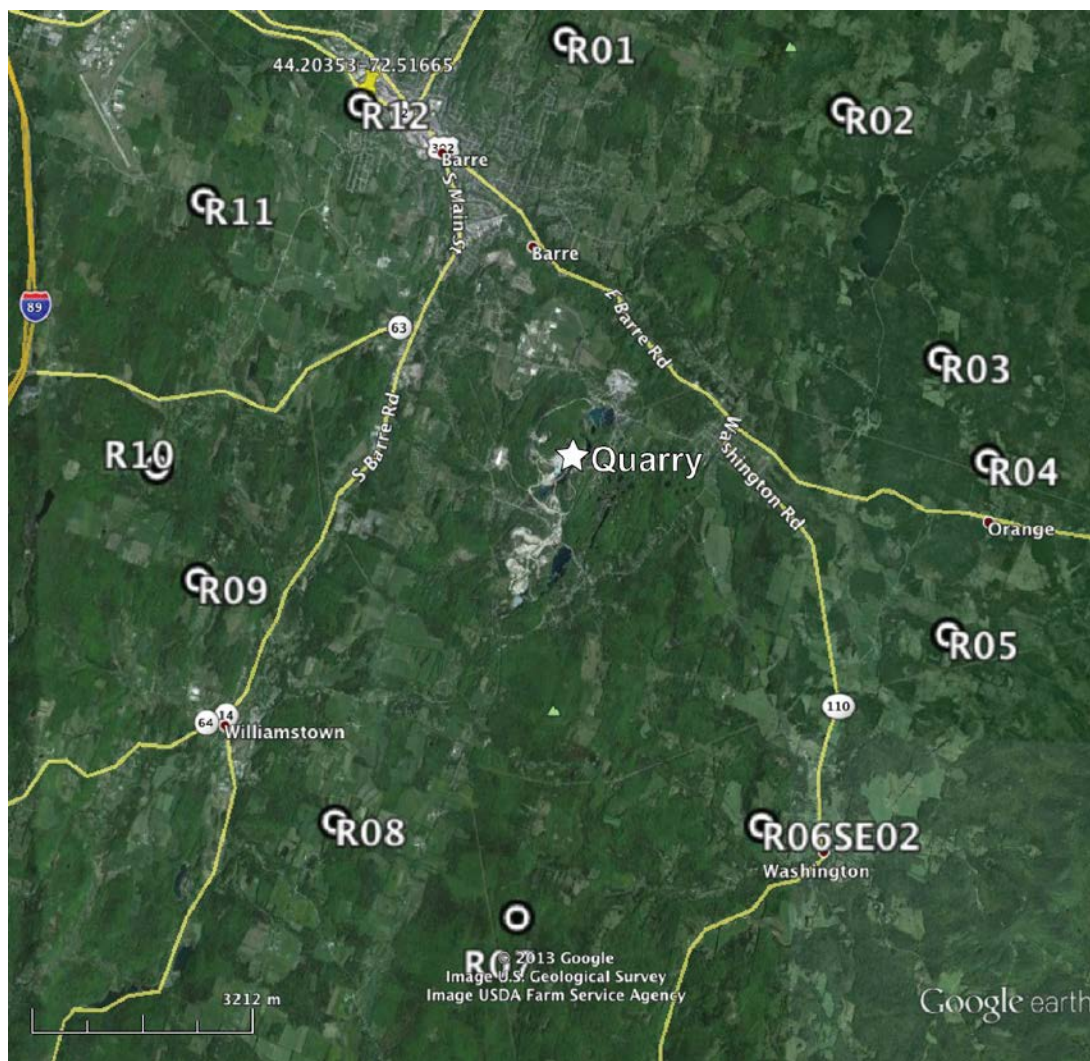


Figure 6-8. Map showing a ring of azimuthal sensors at approximately 6 km from the granite quarry test site. Map from Google Earth.

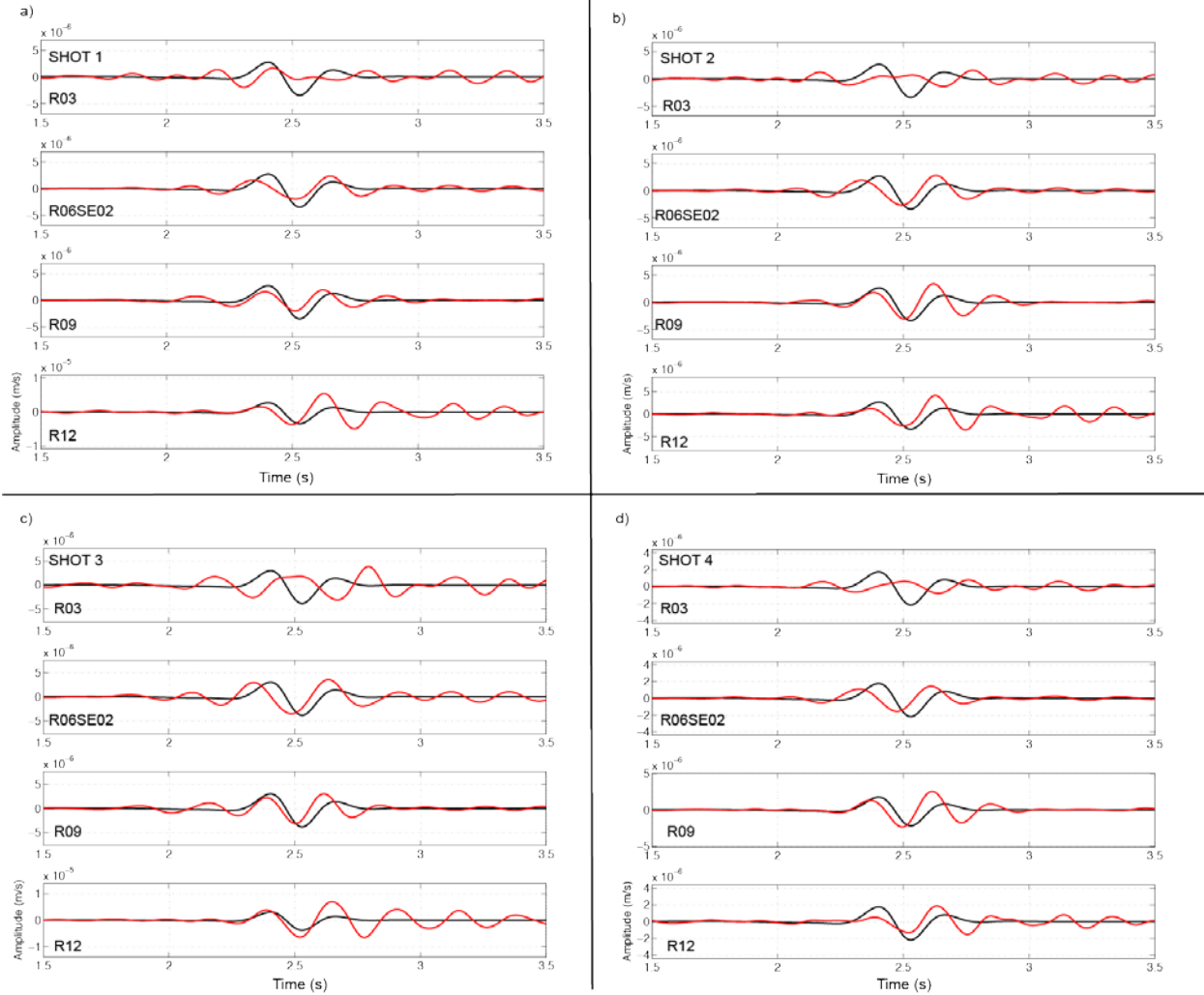


Figure 6-9. A comparison of the synthetic Rg (black) using the Mo estimates in Table 6-3 to observed data (red) from four ring stations (Figure 6-8) that recorded the NEDE2 Shots 1-4 (a,b,c, and d respectively) filtered between 0.5-5 Hz.

The observed spectral amplitudes for Rg recorded on the ring network are presented in Figure 6-10 as a function of azimuth. The distance to these stations is approximately 6 km. The scatter in the spectral amplitudes is higher than we expected. There appears to be as much scatter in these 1-3 Hz spectral estimates as was observed for all the SE stations from 1-20 km (Figure 6-2). We observed order of magnitude variations in the spectral amplitudes at the high frequencies (> 3 Hz) and the scatter does not decrease significantly at lower frequencies. These effects are not distance-related since the station-to-source distance is between 5.5-6.6 km for all stations. Correcting for these slight distance differences does not decrease the scatter. The scatter in the observed data is probably related to either radiation patterns, path effects, or site effects. The fact that the radiation patterns may be so pervasive for these sources leads to complications in trying to model the Rg assuming an isotropic moment.

The azimuthal differences in Rg can be studied with spectral ratios, which effectively reduce path and site effects so that source effects can be isolated. The spectral ratios for the Rg waves recorded on the ring network are presented in Figure 6-11. Shot 3 was chosen as the reference as we had previously observed that it generated the largest surface waves. Shot 3 produced the largest Rg amplitudes for stations R01-R07, which are all northeast or southeast of the test site. However, for stations west of the test site, Shot 3 produced similar Rg amplitudes as Shots 1 and 2, and the amplitude difference between Shot 3 and the over buried Shot 4 is decreased. For most stations, we note that Shots 1 and 2 have similar amplitudes relative to Shot 3, except on the western stations where Shot 1 amplitudes seem reduced relative to Shot 2. The Shot 1 spectra at R03 (NE) were contaminated with noise and were difficult to process.

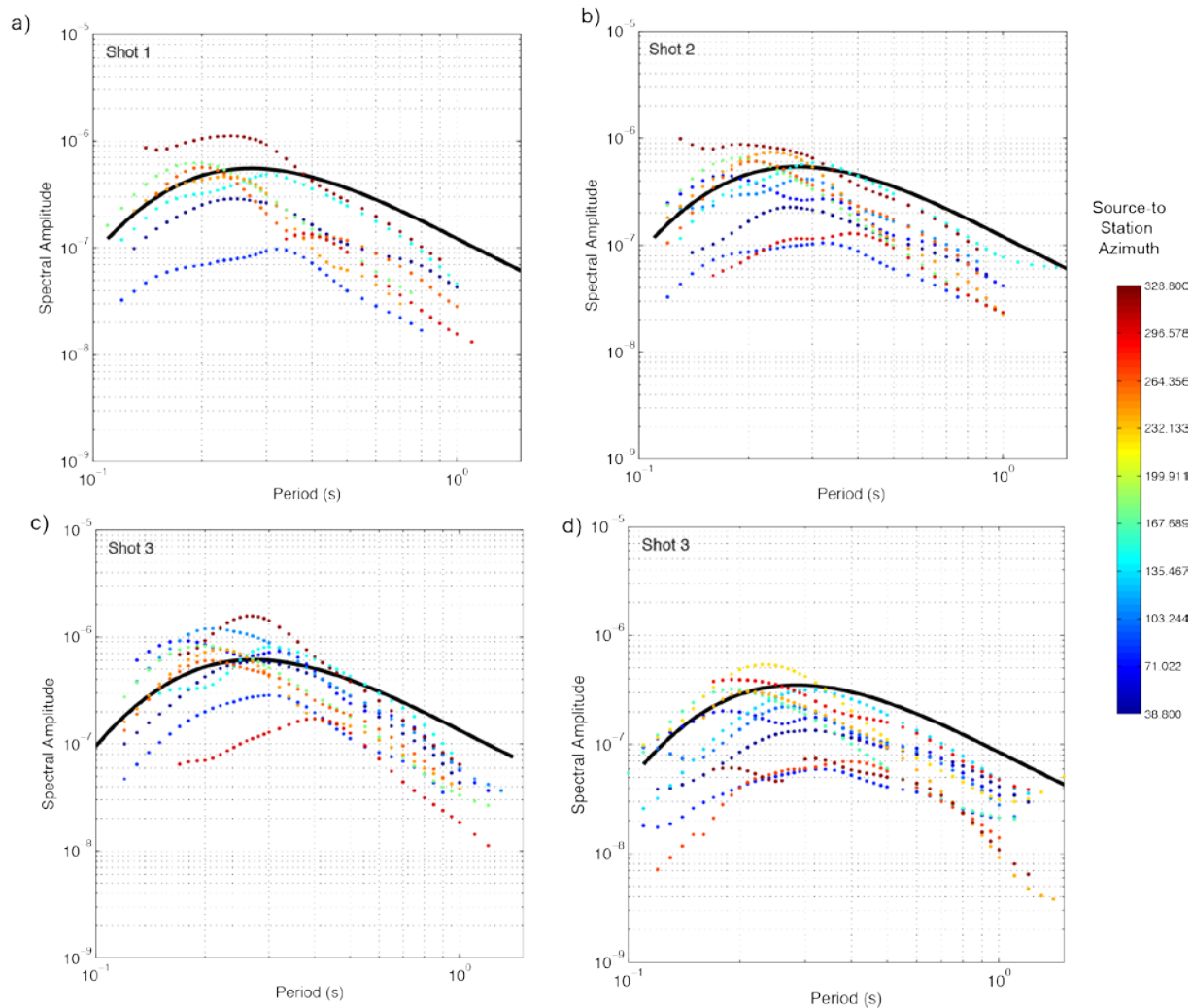


Figure 6-10. Observed versus theoretical spectral amplitudes for NEDE1 a) Shot 1, b) Shot 2, c) Shot 3, and d) Shot 4. The dots represent observed spectral amplitudes on the ring stations at ~6km with the colors representing the source-to-station azimuth. The solid black line is the predicted spectral amplitude based on the DJ91 moments and crustal model derived in this study.

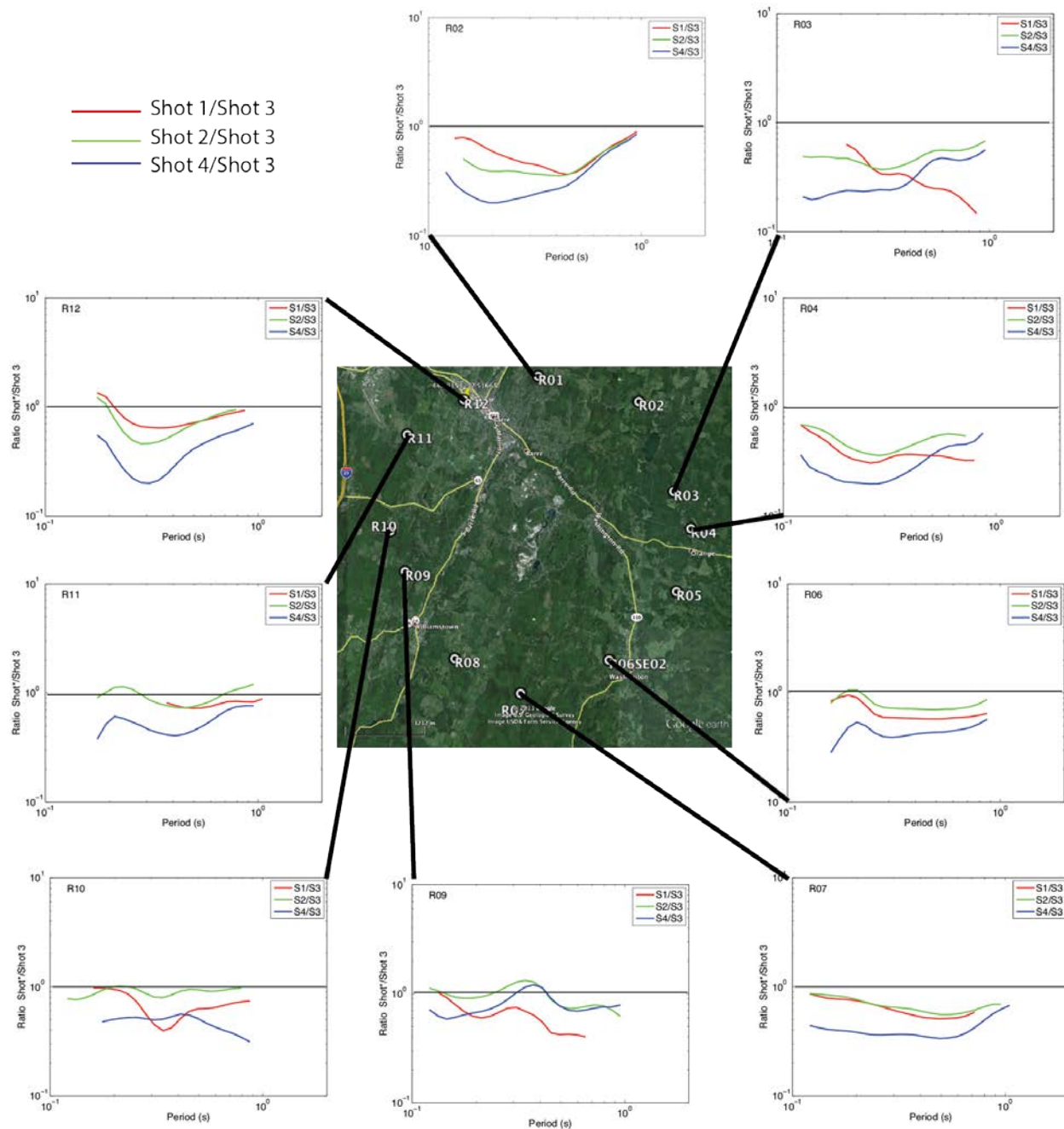


Figure 6-11. Spectral ratios for Rg for the ring network stations. The Shot 3 Rg spectra were chosen for the denominator in each spectral ratio. The ratios are presented as Shot 1/Shot 3 (red), Shot 2/Shot 3 (green), and Shot 4/Shot 3 (blue).

The synthetic spectral amplitudes are also shown in Figure 6-10, and the match between the synthetic and observed amplitudes is best at the high frequencies (> 3 Hz). For Shots 1, 2, and 3, the predicted spectral amplitudes lie near the mean of the observed data between 3-10 Hz; however, at frequencies below 3 Hz, the observed Rg spectra fall off faster than the synthetic spectra. This is likely due to an improper frequency-dependent source model for Rg generated by small explosions. Source models such as DJ91 and MM71 were developed for P-waves, and not surface waves. The long period moment in these explosion source theories is typically flat at frequencies less than the corner frequencies (or slightly tilted due to overshoot). Our observations from numerous small explosion experiments in the past decade have suggested that Rg generation as a function of frequency seems to be yield dependent, with larger explosions generating more longer-period Rg energy relative to the higher-frequencies than smaller explosions. The difference could also be related to a poor Q model at these frequencies, and we examine the use of a different Q model in Figure 6-12.

Figure 6-12a shows the effect of varying the M_0 for Shot 3 to try to better match the observed spectral amplitudes between 1-3 Hz. The M_0 reduction by factors of 2 and 5 provide a better fit to the 1-3 Hz data, but the slopes of the observed and synthetic spectra do not agree. Figure 6-12b presents the results for Shot 3 using a constant Q model (shear wave $Q_s=50$), and the fits between the synthetic spectra to the observed in the 1-3 Hz range are not improved. Also, the shapes of the high frequency Rg spectra are better modeled by the original Q model (Figure 6-12a). These results suggest that all of the spectra fall between an isotropic moment of $1.5 \cdot 10^{10}$ to $1.5 \cdot 10^{11}$ N-m, which does not provide a precise enough estimate for our research objectives.

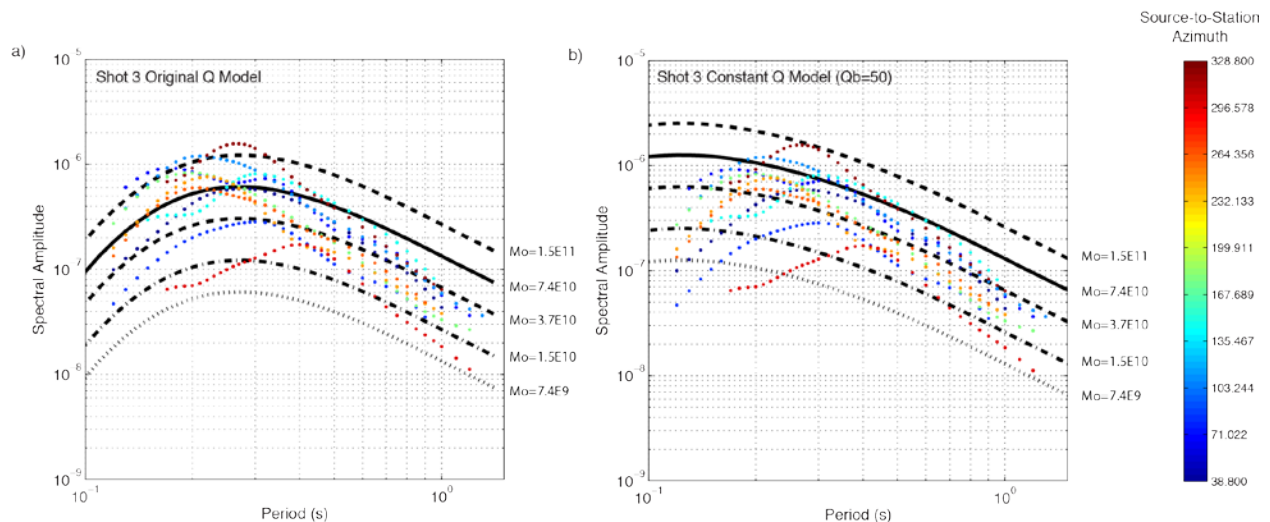


Figure 6-12. Varying the M_0 estimates to provide a range of possible moments to bound the observed data. a) Original Q model. b) Constant Q model with shear wave $Q_s=50$ in all layers in Table 6-2.

MM71 Model. Another often-used nuclear explosion source model is the MM71 model. The predicted moments and corner frequencies from MM71 (Figure 6-13) are larger than those predicted by DJ91, thus the fits between the observed and synthetic spectra are worse. The predicted MM71 moment of 2.35×10^{11} (Shot 3) would result in a synthetic spectra slightly larger than the upper dashed line in Figure 6-12a, which is for a $M_0 = 1.5 \times 10^{11}$. This is without the factor of 2 multiplication for yield which many researchers use when applying MM71 to chemical explosions. Based on our analysis, DJ91 provides a moment estimate that better fits the observed R_g for the NEDE2 Shots 1-4.

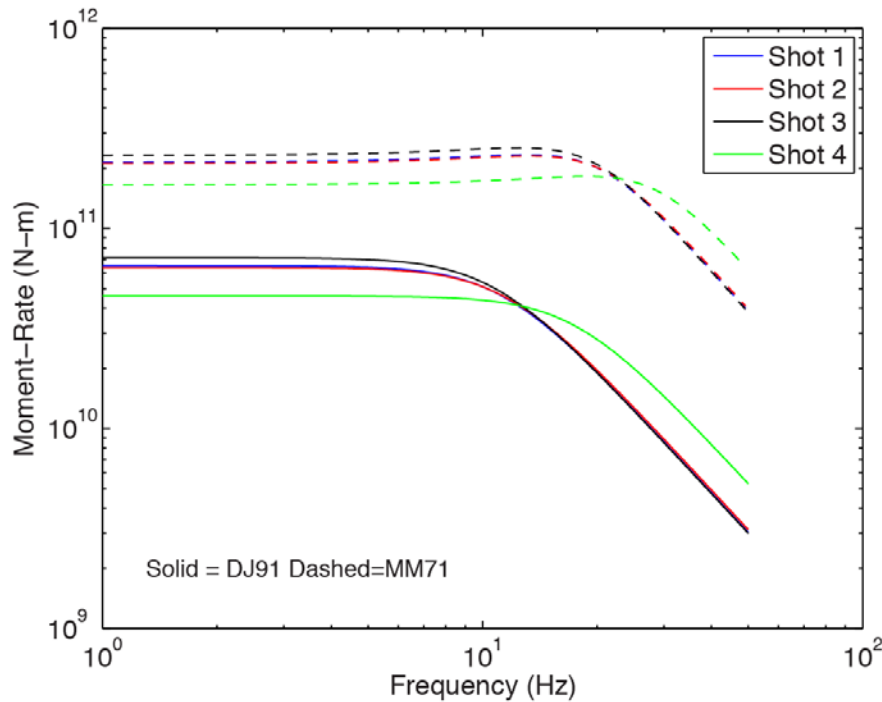


Figure 6-13. A comparison of the predicted source spectra for the NEDE2 Shots 1-4 using DJ91 (solid) and MM71 (dashed).

Patton Explosion Model. Perhaps the mismatch between the synthetics and observed spectral data can have been improved by considering the effects of late-time damage on the seismograms. Patton and Taylor (2011) questioned the DJ91 approach of calibrating observed explosion moment, M_o , to theoretical explosion moment, M_t , without considering the effects of late-time damage. Patton (2012b) models the effects of damage using the superposition of isotropic explosion monopole and compensated linear vector dipole (CLVD) sources. The moment for the isotropic source (M_I) is obtained by modifying the theoretical moment in Equation 6-4 using a damage index, K , by:

$$M_I = M_t \frac{(K+2)}{3} \quad (6-6)$$

A value of $K=1$ means no permanent damage while $K>1$ means damage occurred through dilation of the source medium, which is modeled using a CLVD source with moment:

$$M_{CLVD} = M_I \frac{2(K-1)}{(K+2)}. \quad (6-7)$$

We summed isotropic and CLVD synthetics for $1 < K < 4$ and compared to our observed spectral amplitude data. We did not attempt to vary the depth of the CLVD or delay the start of the CLVD in this pilot study. We are also not trying to match the phase. These things could be completed in a more detailed study, possibly in collaboration with Patton. Our cursory results suggest that a $K=2.6$ would provide a good fit between the observed spectral amplitudes and the synthetic data.

To better understand how the Patton (2012b) source works, we present Figure 6-14. In this image, we show an isotropic explosion synthetic for Shot 3 with M_I determined from Equation 6-6 using a theoretical moment $M_t=2.93E11$ N-m (Table 6-3) and $K=2.6$. The moment tensor convolved with the Green's functions is defined as:

$$\begin{bmatrix} M_I & 0 & 0 \\ 0 & M_I & 0 \\ 0 & 0 & M_I \end{bmatrix}. \quad (6-8)$$

Also shown is the synthetic for a CLVD source with moment defined by Equation 6-7, and the moment tensor convolved with the Green's function is defined by:

$$\begin{bmatrix} \frac{-M_{CLVD}}{2} & 0 & 0 \\ 0 & \frac{-M_{CLVD}}{2} & 0 \\ 0 & 0 & M_{CLVD} \end{bmatrix} \quad (6-9)$$

The resulting isotropic and CLVD synthetics are summed to form a residual synthetic, which has the combined effect of modeling the explosion itself and damage above the source. The damage component reduces the amplitudes of the surface waves, which is thought to be one of the reasons that the $M_s:mb$ discriminant works well in separating earthquakes and explosions.

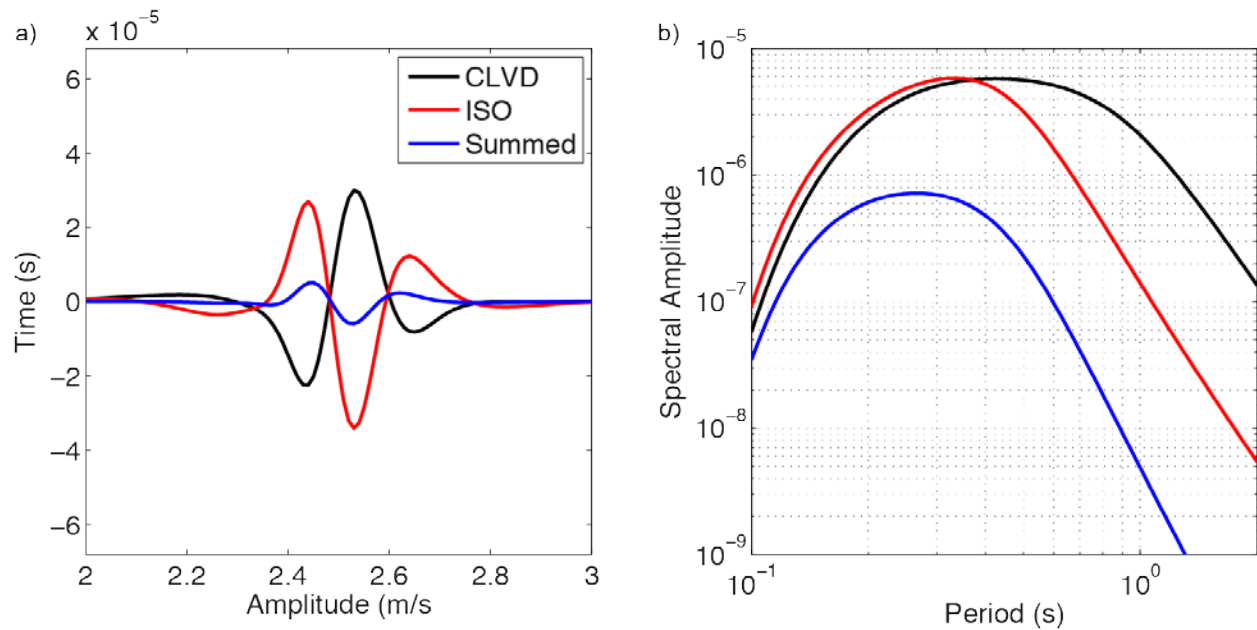


Figure 6-14. a) Synthetic waveforms produced using the Patton (2012b) source model for a $K=2.6$. b) Spectral amplitudes of the synthetics in a).

The comparisons of the isotropic+CLVD synthetics with the observed data are shown in Figure 6-15 (waveforms) and Figure 6-16 (spectra). The main improvement offered by this method is that we have a much better fit between the predicted and observed spectra at 1-3 Hz. The fits above 3 Hz are similar to the fits observed when considering only an isotropic moment defined by the DJ91 Mo (Equation 6-4). It is interesting that a single $K=2.6$ value provided adequate results for Shots 1-3, considering they were different explosive types and Shot 3 had more visible surface damage. The value of $K=2.6$ does not provide as promising results for the over-buried Shot 4. While the shape of the spectra seems to match the observed data, the amplitude level produced by the moment is offset to larger-than-observed levels. Other values of K provided slightly improved fit to the amplitudes, but not the shape of the spectra. It seems possible that actual moment of this explosion is smaller than DJ91 predicts. We believe this dataset provides an excellent opportunity for continued analysis of the Patton (2012b) explosion source.

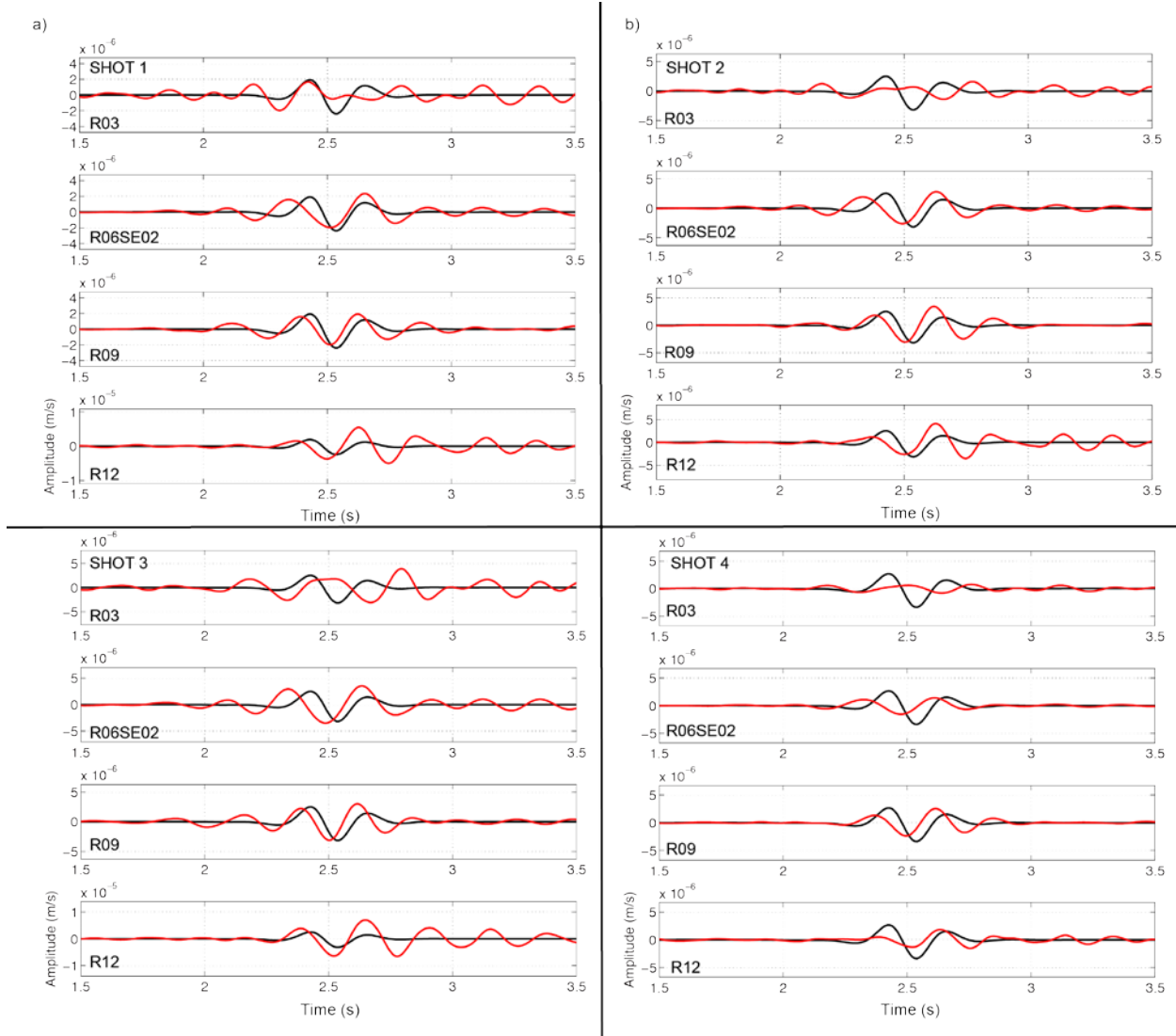


Figure 6-15. A comparison of the synthetic R_g (black) using the Patton (2012b) explosion and damage source model to observed data (red) from four ring stations (Figure 6-8) that recorded the NEDE2 Shots 1-4 (a,b,c, and d respectively).

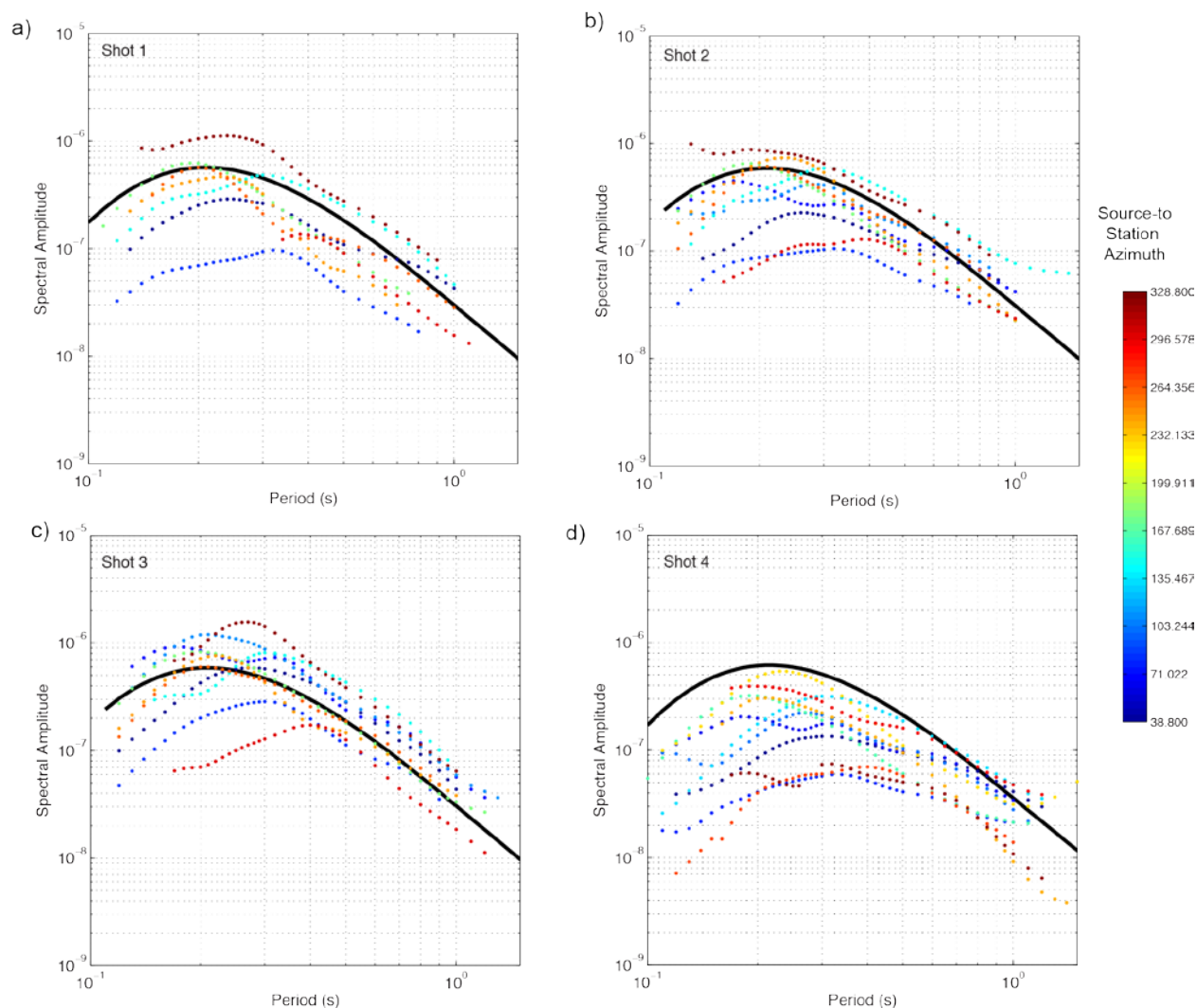


Figure 6-16. Observed spectral amplitudes for NEDE2 a) Shot 1, b) Shot 2, c) Shot 3, and d) Shot 4 compared to synthetic estimates using the Patton (2012b) explosion plus damage model. The dots represent observed spectral amplitudes on the ring stations at ~6km with the colors representing the source-to-station azimuth. The solid black line is the predicted spectral amplitude based on the Patton (2012b) explosion plus damage model.

CONCLUSIONS AND FURTHER RECOMMENDATIONS

This study provides insight into the appropriateness of explosion source theories in modeling small chemical explosions. Some of the difficulties encountered in this study include significant azimuthal scatter in the observed Rg data and lateral variations in velocity and attenuation structure. We have estimated the seismic moments for the NEDE2 explosions using the DJ91, MM71, and Patton source models. The results show that the DJ91 moments (M_0) produced

synthetic data that fit within the scatter of the observed Rg spectral amplitudes above 3 Hz; however, below 3 Hz, the synthetic spectra predict more Rg energy than observed from the explosions. MM71 moments produce synthetic Rg spectral amplitudes too large to match the observed data. Perhaps, the best fit to the observed data results when using the Patton source model, which is tied to the DJ91 theoretical moment (M_t), with an added damage component modeled by a CLVD moment tensor. We estimate that a damage index $K=2.6$ value results in synthetics that fit with the scatter of the observed data at all frequencies, with the exception of the deeply-buried Shot 4. For this shot, the actual seismic moment appears smaller than the predicted moment from both DJ91 and MM71, nor could we find a preferred Patton model that fit the observed data. For future studies, we will combine near-source P-wave moment studies with these Rg studies to determine if similar moments are obtained. We also need to refine the results based on the Patton (2012a) methods to include phase velocity analysis using improved velocity models.

7. EFFECT OF VELOCITY OF DETONATION OF EXPLOSIVES ON SEISMIC RADIATION

ABSTRACT

We studied seismic body wave generation from four fully contained explosions of approximately the same yields (68 kg of TNT equivalent) conducted in anisotropic granite in Barre, VT. The explosions were detonated using three types of explosives with different velocities of detonation (VOD): Black Powder (BP), Ammonium Nitrate Fuel Oil/Emulsion (HANFO), and Composition B (Comp B). The main objective of the experiment was to study differences in seismic wave generation among different types of explosives, and to determine the mechanism responsible for these differences.

The explosives with slow burn rate (BP) produced lower P-wave amplitude and lower corner frequency, which resulted in lower seismic efficiency (0.35%) in comparison with high burn rate explosives (2.2% for HANFO and 3% for Comp B). The seismic efficiency estimates for HANFO and Comp B agree with previous studies for nuclear explosions in granite. The body wave radiation pattern is consistent with an isotropic explosion with an added azimuthal component caused by vertical tensile fractures oriented along pre-existing micro-fracturing in the granite, although the complexities in the P- and S-wave radiation patterns suggest that more than one fracture orientation could be responsible for their generation. Analysis of the S/P amplitude ratios suggests that the BP source mechanism can be almost entirely explained by opening of the tensile fractures as a result of the slow energy release. The P-wave amplitude reduction for the BP shot supports this hypothesis.

INTRODUCTION

Estimation of the amount of energy that an underground explosion transfers to seismic energy is important for predictions of the seismic effect on engineering structures, as well as for estimating the yield of the underground explosions. Seismic efficiency of an explosion is defined as the ratio of the radiated seismic energy to the total energy of the explosives (e.g. Haskell, 1967; Shishkin, 2007). Haskell (1967) estimated that only a small portion of the explosive energy is radiated as a seismic wave (e.g. 3.7% for granite, 1.2% for tuff, 0.1% for alluvium). The energy losses near the source depend on the rock physical properties (e.g. strength and compressibility) as well as energy density and duration of the explosive source. Differences in energy densities likely cause the well-known double equivalency factor for high explosive charges compared to nuclear explosions of the same yield. The results of the Nonproliferation Experiment (NPE) show that chemical explosions of the same yields generate near-source signals that are larger than those from nuclear explosions by approximately a factor of two (e.g. Olsen and Peratt, 1994; Stump *et al.*, 1999). The reduction of the seismic efficiency for nuclear explosions is explained by higher energy losses resulting from extremely high pressures and temperatures. The energy losses can be attributed to rock heating that may lead to melting, evaporation or phase transformation. Mechanical effects of the passing wave include pore closure, and opening of new and sliding along old fractures. Creating new fractures increases the surface energy due to breaking molecular bonds and creation of new surfaces.

While inelastic effects of the passing wave results in energy loss, some of the energy is radiated outward due to fracturing (e.g. Ashby and Sammis, 1990; Ben-Zion and Ampuero, 2009). Laboratory experiments (e.g. Doll, 1984) show that most of the energy expended on fracture propagation is converted into heat, with only about 3% radiated as acoustic emission (e.g. Gross *et al.*, 1993). The remaining energy is dissipated through plastic deformation.

Thus the damage and fracturing around the explosion represents both an energy sink and an additional source of seismic waves. The energy of the passing pressure wave is redistributed by rock failure into both P and S waves of varying frequency content and directivity. The amplitude and duration of the pressure wave affects the extent of the fracture zone (e.g. Sammis, 2011), which in turn affects seismic radiation.

Damage and failure in a conical region above the explosion is one of the mechanisms proposed to explain shear wave radiation by explosions (e.g. Eisler and Chilton, 1964), which can be modeled as a compensated linear vector dipole (CLVD) component added to an isotropic source (e.g. Knopoff and Randall, 1970; Patton and Taylor, 1995).

This study is based on a unique dataset collected during the New England Damage Experiment Phase 2 (NEDE2). Three types of explosives with different VOD were used in order to study the

effect of the burn rate on seismic wave radiation. The main goal of the experiment was to quantify the different levels of rock damage around the source and then relate the seismic wave generation to the degree and distribution of damage and fragmentation. In this chapter, we concentrate on body wave radiation and seismic efficiency for different explosives.

NEDE EXPERIMENTS

The New England Damage Experiment (NEDE) was conducted in a granite quarry located near Barre, Vermont in a homogenous hard rock with low fracture density (Stroujkova *et al.*, 2012). Two sets of jointing are observed in the Barre rocks: nearly vertical micro-fractures oriented approximately N30°E and sub-horizontal sheeting joints. The vertical set of micro-fractures creates strong (up to 20%) seismic velocity anisotropy and defines a rift. The presence of the aligned micro-fractures results in the reduction of tensile strength perpendicular to the rift direction (e.g. Martin *et al.*, 2012).

The main objective of the experiment was to study shear wave generation due to explosives with different velocities of detonation (VOD). The explosives used in this study have different densities, burn rates and energy content per unit mass. Black powder (BP) burns without forming a detonation wave. On the other hand, the high explosives such as Ammonium Nitrate Fuel Oil/Emulsion (HANFO) and Composition B (Comp B) develop a detonation wave propagating at a supersonic speed.

The first part of the NEDE was conducted in July of 2008 (NEDE1; e.g. Leidig *et al.*, 2010; Stroujkova *et al.*, 2012). Five explosions were detonated during the NEDE1: three 61 kg explosions (BP, HANFO and Comp B), and two 122 kg explosions (HANFO and Comp B). Equal weights of the different types of explosives were detonated, however the TNT equivalent yields of these explosions were different due to differences on the explosives' energy content. The VOD was measured for four out of five explosions. The ANFO/Emulsion explosion detonated with a VOD of 5.06 – 5.26 km/s, and Comp B explosives have the highest VOD of all three explosives at 8.31 km/s. BP deflagrated (i.e. burned) with the slowest burning rate of 0.49 km/s.

To quantify the damage to the granite resulting from the explosions, a series of boreholes were drilled before and after the explosions conducted in the NEDE1 and the physical properties of the granite were measured from the recovered cores (Martin *et al.*, 2011b). Significant post-explosion seismic velocity reduction due to micro-fracturing around the source was observed as a result of the laboratory analysis of the rock cores. In addition, large radial fractures predominantly oriented parallel to the rift direction were found as a result of the core analysis.

In the follow-up experiment in the summer of 2013 (NEDE2), six explosions with approximately equal TNT equivalent yields (68 kg TNT equivalent) were detonated. Two of the explosions were the reshoots (i.e. conducted within 2 m) of the NEDE1 explosions, which are not discussed in this chapter. Three of the explosions were detonated using different types of explosives (Shot 1 – BP, Shot 2 – HANFO, and Shot 3 – Comp B) with depths of burial (DOB) of approximately

13 m. The fourth explosion (Shot 4) was an HANFO shot detonated with the DOB of 29 m. Shot 4 was used as a reference shot, because the increase in DOB reduces the effects of the free surface and increases the overburden stress resulting in more symmetrical source mechanism. Table 7-1 lists the parameters of the explosions, including their yields and depths of burial. The TNT equivalency conversion factors for BP, HANFO, and Comp B are also shown as an endnote to Table 7-1.

Table 7-1. Explosive Characteristics for NEDE2 Shots.

Shot #	Explosive	Weight of Explosive (kg)	TNT Equivalent Yield (kg)*	Borehole Diameter (cm)	Charge Center Depth (m)	SDOB (m/kt^{1/3})	Charge Length (m)
1	Black powder	113.5	68.1	22.2	12.89	305.7	2.62
2	HANFO	83.8	68.1	22.2	13.50	320.1	1.5
3	Comp B	45.7	73.2	22.2	12.32	285.2	2.08
4	HANFO	83.8	68.6	22.2	13.50	686.7	1.5

* TNT equivalency conversion factors: Black Powder/TNT – 0.6, HANFO/TNT - 0.8, Comp B/TNT - 1.35

There were differences in Comp B charges between the NEDE1 and NEDE2. For NEDE1 factory made charges made of Comp B were used. The Comp B charges were cast specifically to fit our boreholes with a requirement that the charges should not be larger than 20 cm in diameter so they could easily fit in 22 cm holes with the tubing, wiring, and straps attached. For NEDE2, the manufactured cast charge was larger than specified and did not fit into the borehole. Therefore, a charge was made in the field using Comp B boosters connected together with some HANFO placed between the boosters. As a result, the charge density (defined as the explosive weight per unit length of the charge) was lower for the NEDE2 Comp B shot (Table 7-1). While we did not measure the VOD during the NEDE2 experiment, lowering the charge density due to presence of the voids between the boosters forming the charge would likely reduce the VOD for NEDE2 Comp B shot.

The NEDE2 BP and Comp B explosions generated long surface fractures allowing explosive gases to escape from the cavity. These fractures did not create any vertical displacements. The Comp B shot created a 21 m long fracture approximately 6 m from the shot hole. Hot gas escaping from the explosion started a fire, which burned a data cable for the near-source accelerometer (NS13). The surface fracturing produced by the Comp B shot was unexpected. During the NEDE1, BP and HANFO shots generated surface fractures, while Comp B shots did not. One possible explanation for the surface fracturing is the presence of water in the Comp B shot borehole, which could not be drained because of the recharge from the fractures cutting through the borehole.

SEISMIC DATA ANALYSIS

The NEDE2 explosions were recorded on over 36 seismic instruments, including seismometers, accelerometers, acoustic sensors, and high-definition video cameras. The seismic instrumentation was deployed at the surface at distances of less than 1 m (from the borehole collar) to 24 km from the explosions (Figure 7-1). The seismic systems were deployed as part of three networks including the near-source network at distances less than 1 km, a ring of sensors at approximately 6 km distance with approximate 30° spacing, and a linear array extending 24 km to the SE of the quarry with 3 km spacing. All near-source instruments (< 1 km) recorded three components (3C) of motion at a sampling rate of 1000 samples per second (sps). The local instruments (> 1 km) were recording at 500 sps.

Figure 7-2 shows the near-source accelerograms recorded at the surface approximately 1 m away from the shot borehole collars. The records show the upward acceleration caused by the shock wave followed by a downward motion driven by gravity (spall). The duration of the upward impulse is significantly longer (up to 30 ms) for the BP shot. The duration of the upward motion for the HANFO shot is approximately 4 ms, while the Comp B shot produced two separate impulses ~3 ms each (it is not clear why two impulses were observed). Based on the observed impulse widths we expect the BP shot to have lower frequencies than HANFO and Comp B in the far field. The deep HANFO shot produced a very short spall phase compared to the three shallow shots (Figure 7-2d), indicating that the interaction with the free surface was minimal for this shot.

Using the height of the explosive columns (corresponding to charge lengths) in Table 7-1 and the measured VOD for each explosive we estimate the time required for the detonation for each explosive column. The longest source duration of approximately 5 ms is predicted for the BP shot, while it would take less than 1 ms for both HANFO and Comp B to detonate. Thus, the observed duration for the positive acceleration (Figure 7-2) is up to 5-6 times greater than the time it takes for the detonation.

The examples of the far-field waveform data for different explosives recorded at Station R03 located approximately 5.5 km from the sources are shown in Figure 7-3. The spectra shown in Figure 7-3b were calculated using windowed *P*-waves as shown in Figure 7-3a. The *P*-wave for the BP shot is clearly deficient in high frequencies (Figure 7-3a, top panel). As a result, the BP spectral amplitudes are lower than the spectral amplitudes for HANFO and Comp B shots especially at high frequencies (>10 Hz). The spectral ratios between HANFO and BP spectra vary from 1 at low frequencies to a factor of 30 at higher frequencies (Figure 7-3c). Similarly, the ratios between Comp B and BP are between 1-2 at low frequencies and increase up to 30 at higher frequencies.

The spectra shown in Figure 7-3b show peaks and troughs caused by local site and wave propagation effects, which are different for every station. Since each individual spectrum is affected by propagation and local site effects, we calculated the averaged spectra for different

parts of the network. Figure 7-4 shows the spectral amplitudes for the explosions averaged over two different groups of sensors: the intermediate range seismometers located at distances between 300 and 500 m (NS06, NS08, and NS09, Figure 7-1b), and the local stations situated around the circle at 6 km shown in Figure 7-1a. The HANFO and Comp B shots have higher corner frequencies than the BP shots for all stations. In addition the high-frequency roll off is higher for the BP shot.

The low-frequency amplitudes for Comp B Shot 3 exceed the low-frequency amplitudes for HANFO Shot 2 (e.g. Figure 7-3b,c). Results of the NEDE1, however, show the opposite relationships between the HANFO and Comp B explosions (e.g. Stroujkova *et al.*, 2012). Figure 7-5 shows a comparison between the Comp B shot conducted in NEDE1 (83 kg TNT equivalent, DOB=11.3 m) and the NEDE2 Comp B shot (73 kg TNT equivalent, DOB=12.5 m). Notice that the low-frequency amplitudes for the NEDE1 Comp B shot are significantly smaller than for the NEDE2 Comp B shot, even though the latter has 12% smaller yield and a slightly larger DOB. The faster drop in the high frequency part of the spectrum for the NEDE1 explosion is probably caused by the lower sampling rate used in NEDE1 (250 sps in NEDE1 vs. 500 sps in NEDE2). One possible reason for the amplitude increase is the presence of water in the shot borehole for NEDE2. As shown by Butkovich (1971) water in the emplacement medium evaporates at pressures above 5 GPa, which contributes to further pressure increase in the cavity (“water boost”). The peak pressure in the borehole during Comp B detonation can be as high as 14 GPa (e.g. Stroujkova, 2012), which is above the pressure needed for water evaporation. Notice that the amplitude increase is observed mainly at low frequencies, which corresponds to lower overshoot (e.g. Denny and Johnson, 1991) for the explosion in water-saturated rocks.

Differences in S-wave amplitudes between the variable VOD explosions may provide insight into differences in the source processes. Figure 7-6a-d shows the seismic records for Shots 1-4 recorded at Station R06. Significant amplitudes are observed on the transverse components in the shear wave window. The relative S-wave amplitudes are significantly higher for Shots 1 - 3 than for Shot 4. Since the propagation paths are nearly the same for all events the differences in S-wave amplitudes cannot be a result of scattering or P-S conversion along the propagation path; therefore at least some of the energy arriving as S-wave originates at the source.

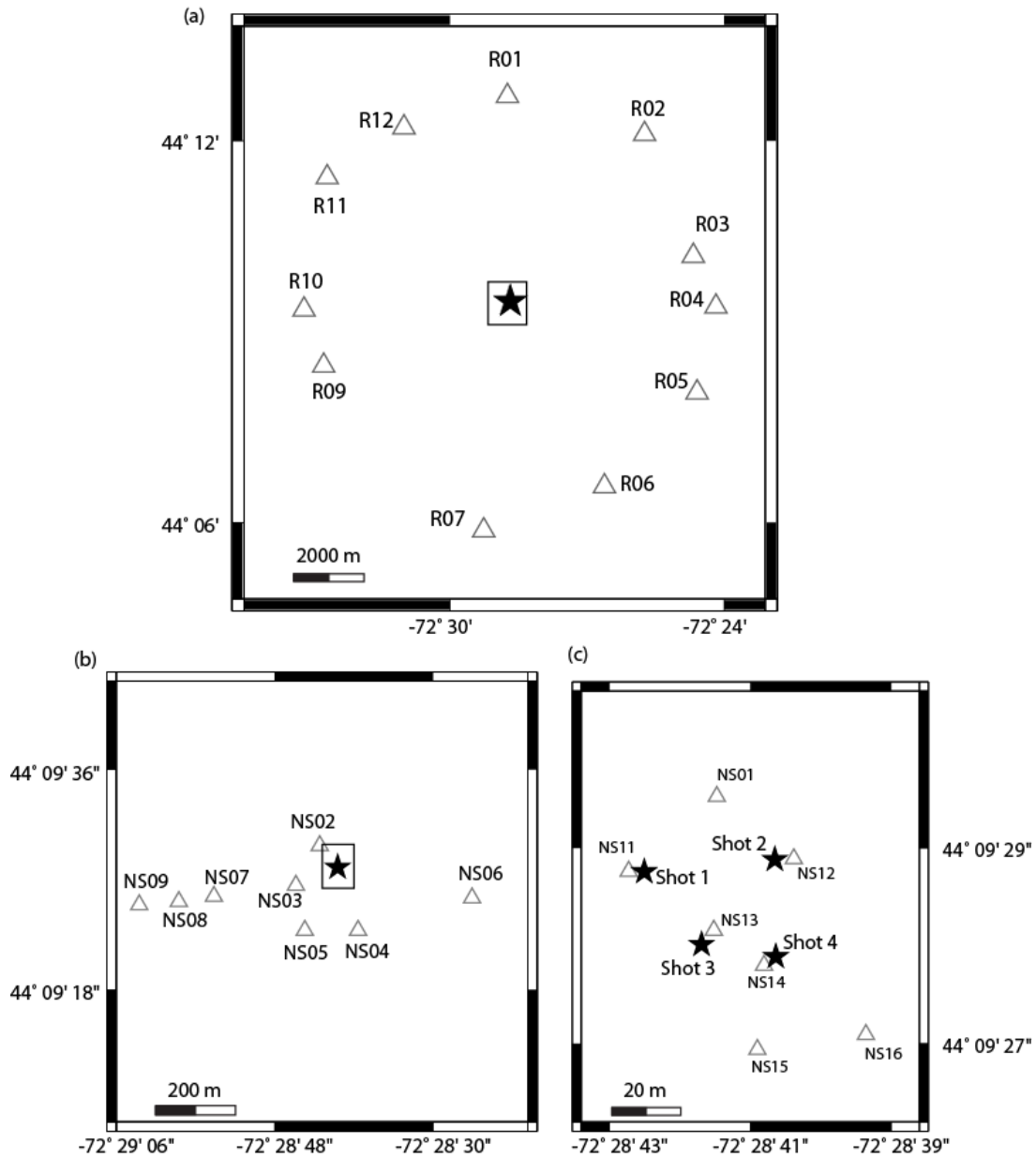


Figure 7-1. (a) The 6 km circle network around the test site at the Rock of Ages Quarry located in Barre, VT. The open triangles show the station locations. The rectangle shows the area enlarged in Figure 7-1b.

(b) Enlarged view of intermediate range stations. The rectangle shows the testing area enlarged in Figure 7-1c. (c) Enlarged view of the testing area showing the near-field accelerometers (triangles) and the explosions (stars).

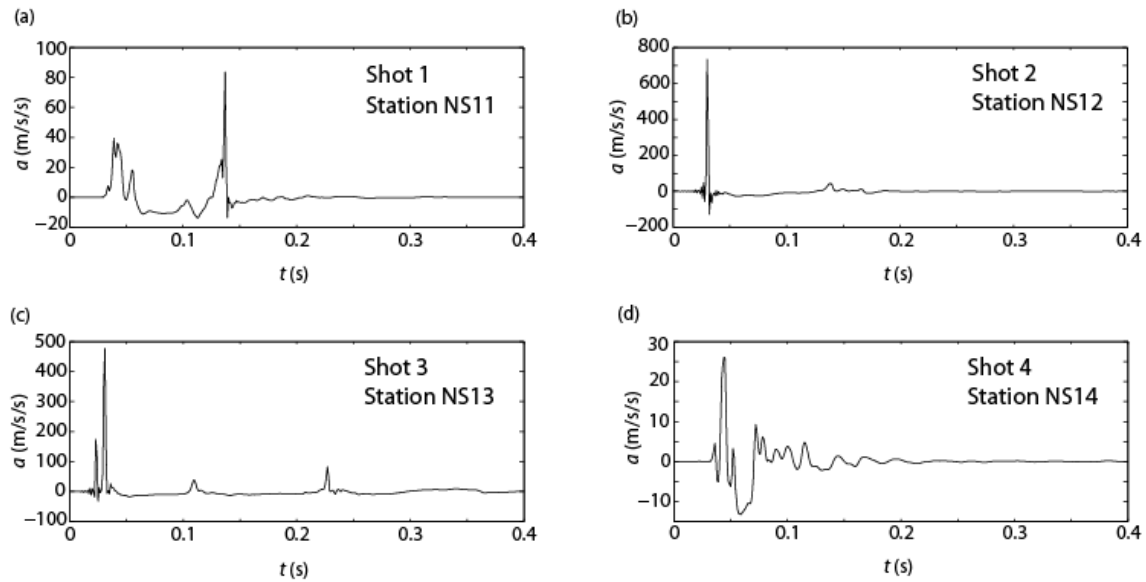


Figure 7-2. Near-source accelerometer data for: (a) Shot 1, (b) Shot 2, (c) Shot 3, and (d) Shot 4. The accelerometers were located at the surface at distances of approximately 1 m from the shot borehole collars.

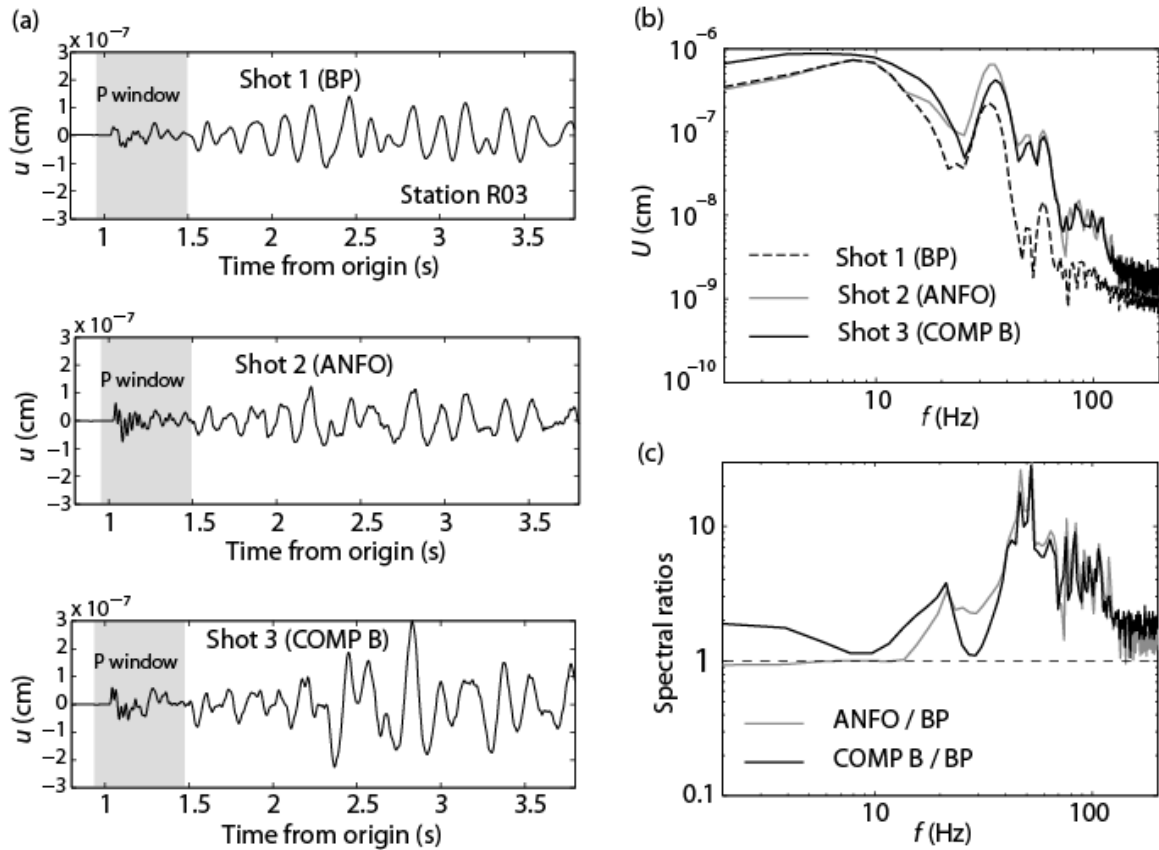


Figure 7-3. (a) Vertical component of the displacement seismograms recorded by Station R03 (at a distance of approximately 5.5 km) for Shot 1 (top panel), Shot 2 (middle panel) and Shot 3 (bottom panel); (b) spectral amplitudes for the traces in (a); (c) spectral ratios between Shot 2 / Shot 1 (grey line) and Shot 3 / Shot 2 (black line).

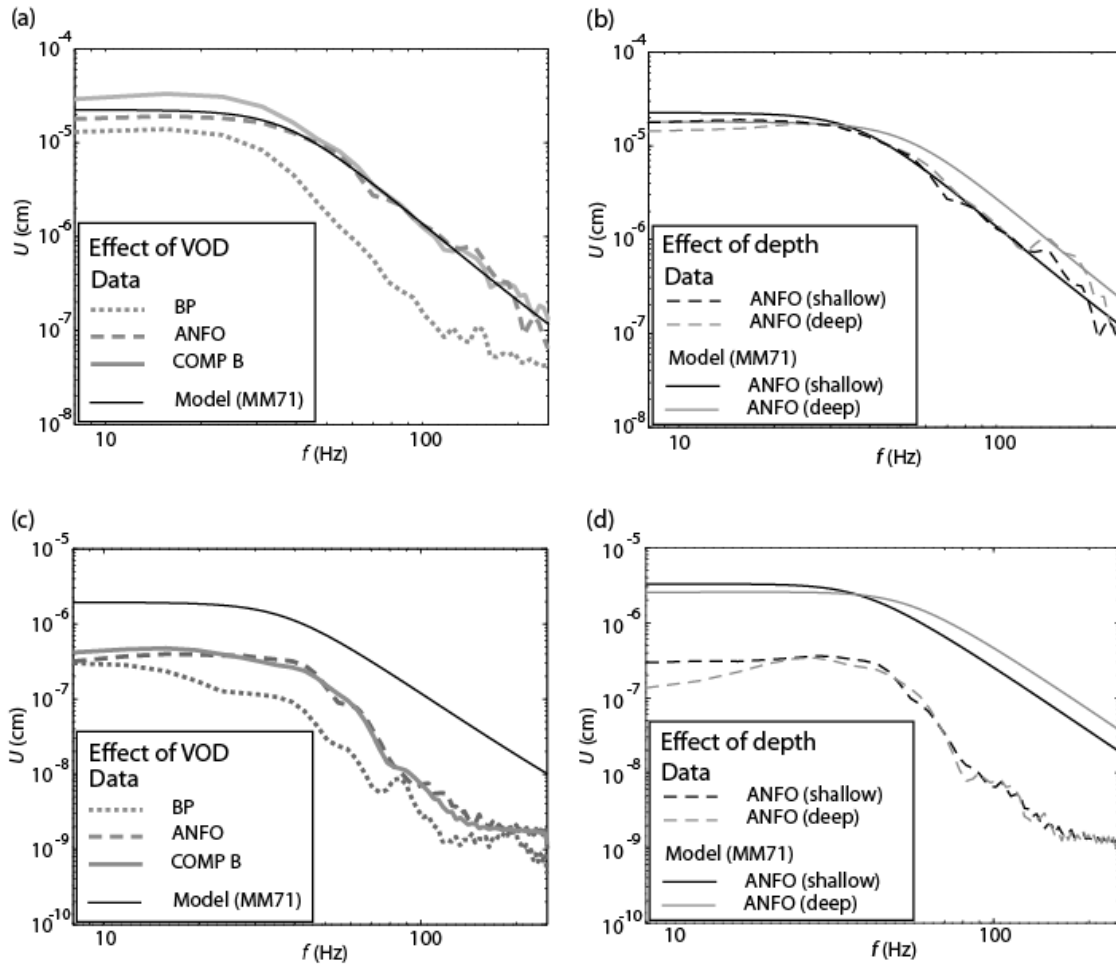


Figure 7-4. (a) Displacement spectra for BP Shot 1 (dotted gray line), HANFO Shot 2 (dashed line) and Comp B Shot 3 (solid gray line) averaged over the intermediate distance instruments (NS07, NS08, NS09); (b) displacement spectra for shallow HANFO Shot 2 (dashed black line) and deep HANFO Shot 4 (dashed gray line) averaged over the same group of instruments as in (a); (c) displacement spectra for BP Shot 1, HANFO Shot 2 and Comp B Shot 3 averaged over the circular (6 km radius) network; and (d) displacement spectra for shallow HANFO Shot 2 and deep HANFO Shot 4 averaged over the same group of instruments as in (c).

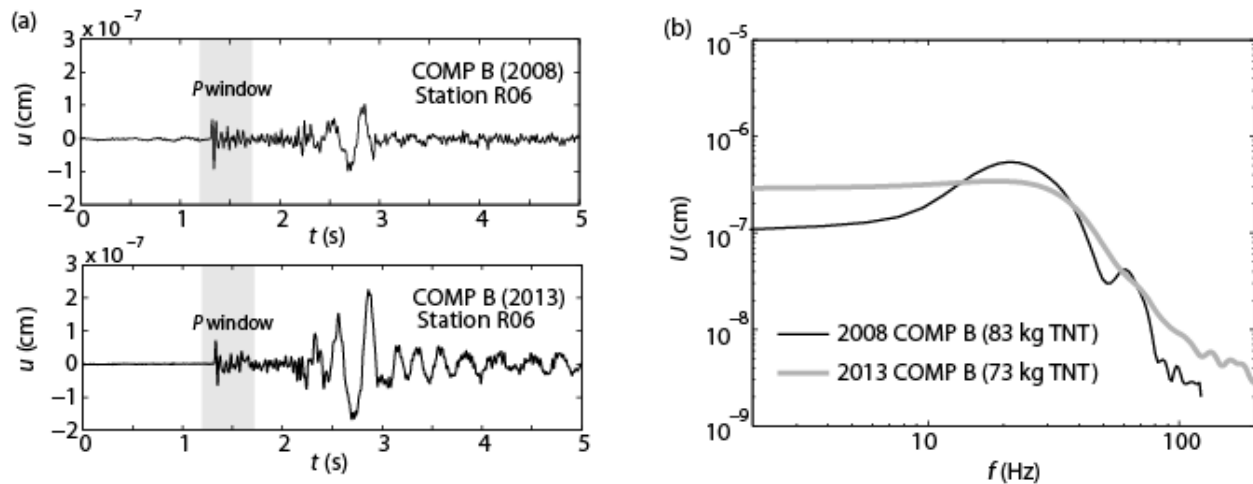


Figure 7-5. (a) Comparison between two Comp B explosions from the NEDE1 (83 kg TNT equivalent, top panel) and the NEDE2 (73 kg TNT equivalent, bottom panel). Vertical components of the displacement seismograms recorded by Station R06/SE02 are shown; (b) spectral amplitudes for the traces shown in (a). The spectra were estimated in the P-wave window marked in (a).

DISCUSSION

Far-field explosion spectra can be characterized by several observable parameters, including low-frequency amplitude asymptote, corner frequency, high frequency roll-off, and the overshoot. Using different types of explosives alters the physical processes at the source and may ultimately affect the observable parameters.

The far field displacements produced by explosions can be expressed in the frequency domain using the Mueller-Murphy model (MM71) after Mueller and Murphy (1971):

$$U(\omega) = \left(\frac{1}{r^2} + \frac{i\omega}{v_p r} \right) \frac{P(\omega) r_{el} V_p^2}{4\mu(\omega_0^2 + i\omega\omega_0 - \beta\omega^2)} \quad , \quad (7-1)$$

where r is the distance to the receiver, greater or equal to the elastic radius r_{el} , λ and μ are the medium Lamé constants, $\beta = (\lambda + 2\mu)/4\mu$, $\omega_0 = v_p/r_{el}$, and $P(\omega)$ is a pressure function applied at radius r_{el} . To estimate the explosion spectra we used the yields and the depths shown in Table 7-1, as well as the medium parameters determined from the lab measurements of the extracted cores: $V_p = 4600$ m/s, $V_s = 2750$ m/s, $\rho = 2600$ kg/m³.

Comparison between the predicted (Equation 7-1) and the observed P-wave spectra for two different groups of sensors is shown in Figure 7-4. For the near-source group of sensors (Figure 7-4a) the HANFO and Comp B spectra agree with the MM71 model prediction. The HANFO spectrum is slightly below the prediction at low frequencies, while the Comp B spectrum slightly exceeds the prediction at the low frequencies. The BP shot spectrum on the other hand is

significantly lower than the model spectrum at all frequencies. The corner frequency f_c is below that predicted by MM71 and the high-frequency roll-off is higher, making the differences at high frequencies even more significant. The spectra estimated for the sensors at local distances (Figure 7-4b) have smaller amplitudes than the model prediction because the model does not account for scattering or attenuation. In addition, due to the ray curvature in heterogeneous media the geometrical spreading can be greater than r^{-1} , which was used to calculate the far-field term in Equation 7-1.

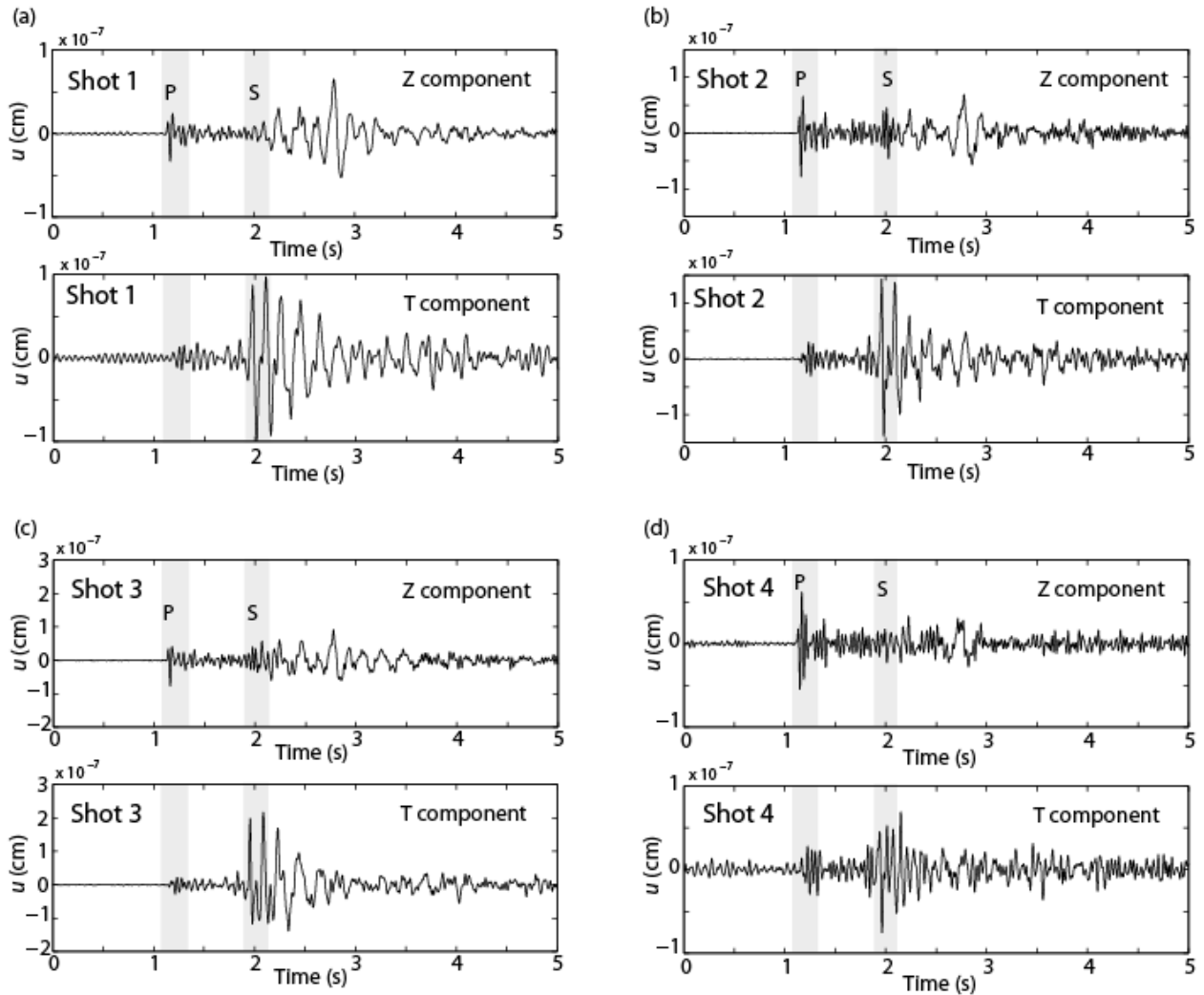


Figure 7-6. Displacement seismograms recorded at Station R06 located approximately 6 km from the test bed. (a) Shot 1, (b) Shot 2, (c) Shot 3, and (d) Shot 4. Top and bottom panels show vertical and transverse components respectively. Shaded areas show P and S wave windows used to estimate amplitudes and spectra.

Comparison of the spectra between shots with different DOB (shallow and deep HANFO shots) is shown in Figure 7-4b,d. The deeper shot has reduction at lower frequencies and very subtle

changes in the high-frequency roll off. The spectrum predicted using MM71 for the deeper shot has significantly higher corner frequency than observed.

The seismic moment can be calculated using the expression (Mueller, 1969; Aki et al, 1974):

$$M_0 = 4\pi\rho V_p \psi_\infty , \quad (7-2)$$

where ψ_∞ is a steady state value of the reduced velocity potential. In the far field the value of ψ_∞ can be approximated as (e.g. Denny and Johnson, 1991):

$$\psi_\infty = U(0)V_p r , \quad (7-3)$$

where $U(0)$ is the low-frequency asymptote of the displacement spectrum measured at a distance r from the source.

Table 7-2 shows the estimated values of M_0 calculated for the near-source stations (NS07, NS08 and NS09) located between 300 m and 500 m. Because of the station proximity to the sources we neglect the inelastic and scattering losses. The results show that the Comp B shot has the highest M_0 , while the BP shot has the lowest.

Table 7-2. Explosion Energy Estimates.

Shot #	Explosive Type	Total Explosive Energy E_t , MJ	f_c , Hz	Roll-off	M_0 , m^3	Radiated Seismic Energy E_s , MJ	Seismic Efficiency k_s	S/P Ratios
1	BP	284.9	26.0	-3.41	$1.48 \cdot 10^{11}$	1.0	0.0035	3.31 ± 1.53
2	HANFO	284.9	36.4	-2.44	$2.25 \cdot 10^{11}$	6.5	0.0228	1.85 ± 1.02
3	Comp B	306.3	32.9	-2.65	$3.09 \cdot 10^{11}$	9.1	0.0297	2.08 ± 0.95
4	HANFO	284.9	40.9	-2.82	$1.35 \cdot 10^{11}$	4.2	0.0147	1.07 ± 0.38

The total radiated energy can be calculated using the relationship (Denny and Johnson, 1991):

$$E_s = \frac{\pi^2 f_c^3 M_0^2}{2\eta\rho V_p^5} , \quad (7-4)$$

where α is the P-velocity, ρ is the rock density, η is the damping factor expressed in terms of the Poisson ratio v :

$$\eta = \sqrt{\frac{1-2v}{2(1-v)}} \quad (7-5)$$

We estimated the corner frequencies and the high-frequency asymptote by fitting straight lines to the low-frequency and high-frequency asymptotes. The results of this estimate are shown in Table 7-2. The highest corner frequency (40.9 Hz) among all shots was observed for the deep HANFO shot. The shallow HANFO shot has a higher corner frequency (36.4 Hz) than other shallow shots and the lowest roll-off ($f^{-2.44}$) among all shots. The BP spectrum shows the lowest corner frequency (26 Hz) and the highest roll-off ($f^{-3.41}$). The Comp B shot has the highest low-frequency asymptote (ψ_∞) determining the seismic moment, followed by the shallow HANFO shot, and finally the BP shot has the lowest. Notice that the near-source impulse duration for the BP shot agrees somewhat with the dominant frequency observed in the far field, while the impulses for HANFO and Comp B are shorter than observed in the far field.

We use the values for the corner frequency and M_0 shown in Table 7-2 to estimate the total energy radiated as seismic waves. The results presented in Table 7-2 (column 9) show that the seismic energy radiated by the HANFO and Comp B shots is greater than the energy radiated by the BP shot. The seismic energy radiated by the deep HANFO shot is lower than by the shallow HANFO shot.

To quantify the fraction of the explosive energy converted into seismic waves we calculated the seismic efficiency k_s :

$$k_s = \frac{E_s}{E_t} \quad (7-6)$$

The total energy of the explosions obtained using the TNT equivalency (1 kg TNT releases $4.184 \cdot 10^6$ J) is also shown in Table 7-2. The seismic efficiency (the ratio of the radiated seismic energy to the total explosive energy) varies between 0.35% for the BP shot, 2.2% for the HANFO shot, and almost 3% for the Comp B shot. The seismic efficiencies calculated for the high explosives (HANFO and Comp B) are consistent with the value of 3.7% reported by Haskell (1967). We note that this is an estimate valid for a spherically symmetric source. The objective of this chapter, however, is to compare the different explosions rather than to estimate the absolute value of the radiated energy, therefore we ignore the non-sphericity of the source.

Figure 7-7 shows P-wave amplitude ratios between BP, shallow HANFO and Comp B and the deep HANFO shot. We used the deep HANFO shot as a reference because due to larger DOB its source processes were least affected by the free surface. The amplitude ratios for the BP shot are less than 1 for all stations and form a complex azimuthal pattern. The amplitude ratios for the shallow HANFO shot are between 1 and 1.5 for all stations except two of the stations located in the NW quadrant. All amplitude ratios for the Comp B shot are between 1 and 1.5. These complexities in the P-wave radiation pattern, particularly for the BP shot, indicate possible deviations from an isotropic source mechanism.

While P-wave energy radiated by the BP shot is lower than for the HANFO and Comp B shots, the shear waves produced by the BP shot are comparable to the shear waves produced by the HANFO and Comp B shots. The deep HANFO shot produced the smallest amplitude shear waves. Figure 7-8 shows the S/P ratios as a function of azimuth for Shots 1-4 calculated using the stations of the circular array. Table 7-2 shows the mean S/P ratios for the explosions and their standard deviations (column 10). The ratios for the BP shot are greater than 1 for all stations with a mean value of 3.31. The ratios are non-uniform as a function of azimuth with pronounced peaks in all four quadrants. The ratios for the Comp B are also non-uniform with a mean value close to 2. The mean ratios for the shallow HANFO shot are smaller (1.85) than for the Comp B, while the ratios for the deep HANFO shot are approximately 1.

The shear wave radiation pattern can be explained as radiation by tensile fractures produced by the explosion. Studies of the pre- and post-shot cores (Martin *et al.*, 2011b) have shown that the predominant direction of the large fractures is parallel to the rift (N30°E) defined by the pre-existing micro-fractures. To examine the possibility of the observed S-waves being generated as a result of opening of the rift-parallel fractures we consider a model of a vertical circular tensile crack with radius a in a Poisson solid ($\lambda=\mu$). The far-field displacement amplitudes ($r \gg a$) due to the crack opening under tension σ_3 for P and S waves in the low-frequency limit ($\omega = 0$) are given by the following expressions (e.g. Aki and Richards, 2002; Walter and Brune, 1993):

$$U^P(\omega = 0) = (2 + \cos(2\theta)) \frac{\sigma_3 a^3}{2\pi\rho V_p^3 r} = R^{FP} \frac{\sigma_3 a^3}{2\pi\rho V_p^3 r}, \quad (7-7)$$

$$U^S(\omega = 0) = (-2 \sin(2\theta)) \frac{\sigma_3 a^3}{2\pi\rho V_s^3 r} = R^{FS} \frac{\sigma_3 a^3}{2\pi\rho V_s^3 r}, \quad (7-8)$$

where θ is an angle in a horizontal plane measured from the plane containing the crack (shown in Figure 7-9a). The factors R^{FP} and R^{FS} represent the radiation patterns in the horizontal plane. Figure 7-9 a shows an azimuthal plot for R^{FP} and R^{FS} produced by a vertical tensile fracture parallel to the rift direction (N30°E). The amplitude ratios calculated as the ratio between Equations 7-8 and 7-7 are shown in Figure 7-9b. The theoretical S/P ratios form a four-lobed shape consistent with the S/P amplitude ratios for BP and Comp B (Figure 7-8a,c). The observed radiation pattern for the deep HANFO shot is close to uniform with a slight increase in the directions of the predicted lobes.

The absolute value of the S/P ratios is determined by the relative strength of the isotropic and the dipole components of the source. For the tensile fracture described by Equations 7-7 and 7-8 the average S/P amplitude ratio is approximately 2.1 (Walter and Brune, 1993). We can write the total S-wave amplitude U_{tot}^S as a sum of the amplitude produced by scattered/converted waves (U_{scat}^S) and the amplitude directly generated by the source (U_{dir}^S):

$$U_{tot}^S = U_{dir}^S + U_{scat}^S. \quad (7-9)$$

For a pure isotropic source no S-wave energy is radiated by the source, so all shear wave energy can be attributed to scattering from other phases ($U_{tot}^S = U_{scat}^S$). For the tensile fracture U_{dir}^S can be approximated using Equation 7-8. We assume that the deep HANFO shot source mechanism is predominately isotropic with some minor effects from opening fractures. In this scenario the shear waves are mainly produced as a result of P-S or Rg-S scattering with only a small portion radiated by the source, suggesting that the portion of S-wave energy responsible for the scattering has amplitude close to P-wave amplitude (Table 7-2, column 9), or $U_{scat}^S \approx U^P$. Assuming that scattering amplitude (relative to P amplitude) is approximately the same for all shots, we find that the S-waves for the shallow HANFO shot consist of approximately 54% scattered waves and 46% radiated by the tensile fractures. For the Comp B shot the scattered S-waves account for 48% of the total amplitude, while radiated S-waves constitute 52%. Using this logic we deduce that the S-wave radiation pattern for the BP shot can be almost entirely explained by opening of the tensile fractures. We note that this is a rough order-of-magnitude estimate. In reality both P and S/P radiation patterns are more complex than the model predictions, suggesting that multiple fractures may have been involved. In addition slip along the rift-parallel fractures can further complicate the radiation pattern produced by the explosions.

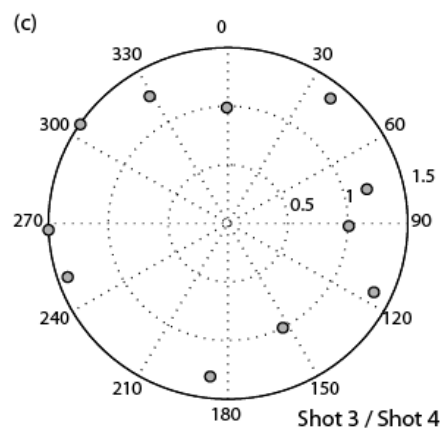
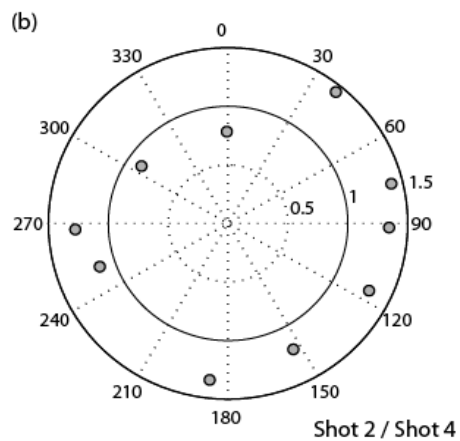
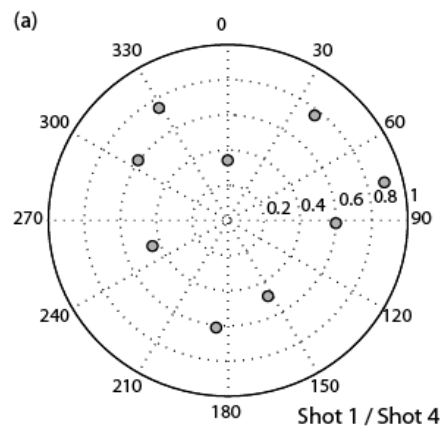


Figure 7-7. Azimuthal variations of P-wave amplitude ratios between: a) Shot 1 and Shot 4, b) Shot 2 and Shot 4, and c) Shot 3 and Shot 4.

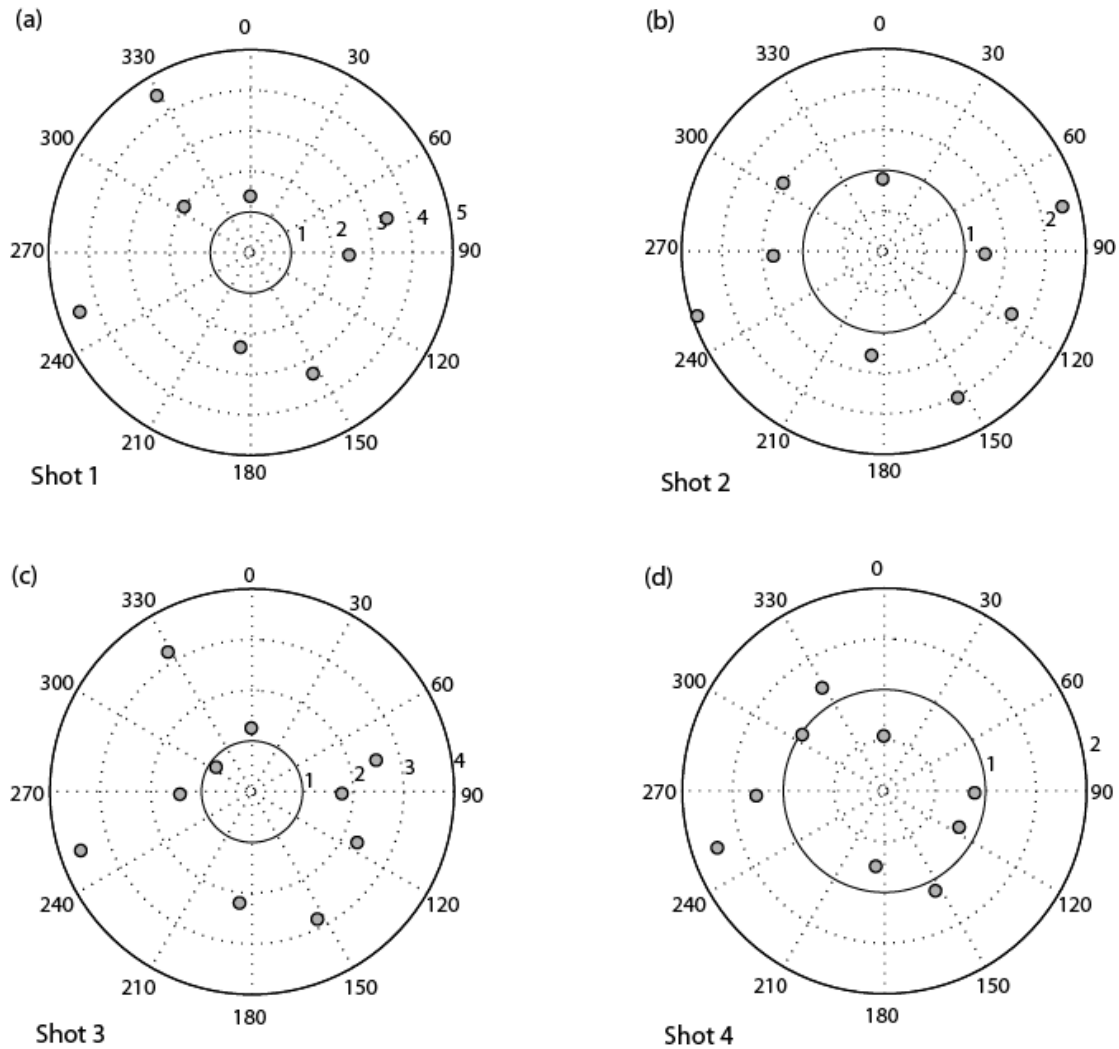


Figure 7-8. Azimuthal variations of S/P amplitude ratios for: a) Shot 1, b) Shot 2, and c) Shot 3, and d) Shot 4. Vertical components were used to measure P-wave amplitudes, while S-wave amplitudes were measured on the transverse components.

Reduced energy radiated by the BP explosion poses an interesting problem related to the mechanism of the energy dissipation near the source. If we assume that the total energy released by all three explosions was roughly equal, lower seismic efficiency can be explained by differences in energy dissipation as a function of the amplitude and duration of the source time function. One mechanism of the energy dissipation is due to creating new fractures and opening old fractures. Studies of the pre- and post-shot rock properties conducted for NEDE1 (Martin *et al.*, 2011b) revealed that the BP shot produced long fractures, some of which broke the surface, and very limited micro-fracturing. On the other hand, HANFO and Comp B shots resulted in significant micro-fracturing damage. This observation agrees with the experimental work and numerical simulations performed by Sammis (2011), who demonstrated that lower amplitude longer duration pressure pulses create longer fractures, while high amplitude pulses pulverize the

rock in the immediate vicinity of the charge. Higher radiated energy from HANFO and Comp B shots suggest that creating new micro-fractures is not a very efficient way of energy dissipation at seismic frequencies compared to opening the new fractures and reopening and sliding along the pre-existing macro-fractures.

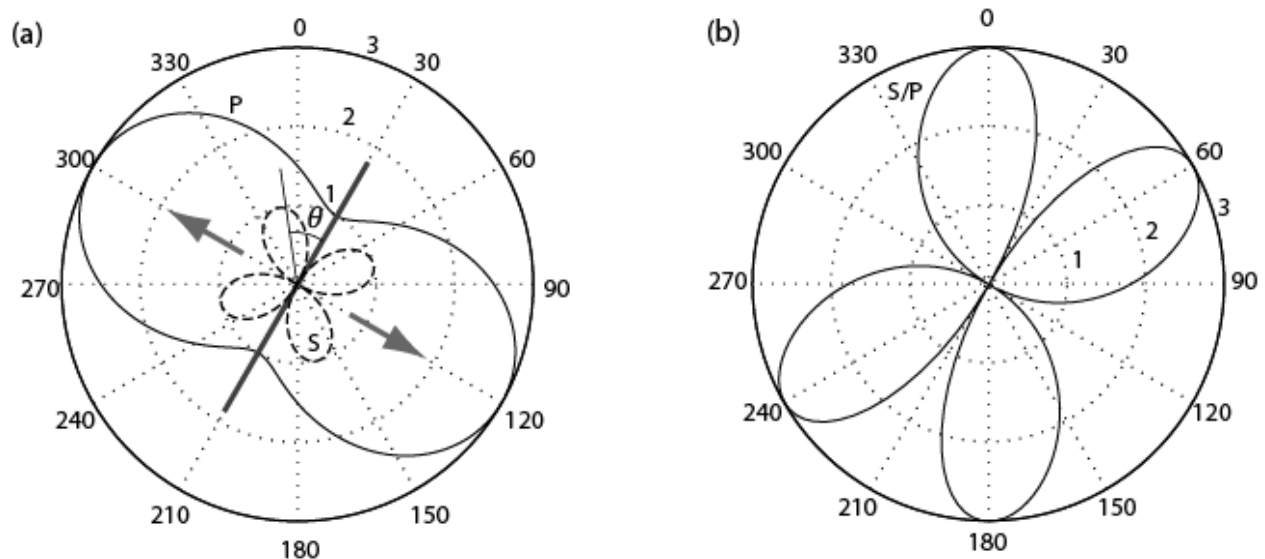


Figure 7-9. (a) Theoretical radiation pattern for P (solid line) and S-waves (dashed line) resulting from an opening of a vertical tensile fracture with N30°E strike. Also shown is the direction of the opening fracture and the angle θ . (b) Theoretical S/P amplitude ratio for the fracture described in (a).

Long radial fractures can also act as conduits allowing explosive gases to escape, potentially leading to reduction in the seismic energy radiation. Slower explosives are known to drive longer fractures. For instance, during the NEDE1, the Comp B shot did not produce surface damage, while the BP and HANFO shots did. The situation changed during the NEDE2, where the Comp B explosion created an extensive surface fracture accompanied by gas venting. Since the radiated seismic energy for the Comp B shot was the highest among all shots, we conclude that gas venting alone cannot be responsible for the seismic radiation reduction for the BP explosion.

CONCLUSIONS

We analyzed the relationships between the VOD of explosives and seismic wave radiation for small chemical explosions. The Comp B shots produced larger *P*-wave amplitudes than equivalent yield (*W* in kg of TNT equivalent) HANFO and BP shots. The BP shot has the lowest amplitude, despite having equal TNT equivalent. Analysis of the source spectra revealed that the BP shot has the lowest corner frequency and steeper high-frequency roll off than the HANFO

and Comp B shots. These observations indicate that the increase in the VOD shifts the seismic energy toward higher frequencies and may reduce low frequency radiation. High frequency deficiency in the far-field spectra for the BP shot can in part be explained by the slower burn rate resulting in longer source impulse duration. Increase in low-frequency seismic energy for the Comp B shot in comparison with the HANFO shot is likely caused by the presence of water in the shot borehole. The NEDE1 Comp B shot was conducted in a dry borehole had reduced low frequency amplitude compared to the HANFO shot as well as the NEDE2 Comp B shot.

The estimated total seismic energy radiated by the BP shot is lower than the energy radiated by the HANFO and Comp B shots. The seismic efficiency for the BP shot is only 0.35%, while it is 2.2% for the HANFO shot, and almost 3% for the Comp B shot. The estimated seismic efficiencies for HANFO and Comp B are consistent with the estimate of approximately 3.7% made by Haskell (1967) for granitic rocks, while the seismic efficiency for the BP is significantly lower.

The observed S-wave radiation pattern is consistent with radiation due to opening of tensile fractures approximately parallel to the rift direction. Opening of the rift-parallel fractures is also confirmed by the analysis of the cores (e.g. Martin, 2011b). Presence of the surface fractures for BP and Comp B shots correlates with the increase in S/P amplitudes for these shots. The HANFO shot, which did not produce surface fracturing, has the second smallest S/P ratios, followed by the deep HANFO shot. Analysis of S/P amplitude ratios suggests that the S-waves for the shallow HANFO shot consist of approximately 54% scattered waves and 46% radiated by the tensile fractures. For the Comp B shot the scattered S-waves account for 48% of the total amplitude, while radiated S-waves constitute 52%. Comparison between the observed and model-predicted S/P ratios for the BP shot indicates that opening of the tensile fracture can account for almost the entire far-field radiation. This observation suggests that the major portion of the energy produced as a result of a slow velocity of detonation can be redirected into opening of the fractures along the direction of pre-existing weakness, which can explain significant differences in the spectral content compared to the HANFO and Comp B shots. Low radiation efficiency of the tensile fracturing can explain the low amplitudes for the BP explosion.

8. EXAMINING THE SHEAR WAVE SOURCE LOCATION THROUGH TRAVEL-TIME MODELING

INTRODUCTION

The Nuclear Explosion Monitoring community utilizes shear phases for event location, discrimination, and yield estimation, yet there is no consensus on the precise generation mechanism of the shear waves from an explosion. Theories range from rock damage to phase conversion at interfaces, or scattering from topography.

In June 2013, the New England Damage Experiment Phase 2 (NEDE2) was performed in the Rock of Ages granite quarry in Vermont, USA. The primary goal of this study was to understand shear wave generation from explosions. The NEDE2 explosions produced anomalously small P/S ratios at local distance stations allowing for easy detection and picking of the shear wave onset.

Three types of explosives were detonated to generate different amounts and types of rock damage to determine if rock damage affects shear wave generation. Nine blasts were detonated, but Shots 7-9 were calibration shots that were too small to be useful for this study. Shots 1-3 consisted of Black powder, Heavy ANFO (HANFO), and Composition B, respectively. They were detonated between 12-14 m depth. Shots 4-6 consisted of HANFO with Shot 4 being over buried at 29 m depth. Shots 5 and 6 being detonated in the damage zones of shots from the first phase of the NEDE in 2008 (NEDE1).

The seismic data from these blasts were recorded by approximately 30 seismic stations at distances ranging from a few meters to more than 20 kilometers. Chapter 2 provides complete details on the experiment. A fundamental method to determine whether the shear energy was generated near the source or along the travel path is to examine the shear wave travel-time with distance from the source. This chapter examines observed and modeled shear wave travel-times to answer this question.

OBSERVED TRAVEL-TIME DATA

Using the Seismic Analysis Code (SAC), three band-pass filtered versions of each seismic record (5-30 Hz for the P wave, 1-10 Hz for the S wave, and 0.5-5 Hz for the S and Rg waves) were created to aid with arrival time picking. P wave and S wave arrival times were then picked and plotted vs. blast-to-station distance using MATLAB. The P wave arrivals clearly exhibited a change in slope at a distance between 1 and 3 km, likely indicating refraction of the wave along a velocity contrast (Figure 8-1 through Figure 8-6). Separate least-squares regression fits were applied to P wave arrival picks at station distances < 1 km and at station distances > 1 km. A least-squares regression was also fit to the observed S wave arrivals at distances > 1 km for each blast. Confident S wave arrival time picks could not be made for station distances < 1 km.

Shot-1 P-wave Refraction Curve with Observed and Theoretical S-wave Regressions

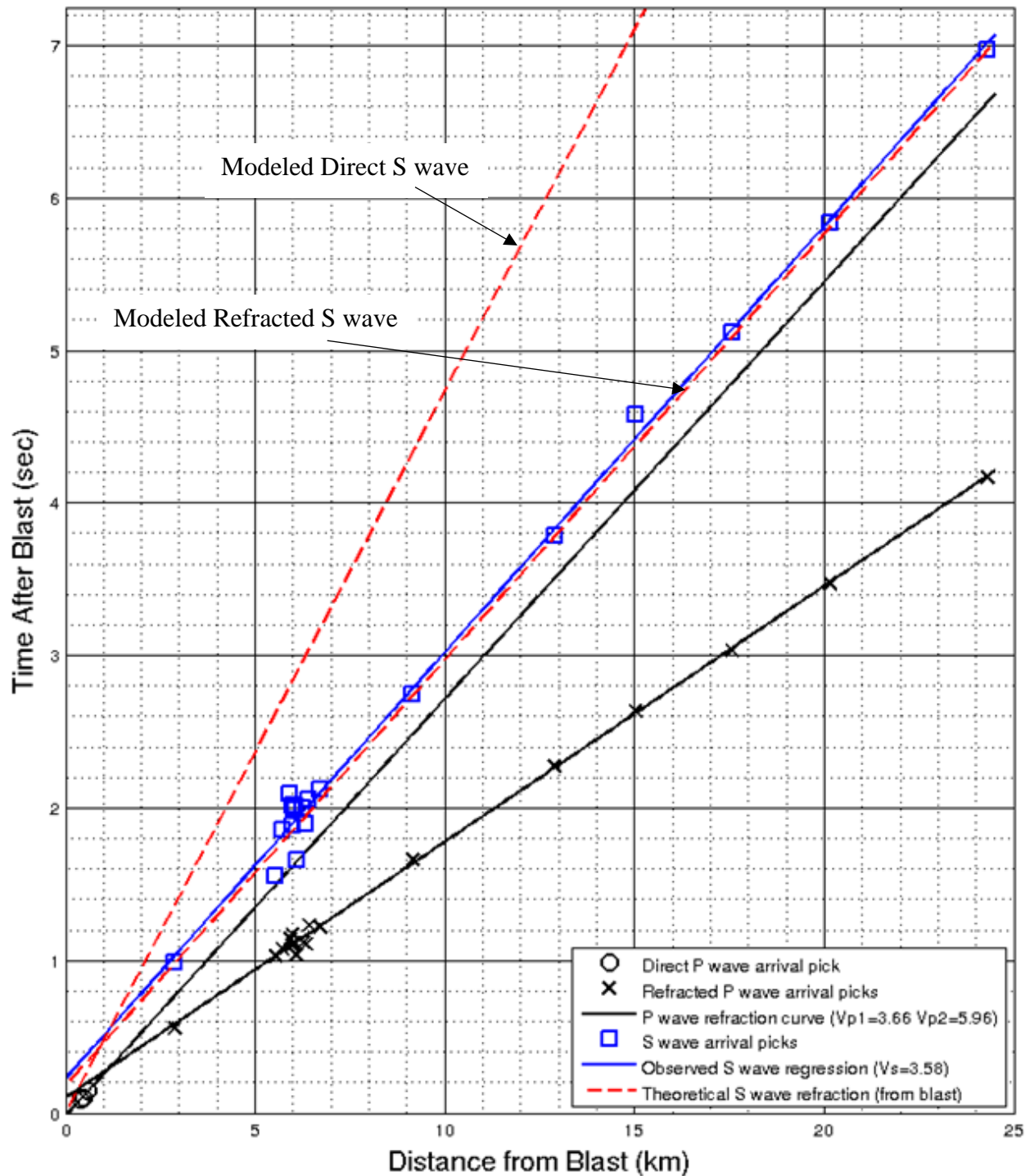


Figure 8-1. Shot 1 P (black) and S (blue) wave travel-time data and least-squares regression line fits. Red dashed lines are theoretical S wave direct and refracted travel-time curves. Calculated body wave velocities are displayed in the legend.

Shot-2 P-wave Refraction Curve with Observed and Theoretical S-wave Regressions

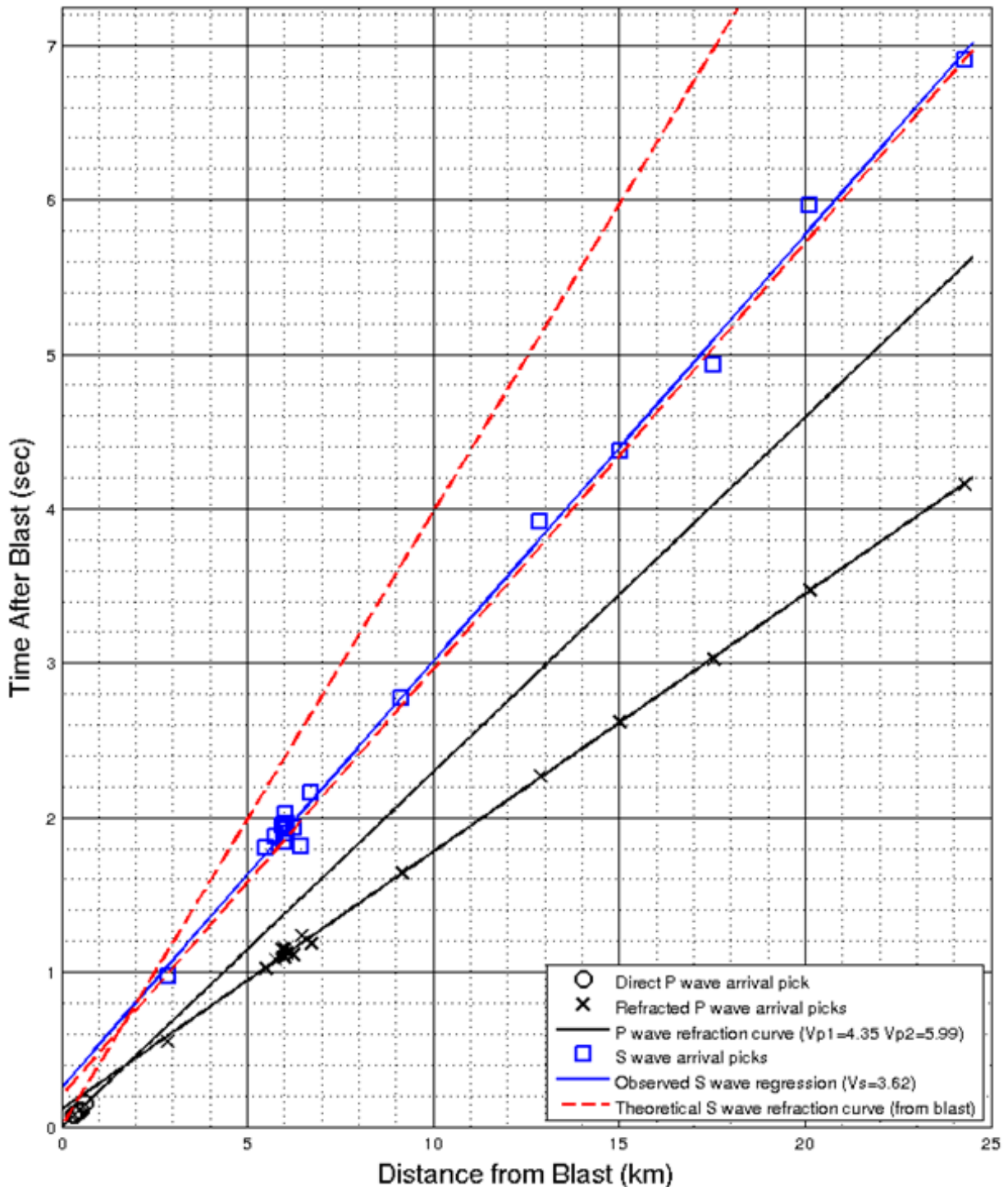


Figure 8-2. Shot 2 P (black) and S (blue) wave travel-time data and least-squares regression line fits. Red dashed lines are theoretical S wave direct and refracted travel-time curves. Calculated body wave velocities are displayed in the legend.

Shot-3 P-wave Refraction Curve with Observed and Theoretical S-wave Regressions

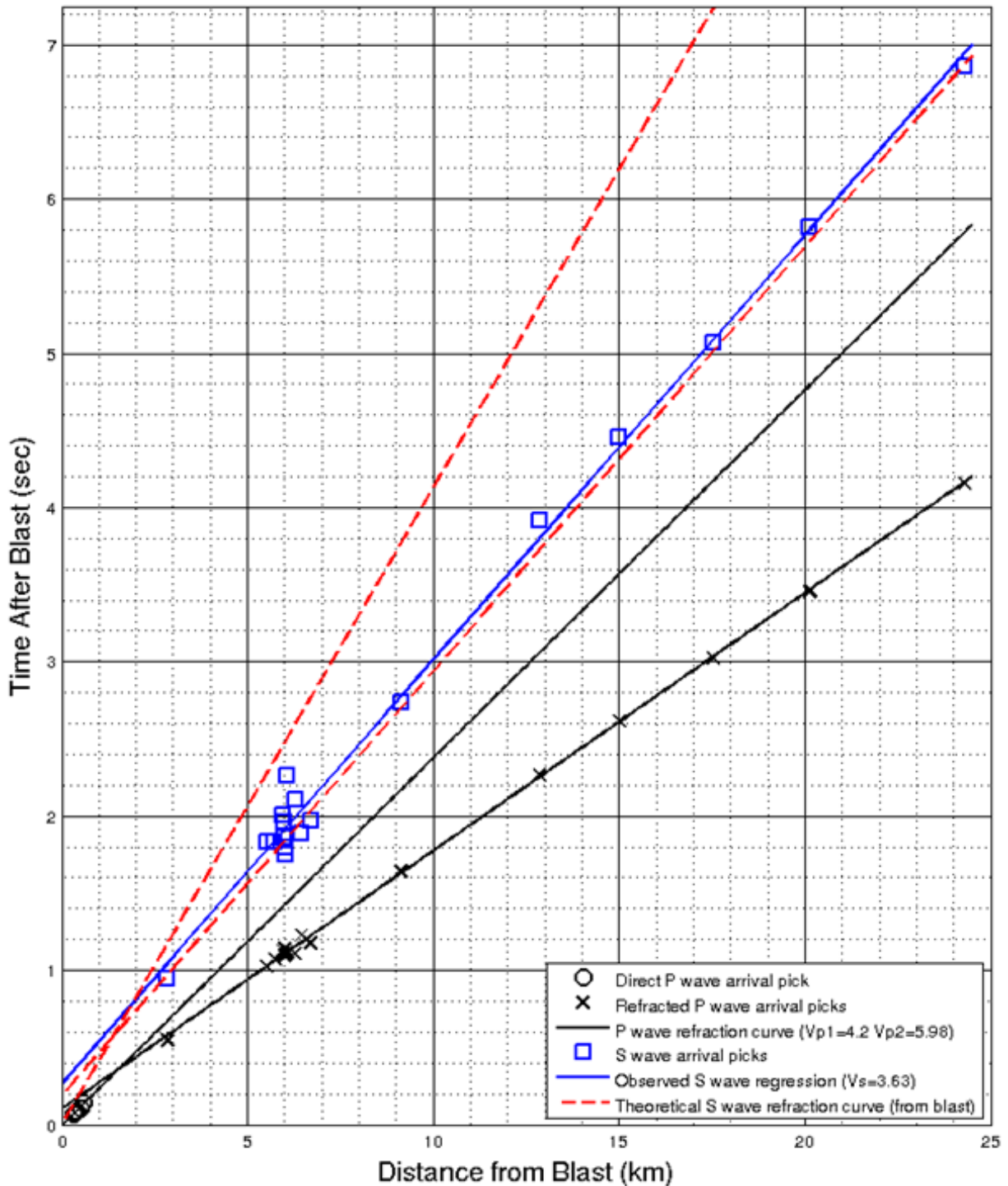


Figure 8-3. Shot 3 P (black) and S (blue) wave travel-time data and least-squares regression line fits. Red dashed lines are theoretical S wave direct and refracted travel-time curves. Calculated body wave velocities are displayed in the legend.

Shot-4 P-wave Refraction Curve with Observed and Theoretical S-wave Regressions

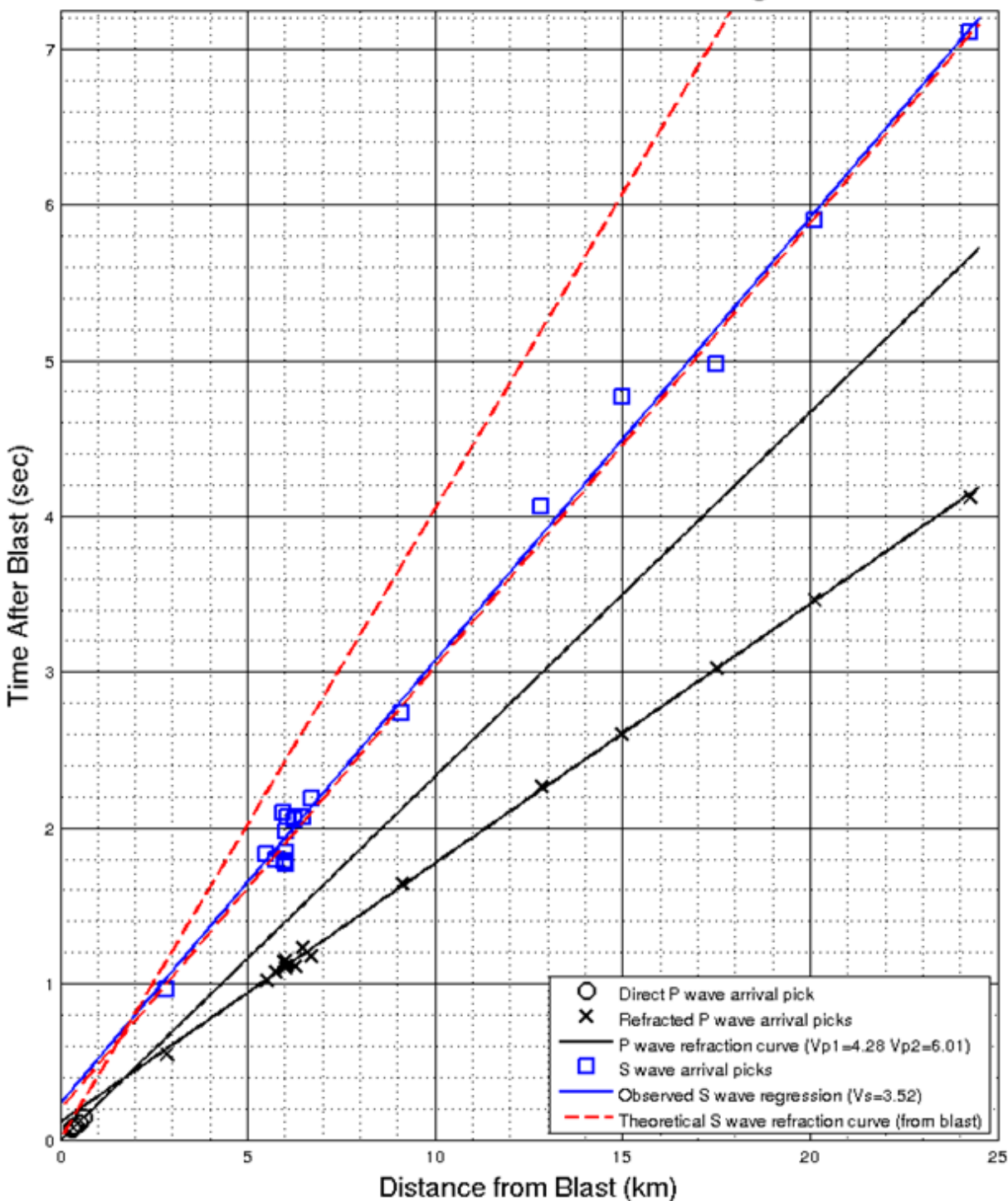


Figure 8-4. Shot 4 P (black) and S (blue) wave travel-time data and least-squares regression line fits. Red dashed lines are theoretical S wave direct and refracted travel-time curves. Calculated body wave velocities are displayed in the legend.

Shot-5 P-wave Refraction Curve with Observed and Theoretical S-wave Regressions

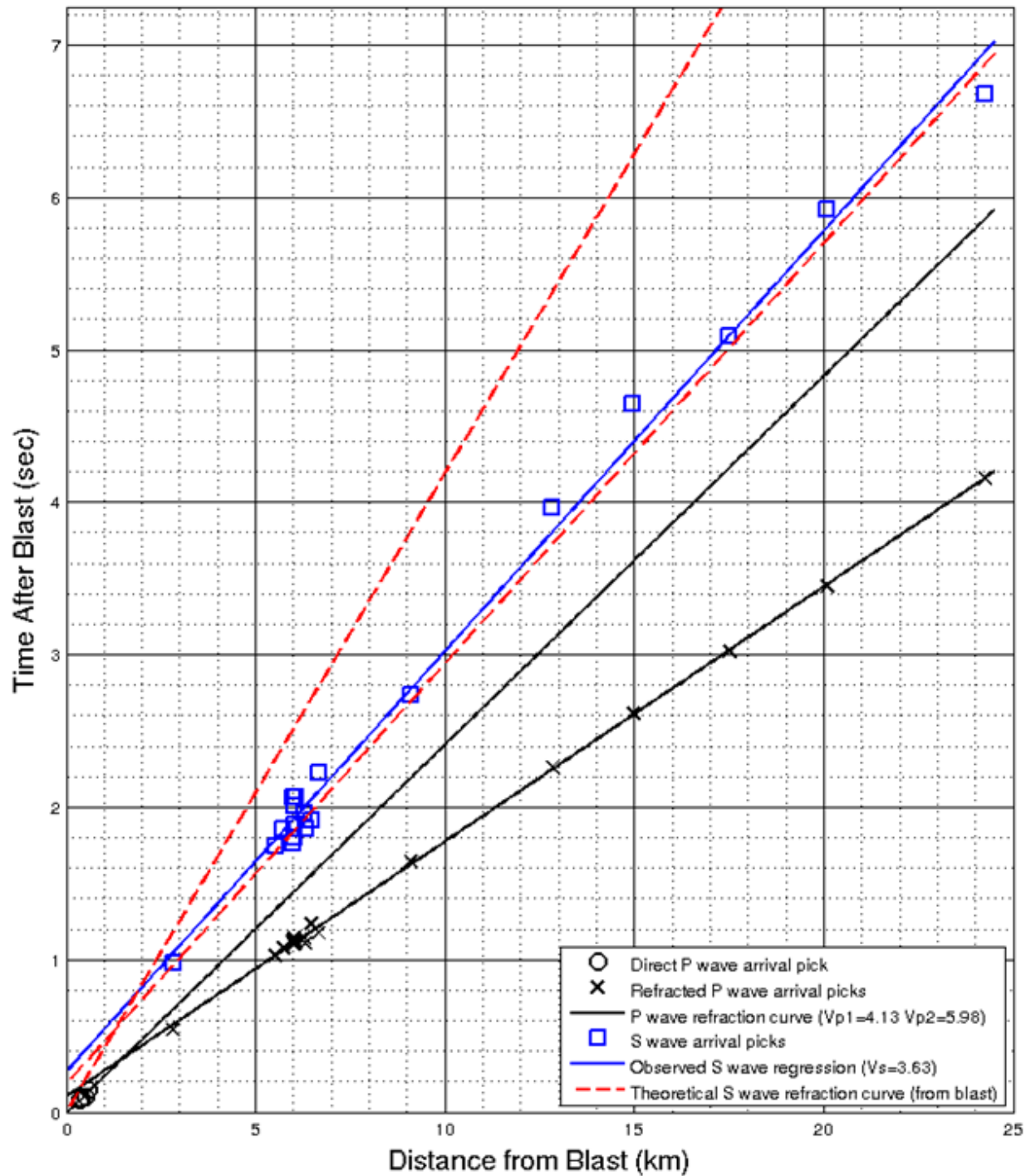


Figure 8-5. Shot 5 P (black) and S (blue) wave travel-time data and least-squares regression line fits. Red dashed lines are theoretical S wave direct and refracted travel-time curves. Calculated body wave velocities are displayed in the legend.

Shot-6 P-wave Refraction Curve with Observed and Theoretical S-wave Regressions

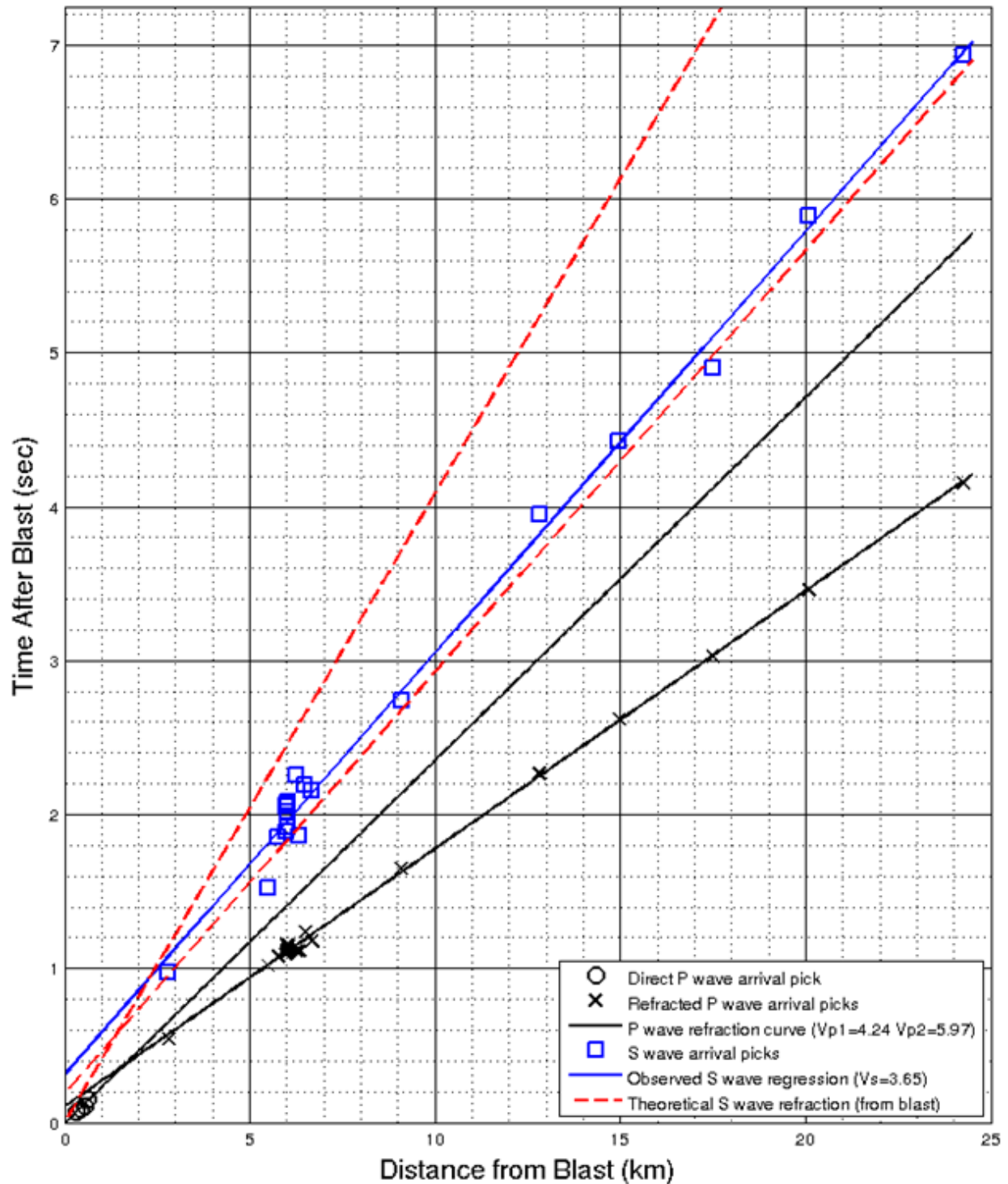


Figure 8-6. Shot 6 P (black) and S (blue) wave travel-time data and least-squares regression line fits. Red dashed lines are theoretical S wave direct and refracted travel-time curves. Calculated body wave velocities are displayed in the legend.

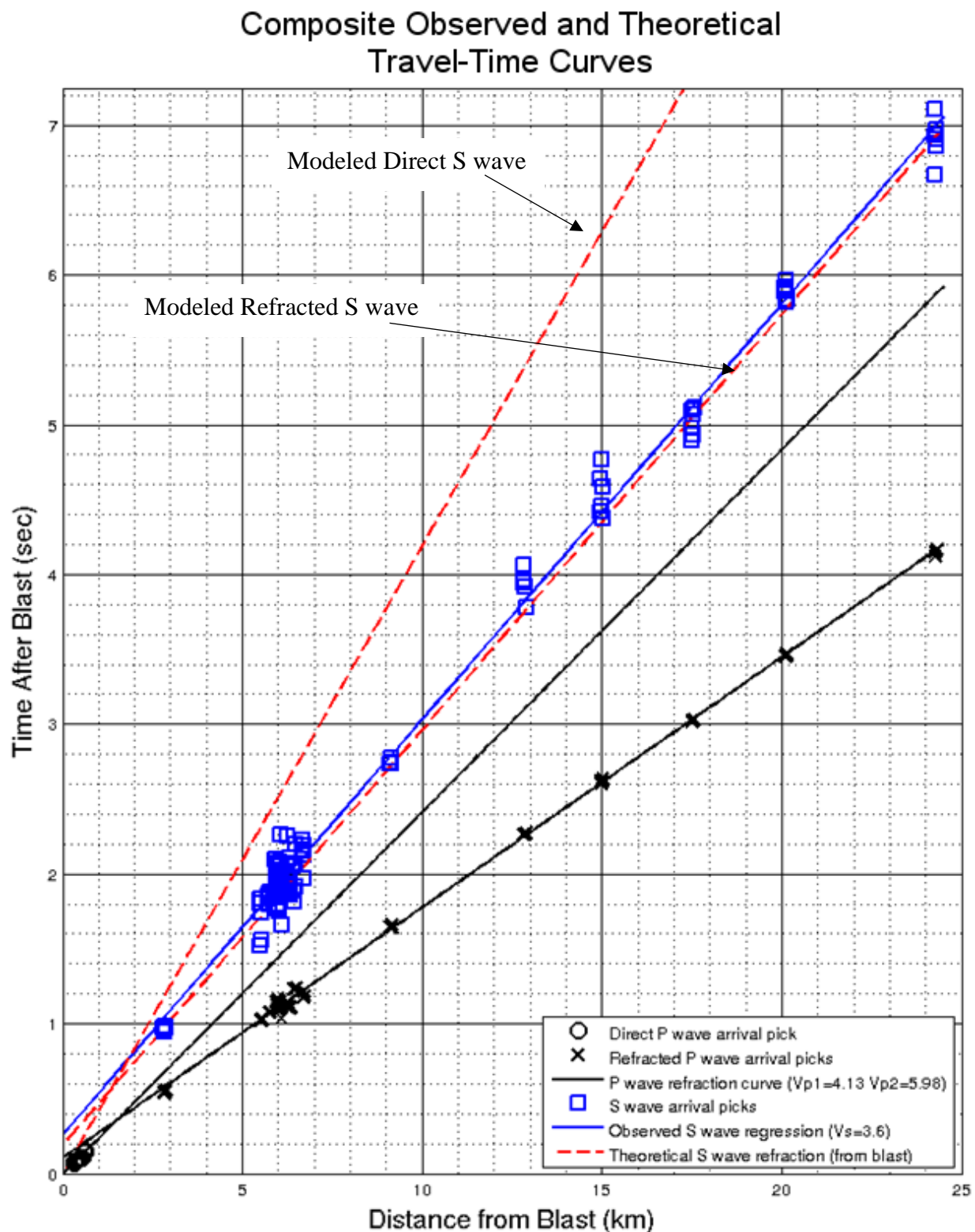


Figure 8-7. Composite P (black) and S (blue) wave travel-time data and least-squares regression line fits. Red dashed lines are theoretical S wave direct and refracted travel-time curves. Calculated body wave velocities are displayed in the legend.

P wave velocities for the layer and half-space and S velocities in the half-space were calculated from the regression fits for each shot, with the values presented in the legend of each figure. In general, the direct P wave velocity observed within the study area is found to be between 4.13-4.35 km/s with the exception of Shot 1, which was calculated to have an anomalously low direct P velocity of 3.66 km/s. Reduced seismic amplitudes and high frequency deficiency resulted in greater picking uncertainty. The refracted P wave velocity is consistent between shots, ranging from 5.96-6.01 km/s. The observed refracted S wave velocity is less consistent between shots, ranging from 3.52-3.65 km/s. Regression fits were made for a composite of travel time data from all 6 shots (Figure 8-7) to reduce measured velocity uncertainty related to a limited number of arrival picks for each shot.

Figure 8-7 shows very little scatter in P wave arrival time picks at the same station (indicated by overlapping symbols at similar distances beyond 7 km), but a higher degree of scatter in the S wave arrival time picks. Further examination is needed to determine if the scatter in S wave picks is related to human-error during arrival time picking or if other factors, such as geology, are affecting the arrival times of the S waves. Except for the cluster of picks near 6 km distance related to the 6 km ring network, the stations lie along a similar azimuth from the test site so an azimuthal radiation pattern is not the cause.

THEORETICAL TRAVEL-TIME CURVES

A velocity model for the region is required to calculate theoretical shear wave travel-time curves from various possible sources. Using the P wave seismic velocities derived from the composite refraction curve (Figure 8-7), the thickness of a flat lying layer over half-space was calculated using the relationship:

$$\tau = 2h \left(\frac{1}{v_{p1}^2} - \frac{1}{v_{p2}^2} \right)^{\frac{1}{2}} \quad (8-1)$$

where $\tau \equiv$ head wave time intercept, $h \equiv$ layer thickness, and v_{p1} and $v_{p2} \equiv$ top layer and half-space P wave velocities, respectively (Stein and Wysession, 2003). We assumed $V_{s1} = V_{p1}/\sqrt{3}$, a standard value for crustal rock, for the layer S wave velocity since direct shear wave arrival-time measurements could not be made. The resulting model is shown in Figure 8-8.

We then estimated the travel-time for a shear wave generated at the explosion source and refracting along the same layer as the P wave using the equation:

$$T_H(x) = \frac{x}{v_{s1}} + 2h \left(\frac{1}{v_{s1}^2} - \frac{1}{v_{s2}^2} \right)^{\frac{1}{2}} \quad (8-2)$$

where $T_H(x) \equiv$ refracted S wave (head wave) arrival time as a function of distance, $x \equiv$ horizontal distance between source and receiver, $h \equiv$ layer thickness, v_{s1} and $v_{s2} \equiv$ top and bottom layer S-wave velocities, respectively (Stein and Wysession, 2003). The theoretical S wave refraction curve was plotted in Figure 8-1 through Figure 8-7 (red dashed line with shallower slope) for comparison to the observed S wave travel-time picks.

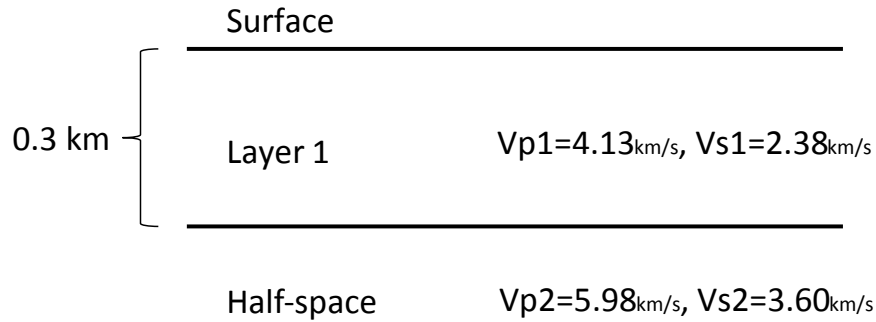


Figure 8-8. Layer over half-space velocity model determined from P and S travel time data near the NEDE2 test site.

We note that Equations 8-1 and 8-2 assume a source at the surface, but the NEDE2 shots were at depths between 12-14 m. This is not an issue though as $2h$ is simply the summation of the source to refracting layer distance, h_1 , plus the refracting layer to receiver distance, h_2 . Since the distances are not equal, $2h$ can be replaced with $h_1 + h_2$. This would make the refracting layer depth at 36.5 m, but this does not change the theoretical travel-time estimates.

DISCUSSION

The theoretical S wave refraction curves (red dashed lines on Figure 8-1 through Figure 8-7 with the shallower slope) represent the modeled S-wave arrival times for an S wave that originates at the source, refracts along a faster velocity boundary, and returns to the surface at the recording station. The theoretical refracted S wave travel-times differ by less than 0.1 seconds from the observed S-wave least-squares regression (Figure 8-7). One possibility for the difference between the observed and theoretical S wave curves is that the V_{p1}/V_{s1} ratio is larger than the ~ 1.73 ratio assumed in the model. We tested ratios ranging from 1.67 to 1.80, values based published models and on core logs from the NEDE1. Using a value of 1.8 increased the theoretical shear wave travel-time by less than 10 msec due to the short travel path in the thin layer. This small amount is insignificant in comparison to the total travel time and error in the S wave arrival picking. The small difference between observed and theoretical travel times suggest the S wave originated at or very near the source, possibly with a delay of up to 0.1 seconds.

We tested a potential S-wave generation from P-to-S phase conversion by reflection or refraction off the lower layer, but the theoretical travel times were much faster than the observed S travel times. With exception of P-to-S conversion off the free surface, the result would be the same for any sort of P-to-S conversion along the travel path, whether it be refraction or scattering. A P-to-S conversion off the free surface would add ~10 milliseconds to the travel time, which would be plausible based on this analysis. Rg-to-S conversion would have to occur within 300 m of the test site to fit the observed S travel times and be a plausible shear wave generation mechanism.

Further analysis may include developing a more sophisticated velocity profile and performing full waveform modeling to match observed arrival times and amplitudes by including refracting layers, topography, and geologic heterogeneity along the travel path in the model.

9. EFFECTS OF WATER SATURATION ON EXPLOSION SEISMIC COUPLING IN INTACT AND FRACTURED GRANITE

ABSTRACT

A series of experiments was conducted in order to define the physical mechanism responsible for the amplitude reduction in fracture zones of previously detonated explosions. Explosions in water-saturated granite were conducted in central New Hampshire in 2011 and 2012. Explosions in dry granite were detonated in Vermont in 2013 (NEDE2). The results of the experiments confirm reduced amplitudes for the explosions in fractured rocks. The amplitude reduction depends on the extent of the damage zone and the pore water content. The frequency dependence of the decoupling ratios is different for dry and water-saturated rocks.

We used the Mueller-Murphy (1971) model (MM71) to calculate spectra of the first and repeat explosions. To calculate spectra in damaged/fractured medium we used elastic moduli calculated using a poroelastic effective medium model. The theoretical spectra for the fractured rock explosions exhibit amplitude reduction at high frequencies and amplitude increase at low frequencies, which is not observed in the empirical data. To explain the amplitude reduction in the entire frequency range, we created a “hybrid” medium model with the original unfractured medium outside the elastic radius and reduced elastic moduli inside the elastic radius. This model predicts reduced amplitudes at all frequencies and qualitatively agrees with the observations, although there are some slight differences between the estimated and observed ratios. Due to uncertainties in the damage zone configuration, a simplified model (e.g. MM71) may not exactly reproduce the explosion source; however using the models with a combination of the parameters can provide bounds on the resulting spectral ratios.

INTRODUCTION

Conducting explosions in low coupling (porous or damaged) medium can pose difficulties for nuclear monitoring, because a low coupling medium may result in erroneous seismic yield estimates. Porous rocks can be natural (e.g. tuffs and alluvium) or man-made (e.g. fracture zones from previous explosions). For example, data from nuclear explosions conducted above the water table in tuffs and alluvium at the former Nevada Test Site show that the magnitudes are lower than for the explosions conducted below the water table by on average 0.5 ± 0.25 magnitude units (e.g. Murphy *et al.*, 2011). Evidence of lower amplitudes from the “repeat shots”, i.e., explosions conducted in the fracture zones created by previous explosions, was reported for some of the nuclear tests from the Degelen Mountain Testing area at the Semipalatinsk Test Site (e.g. Sokolova, 2008).

In order to verify the amplitude reduction for the “repeat shots” a geophysical field program, designated the Fracture Decoupling Experiment (FDE), was conducted in 2011-2012 in central New Hampshire. The objectives of the FDE also included quantification of the effect in terms of a “decoupling factor” as a function of frequency and defining the physics responsible for the reduction. The experiment involved detonating a series of chemical explosions accompanied by booster shots (0.454 kg Comp B) in closely located boreholes. The New Hampshire explosions were conducted below the water table in water-saturated granite. Additional repeat shots in dry granite in Barre, VT, were conducted in late June of 2013 (NEDE2). Comprehensive characterization of the rock properties before and after the explosions was performed. In this chapter, we provide a quantitative analysis of the differences in seismic amplitudes and spectra between explosions conducted in saturated and dry granitic rocks.

EXPERIMENT IN WATER-SATURATED GRANITE

Weston Geophysical Corp. conducted a series of explosions in granitic rock in central New Hampshire as a part of the Fracture Decoupling Experiment (FDE) in 2011 and 2012 (Stroujkova *et al.*, 2013). The rocks at the site are represented by granodiorites and pegmatites. The intact rock matrix has low porosity ($<0.5\%$), however the rock is penetrated by a network of water-filled fractures. Due to excessive precipitation preceding both phases of the experiment, the fractures and rocks at the site were saturated with water.

The FDE involved detonating three co-located pairs of explosions. The first explosions of each pair were detonated in virgin rocks; the second explosions were subsequently detonated in the fracture zones created by the first explosions. The parameters of these explosions are summarized in Table 9-1.

Phase I of the experiment was conducted in October of 2011 (Stroujkova *et al.*, 2013). The first virgin shot FD1 (231.8 kg) resulted in significant containment failure and formation of a crater with a diameter of approximately 12 m. Subsequently two smaller shots with the same yields (FD2 and FD3, Figure 9-1b) were conducted. Both FD2 and FD3 holes were drilled to a depth of 14.94 m. The first, FD2, was in virgin (undamaged) rock with very few native fractures 35 m from the damaged test region. The second, FD3, designated the “damage zone shot,” was located approximately 6.5 m from the FD1 borehole.

During Phase II of the FDE (Fall of 2012) we detonated 3 co-located pairs of explosions (the first explosion detonated in virgin rocks, the second explosion in the fracture zone created by the first explosion). In addition four calibration explosions were detonated near two pairs of explosions. Phase II explosions were conducted at a site located approximately 150 m away from the Phase I site. Explosions FD11 and FD12 were conducted in separate boreholes (22.9 cm in diameter) located 20 m apart (Figure 9-1c). Parameters of these explosions are shown in Table 9-1. The charges were custom made by placing ANFO/emulsion mixture into cardboard tubes 20 cm in diameter with Comp B boosters. The calibration shots were conducted at the bottom of the boreholes located approximately 1.8 m from their respective shot holes for larger explosions.

Extensive site characterization, including cross-hole seismic tomography and borehole logging, was conducted before and after the first series of shots for both Phase I and II experiments. The objective of the survey was to measure the change in rock properties resulting from the blast. The logging included caliper log, optical/acoustic televiewer, and sonic log. Cores were extracted from a core hole located 1.8 m from the FD11 shot hole. The pre-shot velocities and other rock properties are presented in Table 9-2.

Table 9-1. Explosion characteristics.

Shot	Borehole depth, m	Centroid depth, m	sDOB, m/kt ^{1/3}	Borehole diameter, cm	TNT equiv yield, kg*	First explosion (when applicable)		
						Shot	TNT equiv yield, kg*	Distance, m
Saturated rocks								
FD2	14.94	14.30	429	20.32	37.0	-	-	-
FD3	14.94	14.22	425	20.32	37.4	FD1	185.4	6
FD11	17.99	16.36	349	22.86	102.9	-	-	-
FD12	16.77	16.16	449	22.86	46.5	-	-	-
FD21	17.99	16.36	349	22.86	102.9	FD11	102.9	0
FD22	16.77	16.16	449	22.86	46.5	FD12	46.5	1.8
Dry rocks								
NEDE2-2	14.25	13.50	331	22.2	68.1	-	-	-
NEDE2-5	14.02	13.31	326	22.2	68.1	Shot 4	98.1	1
NEDE2-6	13.51	12.80	313	22.2	68.1	Shot 5	165.5	1

* The TNT equivalency conversion factors are: HANFO/TNT - 0.8, Comp B/TNT - 1.35

Table 9-2. Rock properties from laboratory measurements.

Site	Rock type	v_p , m/s	v_s , m/s	ρ , kg/m^3	Compressive strength, MPa	Water saturation
Barre, VT	Granite	4600	2750	2600	275	Mostly dry
Groton, NH	Metamorphically altered pegmatites and granodiorites	5100	2750	2700	120	Saturated

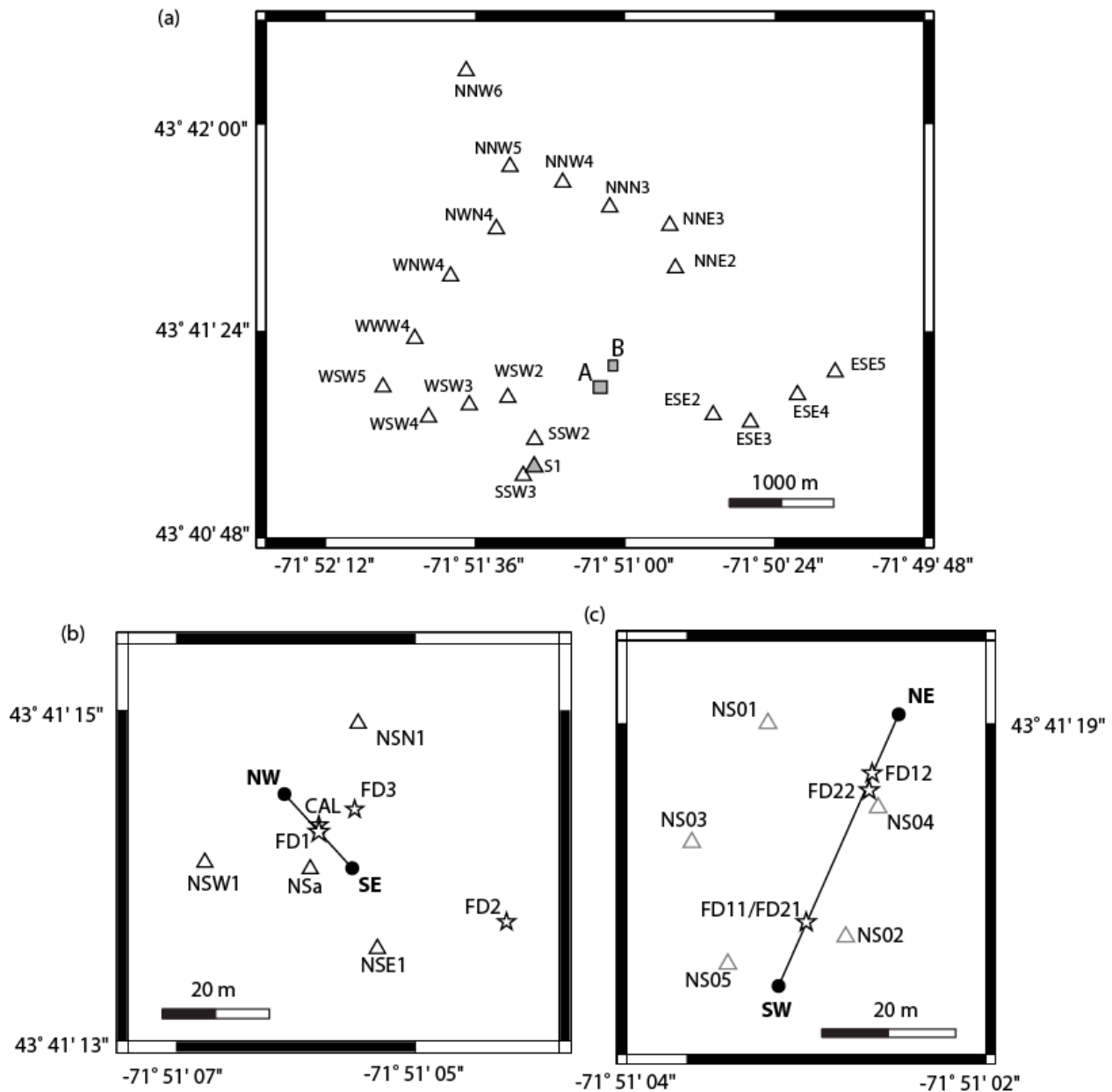


Figure 9-1. (a) The near-source network located on Spruce Ridge, New Hampshire. The open triangles show the station locations for the Phase II experiment. The shaded triangle shows Station S1 from Phase I experiment. The shaded rectangles A and B are enlarged in 1b and 1c respectively. (b) Enlarged view of the Phase I testing area (Shots FD1, FD2, and FD3), showing the near-field accelerometers (triangles) and the explosions (stars). Also shown NW-SE line connecting the boreholes used for tomography. (c) Enlarged view showing of the Phase II testing area (Shots FD11, FD12, FD21, and FD22), showing the near-field accelerometers (triangles) and the explosions (stars). NE-SW line connecting tomographic boreholes is also shown. Phase I and Phase II testing areas are located approximately 130 m from each other.

Figure 9-2 shows the tomographic cross-section between boreholes NW and SE (Figure 9-1b). There is a low-velocity feature in the pre-shot cross-section dipping from the NE to the SW. Based on the borehole survey this dipping fracture zone provides a conduit for the ground water. We observe significant velocity reduction after FD1 (pre-shot $v_p \approx 4000\text{--}6000$ m/s, post-shot $v_p \approx 1500\text{--}4000$ m/s) to a depth of at least 20 m. The tomography results confirmed that the damage from FD1 extends below the shot, as well as laterally significantly beyond the crater zone. Therefore, the designated damage zone shot (FD3) was detonated in the extensive damage zone.

During Phase II, the extent of damage from the first explosions was significantly different. The tomographic cross-section in Figure 9-3 shows changes in P -wave velocity after Shots FD11 and FD21 compared to the pre-shot velocity. The areas of greater damage are not spherical and appear to correlate with the zones of pre-existing weaknesses. For instance, mica-rich layers with reduced strength (50 MPa) identified from the core analysis can be seen as the areas of greater damage below and above FD21 working point. The post-shot velocity reduction is rather subtle in comparison with the velocity reduction created by Shot FD1 (Phase I). As a result the amplitude decrease in the repeat shots is less pronounced for the Phase II shots.

The explosions were monitored by a network of seismic instruments located from near-field to local distances. The intermediate-range stations were located at distances between 0.6–1.6 km (Figure 9-1a). Ten accelerometers were installed in close proximity to the explosions to record the near source ground motions (Figure 9-1b) for the Phase I experiment and Figure 9-1c for the Phase II experiment). All instruments recorded three components (3C) of motion at a sampling rate of 1000 samples per second (sps) using Reftek 130 (RT130) data loggers.

Figure 9-4a shows a comparison between FD2 (46.3 kg, virgin rock) and FD3 (46.8 kg, fractured zone) shots recorded by Station S1 located approximately 600 m away from the source. The P -wave amplitudes produced by the FD2 explosion exceed the amplitudes produced by FD3 by a factor of 2.5. Notice however, that the R_g amplitude for FD2 is almost the same as for FD3. A similar effect is observed for the Phase II explosions, however it was less pronounced. Figure 9-4b shows FD11 and FD12 waveforms recorded at Station SSW2 located 600 m from the source. The waveforms are almost the same with only 5% average reduction for the second explosion. The waveforms for FD21 and FD22 also look very similar (Figure 9-4c) with an average amplitude reduction of approximately 20%.

Figure 9-5 shows the spectra and the spectral ratios computed for the three explosion pairs. The FD2 and FD3 spectra are similar in the low-frequency interval (**Figure 9-5a**); however the FD2 spectrum has a slightly higher corner frequency than FD3. Consequently, their amplitude ratios asymptotically approach unity at low frequencies, and reach a factor of 3 between 40 and 100 Hz. Above 100 Hz the amplitudes and ratios become spurious and show larger scatter. FD11-FD12 and FD21-FD22 pairs also show a slight reduction in the corner frequency for the second shots, however it is less pronounced than for the FD2-FD3 pair.

Our results are consistent with the SPE-N results. According to Townsend *et al.* (2012) the SPE-N experiment was conducted below the water table. The first (SPE-N-2) and the second (SPE-N-3) explosions were approximately the same yields and were overburied. Their amplitudes were very close, similar to our Phase II shots.

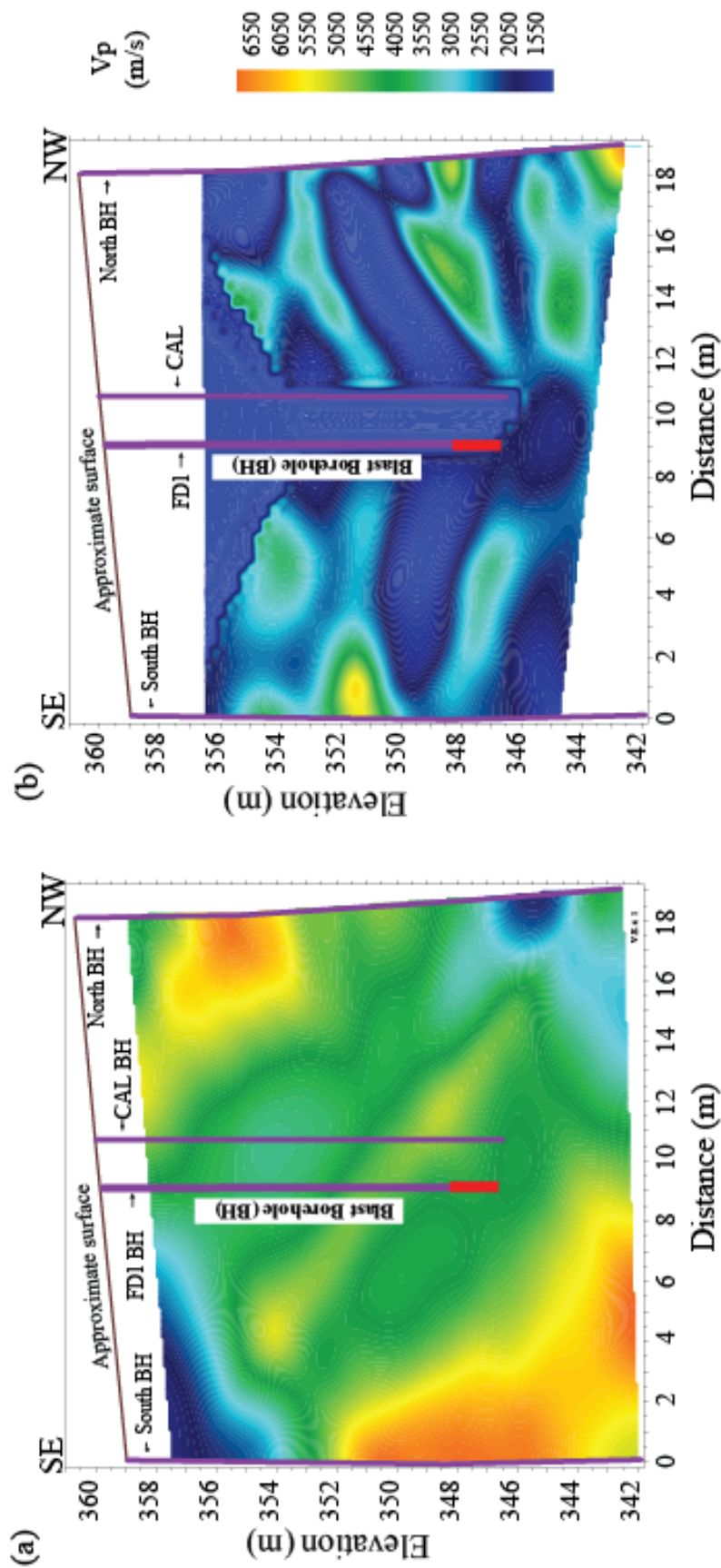


Figure 9-2. Seismic tomography results (Phase I) showing P -velocity (a) before and (b) after FD1 explosion along the SE-NW borehole cross-section (Figure 9-1b).

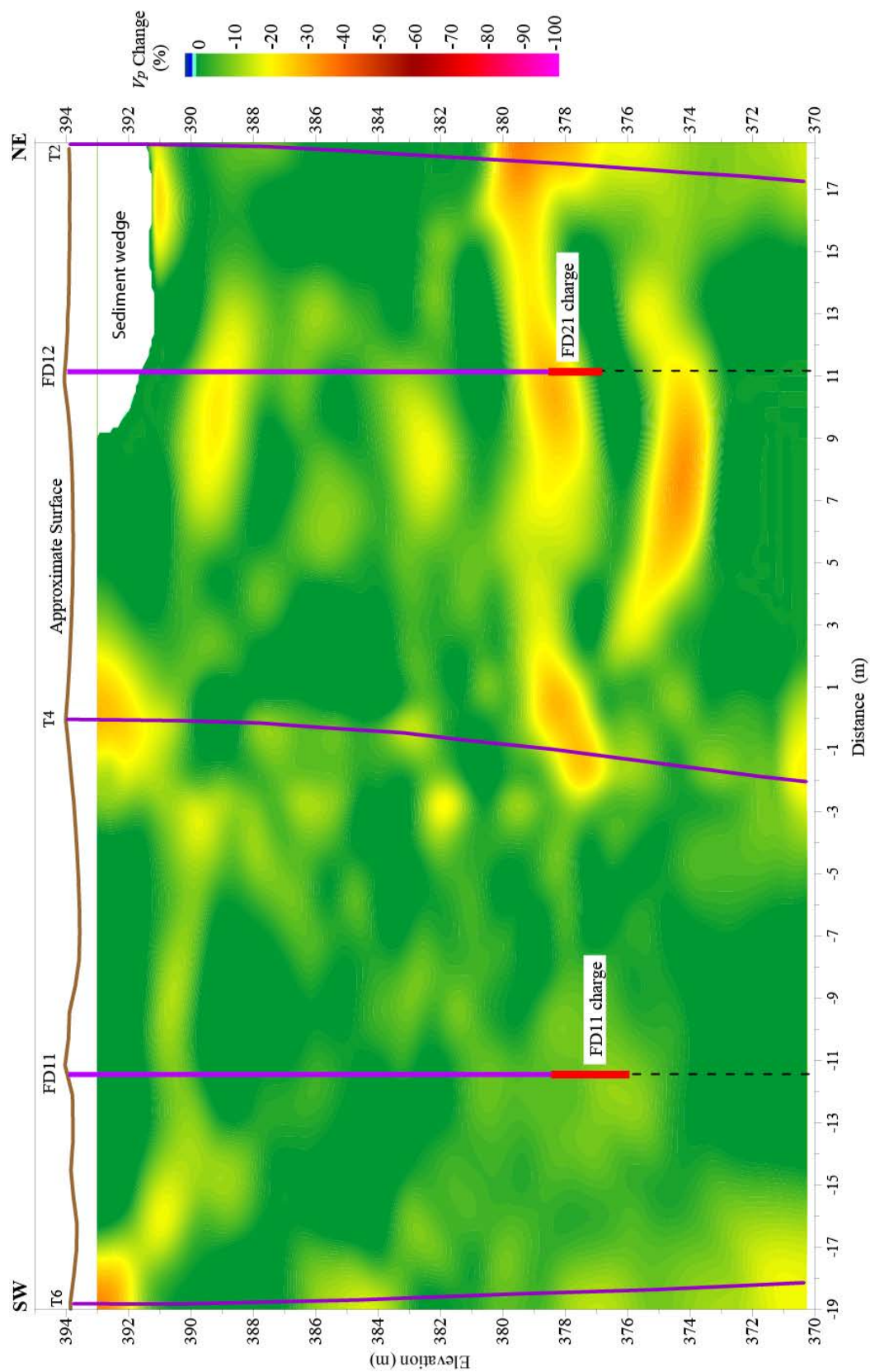


Figure 9-3. Seismic tomography results (Phase II) showing the changes in P -velocity (in percent) after FD11 and FD21 explosions along the SE-NW borehole cross-section (Figure 9-1c).

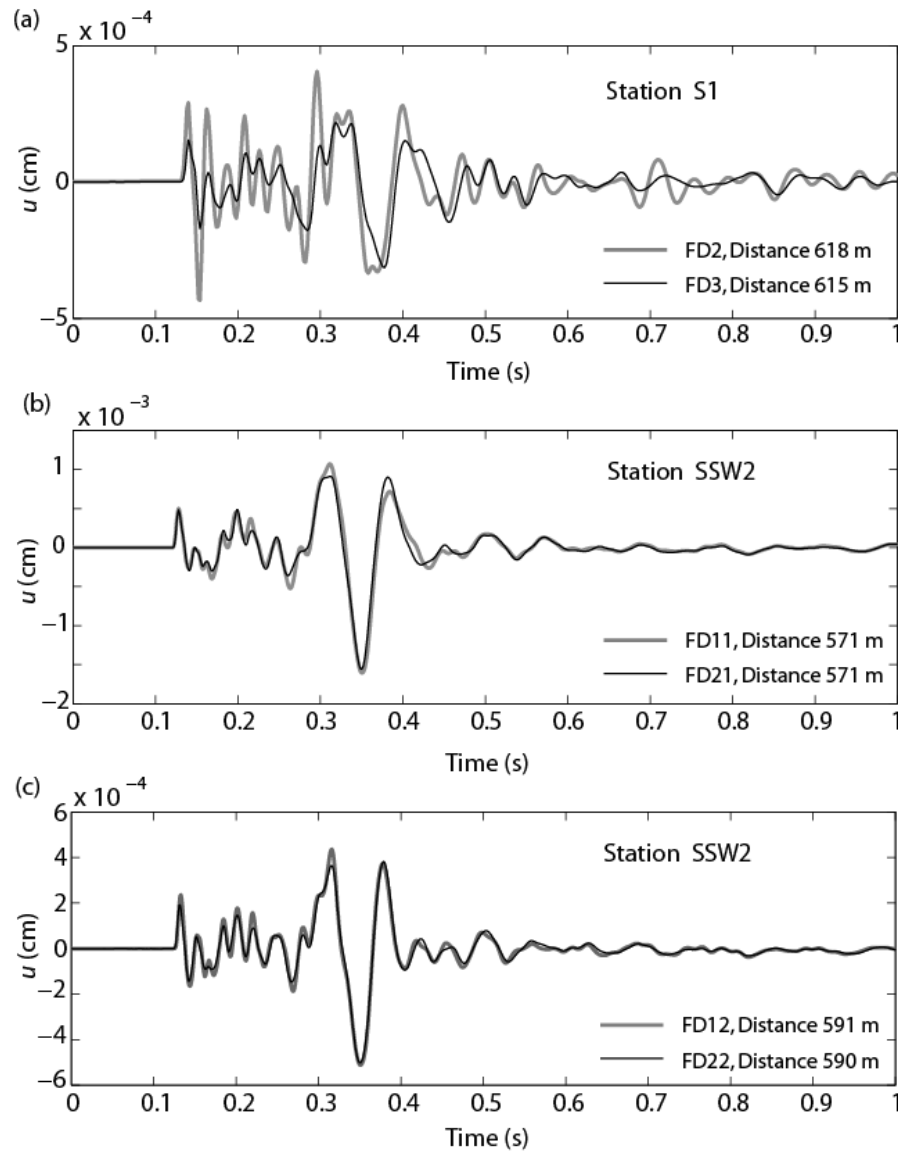


Figure 9-4. Examples of the vertical component waveforms from the co-located explosions conducted in NH recorded approximately 600 m from the sources. (a) Shots FD2 and FD3 recorded by station S1. (b) Shots FD11 and FD12 recorded by station SSW2. (c) Shots FD12 and FD22 recorded by station SSW2. Stations S1 and SSW2 are located approximately 160 m from each other as shown in Figure 9-1a.

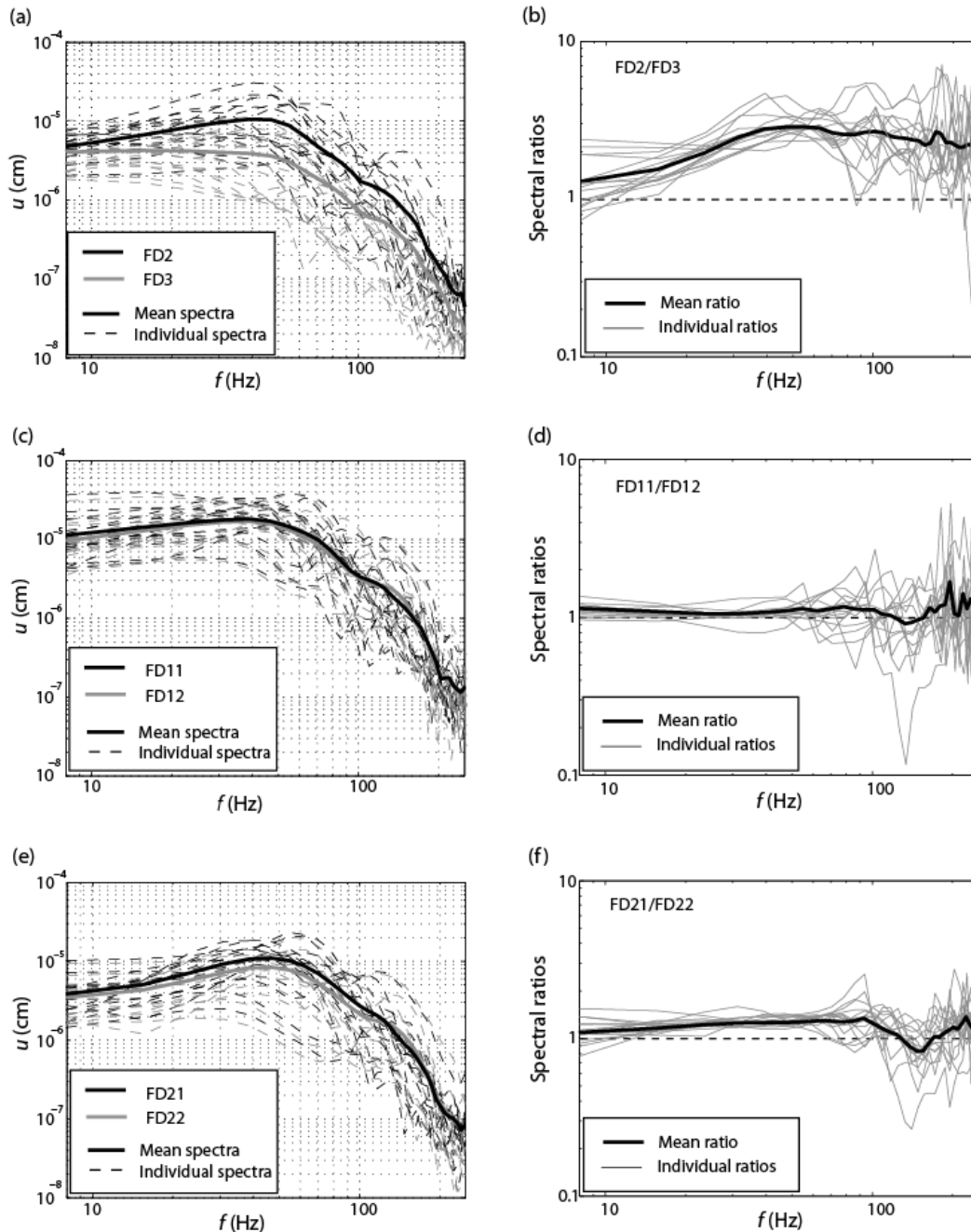


Figure 9-5. (a) FD2 and FD3 spectra computed for the intermediate range network stations shown in Figure 9-1a. *The dashed lines show individual spectra, the solid lines corresponds to the mean spectrum.* (b) Spectral ratios between FD2 and FD3 calculated using the same set of stations as in (a). (c) FD11 and FD12 spectra calculated for the intermediate range network (stations shown in Figure 9-1a). (d) Spectral ratios between FD11 and FD12 calculated using the same set of stations as in (c). (e) FD12 and FD22 spectra calculated for the intermediate range network. (f) Spectral ratios between FD12 and FD22 calculated using the same stations as in (e).

EXPERIMENT IN DRY GRANITE

The first part of the New England Damage Experiment (NEDE) was conducted in July of 2008 (NEDE1; e.g. Stroujkova *et al.*, 2012); the second part was completed in June of 2013 (NEDE2; Chapter 2). The main purpose of the experiment was to study shear wave generation due to explosives with different velocities of detonation (VOD). The experiment was conducted at the Rock of Ages Quarry located in Barre, VT. The rock at the site is composed of solid relatively low fracture density granite with two different sets of joints: nearly vertical joints oriented approximately N30°E (defining a rift direction) and sheeting joints that follow the topography (Richter, 1987). The rift-parallel fractures cause strong (up to 20%) seismic velocity anisotropy (e.g. Martin *et al.*, 2011b).

In this chapter, we discuss reshooting of two of the explosion damage zones created during the NEDE1. Shots NEDE2-5 and NEDE2-6 (HANFO explosions, 68.1 kg of TNT equivalent) were reshoots of the NEDE1 122 kg TNT equivalent HANFO explosion (AN122 in Stroujkova *et al.*, 2012) and NEDE1 122 kg TNT equivalent of Composition B (Comp B) explosion (CB122 in Stroujkova *et al.*, 2012), respectively. In addition, a control explosion (NEDE2 68.1 kg TNT equivalent HANFO) was detonated in undamaged granite.

No tomographic survey was performed for this experiment. Instead, extensive coring was completed before and after the NEDE1 shots in order to delineate damage zones (e.g. Stroujkova *et al.*, 2013; Martin *et al.*, 2011b). The pre-shot cores showed few native fractures, while the post-shot cores show micro- and macro-fracturing surrounding the source region. The fracturing caused significant impact on physical properties, including acoustic velocity reductions on the order of 20% after the explosions over a 5 m interval surrounding the working point (e.g. Martin *et al.*, 2011b).

Figure 9-6a shows *P*-wave velocities measured using pre- and post-shot core samples within 1 m from the explosions. Core hole CH-5 is located 0.61 m from AN122 and core hole CH-4 is located 0.51 m from CB122. Post-shot *S*-wave velocities are shown in Figure 9-6b. There is a significant velocity reduction surrounding the interval corresponding to the explosive column. Some data points are missing, because the velocities could not be measured due to severe damage to the rock. The lowest value of the compressional velocity (along the fast direction of anisotropy) that could be measured in CH-4 hole is 3171 m/s, with the corresponding velocity along the slow direction of 2582 m/s. Measured shear wave velocities are 1817 m/s (fast direction) and 1667 m/s (slow direction). Notice that the extent of the reduced velocities due to micro-fracturing for the HANFO shot is greater than for the Comp B shot. In addition, a number of long radial and rift-parallel fractures were found during extensive drilling near AN122.

Post-shot porosity measurements were made for the core extracted from the core hole CH-3 drilled at a distance of 0.51 m from Shot AN61 (61 kg of HANFO, DOB=11.3 m, Stroujkova *et al.*, 2013). The measured porosity due to microfracturing at the shot depth in CH-3 is approximately

2 – 2.5 %, corresponding to the measured compressional velocity (fast direction) of 3264 m/s and 2742 m/s (slow direction), and the measured shear velocity of 1786 m/s (fast direction) and 1599 m/s (slow direction). These values are in a good agreement with the minimum velocity measured in the CH-4 hole. The porosity measurements were made for an intact sample with no macrofractures. *In situ* rocks surrounding the explosions had significant macro fractures (radial and rift-parallel), which likely contributed to the effective porosity of the medium sampled by the passing wave.

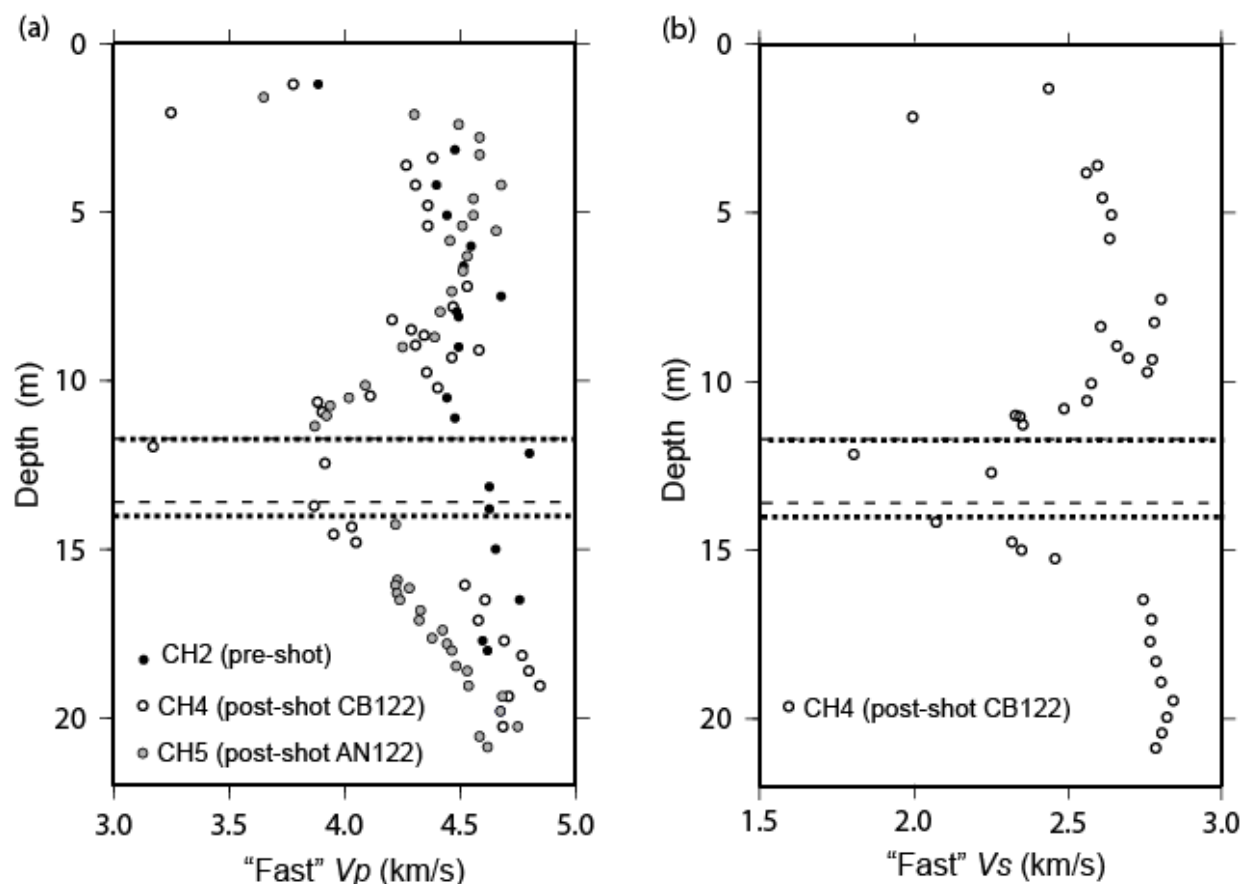


Figure 9-6. a) Pre- and post-shot *P*-wave velocities measured from the cores. Black circles show the pre-shot velocities measured for core hole 2 (CH2), the grey circles show the velocities measured after the AN122 shot in CH5 hole located 0.61 m from the shot hole, the open circles show the post-shot (fast) velocities (Shot CB122) for core hole CH4 located 0.51 m from the shot hole. Due to strong anisotropy, the seismic velocities along the rift axis are 10-20% higher than the velocities across the rift axis. For clarity only the fast velocities are shown, however the slow velocities exhibit the same features. b) Post-shot (fast) *S*-wave velocities (Shot CB122) for the core hole CH4.

We note that during NEDE2 the rock at the site was not completely dry because of rain in the previous weeks. The sub-horizontal sheeting joints described earlier were acting as conduits for the surface run-off and caused some problems with other explosions also conducted at the site. However the boreholes for the explosions described in this chapter had minimal amounts of water removed and remained dry for an extended period of time after pumping. Therefore we believe that there was significant air-filled porosity in the damage zones left by the previous

explosions. As evidence, drilling the reshoot NEDE2-5 hole produced steam from a core hole 7 m from the NEDE1 AN122 shot point. The steam was generated from using water to cool the rotary hammer bit and reduce dust production during drilling.

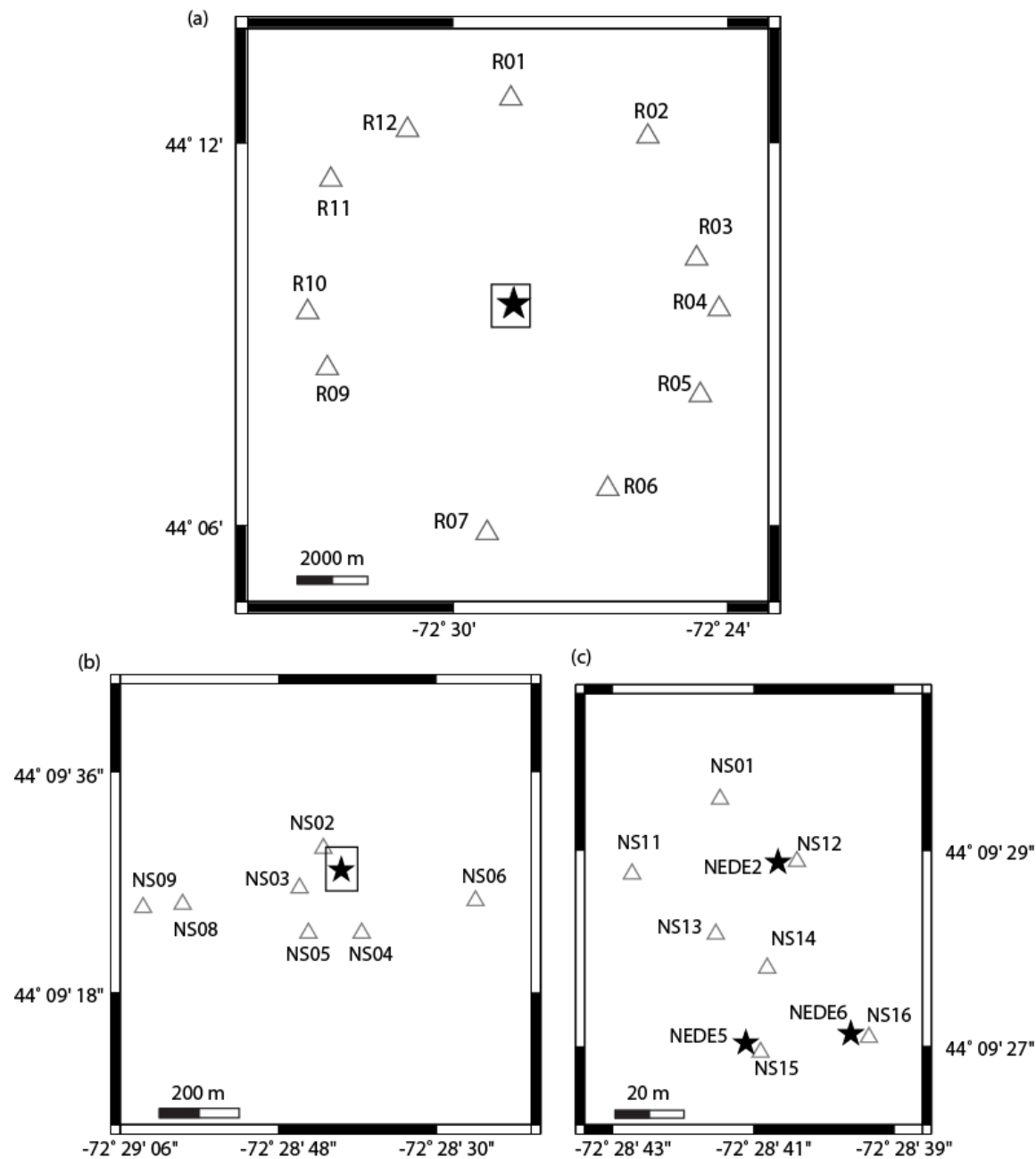


Figure 9-7. (a) The 6 km circle network around the NEDE2 test site at the Rock of Ages Quarry located in Barre, VT. The open triangles show the station locations. The rectangle shows the area enlarged in Figure 9-7b. (b) Enlarged view of intermediate range stations. The rectangle shows the testing area enlarged in Figure 9-7c. (c) Enlarged view of the testing area showing the near-field accelerometers (triangles) and the explosions (stars).

A seismic network was installed to monitor the experiment. Sixteen accelerometers were installed between 3 and 150 m from the explosions to record the near source ground motions. The intermediate range stations were located at distances between 0.3–0.6 km (**Figure 9-7b**). Additionally a circular network with 6 km radius was deployed to examine source radiation pattern effects. All instruments recorded three components (3C) of motion at a sampling rate of 1000 sps.

Figure 9-8 shows a comparison between the virgin and the fractured rock shots recorded by Station NS09 located approximately 500 m from the sources. The *P*-wave peak-to-peak amplitudes produced by the NEDE2-2 explosion exceed the NEDE2-5 amplitudes by a factor of 1.64 (Figure 9-8a). The amplitude reduction for NEDE2-6 is slightly less significant (factor of 1.24) as shown in Figure 9-8b. The average peak-to-peak amplitude ratio computed for the entire network is 1.88 for the NEDE2-2 / NEDE2-5 pair, and 1.49 for the NEDE2-2 / NEDE2-6 pair.

Figure 9-9 shows the spectra and spectral ratios between the virgin rock shot and the reshoots. NEDE2-2 amplitudes exceed NEDE2-5 and NEDE2-6 amplitudes at all frequencies (Figure 9-9a,c). The amplitude ratios are between 1 and 2 at low frequencies, and exceed 2 at the corner frequency and above. The amplitude reduction for Barre explosions is more uniform through the entire frequency band and does not fall to 1 at low frequencies, as was observed for the repeat explosions in water-saturated rocks. We also observe that the amplitude reduction by a factor of 2 is observed between NEDE2-2/NEDE2-5 explosions, even though the damage from the previous explosion was not as extensive and did not cause cratering.

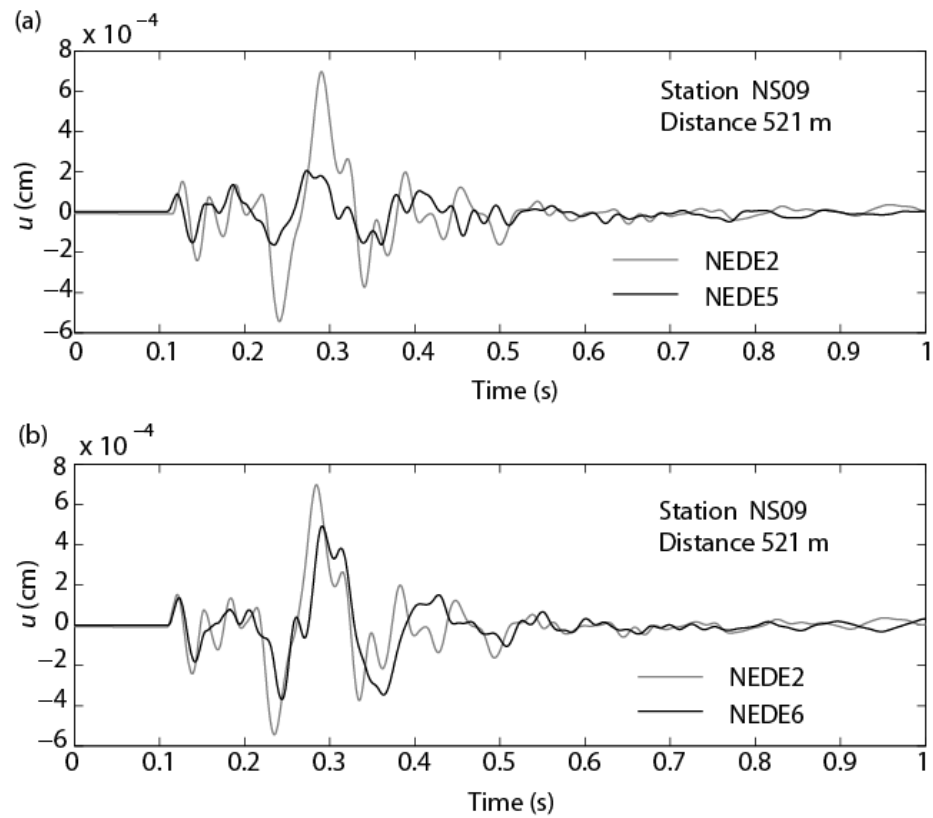


Figure 9-8. Waveform comparison between the NEDE2 virgin and fractured rock explosions conducted in Barre, VT recorded by Station NS09. (a) Shots NEDE2-2 and NEDE2-5. (b) Shots NEDE2-2 and NEDE2-6.

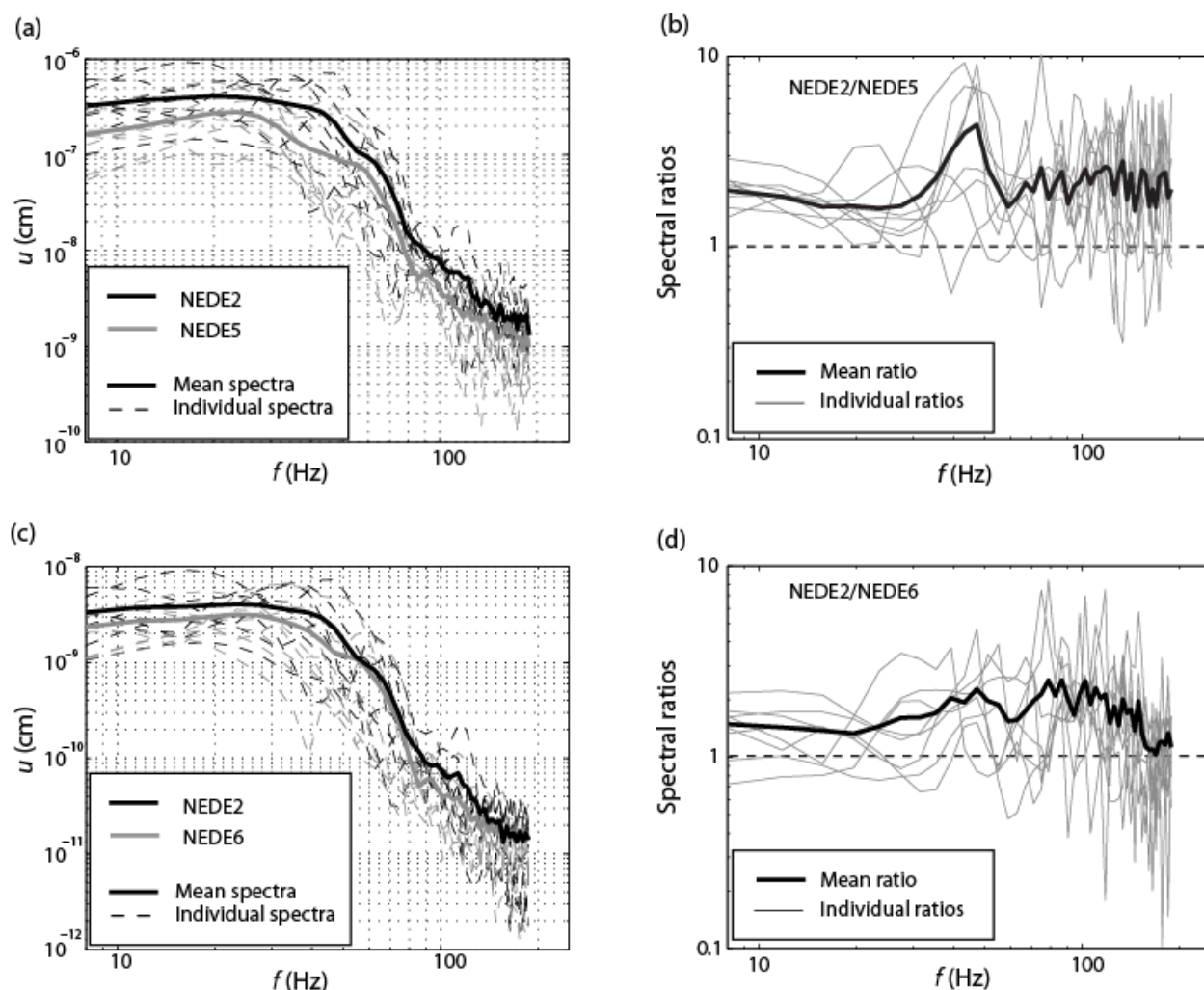


Figure 9-9. (a) NEDE2-2 and NEDE2-5 spectra computed for the 6 km circle stations shown in Figure 9-4a. *The dashed lines show individual spectra, the solid lines corresponds to the mean spectrum.* (b) *Spectral ratios between NEDE2-2 and NEDE2-5 calculated using the same set of stations as in (a).* (c) NEDE2-2 and NEDE2-6 spectra calculated using the same set of stations as in (a). (d) *Spectral ratios between NEDE2-2 and NEDE2-6.*

DISCUSSION

Underground explosive detonations cause rock fracturing, resulting in increased porosity, and reduced seismic velocity and yield strength. These parameters are coupled; therefore a comprehensive porous/fractured medium model should be used for a proper description of the explosive source. Appendix 9-A describes the relationships between porosity and other elastic parameters. In cases where the extensive site characterization is performed, the measured medium parameters should be used. However, if some of the measurements necessary for the seismic source estimation are missing, their values can be predicted from other available information. For example, detailed laboratory investigations were carried out for the Barre experiment, including the measurements of compressional and shear velocities, bulk density and porosity before and after the explosions. The results of these measurements were used to validate

the effective porous/fractured medium model (Appendix 9-A). For the FDE in New Hampshire the measurements of compressional velocity were made before and after the explosions, while density, porosity and shear velocity measurements were only made before the explosions. Using the P -velocity values for the damaged medium we obtain an approximate value of porosity, which then can be used to approximately estimate other parameters (e.g. shear wave velocity and density) in order to calculate the seismic source spectra.

To predict how changes in elastic parameters affect the seismic amplitudes we use Mueller-Murphy model (Mueller and Murphy, 1971; MM71):

$$u(\omega) = \left(\frac{1}{r^2} + \frac{i\omega}{v_p r} \right) \frac{P(\omega) r_{el} v_p^2}{4\mu(\omega_0^2 + i\omega\omega_0 - \beta\omega^2)} = P(\omega) \cdot T(\omega) \quad , \quad (9-1)$$

where r is a distance to the receiver greater or equal to the elastic radius r_{el} , $\beta = (\lambda + 2\mu)/4\mu$, $\omega_0 = v_p/r_{el}$, and λ and μ are the medium Lamé constants. Equation 9-1 represents the medium motion due to a pressure function $P(\omega)$ applied at the boundary of a sphere of radius r_{el} . The function $T(\omega)$ represents a transfer function between the elastic radius and the receiver. We note that the transfer function was derived using a model of a pressurized cavity (Sharpe, 1942), which in this case was extended to the volume outside the elastic radius. Thus the expression for $T(\omega)$ uses the elastic parameters outside the elastic radius.

The pressure function $P(\omega)$, however, is affected by the material inside the elastic radius. The time-domain expression for the pressure function is given by the sum of a step function and a decaying exponential function (overshoot):

$$p(t) = (p_0 e^{-\alpha t} + p_{0c})H(t) \quad , \quad (9-2)$$

where $p_0 = p_{0s} - p_{0c}$, α is the inverse characteristic time:

$$\alpha = k v_p / r_{el} \quad , \quad (9-3)$$

and k is an empirically determined constant (e.g. $k = 1.5$ for granite). The values for p_{0s} and p_{0c} are given by:

$$p_{0s} = 1.5 \rho g h \quad , \quad (9-4)$$

$$p_{0c} = \frac{4\mu}{3} \left(\frac{r_c}{r_{el}} \right)^3 \quad . \quad (9-5)$$

In this expression the radius of the explosive cavity r_c is estimated using Heard and Ackerman (1967) scaling:

$$r_c = 16.3 W^{0.29} (E^{0.62} \rho^{-0.24} \mu^{-0.67}) h^{-0.11} \quad (9-6)$$

where W is the yield in kt, E and μ are the rock's Young's and shear moduli. The steady state pressure p_{0c} (Equation 9-5) was derived using incompressibility assumptions within the volume inside the elastic radius (MM71). The values of the elastic and cavity radii according to MM71 also depend on the material properties in the immediate vicinity of the working point. A traditional way to describe the fractured medium is to use the fractured medium parameters to calculate both $P(\omega)$ and $T(\omega)$, corresponding to the case of the entire medium between the source and the receiver being fractured. However, the extent of the damage zone is limited depending on the size of the first explosion as schematically shown in Figure 9-10. Based on the laboratory core measurements (e.g. Martin *et al.*, 2011b), the damage zone from AN122 is not spherical and extends to approximately 7-10 m laterally and toward the surface. The elastic radius calculated for the first shot of the pair (AN122) is approximately 19 m. The elastic radius for the reshoot (NEDE2-5) conducted in the damage zone of AN122 is estimated to be 15 m. Therefore the damage zone for AN122 is contained within a spherical region inside the elastic radius. In cases where the first explosion had significantly larger yield the situation may be different. For example, the size of the damage zone for Shot FD1 is not known precisely, but it is greater than the dimensions of the tomographic survey, which extended 9-10 m in each direction from the explosion (Figure 9-2b). Shot FD3 conducted in this fracture zone was located 6 m from the FD1 working point and had an elastic radius of approximately 14 m. Thus the damage zone may exceed the elastic radius at least in some places.

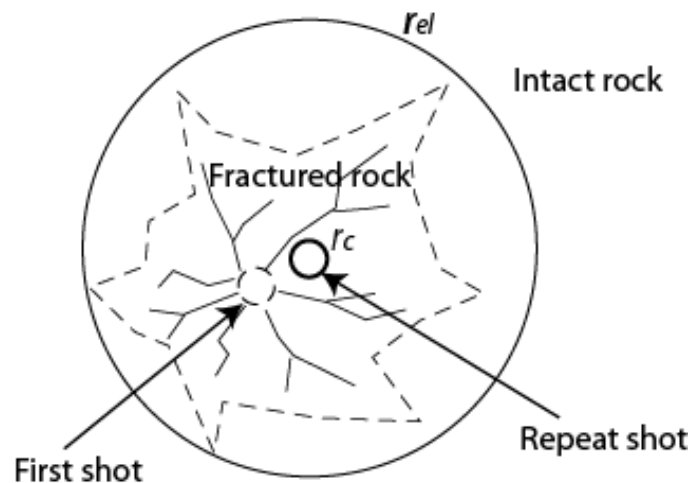


Figure 9-10. Schematic configuration of the repeat shot with respect to the damage zone created by the first shot of similar size. The rock outside of the elastic radius is intact, therefore original elastic moduli should be used. Inside the elastic radius rock is fractured. Therefore using the porous medium description is appropriate for the zone bounded by the elastic radius.

To model this situation we can use the intact rock elastic moduli to calculate the transfer function part of the displacement $T(\omega)$, and use the reduced (fractured) moduli to calculate the pressure function $P(\omega)$. The damage zone is diffuse with no sharp boundary; therefore we do not expect a sharp impedance contrast which may complicate the analysis. The model with the elastic moduli reduced inside the elastic radius will be called a “hybrid” model. For the sake of brevity we will call the model with the original properties (both inside and outside the elastic radius) Model A, and the model with the porous or “fractured” properties Model B.

Using the laboratory rock property measurements and equations in Appendix 9-A we estimated the effective porosity of the dry granite for the Barre experiment at approximately 2%-3%. Using Model A for the dry fractured medium (Figure 9-11a) results in reduced corner frequency and an increase in the low frequency part of the spectra compared to the undamaged case. The “hybrid” model predicts a uniform decrease in spectral amplitudes for all frequencies. The observed spectra for the explosion in intact rocks (NEDE2-2) also show increase in amplitudes at all frequencies compared to both NEDE2-5 and NEDE2-6 (Figure 9-12a). At high frequencies the model predicts the observations reasonably well, at low frequencies the observed spectra undulate between the “hybrid” model estimate as an upper bound and unity as a lower bound.

The computations for the saturated fractured model show the same features as for the dry medium (Figure 9-11b). The observed ratios for the saturated rocks are close to 1 in the low-frequency limit, increase around the corner frequency and then decrease (Figure 9-12b-c). The decrease in the observed spectral ratios toward the low frequencies resembles the ratios predicted using Model B for the saturated medium. However, the low-frequency amplitudes predicted for Model B exceed the amplitude for the Model A (intact medium), which does not agree with the observations. As with the dry rock case, the observed ratios appear to be bounded by “hybrid” model prediction from above, while Models A and B provide the lower bound.

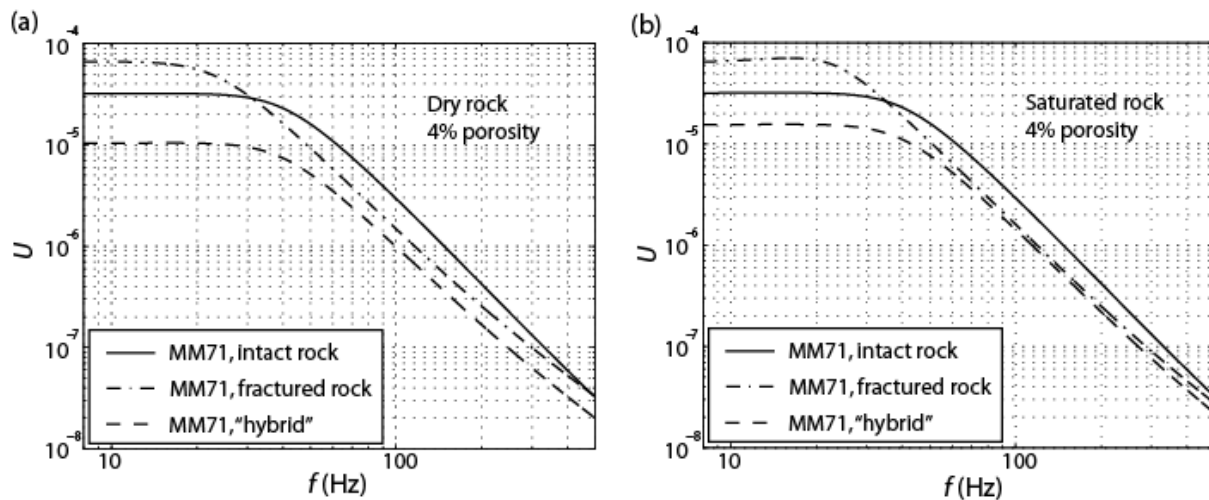


Figure 9-11. MM71 model predictions for intact rock (solid line, Model A), fractured rock (dash-dot line, Model B) and the “hybrid” model (dashed line) with fractured rock inside the elastic radius and intact rock outside the elastic radius. *a) dry rock, 4% porosity, and b) saturated rock, 4% porosity.* The matrix density and velocities were kept the same for comparison ($v_p^m \approx 4600$ m/s, $v_s^m \approx 2750$ m/s, $\rho^m \approx 2600$ kg/m³).

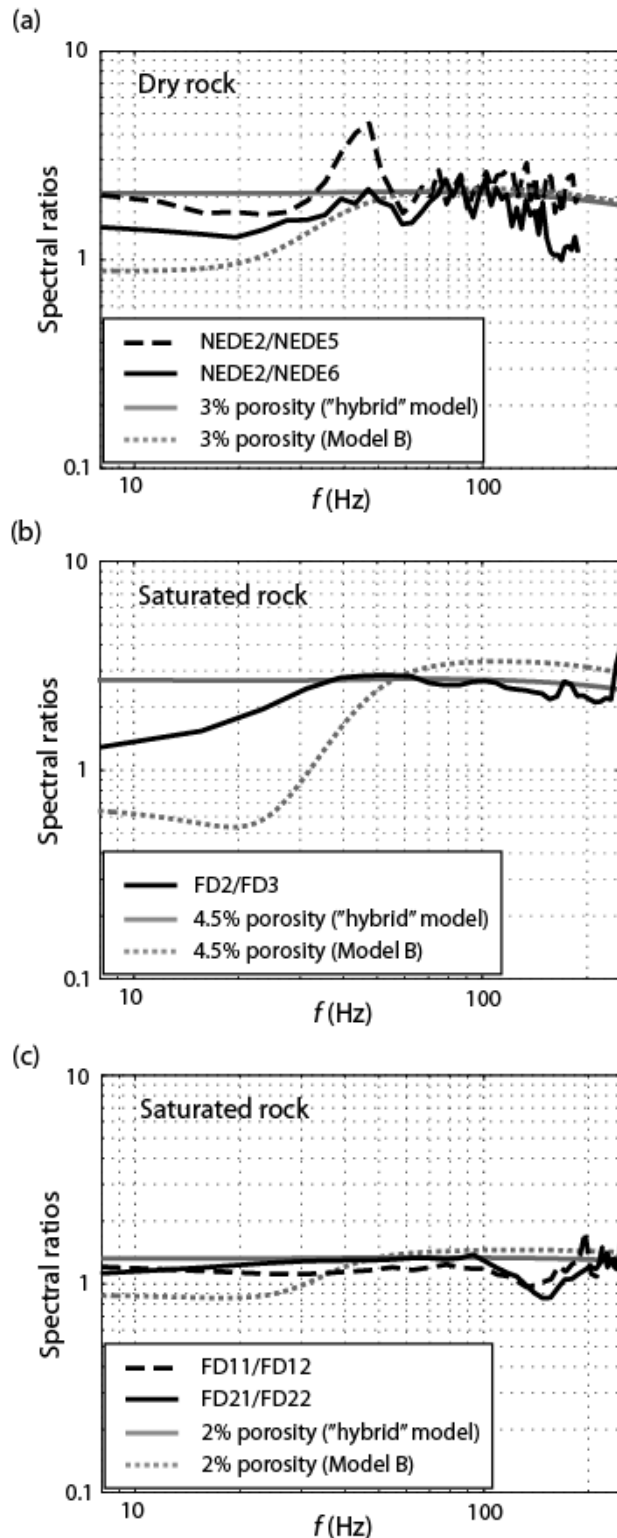


Figure 9-12. Comparison of the theoretical spectral ratios predicted using MM71 model between explosions in intact and “porous” media and the data. The “porous” medium was modeled by calculating elastic moduli and densities for the porous medium (Equations 9-A1, 9-A2, 9-A3 for dry rock, and Equations 9-A1, 9-A4, 9-A5 for saturated rock). The solid grey lines show the “hybrid” model predictions, while the grey dashed lines show the Model B predictions. (a) Spectral ratios for the NEDE2 pairs NEDE2-2/NEDE2-5 and NEDE2-2/NEDE2-6 modeled using dry porous medium with 3% porosity ($v_p^{\text{dry}} \approx 3231 \text{ m/s}$, $v_s^{\text{dry}} \approx 1974 \text{ m/s}$, $\rho^{\text{dry}} \approx 2522 \text{ kg/m}^3$). (b) Spectral ratios between FD2 and FD3 modeled using fluid saturated medium model with 4.5% porosity ($v_p^{\text{sat}} \approx 3323 \text{ m/s}$, $v_s^{\text{sat}} \approx 1152 \text{ m/s}$, $\rho^{\text{sat}} \approx 2615 \text{ kg/m}^3$). (c) Spectral ratios for the pairs FD11/FD12 and FD21/FD22 modeled using fluid saturated medium with 2% porosity ($v_p^{\text{sat}} \approx 4488 \text{ m/s}$, $v_s^{\text{sat}} \approx 2268 \text{ m/s}$, $\rho^{\text{sat}} \approx 2666 \text{ kg/m}^3$).

Using the expressions for the porous medium and applying the Gassmann (1951) formula for the fluid substitution (Equations 9-A5 and 9-A6), we estimated the effective porosity of the medium for the FDE. The estimate for the porosity for the FD2/FD3 explosion pair is at least 4% (see the

explanation in Appendix 9-A). For FD11/FD12 and FD21/FD22 pairs, the porosity estimate is approximately 1-2%. Thus the medium porosity inferred from the rock property measurements correlates with the seismic amplitude reduction.

Murphy *et al.* (2011) proposed an empirical formula to account for effects of gas porosity in the emplacement medium. This method involves modifying the pressure function $P(\omega)$ by a frequency independent factor depending on the gas porosity GP:

$$RF = 1.75 \times 10^{0.024GP}. \quad (9-7)$$

The factor of 1.75 is used to compare the amplitudes in dry porous tuffs to saturated tuffs with low porosity. In our case, both virgin and fractured rock explosions were conducted in dry rocks. Therefore the factor should be omitted if we compare two explosions with the same degree of saturation, and the amplitudes should be scaled proportionally to $10^{0.024GP}$. Using the measured value of GP=2.5% (for dry granite in Barre, VT) the amplitudes for the explosions in the fractured rocks should be reduced by a factor of 1.15. To produce the actual reduction by a factor of 1.5-2 the porosities would have to be on the order of 7–12.5%.

CONCLUSIONS

We present and discuss the data from chemical explosions conducted in granite in New Hampshire and Vermont. Multiple repeat explosions were conducted in both water saturated and dry granite in order to compare the amplitude reduction and the decoupling factors.

Water-saturated rock

The amplitude ratios between the first and the second shots vary from 1.07 – 1.25 for Phase II compared to approximately 2.25 for Phase I. The amplitude ratios increase with the increase in the extent of damage. For the shots in saturated rocks the spectral ratios are close to 1 at low frequencies and reach the maximum near the corner frequency. Some reduction in corner frequency is noted for the shot in the extensive rubble zone (Phase I). Our results are consistent with the SPE-N results. According to Townsend *et al.* (2012) the SPE-N experiment was conducted below the water table. Co-located explosions conducted as a part of the SPE-N (SPE-N-2 and SPE-N-3) had similar yields and far-field amplitudes. The amplitude reduction for the Phase II shots is only 5-20%, which is in agreement with the SPE-N observations.

Dry rock

The amplitude ratios between the first and the second shots in dry granite vary between 1.5 – 2. The amplitude reduction in dry fractured rock can be achieved even without extreme

emplacement medium damage. Our limited dataset shows that the spectral ratios slightly increase toward low frequencies and toward the corner frequency.

Modeling the intact and fractured rock shots using MM71 revealed that reduced velocities can explain decreased corner frequency; however it predicts increase in the low frequency amplitudes, which is not observed in the data. To explain the amplitude reduction at low frequency we created a “hybrid” model based on MM71, where the medium inside the elastic radius has reduced elastic moduli and the medium outside the elastic radius is represented by the original unfractured medium. This is a very simplified model, which does not account for the inelastic effects, including pore crushing. The “hybrid” model predicts the amplitude reduction at all frequencies for the repeat shots, which agrees with the observations. Using MM71 with the original and with reduced elastic moduli (Models A and B) and our “hybrid” model provide bounds on the observed spectral ratios. Due to uncertainties in the configuration of the damage zone with respect to the elastic radius, the quantitative fitting of the spectra may be difficult. However using a hybrid model may provide a simple way to estimate bounds on the decoupling factors based solely on the changes in the elastic moduli.

Chapter 9. Data and Resources

Data from the Phase II FDE will be proprietary until Oct. 31, 2014. Data from the NEDE2 experiment will be proprietary until June 31, 2015. Please contact Anastasia Stroujkova at ana@westongeophysical.com for information concerning access to the FDE dataset. To inquire about NEDE2 data please contact Mark Leidig at mleidig@westongeo.com.

Chapter 9. Acknowledgements

The Fracture Decoupling Experiment was sponsored by DTRA grant HDTRA1-11-1-0029. The explosions in Barre, VT were conducted by leveraging funds with AFRL Contract No AFRL-FA9453-10-C-0257. This project would not be possible without help from Maxam NE and Rock of Ages Corporation. We thank IRIS PASSCAL for providing sensors and for their help in the field. We would also like to thank our field crew including Jessie Bonner, Aaron Ferris, Chris Sanborn, Amy Gilligan, William Hudasek, and Won-Young Kim. Jim Lewkowicz provided invaluable field support and helped editing the manuscript.

APPENDIX 9-A. DESCRIPTION OF THE POROUS MEDIUM

An underground explosion creates fractures in the adjacent rocks, which can be filled by either gas or fluid. The amount of void is characterized by porosity ϕ . The bulk density of the porous rock ρ_b is given by:

$$\rho_b = (1 - \phi)\rho_m + \phi\rho_f, \quad (9-A1)$$

where ρ_m and ρ_f are the densities of the matrix and fluid respectively.

The elastic moduli of the solid-fluid mixture can be calculated using effective medium models (e.g. Mavko *et al.*, 2009). According to Nur *et al.* (1995) the seismic velocities change from the velocities of the mineral matrix in the low-porosity limit to the velocity of mineral-pore-fluid suspension at high porosities. The transition from a high to low porosity regime occurs at a critical porosity ϕ_c . For porosities lower than ϕ_c the mineral skeleton is load-bearing, above ϕ_c the material “falls apart” and behaves as a suspension (e.g. Mavko *et al.*, 2009). For fractured crystalline rocks $\phi_c \approx 0.06$ (e.g. Nur *et al.*, 1995). According to this model the elastic moduli are given by:

$$K_{dry} = K_m \left(1 - \frac{\phi}{\phi_c}\right), \quad (9-A2)$$

$$\mu_{dry} = \mu_m \left(1 - \frac{\phi}{\phi_c}\right), \quad (9-A3)$$

where K_{dry} and μ_{dry} are the bulk and shear moduli for the dry porous skeleton, K_m and μ_m are the elastic moduli for the rock matrix. Using Equations 9-A1, 9-A2 and 9-A3 the velocities of the post-shot porous (fractured) medium are given by:

$$v_{p,s}^{dry} = v_{p,s}^m \sqrt{\frac{\phi_c - \phi}{\phi_c(1 - \phi)}}. \quad (9-A4)$$

We can use the measured pre-shot velocities for Barre granite as the velocity of the matrix $v_{p,s}^m$ and the dry bulk velocity $v_{p,s}^m$ respectively to estimate the porosity. From Figure 9-6a, the original compressional velocity $v_p^m \approx 4600$ m/s, while the velocity of the damaged medium is $v_p^{dry} \approx 3900$ m/s, yielding the porosity of approximately 0.01 or 1%. Using an S-velocity (Figure 9-6b) $v_s^m \approx 2750$ m/s, $v_s^{dry} \approx 2300$ m/s, the porosity is approximately 0.019 or 1.9%. This estimate is for the laboratory measured velocities using core samples with porosity mainly

represented by micro-fractures. The measured porosity due to microfracturing at the shot depth is approximately 2 – 2.5% with the measured compressional velocity of approximately 3.2 km/s. The measured value of porosity was made for an intact sample with no macrofractures, while the rock surrounding the explosions also had macro-fractures (e.g. Martin *et al.*, 2011b). Therefore *in situ* porosity can be slightly higher than the laboratory estimate. Using a porosity value of 3% produced spectral estimates that fit the data (Figure 9-12a). The measured values of the minimum seismic velocities in CH-4 ($v_p^{meas} \approx 3171 \text{ m/s}$, $v_s^{meas} \approx 1817 \text{ m/s}$) are close to the estimated values using 3% porosity ($v_p^{est} \approx 3231 \text{ m/s}$, $v_s^{est} \approx 1974 \text{ m/s}$), which shows that the chosen model is adequate to describe the observations.

To estimate elastic moduli for the saturated rocks we use the Gassmann equation for fluid substitution (Gassmann, 1951) given by:

$$K_{sat} = K_{dry} + \frac{(1-K_{dry}/K_m)^2}{\frac{\phi}{K_f} + \frac{1-\phi}{K_m} - \frac{K_{dry}}{K_m^2}}, \text{ and} \quad (9-A5)$$

$$\mu_{sat} = \mu_{dry}, \quad (9-A6)$$

where K_{sat} and μ_{sat} are the bulk and shear moduli for the saturated porous rock. These equations provide good approximations for low frequencies (in the seismic frequency range, e.g. Mavko *et al.*, 2009).

The laboratory measurements of the pre-shot velocity in the vicinity of Shot FD11 yield approximately $v_p^m \approx 5100 \text{ m/s}$. This estimate agrees with the pre-shot tomography results (Figure 9-2 and Figure 9-3). The post-shot velocity for Phase I explosion pair (FD2–FD3) was $v_p^{sat} \approx 2000 - 4000 \text{ m/s}$. Given the large uncertainty in velocity our estimate of porosity is on the order of 4-6%, with the upper bound close to the critical porosity. During drilling of the shot borehole for FD3 the driller noticed that the borehole “stayed open” below approximately 10 m, even though it had to be cased above 10 m. Therefore we conclude that the rock below 10 m was likely below the critical porosity. The porosity value of approximately 4.5% yields P -wave velocities of 3323 m/s, which is representative of the observed velocities from the tomographic survey (Figure 9-12b). It also provides a reasonable fit to the seismic data (Figure 9-12b).

For the Phase II explosions the velocity changes were not as drastic as for Phase I. According to the tomography results (Figure 9-3) the post-shot velocity reduction is on the order of 10-20% (15% on average). Solving Equations 9-A5 and 9-A6 numerically provides a porosity estimate of 1.5-2%. Calculated spectral ratios (Figure 9-12c) also agree with this estimate.

10. FORWARD MODELING OF SEISMO-ACOUSTIC SIGNALS FROM EXPLOSIONS: NEDE2 EXAMPLES

ABSTRACT

Yield estimates from combined seismo-acoustic signals require forward models that can accurately predict amplitudes as a function of yield and depth of burial or height of burst. We continue to develop and validate an empirical modeling tool, called *SARANGE*, designed to predict seismic and acoustic measurements for above and below ground explosions to less than 50% error. The NEDE2 consisted of 6 over buried explosions in the yield range of 68-73 kg and provides an excellent study of the capabilities of the tool. I measured the peak particle velocities and overpressures on local seismic and infrasound recordings of the explosions, respectively. I estimate less than 50% error between observed and predicted seismo-acoustic data for 3 of 6 events. Error larger than 50% can be explained as either an effect of explosion type (slow burning black powder), explosion depth, or fracture decoupling for rubble zone shots.

OBJECTIVE

The objective of this study is to employ a forward modeling tool called *SARANGE* to predict seismic peak particle velocities (PPVs) and acoustic peak pressures (POPs) as a function of distance for comparison to observed data from the second part of the New England Damage Experiment (NEDE2). NEDE was a two-phase explosion experiment conducted in 2008 (NEDE1) and 2013 (NEDE2). For the details on the NEDE1, the reader is referred to Leidig *et al.*, 2010 and Stroujkova *et al.*, 2012. For NEDE2, nine explosions were detonated at a granite quarry near Barre, VT and recorded on a network of accelerometers and seismometers. Shots 1-6 (Table 10-1) are the focus of this study and represent explosions of different explosive weights (45.7-113.5 kg) but similar TNT-equivalent yields (68-73 kg TNT equivalent) in undamaged (Shots 1-4) and damaged (Shots 5-6) granite. Different explosives types were used including black powder (Shot 1), heavy Ammonium Nitrate Fuel Oil (HANFO; Shots 2, 4-6), and Composition-B (Shot 3). Shots 1-3 and 5-6 had similar depths (12-14 m) while Shot 4 was significantly over buried at 29 m. The other NEDE2 shots conducted (Shots 7-9) were 0.5 kg calibration explosions and not studied in this chapter, primarily because we did not observe acoustic signals. In the following sections we discuss the *SARANGE* model, provide information on the deployments and data used, and the compare the observed data to the forward models.

RESEARCH COMPLETED

The objective of *SARANGE* (Seismo-Acoustic RANGE calculations) is to predict overpressures and peak particle velocities from surface and buried explosions at local distances (< 50 km). The purpose for developing the tool is two-fold. First, we wanted to employ the method to predict overpressures and seismic ground motions for explosion planning purposes. Thus the method must have low error especially in cases where overpressure or vibration limits may exceed safety

limits at nearby structures. Second, they desired to use the calibrated models in the tool to estimate yield and depth of burial (DOB) of explosions using overpressure and seismic data collected from nearby stations. The reasons for estimating yield may be related to monitoring of clandestine nuclear explosions or determining the yield of a terrorist explosion in an urban center.

Table 10-1. Origin, yield, and weather information for the NEDE2 explosions in this study.

Shot	Latitude (WGS84)	Longitude (WGS84)	Elev (m)	Date (UTC)	Time (UTC)	Explosive	TNT Equivalent Yield (lbs)	SDOB TNT Equiv (m/kt ^{1/3})	Temp (deg C)	Pressure (mbar)	Wind Direction & Speed (m/s)
1	44.15794	-72.47843	507.2	6/21/13	20:22:10.701	Black Powder	68.0	305.7	25.4	1024	WNW 3.6
2	44.15797	-72.47791	509.0	6/22/13	17:29:09.320	HANFO	68.0	320.1	24.9	1021	Calm
3	44.15776	-72.47816	508.1	6/22/13	18:15:33.492	Comp B	73.1	285.2	23.5	1021	E 1.3
4	44.15770	-72.47795	511.5	6/22/13	14:46:42.734	HANFO	68.6	686.7	22.2	1022	Calm
5	44.15751	-72.47803	506.8	6/21/13	21:42:36.444	HANFO	68.0	315.6	24.1	1023	Calm
6	44.15753	-72.47765	511.1	6/21/13	20:51:33.925	HANFO	68.0	303.6	25.8	1023	W 1.6
Weather from NCTWORCE1 (Worcester, VT)					Lat: 44.38	Long: -72.58					

Overpressure Model Development

To estimate the overpressure, P_f , observed at local distances from surface and buried explosions, we have developed a model with the form:

$$P_f = P_s S_z A_\theta, \quad (10-1)$$

where P_s is the overpressure for a surface blast, S_z is an adjustment made to the overpressure for depth effects, and A_θ is an adjustment factor used to correct the data for directionality effects. For a surface blast S_z is set to 1. Directionality typically occurs for blasts on free faces or in tunnels with openings. The NEDE2 test site had no significant sources of directionality, so I set it equal $A_\theta=1$.

For surface blasts, the main source of overpressure is from the shock wave. SARANGE employs three published formulas to estimate the overpressure, P_s , for an explosion on the surface or above the ground. The first is an empirical relationship adopted by the American National Standards Institute (ANSI, 1983) and is defined by:

$$P_s (Pa) = 8.720 w^{0.3667} R^{-1.1} \left(\frac{p}{1013.25} \right), \quad (10-2)$$

where w is HE chemical explosion charge weight accounting for TNT equivalence (in metric kilotons), R is distance (km), and p is the atmospheric pressure at the explosion (in mbar). Because it was developed for free-air bursts, the yield is doubled for a surface blast.

The second formula used to evaluate overpressures is often used by the US Mining industry for open-air detonations (e.g., surface detonators, detonation cords, etc.) and is from Perkins and Jackson (1964):

$$P_s (Pa) = 187 \left(\frac{3.28 * R}{w^{0.333}} \right)^{-1.38} * 6894.8 \quad (10-3)$$

where R is in meters and charge weight w is TNT HE equivalent in lbs (please note the unit change compared with Equation 10-2). Our studies often take us to quarries, thus we wanted a formula that the quarry operators would be familiar with when predicting expected overpressures.

The Blast Operational Overpressure Model (BOOM) is a semi-empirical model of broadband peak acoustic overpressure from an explosion developed by Lorenz (1981) for distances up to 50 kilometer that uses a single parameter B to represent the combined effect of coupling, atmospheric temperatures, and winds at a range of altitudes on air blast refraction. The formula is defined as:

$$P_s (dB) = 103.1 + \frac{B}{5.3} + 20 * \log_{10} \left[\left(\frac{p}{1013} \right)^{0.556} \left(\frac{w}{110} \right)^{0.444} \left(\frac{25}{\frac{R}{1000}} \right)^{1.333} \right], \quad (10-4)$$

where w is TNT HE equivalent in kg (again note unit change from Equations 10-2 and 10-3), which is doubled when the event is on the surface, and is converted to Pascals using the equation:

$$P_s (Pa) = 2E - 5 * 10^{\frac{P (dB)}{20}} \quad (10-5)$$

The parameter B is set to 0 for a uniform atmosphere, and can be changed for atmospheric conditions. There were no radiosonde launches during NEDE2, thus I assume a uniform atmosphere with atmospheric pressure obtained from a nearby weather station (Table 10-1).

For explosions at depth, the source of overpressure/acoustic signals is either gas venting, rock displacement (retarc), or strong near-source ground motions (Vortman, 1965). As a result, buried explosions have suppressed acoustic signals when compared to surface shots. To account for the suppression in our P_f model, we used the HUMBLE REDWOOD (HR) data (Foxall *et al.*, 2008, 2010) to provide an initial estimate of the acoustic amplitude suppression with depth. The experiment included detonation of ten (10) 539 kg ANFO explosions from 5 m height-of-burst

(HOB) to 10 m depth of burial (DOB). The peak-to-peak amplitudes from the HR data were plotted as pressure suppression factors, S_z , in Figure 10-1. The suppression factor is defined as:

$$S_z = P(sHOB)/P_s, \quad (10-6)$$

where $P(sHOB)$ is the zero-to-peak pressures at different scaled heights-of-burst (sHOB) obtained from the data and P_s is the zero-to-peak pressure from shot HRE (a shot on the surface). To extend the suppression factors beyond the data, we fit an exponential to the HR data similar to relationships developed by Vortman (1965) for high-explosive charges and nuclear explosions. The model used to calculate the pressure suppression factors is shown in Figure 10-1. An example of the forward model for a 1-ton surface and tamped explosion is shown in Figure 10-2.

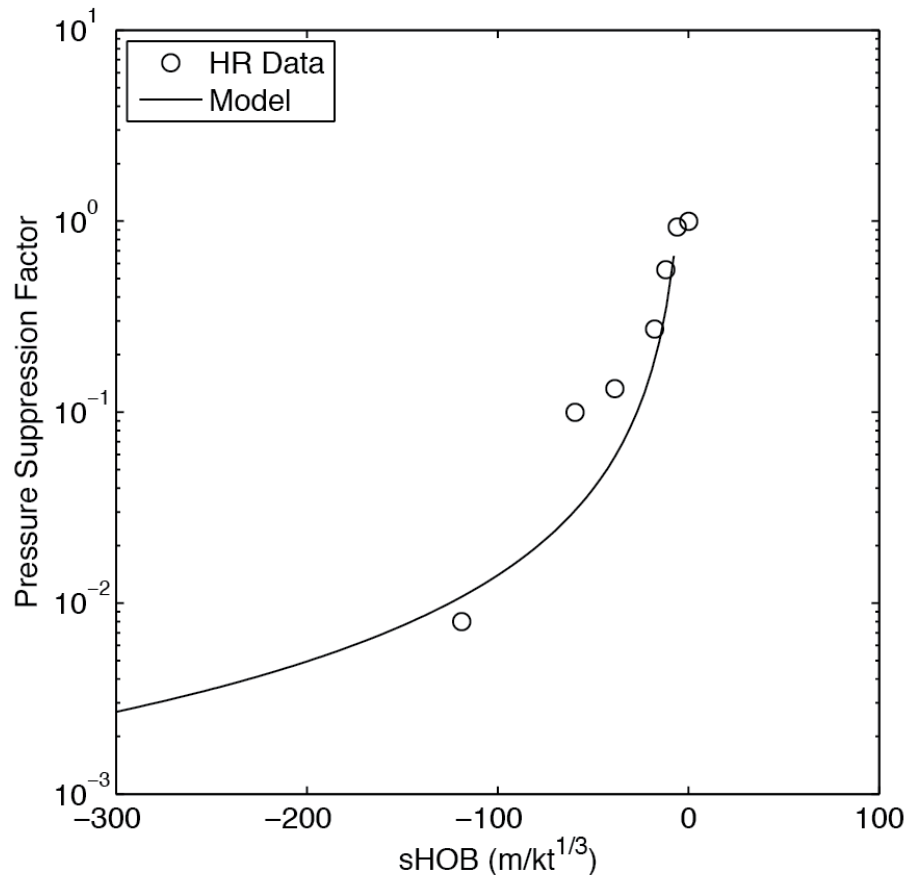


Figure 10-1. Blast suppression factors (S_z) versus scaled heights-of-burst (sHOB) for peak overpressures from HUMBLE REDWOOD data (circles). The model used in SARANGE is shown as the line and is based on a fit to the data and a similar relationship from Vortman (1965).

Seismic Model Development

A similar model was developed for seismic peak particle velocities from explosions at depth up to the surface. The model is defined as:

$$V_{max} = V_d A_z, \quad (10-7)$$

where V_{max} is the estimated Peak Particle Velocity (PPV), V_d is the PPV estimate for a fully confined explosion, and A_z is an adjustment factor for loss of coupling as an explosion is moved towards the surface or above ground, or loss of amplitude as the event is over buried. V_d is estimated using numerous published relationships for ground motion amplitudes as a function of range for explosions. The relationships are derived from nuclear explosions at NTS (Perret and Bass, 1975) and chemical explosions in Alaska, the eastern and western United States, and New England (Kohler and Fuis, 1992; Medearis, 1979; Fuis *et al.*, 2001; Leidig *et al.*, 2010). The relationships have been derived for wet and dry alluvium and tuff, “hard rock,” and granite, thus providing a variety of different emplacement conditions to consider when predicting explosion amplitudes with range. The published Perret and Bass (1975) estimates have been corrected by a factor of 2 for nuclear-to-chemical explosion equivalency. Unlike the overpressure model, there is no directionality correction for the seismic model.

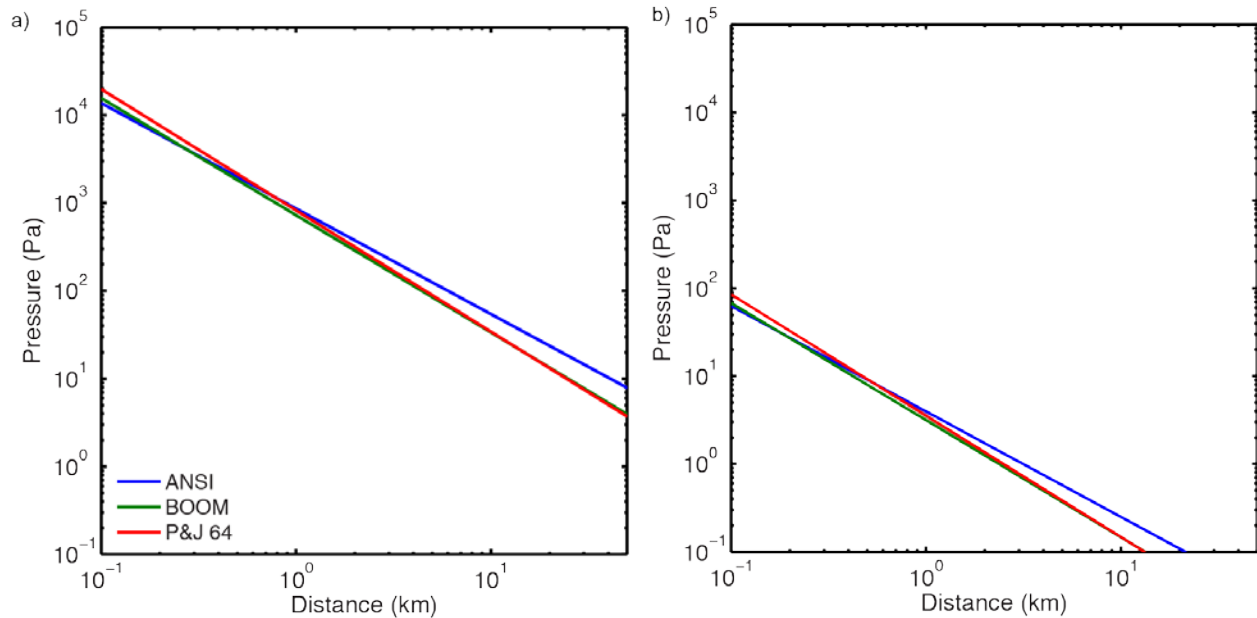


Figure 10-2. Peak overpressure estimates for 1-ton explosion detonated on the a) surface and b) fully-coupled using the ANSI (blue), BOOM (green) and Perkins and Jackson (red) models.

The ground motion scaling models are for confined explosions, and thus do not consider the loss of seismic energy due to the sources being detonated on the surface. In order to account for this effect, the PPV range estimates require an adjustment factor (A_z) in order to reduce the predicted seismic ground motions from fully confined to surface bursts. While there has been limited theoretical research relating air burst yield to ground motion amplitudes (Murphy, 1981; Murphy and Shah, 1988), we used the unique HUMBLE REDWOOD dataset to develop an empirical adjustment factor.

Figure 10-2 shows the normalized surface wave amplitudes at a single station for all the 539 kg ANFO HR I and II explosions in alluvium as a function of sHOB. The amplitudes were normalized to the amplitude of the deepest explosion to determine a seismic adjustment factor, A_z defined as:

$$A_z = A(sHOB)/A_d, \quad (10-8)$$

where $A(sHOB)$ are the amplitudes observed for various shots, and A_d is the amplitude for the HR shot at an optimum sHOB of approximately $-122 \text{ m/kt}^{1/3}$. Note that by convention $DOB = -HOB$. The data show that the Rg amplitudes decrease by a factor of more than 4 from an sHOB of -122 to $0 \text{ m/kt}^{1/3}$ while the P -waves decrease by a factor of almost 3 (P waves results are not shown in Figure 10-3). We chose to use the surface wave amplitudes to develop the adjustment factors primarily because the phase is often measured as the PPV at local distances. The seismic amplitudes for the slightly above-ground shots do not vary with height and are approximately the same amplitudes as the shallowest buried HR shot. This results in poor HOB/DOB resolution for sources in this region.

Preliminary results from two explosions in limestone suggest a larger seismic adjustment factor (~ 15) is needed for more competent rock than alluvium. These two measurements are included in Figure 10-3 and provide an initial “hard rock” coupling model. Plans are to conduct eight explosions from optimal sDOB to above ground in granitic rock to develop an improved coupling curve for hard rock in 2014.

Because amplitudes for over buried explosions decrease as a function of increased depth, we used the Denny and Johnson (1991) model to estimate the change in amplitude as a function of increasing depth beyond the optimum sDOB. Figure 10-4 shows how the model works using the PPV relationships for a 1-ton tamped and surface explosion.

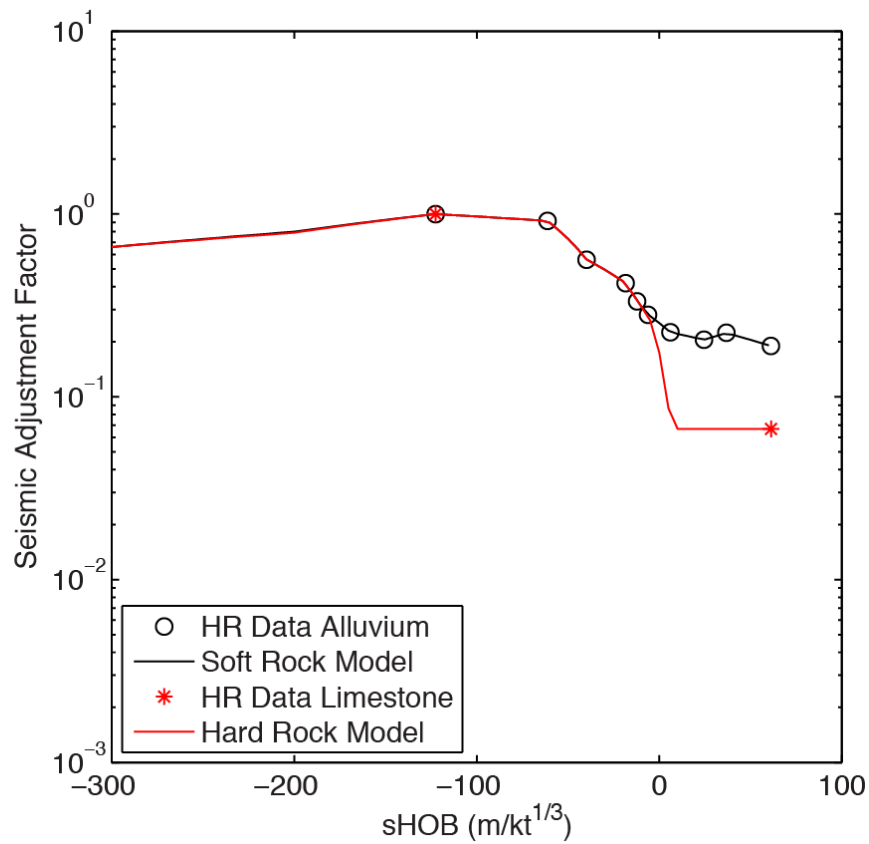


Figure 10-3. Amplitude reduction for seismic waves recorded from the ten 539 kg explosions conducted in alluvium during the HR I & II experiments (black circles) as a function of scaled height of burst (sHOB). Also shown are two explosions from the HR III experiment in limestone. *The alluvium data were used to develop a model for the seismic adjustment factor in soft rock. The limestone data used to develop a preliminary hard rock model that will be used until more data become available.*

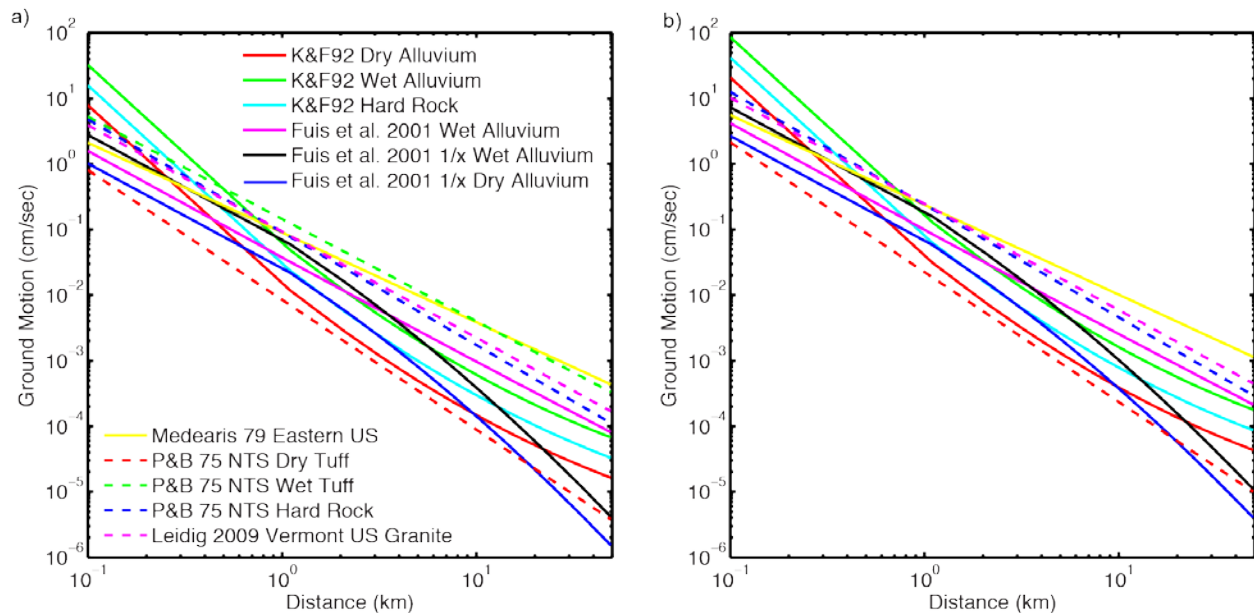


Figure 10-4. PPV relationships for a 1-ton a) surface explosion b) fully-coupled explosion using the soft rock coupling curve shown in Figure 10-3.

Data and PPV/POP Analysis

The NEDE2 was primarily a seismic experiment as 22 short-period seismometers were deployed at distances between 300 m and 24.2 km of the test site (Figure 10-5). I have used these seismometers to estimate the peak particle velocity (PPV) on the vertical component. Noisy signals, mainly passing cars, were either removed or, if possible, the noise was not included in the analysis window. The data were filtered between 1-40 Hz prior to estimating the PPV in m/s on the envelope of the waveform. Figure 10-6 shows examples of the vertical component seismic signals recorded at station R06SE02 (6 km) for Shots 1-6. This plot shows several characteristics that are observed on most of the sensors, such as Shot 1 (black powder) exhibiting the smallest amplitudes and lowest frequency content of all the 68-73 kg explosions. In addition, Shots 2 (HANFO) and 3 (Comp B) show similar amplitudes that are larger than the over buried Shot 4 (HANFO) and Shots 5 and 6 conducted in damaged rock.

Two NCPA infrasound sensors were deployed with the seismic sensors at NS06 (0.36 km) and NS10 (0.6 km). The data from these sensors were detrended, tapered, and filtered between 0.1 and 40 Hz to help remove noise. The peak overpressures (POP) were estimated in Pascals, and I used the largest absolute value of the signal (e.g., did not require the pressure to be positive).

The signals recorded on the two infrasound sensors for Shots 1-6 are shown in Figure 10-7. I did not observe any obvious signals for the 0.5 kg calibration shots, and the over buried Shot 4 was also difficult to determine the POP (especially for NS06). The largest acoustic amplitudes were recorded for Shot 3, which had significant gas venting that ignited and burned wires and a sensor positioned over opened fractures (Chapter 2). The acoustic signals are complex, varying between as few as one and as many as four cycles, and do not resemble the standard overpressure “N” wave often observed from surface explosions. The peak pressures for the signals occur between 4-12 Hz. The arrival times also vary, probably a result of changes in wind directions during shot

times. Note that ground accelerations are recorded on the infrasound sensors prior to the direct acoustic wave, because these NCPA sensors had not been retrofitted for seismic decoupling prior to deployment (Kleinert, pers. comm, 2013). I also measured the impulse of the first positive pressure pulse for future analysis.

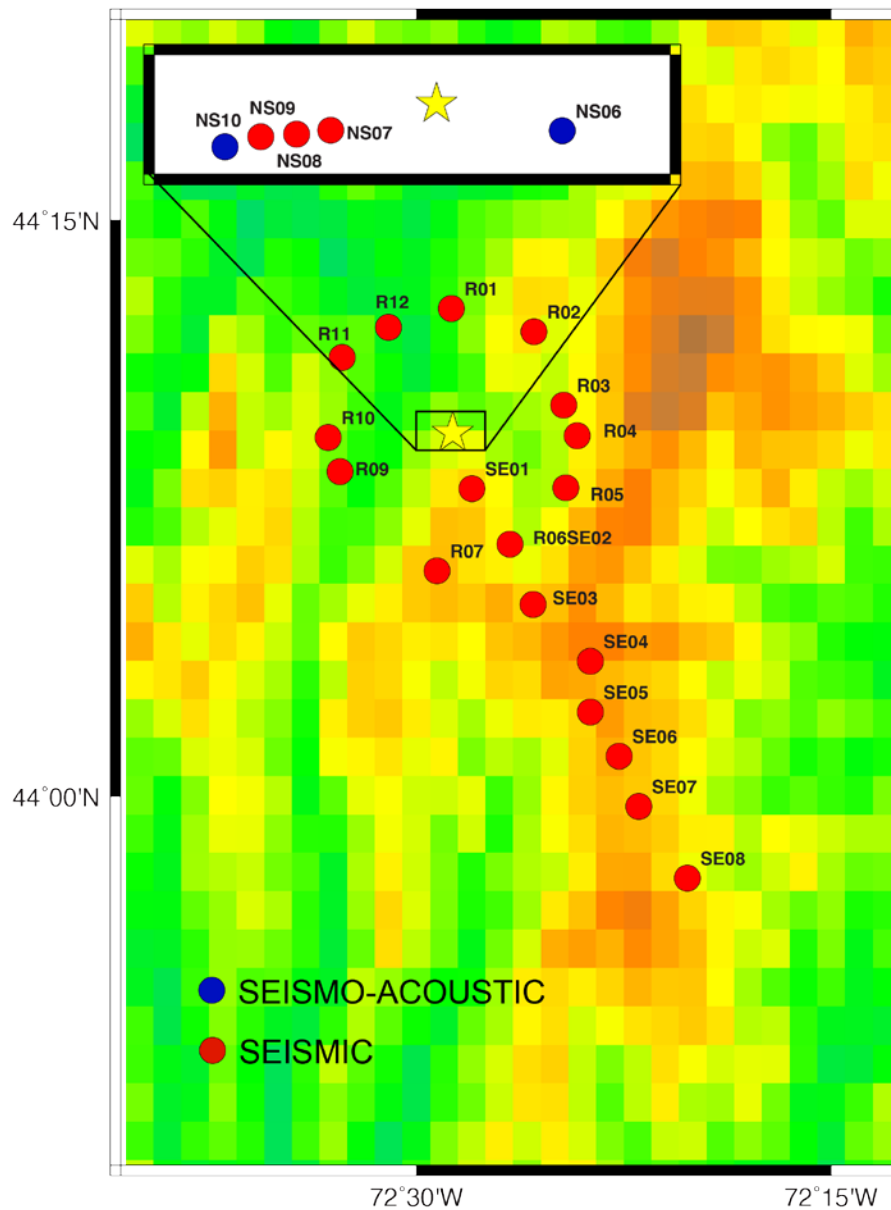


Figure 10-5. Map showing the locations of seismic stations (red) and seismo-acoustic stations (blue) used in this study. *The color map shows the topography in the region. The ring of sensors is approximately 6 km from the test site, and the distance between the SE sensors is ~3 km.*

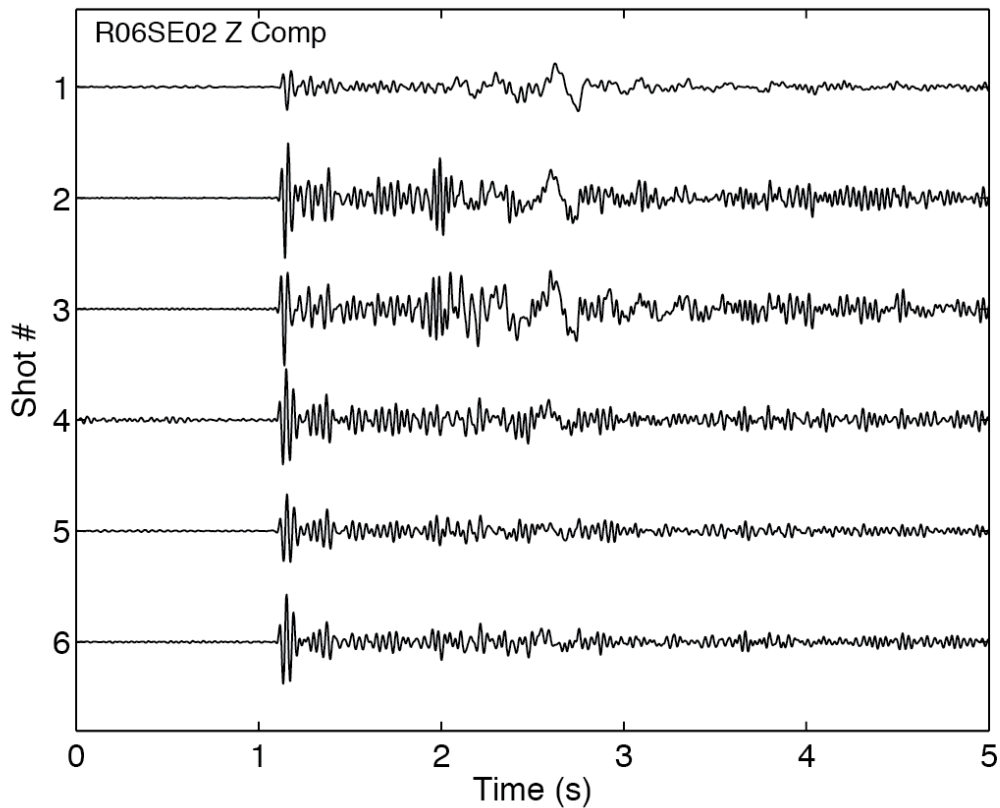


Figure 10-6. Vertical-component recordings for Shots 1-6 of NEDE2 from the 6 km station R06SE02.

Forward Modeling

I used *SARANGE* to predict the PPV and POP for Shots 1-6 of NEDE2 using the yields and sDOBs presented in Table 10-1. For the PPV predictions, I used the Leidig *et al.* (2010) granite model, which was developed from the NEDE1 explosions and is expected to perform well for these shots. I also used the hard rock coupling model. For the peak overpressure predictions, I used the BOOM model with a quiescent atmosphere defined by temperatures and pressures in Table 10-1. The comparison of the predicted and observed data is shown in Figure 10-8 through Figure 10-13. I estimated a percentage error (E_{POP} and E_{PPV}) between the predicted and observed measurements defined as:

$$E_{POP} = \frac{P_{obs} - P_f}{P_{obs}} * 100 \text{ and } E_{PPV} = \frac{V_{obs} - V_{max}}{V_{obs}} * 100. \quad (10-9)$$

where P_{obs} (V_{obs}) is the observed peak overpressure (or peak particle velocity) and P_f (V_f) is the predicted overpressure (or particle velocity). The absolute value of the mean of all stations' E_{POP} and E_{PPV} measurements were estimated and labeled on each plot and compiled in Table 10-2. The error could serve as a proxy for yield estimation uncertainty if the forward models were incorporated into an inversion methodology. With only two infrasound measurements, over-interpretation of the successes and failures of the method should be restrained.

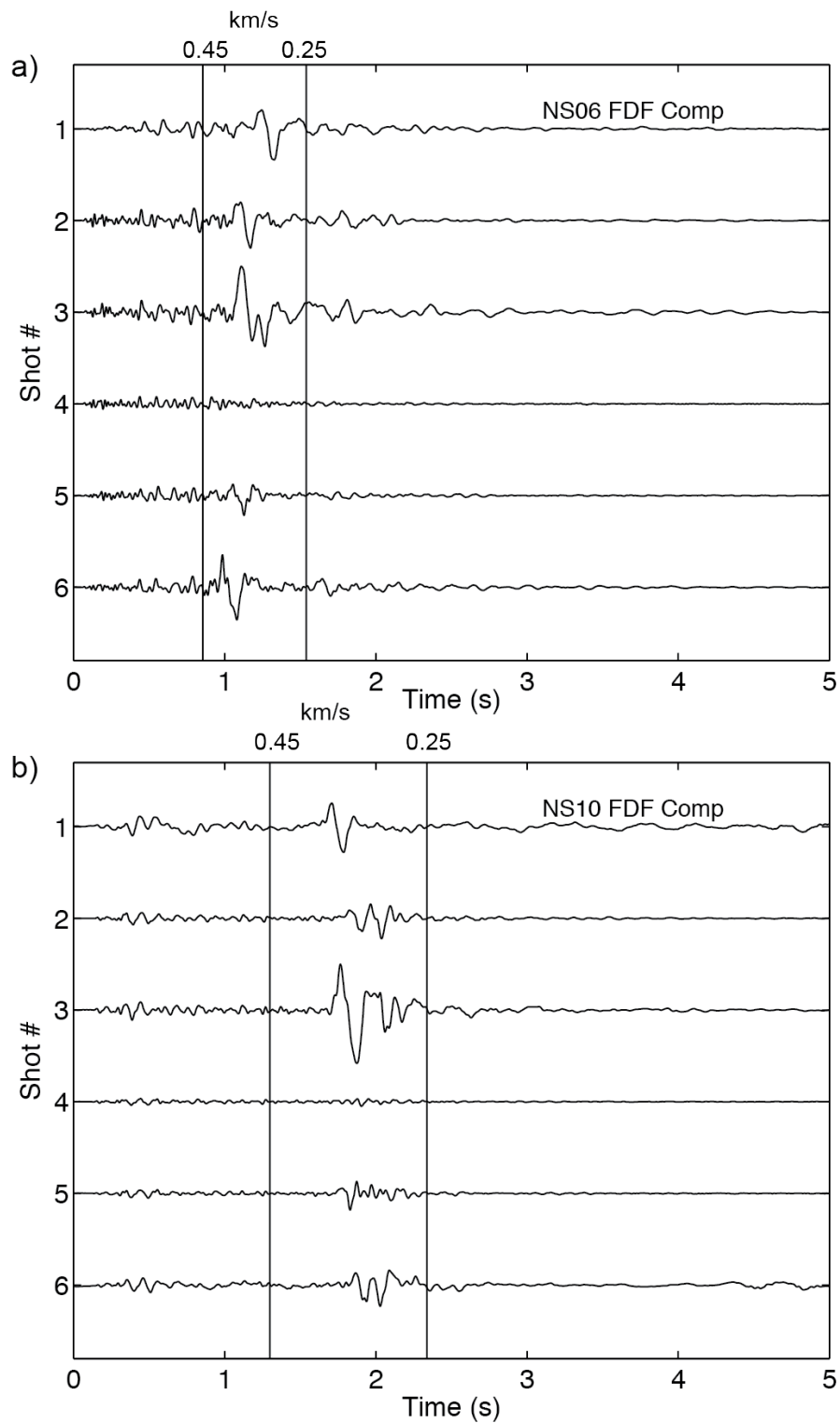


Figure 10-7. Infrasound recordings for Shots 1-6 of NEDE2 from the 0.35 km NS06 (a) and the 0.6 km (b) NS10 stations. The vertical lines mark 0.45 and 0.25 km/s analysis window used for POP analysis.

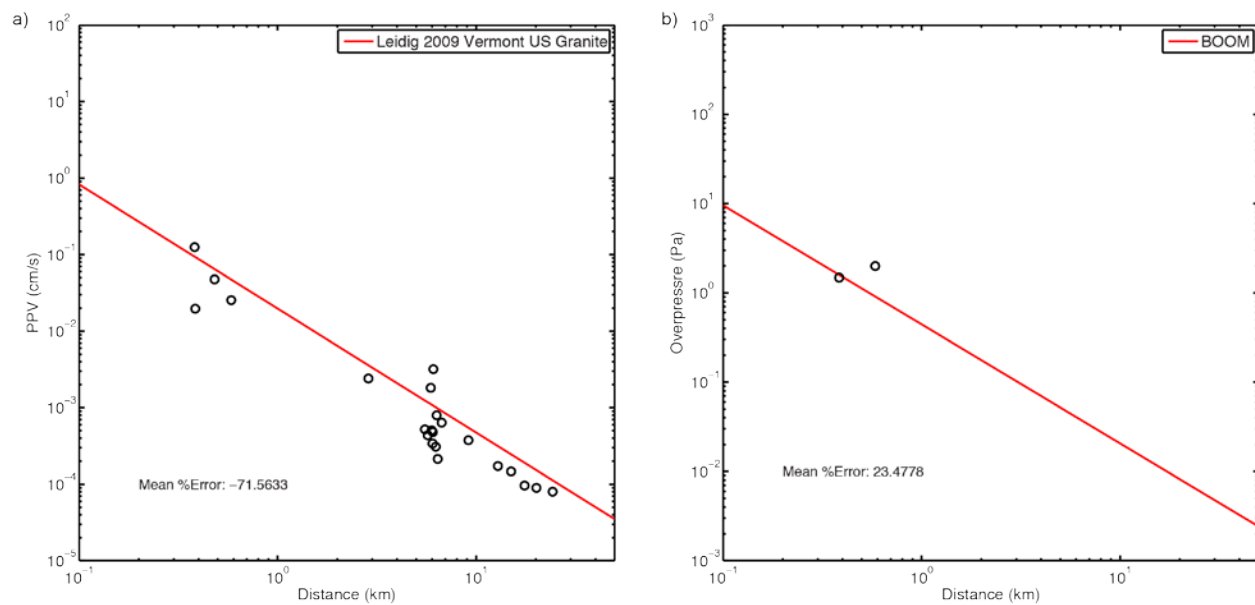


Figure 10-8. Predicted a) PPV and b) POP (red lines) for Shot 1 compared to observed data (black circles).

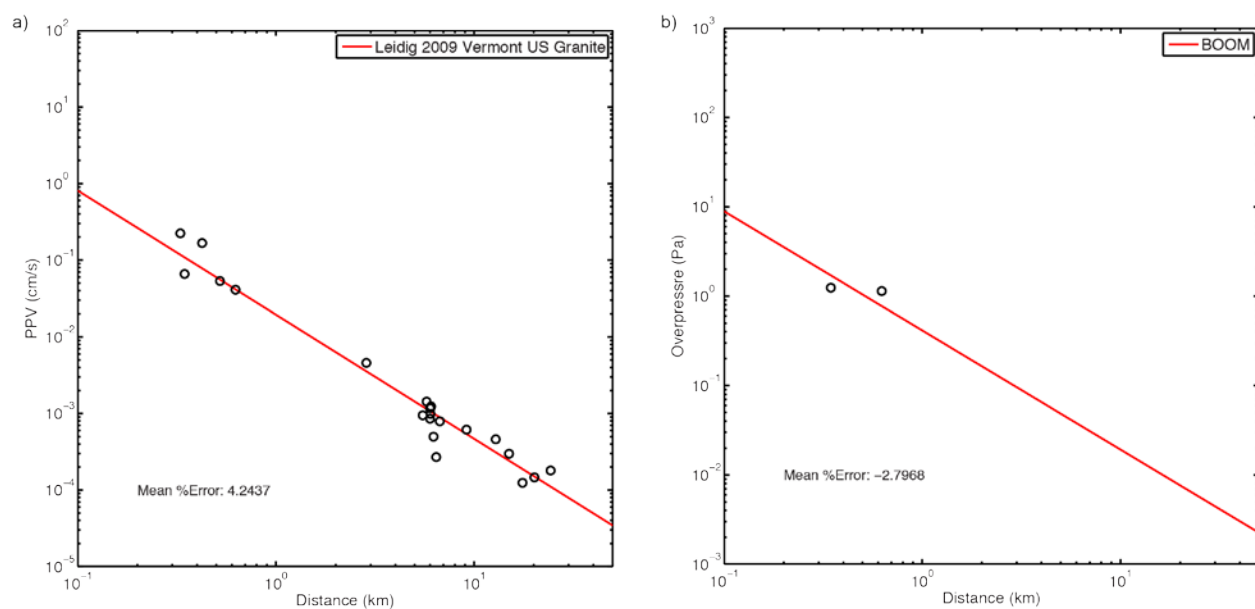


Figure 10-9. Predicted a) PPV and b) POP for Shot 2 compared to observed data.

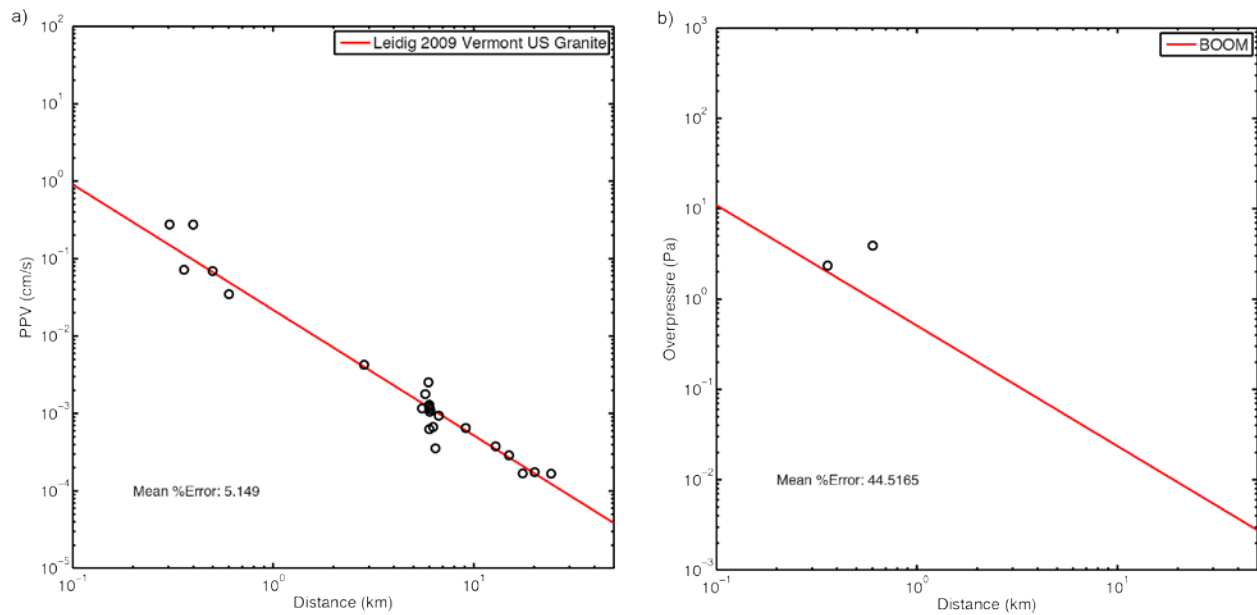


Figure 10-10. Predicted a) PPV and b) POP for Shot 3 compared to observed data.

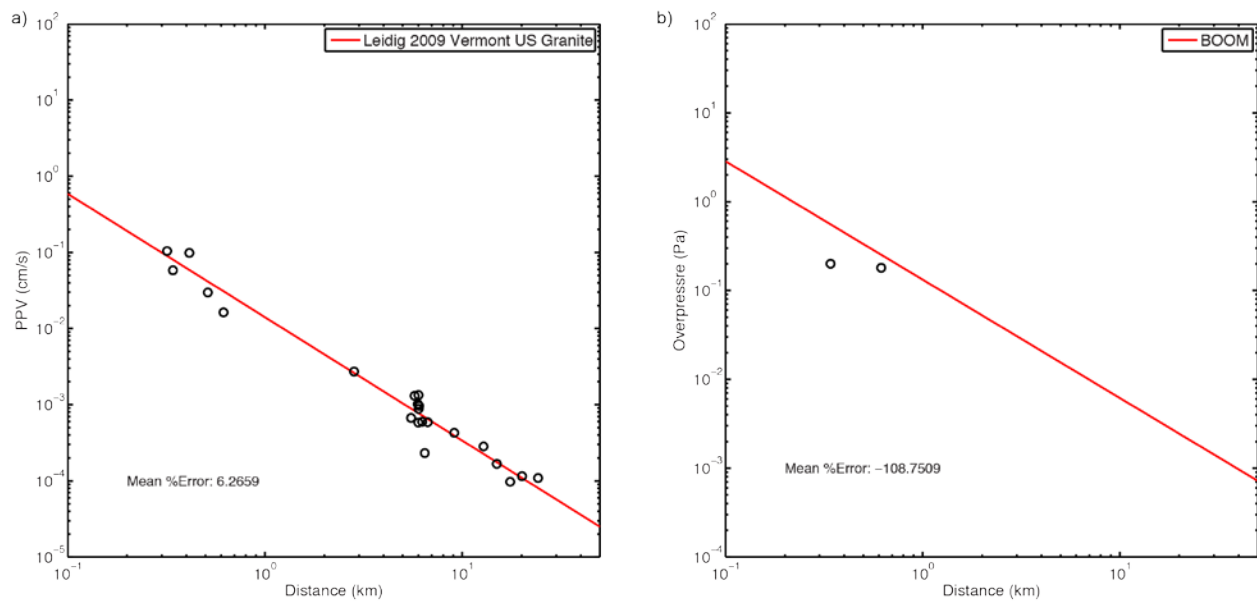


Figure 10-11. Predicted a) PPV and b) POP for Shot 4 compared to observed data.

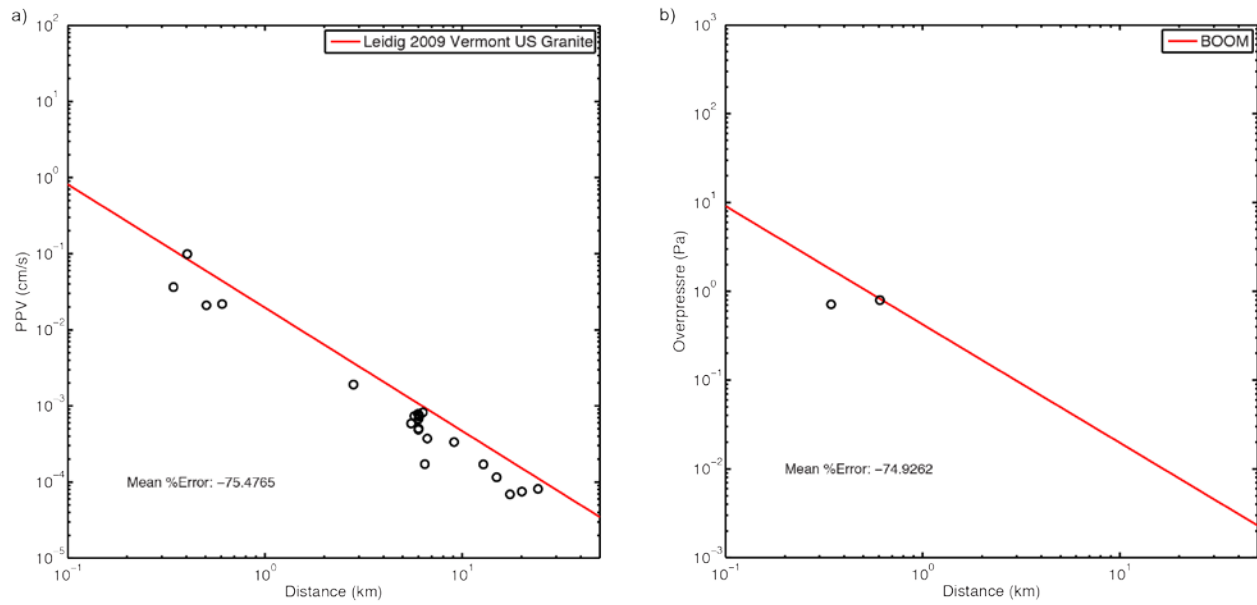


Figure 10-12. Predicted a) PPV and b) POP for Shot 5 compared to observed data.

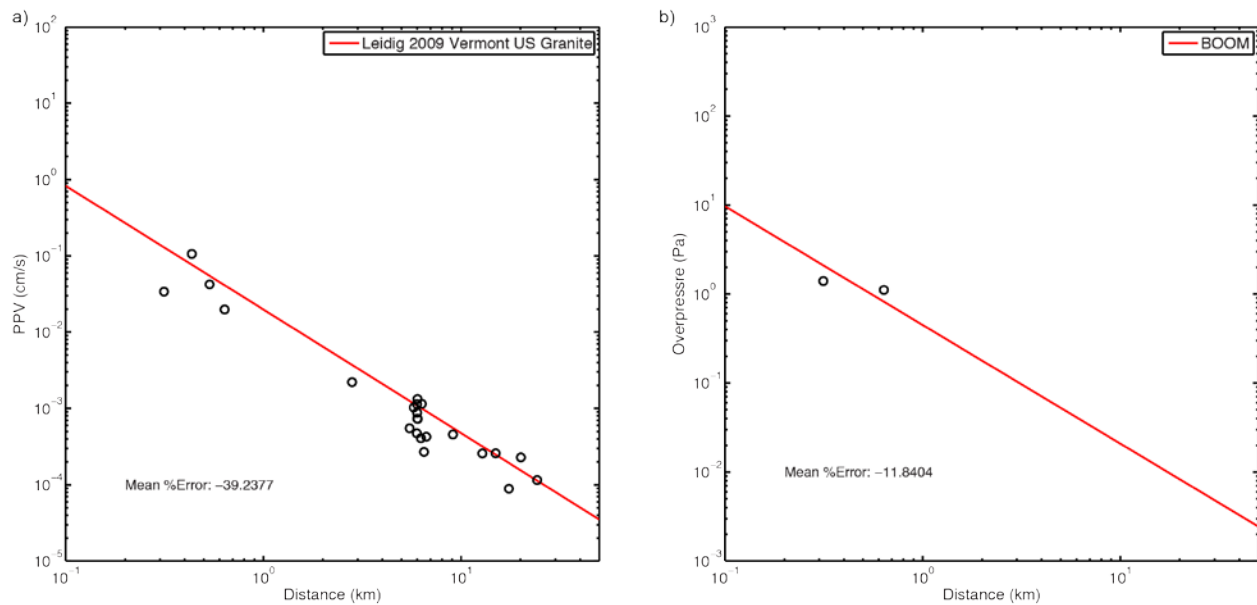


Figure 10-13. Predicted a) PPV and b) POP for Shot 6 compared to observed data.

CONCLUSIONS

Table 10-2 summarizes the error between predicted and observed PPV and POP measurements. A performance objective for *SARANGE* is 50% error or better for each phenomenology, which I was able to achieve for 3 of 6 events (Shots 2, 3, and 6). Shot 1 was comprised of black power,

which is a slow burning (deflagrating) explosive that produces a long source duration (Stroujkova *et al.*, 2013) that reduces P-wave amplitudes. Thus, I discovered 72% error in the PPV estimates. The POP estimates were within the 50% error objective at 24%. The observed overpressure data for Shot 3 is larger than the predictions probably due to the significant gas venting for this event; however, the error remained less than 50%. Shot 4 has low seismic error (6%) but increased overpressure error as the model predicts larger pressures than observed. Shot 4 is one of the largest sDOB events tested with *SARANGE*, thus it is not surprising that there is large error given there are currently no data supporting the curve shown in Figure 10-1 at these sHOBs. Shot 5 exhibited 75% error and was a re-shoot in the damage zone of a previous chemical explosion. *SARANGE* predicts larger PPVs and POPs from this event than observed because fracture decoupling reduces seismic amplitudes. Shot 6 was also a re-shoot in what is believed to be a smaller damage zone of a previous explosion, and the estimated error meets the 50% or less objective. I will continue to test and validate *SARANGE*, with hopes of studying data from over buried shots from the Source Physics Experiment.

Table 10-2. Percent Error for Predicted and Observed Data

Shot	E-PPV (%)	E-POP (%)
1	-72	24
2	4	3
3	5	44
4	6	-108
5	-76	-75
6	-39	-12

11. NEAR-SOURCE ROCK DAMAGE FROM SINGLE-HOLE EXPLOSIONS TO SEISMIC WAVES

ABSTRACT

Weston Geophysical Corporation and New England Research, Inc. conducted the New England Damage Experiment (NEDE) in July 2008. The experiment included the detonation of five small (135 to 270 lbs) chemical explosions in relatively unfractured, homogeneous Barre granite in Vermont, USA. Barre granite has been a worldwide standard for homogeneous, low fracture-density granite in commercial, monument, and industrial settings. The emplacement granite was characterized before and after the experiment using borehole cores and acoustic imaging. The explosions were designed with variable velocities of detonations (VOD) to fracture the rock differently. Our hypothesis was that different damage would lead to possible variations in S-wave generation.

Pre shot site characterization indicates that although the Barre granite is massive with a low fracture density, it is transversely isotropic. The anisotropy is largely due to the rift, a planar array of microcracks. The elastic anisotropy is on the order of 20%. After the five shots were detonated, a coring program was undertaken to determine the subsurface characteristics of the damage generated by each detonation at various distances from each shot point. The pre-shot cores were recovered with few pre-existing fractures. In contrast, the post-shot cores show extensive damage. The intensity of the damage decreases with range.

The large scale and microscale damage of each core were studied. Based on the degree damage, five distinct zones were identified. The damage ranged from highly pulverized/granulated rock with possible cavity development through intact with high angle fractures parallel to the rift in above the emplacement level to mostly intact with few fractures that are generally randomly oriented. The shape of damage zones are non-spherical with lateral extension at the emplacement depth of the charge. Microscale damage is concentrated in the horizontal plane at the emplacement depth and a vertical ellipsoid through the working point. There is little off axis microscale damage resulting in a decidedly non-spherical damage surface.

OBJECTIVES

Shear wave generation from explosions continues to be an important problem for the nuclear explosion monitoring community. Rock damage from the explosions may also play an important role in shaping the seismic waves from an explosion. Most recently, Patton and Taylor (2011) have demonstrated the importance of considering the moment from the damage separate from the explosion moment. Additional proposed mechanisms of explosion-generated *S*- waves involve processes related to the damage and deformations caused by the explosions. Nonlinear effects in the immediate vicinity of the explosion cause rock damage that can effectively generate *S*- waves provided that asymmetries exist in the damage pattern. Sammis (2003) has suggested that movement along pre-existing cracks can also produce large amplitude *S*-waves. Bykovtsev (2007) has postulated that radial crack generation from explosions should generate *S*-waves with distinct radiation patterns.

In order to test these models, a program was developed to quantify the damage in the rock mass surrounding chemical explosions. Experiments were conducted in Barre Granite at a quarry in Barre, Vermont. The overall objective of the study was to investigate correlations between the damage generated by the explosions and the seismic response observed on a dense array of three component instruments up to 35 km from the detonation. Of particular interest was the shear wave energy generated due to the blast. Shear wave generation from a point source has long been observed but there is no effective model to describe how they are generated. The overall objective of the study was to investigate correlations between the damage generated by the explosions and the seismic response observed on a dense array of three component instruments up to 35 km from the detonation. Of particular interest was the shear wave energy generated due to the blast. Shear wave generation from a point source has long been observed but there is no effective model to describe how they are generated.

To quantify the damage and define its spatial distribution, cores from vertical holes drilled radially outward from the working point were analyzed. Comparison of the rock properties of the pre and post shot core in conjunction with visual inspection should result in detailed characterization of the damaged zone. In turn, these results are used to infer the mechanisms of deformation and the stresses acting on the rock mass as a function of position. Utilizing this core

base probing technique rather than a mine back approach provides a less costly and more thorough investigation of the vertical and lateral extent of the damage associated with the detonation.

TEST SITE GEOLOGY

The Barre Granite test site was selected for the study because it is a monument grade rock mass with a low fracture density. A prominent feature of Barre Granite is the rift; a nearly vertical planar feature that strikes at N30°E at the test site. The rift is defined by a set of pervasive, similarly oriented, open and partially healed, inter- and intra-granular microcracks (Nasseri and Mohanty, 2008) as shown in Figure 11-1. A similar microscale fabric exists in most, if not all, granite bodies. Three planes (the rift, the hardway and the grain) are typically identified within the granite, and they are often found to be orthogonally oriented to one another Figure 11-1B. These planar features are identified by quarrymen and stone workers, who take advantage of their different breakage characteristics. The Barre granite exhibits this fabric very strongly and consistently over the entire pluton. Nasseri and Mohanty (2008) show that the Barre granite is a fine to medium grained rock. Quartz grains average 0.9 mm. The composition of the granite is microcline 21%, orthoclase 35%, quartz 27%, biotite 9%, muscovite 6% with various accessory minerals (VT Geological Society, web 2008). The composition of the granite is uniform throughout the test site (Richter, 1987).

Little planarity due to preferred mineral grain shape and alignment was observed in the Barre granite. The microstructural fabric was found to be mostly due to microcracks which were determined to average approximately 1.07 mm in length, with the largest (2–3 mm long) oriented within the denoted rift plane (“rift”). Figure 11-1A illustrates the three dimensional relationship between the three planes. The rose diagrams in the figure also show that the microcracks within the rift have the strongest preferred orientation. The rift is therefore defined by this set of pervasive, similarly oriented, open and partially healed, inter- and intra-granular microcracks. The actual azimuthal relationships in the field are shown in Figure 11-1B.

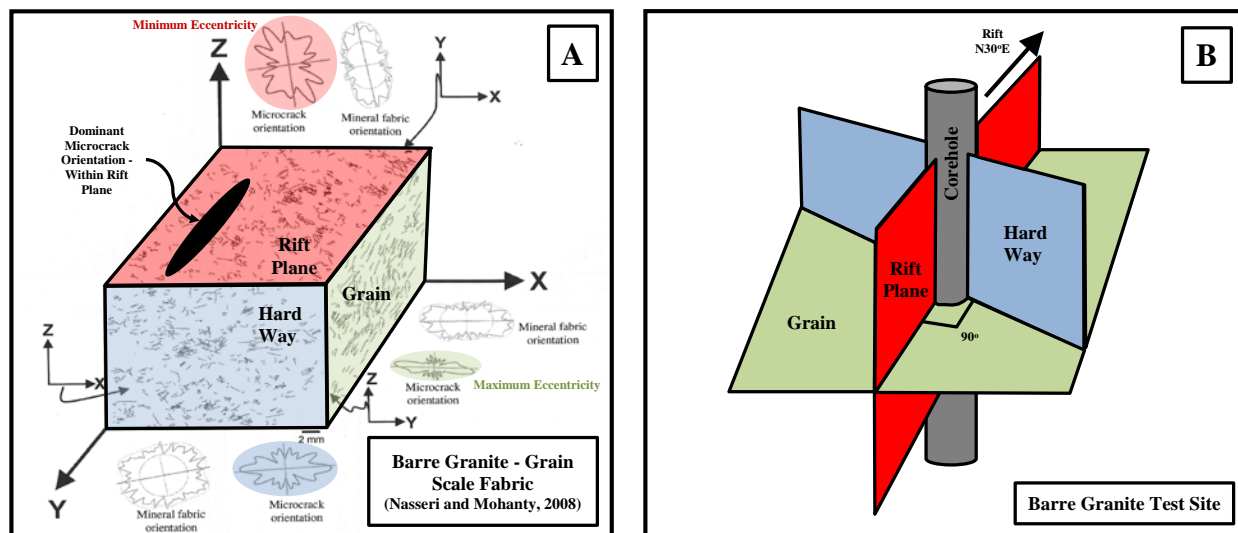


Figure 11-1. Pervasive rift microfabric due to microscale fractures, in Barre Granite. A: Microscopic analysis interpretation by Nasseri and Mohanty, 2008. B: Granite planarities orientations at the test site.

Visible fractures were observed on quarry faces with spacing on the order of 4 to 5 m. The fractures are typically clean, planar sub horizontal features, which represent sheeting joints that follow the topography (Richter, 1987). The general homogeneity was confirmed with a ground penetrating radar (GPR) study of the site and a borehole geophysical logging program using an oriented acoustic televiewer, an optical televiewer, and a caliper log. In addition, detailed observations on two pre-shot coreholes verify the low fracture density. The site is above the water table; no water infiltrated the emplacement holes for the explosives.

The Barre Granite is mineralogically homogeneous over a wide area. Little variability in bulk density and grain density were noted, so limited measurements were carried out on the pre-shot specimens. Representative data are presented in **Table 11-1**. The data show small variability in the undisturbed cores, but a clear reduction in density and increase in porosity over the blast interval in CH-3. These changes are most likely due to an increase in the size and density of microcracks. A photomicrograph of the Barre is shown in Figure 11-2. The composition of the granite is microcline 21%, orthoclase 35%, quartz 27%, biotite 9%, muscovite 6% with various accessory minerals (VT Geological Society, web 2008). The composition of the granite is uniform throughout the test site (Richter, 1987).

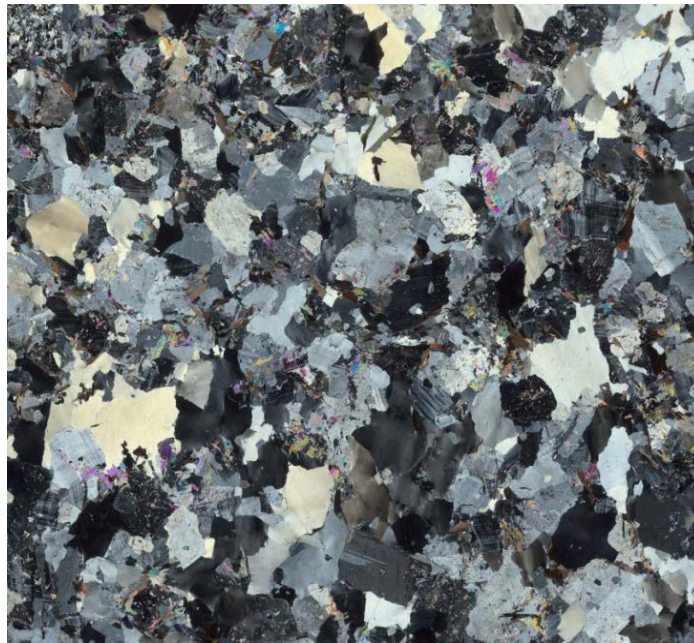


Figure 11-2. Photomicrograph of Barre Granite thin section taken at a depth of 46.5 ft (14.2 m) in the CH-1 core. View taken with polarized light. The plane of the section is perpendicular to the rift plane.

COREHOLES

After the five detonations fourteen additional coreholes were drilled to examine the spatial distribution of damage . The locations of the boreholes are shown in Figure 11-3.

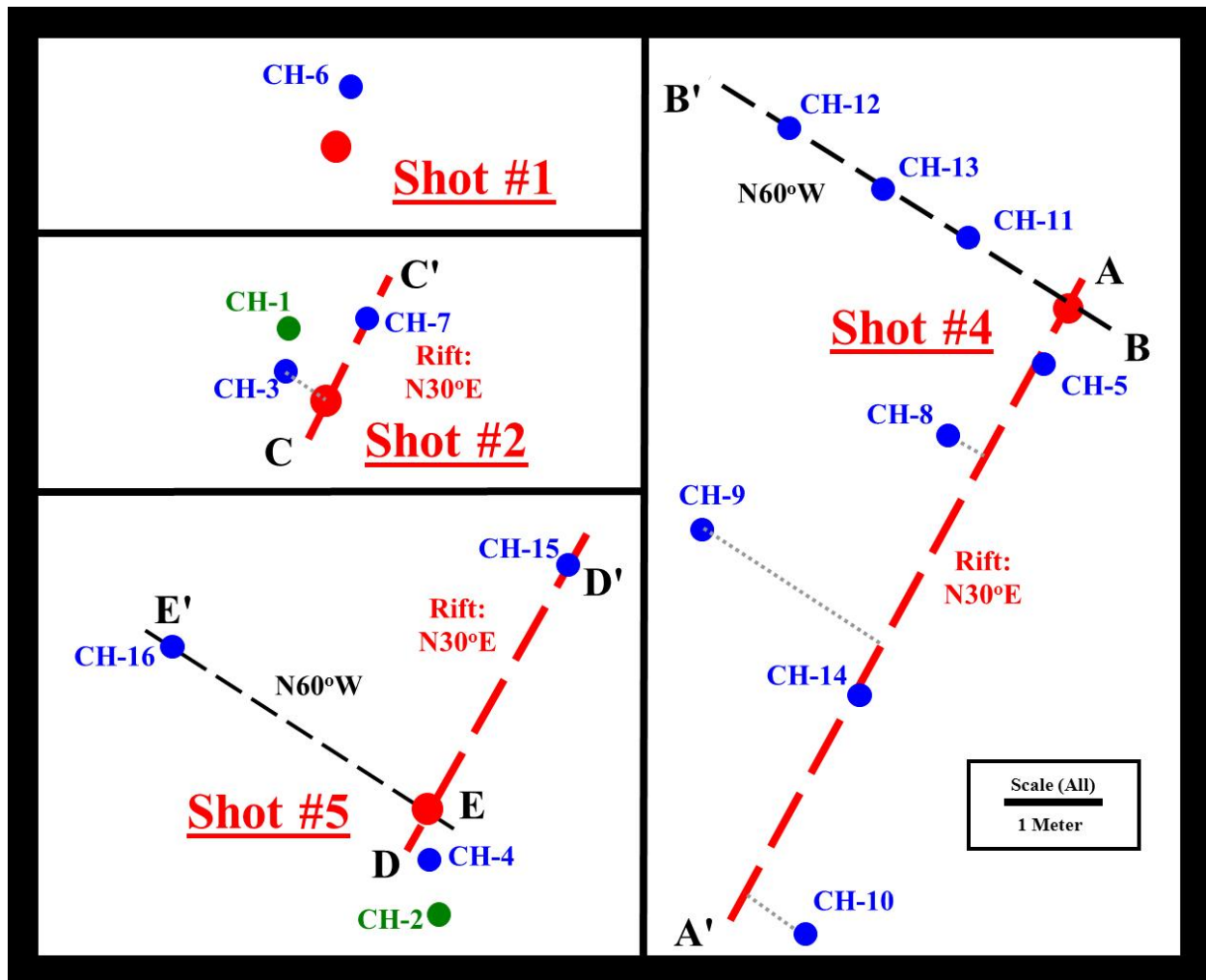


Figure 11-3. Locations of shotholes and coreholes (Green – pre-shot and Blue – post-shot) at the NEDE site. No cores were retrieved at Shot #3. Core diameter is nominally 51 mm.

ROCK PROPERTIES

A comprehensive suite of laboratory scale measurements were performed on the core to determine the properties of the site in the pre-shot condition. The measurements included:

- Bulk properties,
- Diametral P and S-wave velocities along the axis of the core recovered from coreholes,
- Compressional and shear wave velocities as a function of pressure,
- Linear compressibility as a function of pressure,
- Fluid permeability as a function of pressure,
- Electrical resistivity as a function of pressure, and
- Rock strength.

Table 11-1. Bulk Properties of Barre Granite

	Pre Shot	Post Shot
Grain Density, g-cm ⁻³	2.66-2.76	2.66-2.76
Dry Bulk Density, g-cm ⁻³	2.63-2.65	2.60-2.63
Porosity, %	0.7-1.3	1.4-2.5

DAMAGE ANALYSIS

To quantify the damage to the granite resulting from the explosions, the physical properties of the granite were measured from cores recovered from holes drilled before the detonations for comparison to the post-shot results. Two control holes were cored, one adjacent to the emplacement hole for Shot #2 and one adjacent to Shot #5, as shown in Figure 11-3. There was complete core recovery from the pre-shot coreholes.

The *P* and *S*-wave velocities were measured on the each core as a function of depth and azimuth at ambient conditions. Time of flight velocity measurements were performed normal to the core axis along the core in a bench top apparatus. At each point, the core was rotated between the transducers. The velocity varied with azimuth. A typical data set collected with the bench top setup is shown in Figure 11-4. Velocity increases from a minimum value of 3.84 km/sec to a maximum value of 4.56 km/sec as the core was rotated 90° from the minimum value. The two pre-shot cores were evaluated in this way and the location of the rift was marked on the surface of the core. This facilitated sub-coring for subsequent experiments at pressure. Figure 11-5 shows the velocity data parallel and normal to the rift as a function of depth for the core recovered from pre-Shot #2 corehole CH-2. Note that there is scatter in the velocity and a gradual increase with depth.

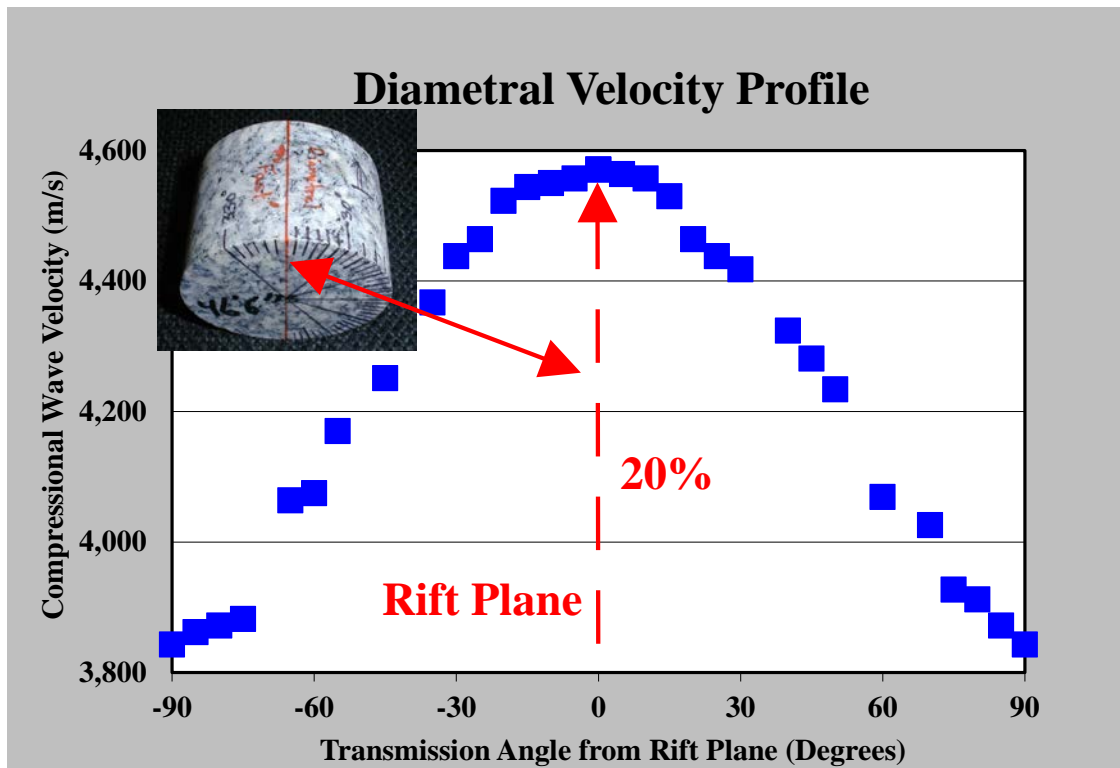


Figure 11-4. Compressional wave velocity measured as a function of orientation in the Barre granite. *The rift plane is oriented in the direction of fastest velocity and is parallel to the core axis.*

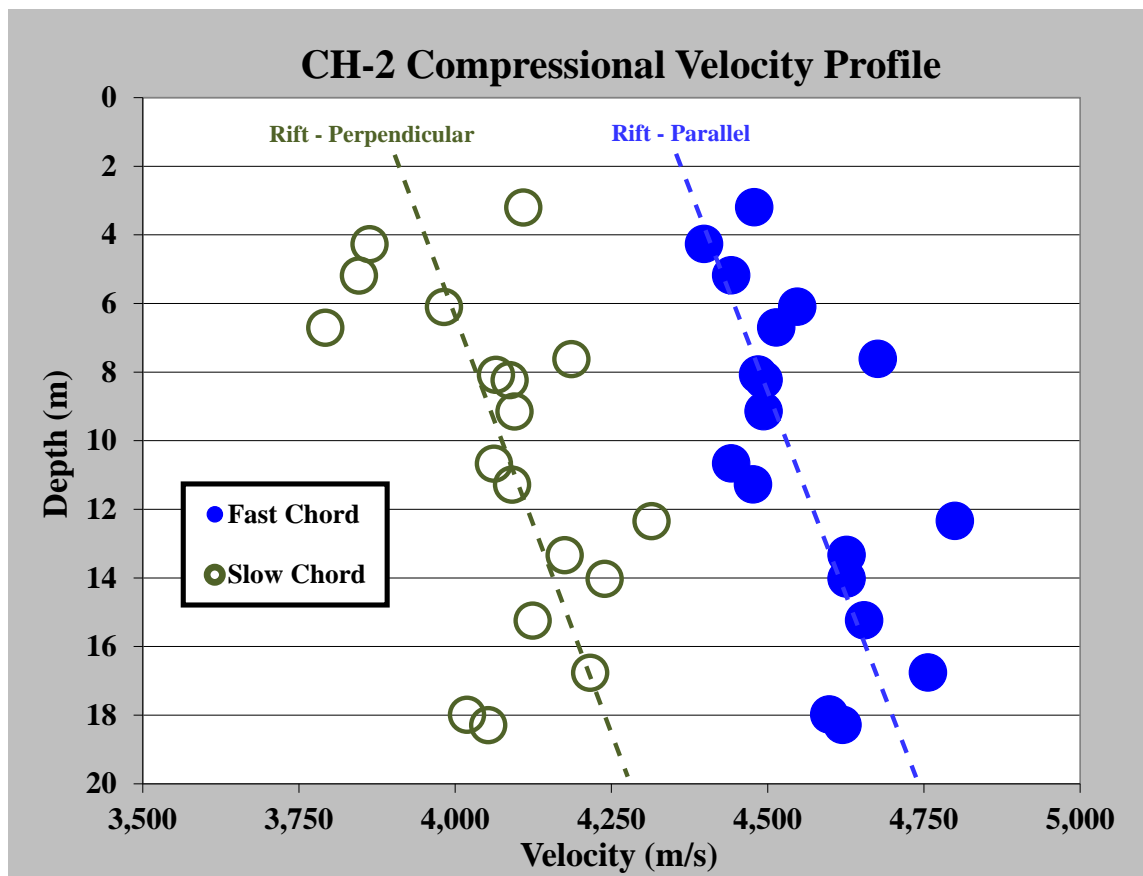


Figure 11-5. Pre-Shot #2 fast (parallel to the rift) and slow (perpendicular to the rift) compressional wave velocities as a function of depth at corehole CH-2. *Note the increase in velocity with depth at this location.*

To further evaluate the anisotropy oriented sub-cores 38 mm in diameter and 38 mm in length were cut parallel, normal and at 45 degrees to the rift. Measurements of compressional and shear wave velocity, compressibility, electrical resistivity, and permeability were performed as a function of pressure and orientation to the major granite planarities. An example of the change in compressional wave velocity as a function of confining stress is shown in Figure 11-6. These data are discussed in more detail in the Experimental Studies on Barre Granite section.

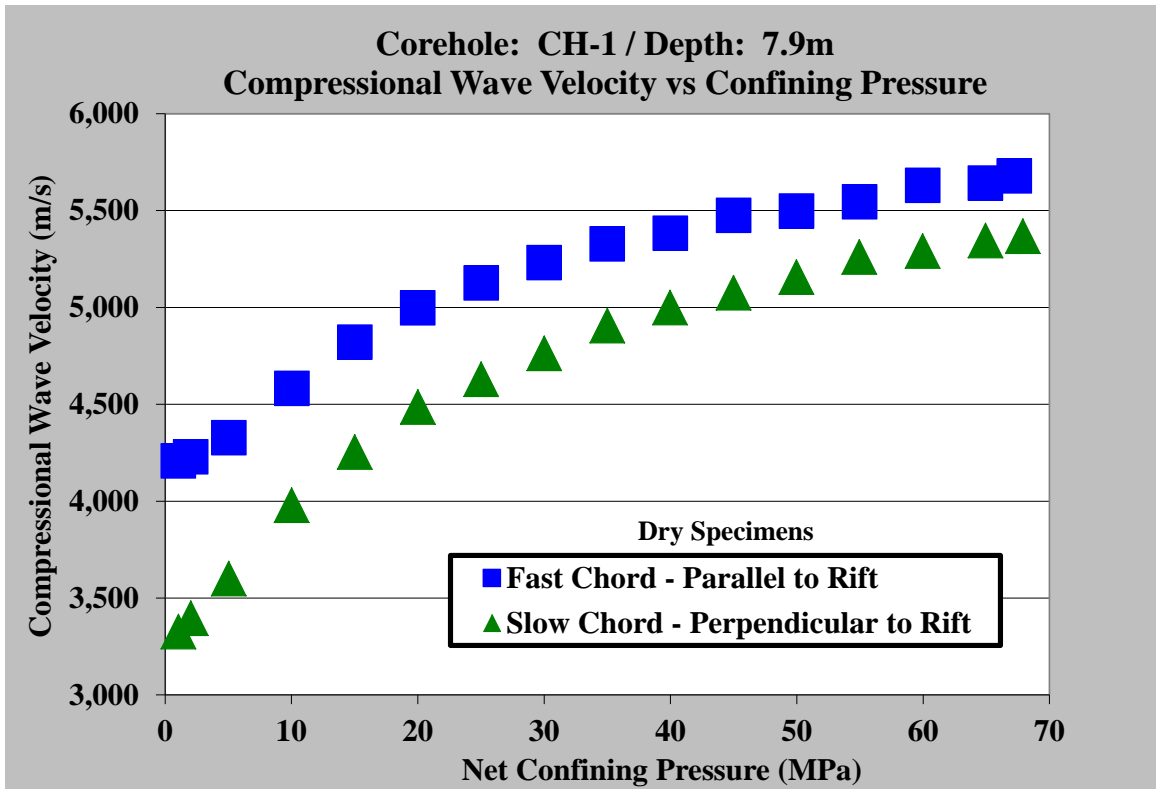


Figure 11-6. Example of compressional wave velocity change as a function of confining stress. Responses of both the fastest (parallel to rift) and slowest (perpendicular to rift) orientations are presented. The slow chord experiences the most significant velocity increase with pressure.

The initial velocities were 3.325 km/sec normal to the rift and 4.205 km/sec parallel to the rift. With increasing pressure the velocities increased; the rate of increase was greater for propagation perpendicular to the rift. The initial elastic anisotropy of 21% decreased to 5.5% at a pressure of 70 MPa. Presumably, if the tests were carried out to pressures of several hundred MPa, most of the microcracks would close and the velocities would asymptotically approach the same value. The samples were then saturated with a weak brine and measurements of permeability and electrical resistivity were carried out as a function of pressure. The initial permeability anisotropy decreased from 27% to near zero with a moderate increase in pressure. The resistivity anisotropy did not exhibit the strong pressure dependence observed for velocity and permeability. Although the resistivity for both orientations increased three-fold with pressurization to 50 MPa, the anisotropy remained more or less constant at 26 to 28%. These data are consistent with previous studies on granite.

Damage Analysis: Post-Shot Studies

After the five shots were detonated, a comprehensive study was undertaken to examine the damage generated in the vicinity of four of the shot holes (Shot #3 was not examined). Of particular interest are the types of damage that occurred and the extent of the damage laterally and vertically away from the working point. Blast induced damage can be characterized at three scales: macro (distinct, singular fractures at hand specimen/core scale), meso (highly fragmented to granulated zones with indistinct fracture planes), and micro (microscopic). Larger scale

damage is present at all shot locations, but microscale damage is only observed at the higher VOD (ANFO and COMP-B) shots. Characteristics of the explosives are given in Figure 11-7.

<ul style="list-style-type: none">• Black Powder – <u>Slow VOD</u> (< 0.5 km/sec)• Heavy ANFO – High Explosive – <u>Fast VOD</u> (~ 5 km/sec)• Composition B – High Explosive – <u>Fast VOD</u> (> 7.2 km/sec)	
---	---

Figure 11-7. Characteristics of the explosives used at the test site. *Rock damage is strongly dependent on the Velocity of Detonation (VOD). Shot #1: Blackpowder / Shots #2 and #4: ANFO / Shots #3 and #5: COMP-B.*

There was little surface expression due to the explosions. Surface fractures were observed at the black powder and the two ANFO shots; none were observed in the vicinity of the COMP-B shots. To further characterize changes in the vicinity of each shot point, a GPR study was initiated. The goal of the study was to look for new fractures that developed due to the explosions and to examine the extent of fracturing away from the shot point. These studies proved inconclusive. They were unable to delineate fragmentation or new fractures that developed in the vicinity of each shot point. However, the GPR survey verified that the site was generally homogeneous.

A detailed coring program was undertaken to allow for the examination of subsurface characteristics of the damage generated by each detonation. Following the detonations, fourteen coreholes were drilled at various distances from each shot point. Figure 11-3 gives the location of the coreholes with respect to the shot points. The depths of the coreholes ranged from 19.8 to 23 m. The pre-shot cores were recovered with few pre-existing meso- or macroscale fractures, and only had evidence of the rift at the microscale. In contrast, the post-shot cores show extensive damage. The intensity of the damage decreases with range from the blast point. Importantly, the core collected adjacent to Shot #1 (the lowest VOD shot), although having

extensive larger scale damage, showed no microscale damage. This shot also produced the greatest shear wave amplitudes.

In order to quantify the radial and vertical extent of the damage, Shot #4, a 122.7 kg ANFO detonation, was selected for detailed study. Five coreholes were drilled along the trend of the rift, from the working point to a range of 7.01 m, as shown in Figure 11-3. Additionally, three coreholes were perpendicular to the rift. The large scale and microscale damage within the core were studied. Figure 11-8 presents a schematic interpretation of these data. The geometries of the distinct damage regions are complex. The most definitively defined are the microscale features. Of particular note is that macroscale fracturing extends below the explosive charge only in very close proximity to the working point, but it is not found below the working point just a short distance away, and it extends laterally beyond the farthest borehole parallel to the rift. The free surface and confinement with depth below the blast control this result.

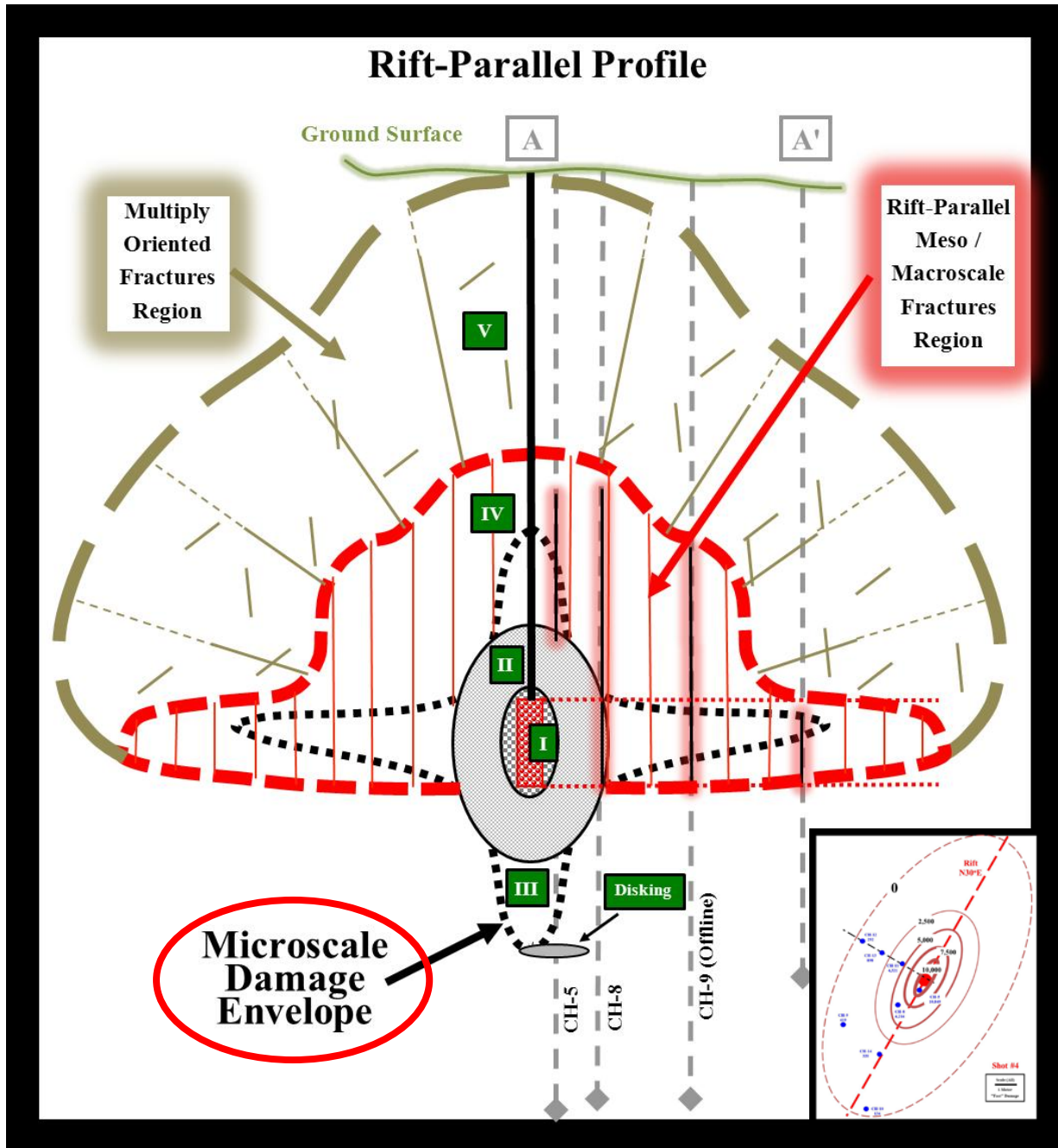


Figure 11-8. Schematic cross section at Shot #4 showing the distribution of damage at all scales. Distinct damage regions are identified. The non-spherical geometry of damage is evident, including in plan view, as depicted at lower right.

We identified five distinct zones based on the degree of rock damage, which are delineated in Figure 11-7. Figure 11-8 shows examples of core specimens from each zone, and a brief description of each follows. An assessment of the data yields a damage surface that is non-spherical. Similar findings were also seen for a limited number of cores recovered adjacent to the 61.4 kg ANFO shot and the 122.7 kg COMP B shot.

The distinct damage zones include:

- **Damage Region I:** Highly pulverized/granulated with cavity development (wall collapse) possible. Microscale damage is extreme.
- **Damage Region II:** Significant disaggregation with numerous high angle fractures that strike parallel to the rift. Extreme microscale damage is also evident in intact core pieces. Damage extends above and below explosives emplacement level.
- **Damage Region III:** Generally intact. Extent of region determined with acoustic velocity measurements; the microscale damage greatest nearer to shot point. Core can take on a "milky" appearance due to the microscale damage. High angle fractures parallel to the rift present in only the portion of region above the emplacement level.
- **Damage Region IV:** Generally intact with few high angle fractures that are all parallel to the rift. Microscale damage only exists close to the working point.
- **Damage Region V:** Mostly intact with few fractures that are generally randomly oriented. Large scale fracturing extends to the surface at the Black Powder and ANFO/Emulsion shots. Microscale damage is not present.
- **Core Disking Feature:** Core disking was encountered in three coreholes. It was most prevalent at Shot #5 in CH-4, and in all cases is located within or very near the explosives column level. Disking is created by the action of the coring operation and is attributable to residual horizontal stress at depth. In this case, the stresses had most certainly been induced by the blasts.

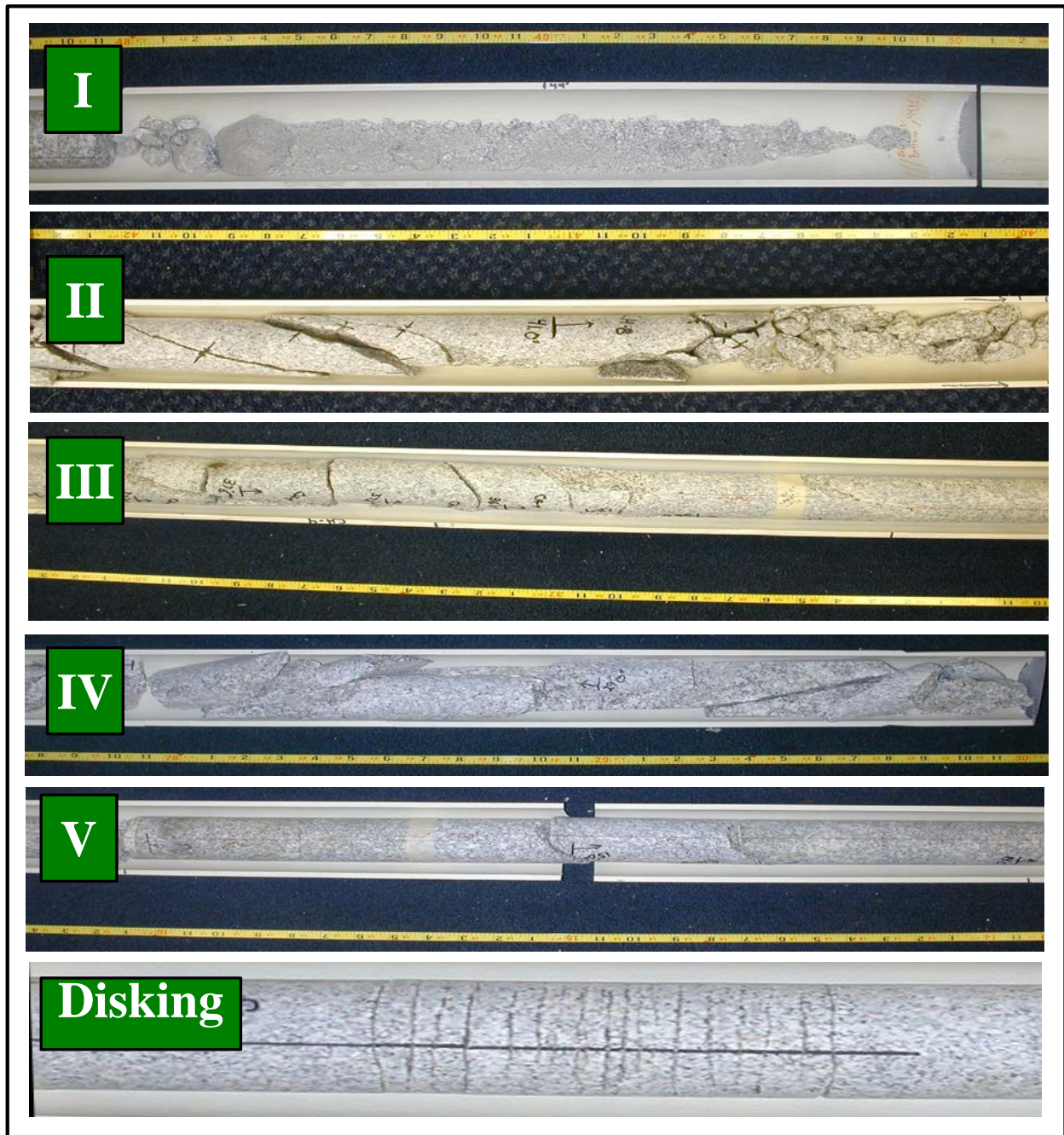


Figure 11-9. Examples of damage regions outlined in Figure 11-8. *The damage is transitional in intensity and in mode of formation.*

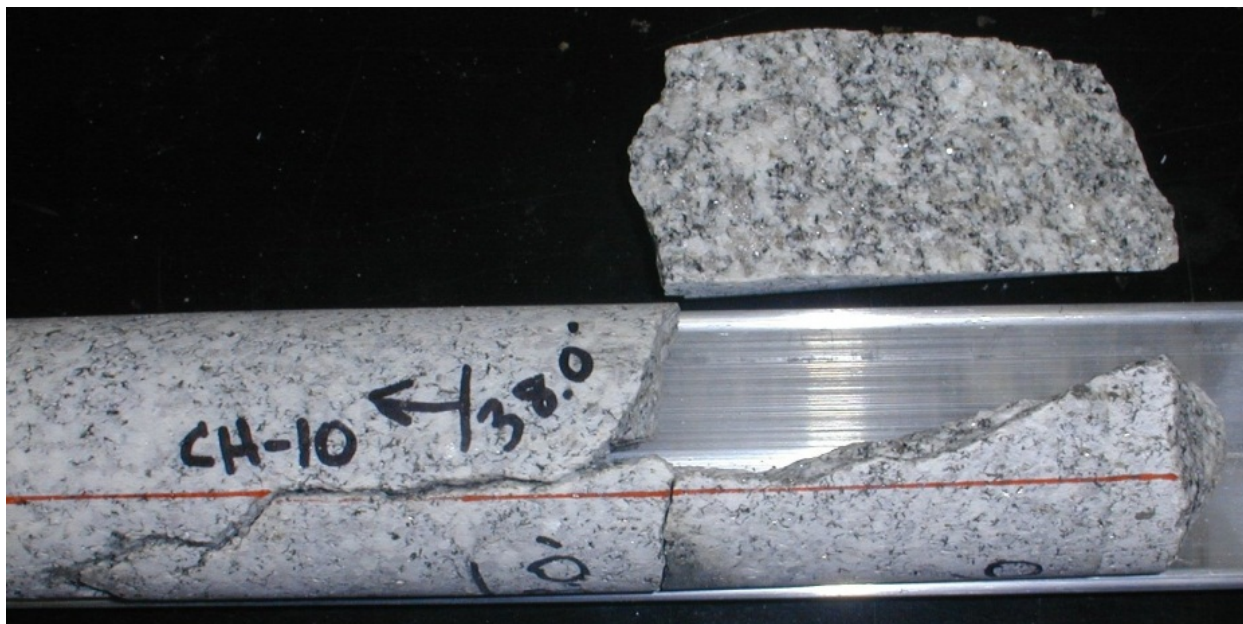


Figure 11-10. A section of core from CH-10 recovered from a depth of 38 feet exhibits fracturing in the plane of the rift.

The rift is well known to be a plane of weakness that has long been taken advantage of by stone carvers. On many of the pieces of core (particularly near the working point, see Region IV) the strike of the fracture planes parallel the rift as shown in Figure 11-10. This suggests that the rift at the site controls not only the elastic properties, but also the mechanical properties. To study this effect, a confined compression experiment was carried out on a cylindrical sample with its axis parallel to the core hole. The rift was identified and the specimen was instrumented to monitor strain parallel and normal to the rift, and parallel to the loading axis. In addition, compressional and polarized shear waves were propagated parallel to the core axis (see Figure 11-11). The shear wave polarizations were oriented parallel and normal to the rift. The sample compacted to approximately half the compressive strength and then began to dilate, that is cracks began to open (predominantly parallel to the loading axis). The transverse strains did not increase equally. The transverse strain normal to the rift increased more rapidly than the transverse strain in the rift plane. The difference persisted until the sample failed. At failure, the strike of the fracture plane was parallel to the rift. The shear velocities increased up to approximately half the compressive strength, remained more or less constant to three quarters of the strength, and then decreased continuously until the rock failed. For the shear wave polarization in the rift, velocities increased more than those normal to the rift. As the sample began to dilate, the velocity for the vibration direction normal to the rift decreased with respect to waves vibrating parallel to the rift. A more detailed discussion of this test is given in the Experimental Studies on Barre Granite section.

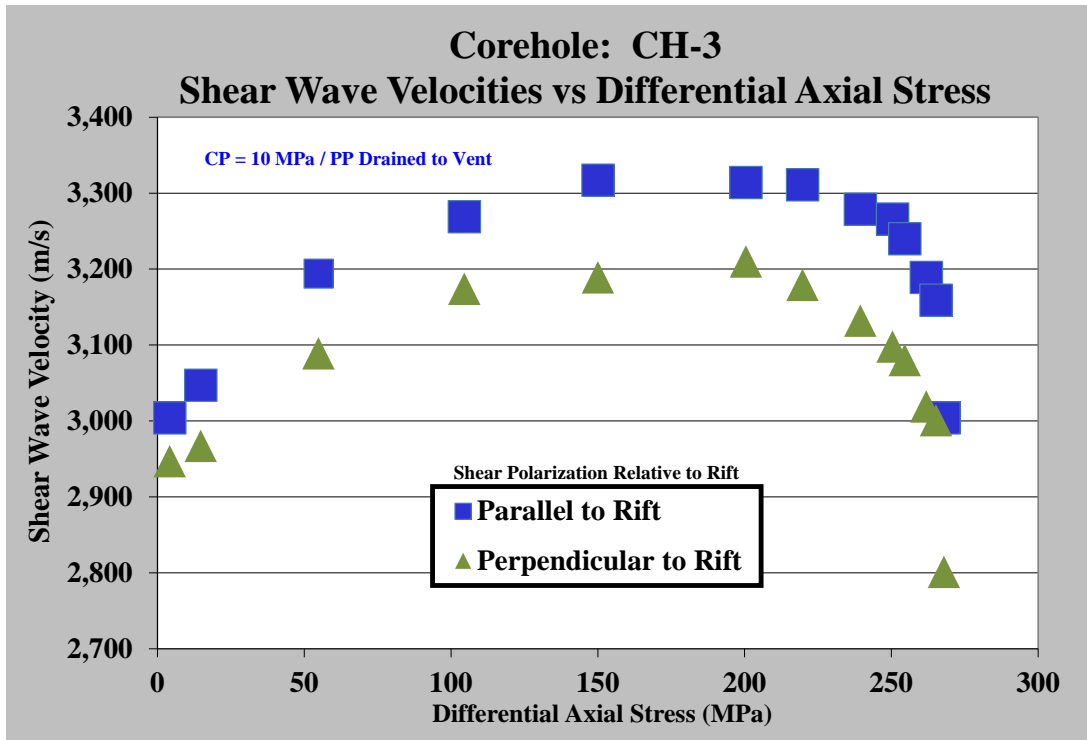


Figure 11-11. The effect of differential axial stress on shear wave velocity in a Barre granite specimen loaded to failure in confined compression.

Microscale damage is quantifiable and can be accurately delineated at the site. Interestingly, a much earlier investigation on the HARDHAT shot in granite at the National Test Site in Nevada (Short, 1966) also reported blast induced microscale damage, but that analysis was unable to delineate the three dimensional geometry of damage. For the Barre site, each core was photographed and then bench top *P*- and *S*-wave velocity measurements were carried out on the otherwise intact pieces of core to infer the magnitude of the microscale damage with depth and azimuth. Figure 11-12 shows the *P*- and *S*-wave velocities as a function of depth for a core recovered adjacent to Shot #5. The emplacement zone for the explosive is shown. The compressional and shear wave velocities decrease by 15 to 20%, or more compared to the pre-shot values over a 5m interval centered on the working point.

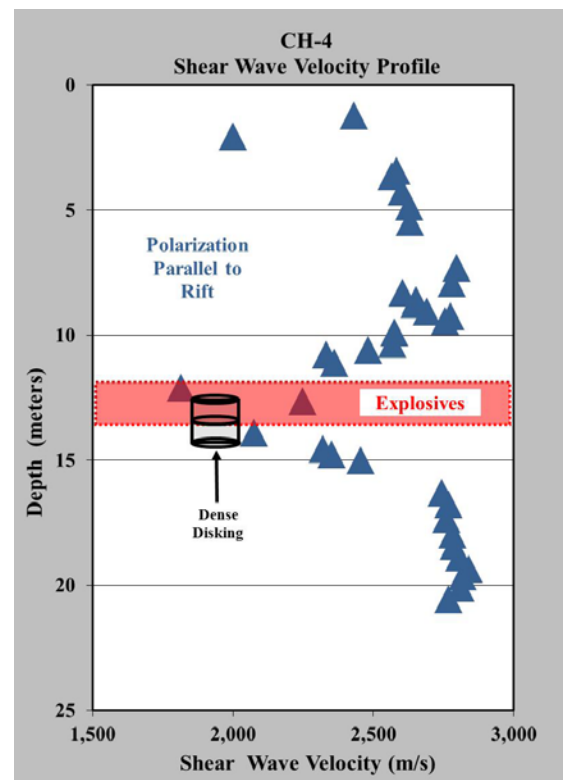
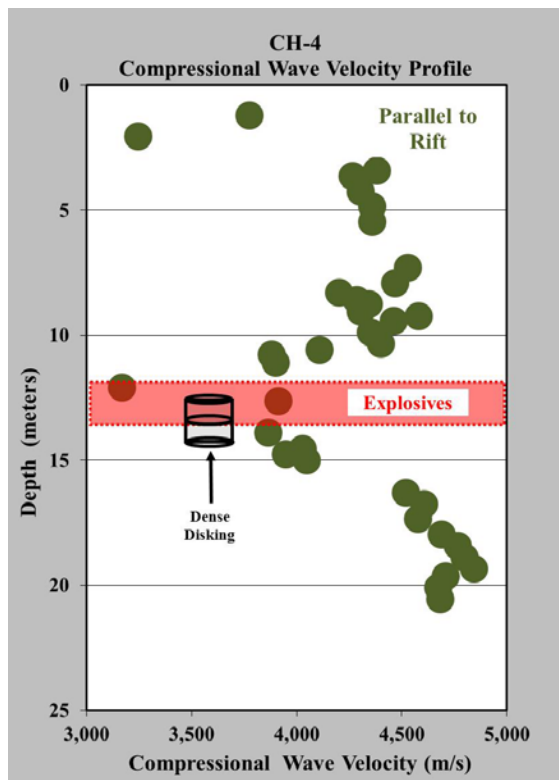


Figure 11-12. Corehole CH-4 P-and S-Wave velocity profiles at Shot #5 (COMP-B). *The low velocity region reflects the microscale damage induced by the blast. Note that the damage intensity increases with greater proximity to the explosive charge. The extent of the damaged zones also scales with the yield of the blast.*

Microscale damage was also evident from measurements of permeability and resistivity, as shown in Figure 11-13. The increase in microscale fracture density is significant enough to noticeably impact all of these microscale sensitive laboratory measurements. Similar effects were observed in each of the post-shot coreholes adjacent to the high VOD Shots, but were not observed at the low VOD Shot #1 (see Figure 11-14).

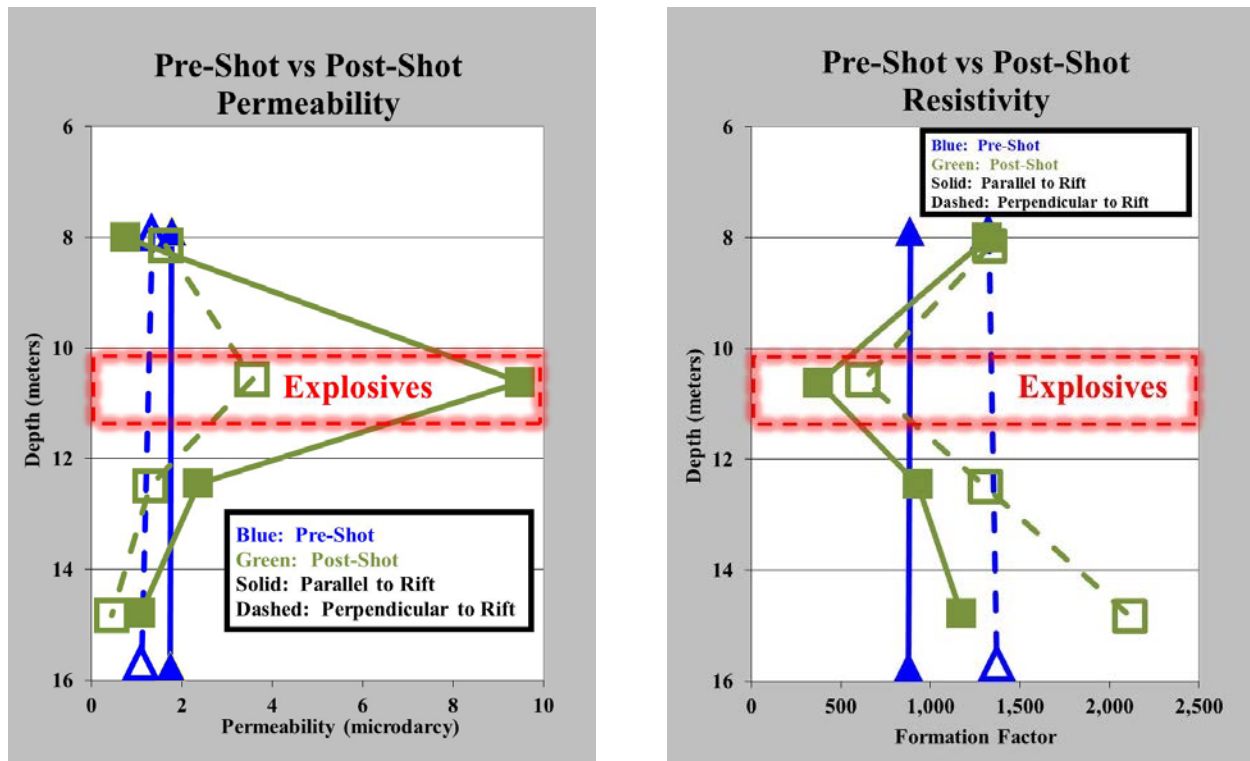


Figure 11-13. Pre-Shot (CH-1) and Post-Shot (CH-3) permeability and resistivity results at Shot #2 (ANFO). *Microscale fracturing due to the explosion impacts measurements that are sensitive to that scale. Anisotropy due the rift is also evident.*

As shown in Figure 11-3, eight coreholes were drilled near Shot #4. The locations of the coreholes were selected to investigate the extent of damage outward from the blast parallel (N30°E) and perpendicular to the rift strike. Each new corehole position was based on the extent of damage (slowing of the compressional wave velocity due to microscale damage) observed in the previous one. The objective was to determine the boundary between the damaged (inelastic) zone and the elastic regime.

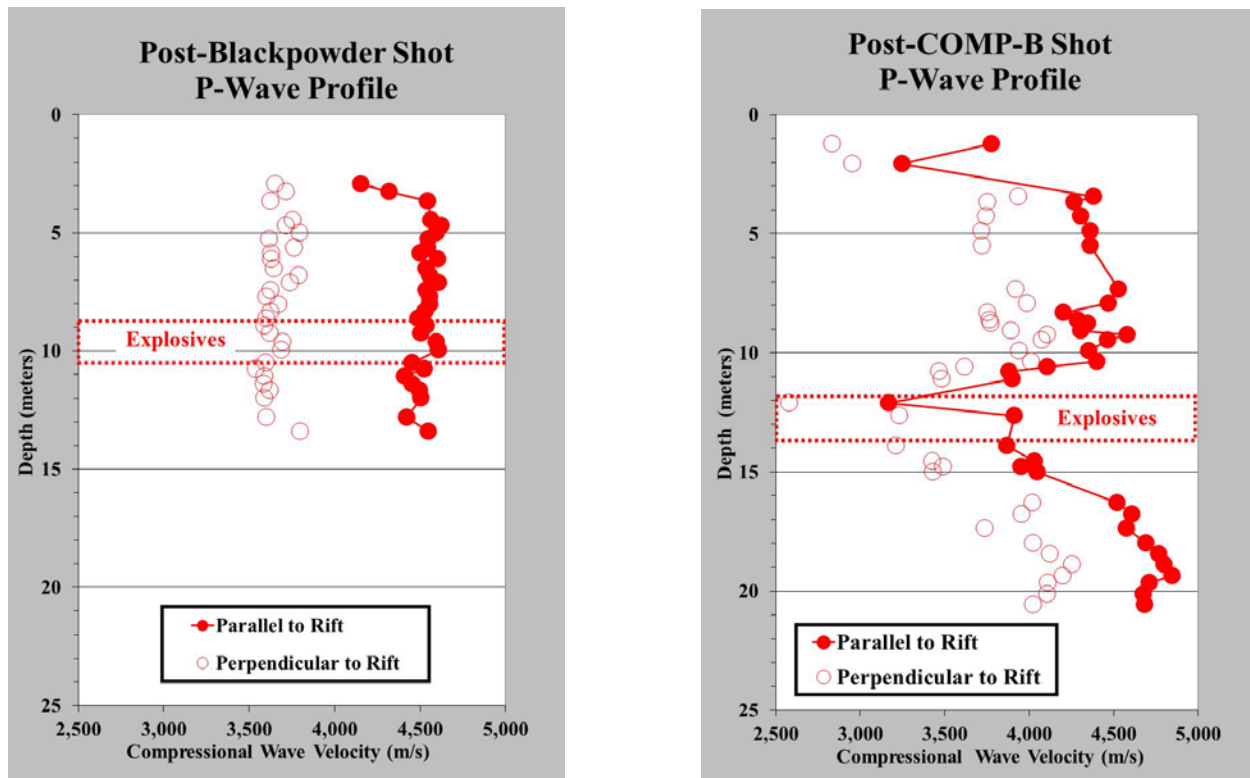


Figure 11-14. Comparison between microscale damage, as evidenced by compressional wave slowing at high explosive Shot #5 (COMP-B), vs no microscale damage evidenced at low VOD Shot #1 (Blackpowder).

The vertical velocity profiles, as compiled into the cross section shown in Figure 11-15, were analyzed to determine the boundary between the elastic and inelastic (damaged) regions. Moving away from the working point of the blast, the thickness of the microscale damage zone decreases from as much as 13 m adjacent to it, to approximately 1 m at a range of 7.01 m. The same section, at equal scales, is shown in Figure 11-16. The non-spherical nature of the damage is evident, and its reach is greater than had been predicted from previous studies.

The microcrack damaged interval is large near the shot, but narrows within a short distance from the shot and extends horizontally for several meters. The cross sectional shape of the microcrack damage zone was not what has been suggested in the past (Figure 11-8 and Figure 11-16). Based on the existing literature, we expected a more spherical shape for the transition to elastic behavior.

The analysis of the cores collected for coreholes CH-5, CH-11, CH-12, and CH-13 normal to the rift confirm the influence of the rift on the explosion generated damage. In Figure 11-17, the damage profile perpendicular to the rift is shown alongside the damage profile parallel to the rift. The damage zones are compressed for the section normal to the rift but the shape of the profile is the same as the section parallel to the rift. Based on these data, a contour map of the damage in the vicinity of Shot#4 was constructed.

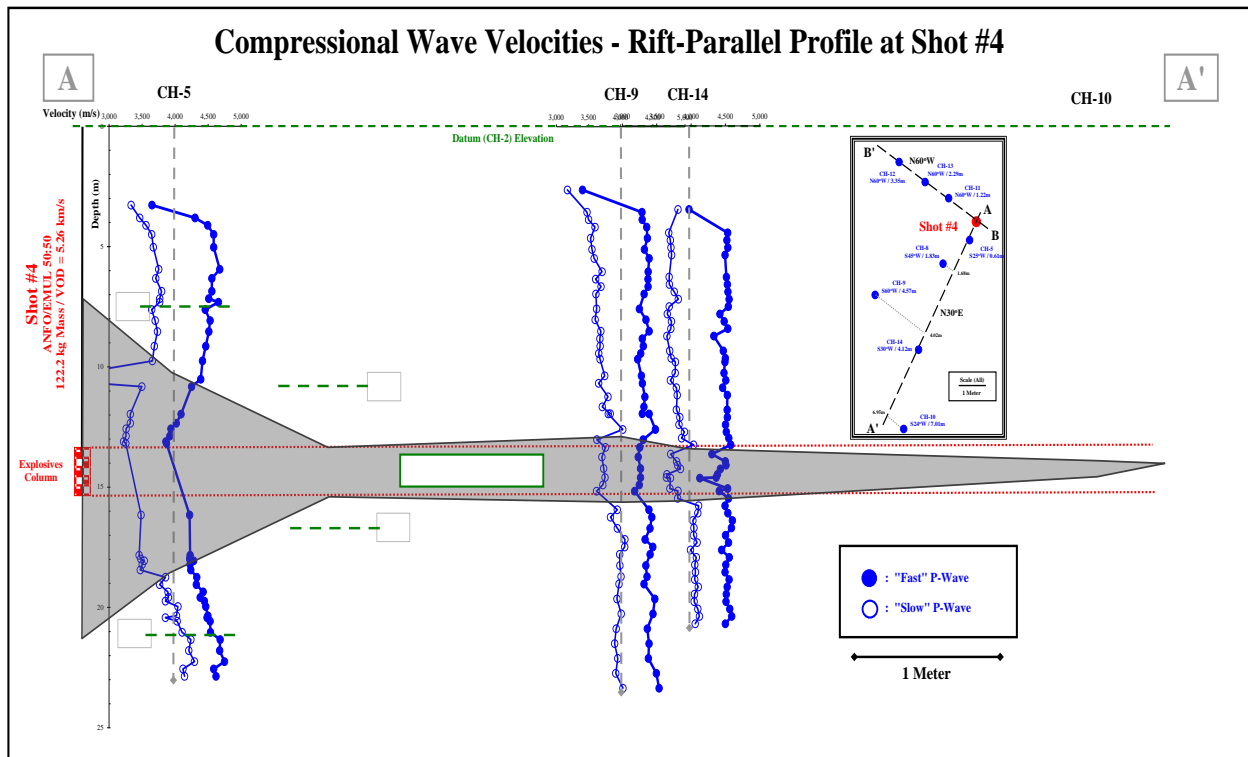


Figure 11-15. Cross section, based on detailed vertical velocity profiles of the coreholes at Shot #4, are drawn parallel to the rift. *The horizontal scale is expanded. Lateral extent of the damage parallel to the rift is evident. Corehole locations are also shown in Figure 11-3.*

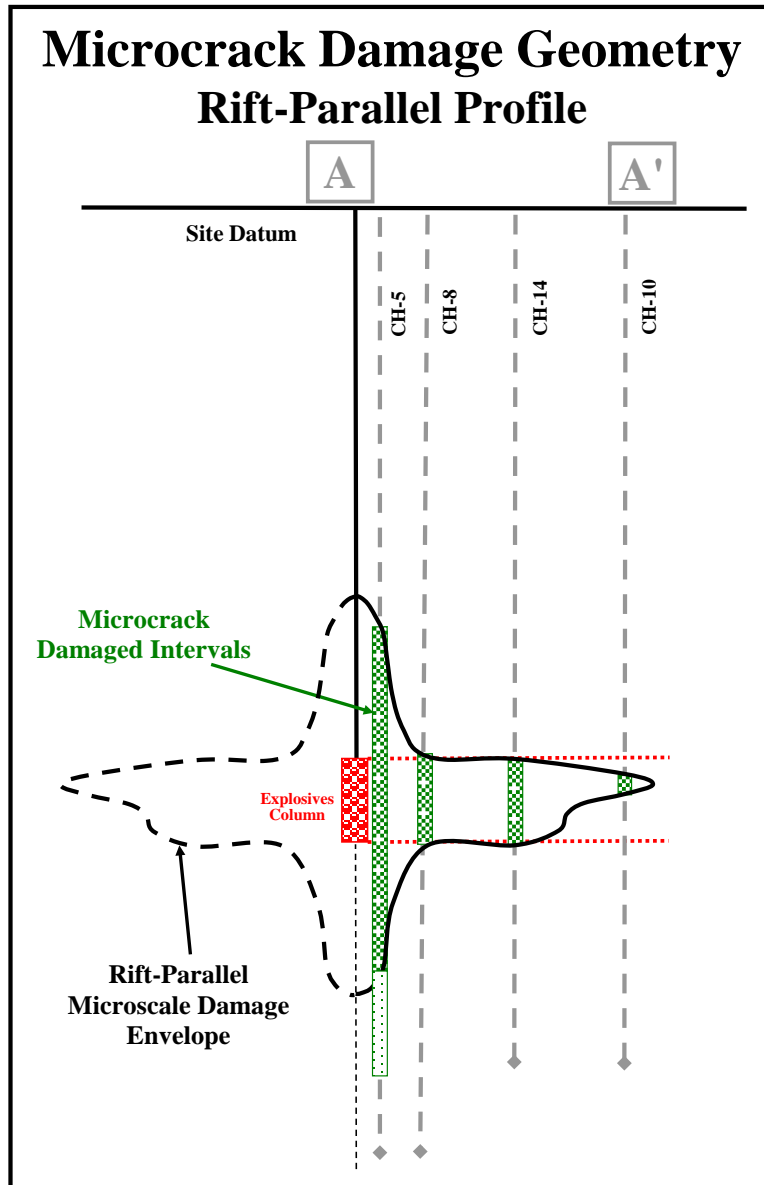


Figure 11-16. Cross sections, as in Figure 11-14, but drawn with vertical and lateral scales equal. *Microscale damage is non-spherical and its reach is greater than had been predicted. The coreholes analyzed to define the damage geometry are shown in the cross section.*

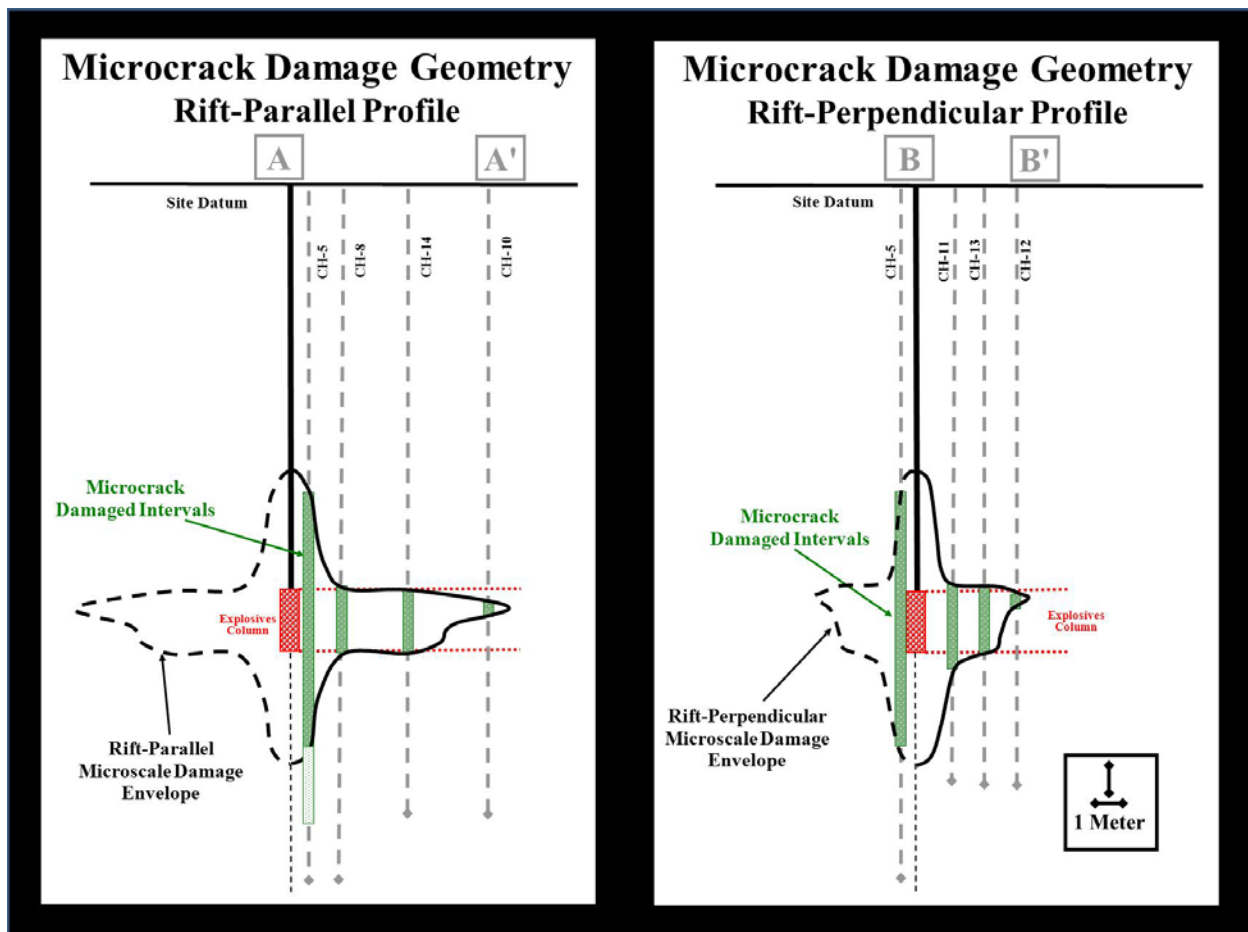


Figure 11-17. The coreholes analyzed to define the damage geometry are shown in the cross section. Microcrack damage profiles for a 122.7 kg ANFO shot in Barre, VT. The cross section in the plane of the rift is on the left. The cross section perpendicular to the rift is on the right. The relative location of the coreholes and their depth are shown for each projection. The charge was emplaced at a depth of 12.8–13.7 m.

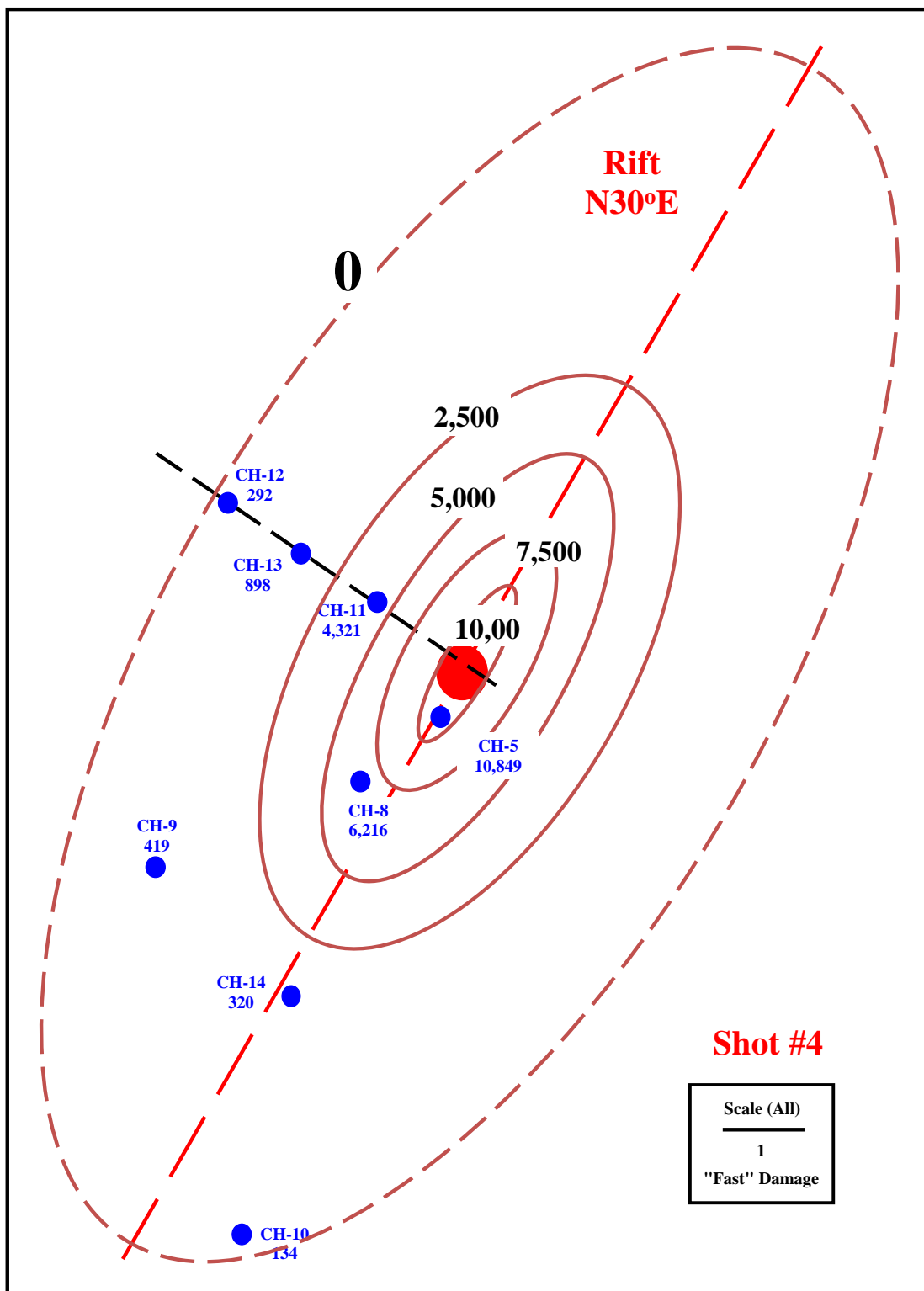


Figure 11-18. Plan view of the damage contours for a 122.7 kg ANFO shot in Barre, VT. The locations of the vertical coreholes are shown. Core recovery was limited to the SW quadrant. Symmetry was assumed along the plane of the rift to develop representation of the iso-damage levels.

SUMMARY AND CONCLUSIONS

Pre- and post-shot cores show that after the blast, the rock near the shot point had decreased density, increased porosity, higher permeability, lower resistivity, higher compressibility and acoustic velocity reductions on the order of 20%, or more. The damage region is non-spherical with enhanced damage occurring in the horizontal plane of the explosives emplacement. As illustrated in Figure 11-18, one interpretation of the data is an elliptical shape of the damage in plan view. The compilation of these observations coupled with the larger scale fracture damage suggests that the existing models for the nature of the damage, and the zonation of that damage, generated by underground explosions, needs to be reconsidered. Obviously, the incorporation of these data into models for shear wave generation may help explain many of the seismic observations.

Initially, the field program was designed for an isotropic rock mass with low fracture density. The Barre granite is strongly anisotropic. An anisotropic rock mass is a disadvantage for a field study. Modeling the response of the site due to an external stimulus, such as an explosion, in terms of fluid flow, electrical resistivity, seismic wave propagation, static elastic constants or failure require extensive knowledge of the anisotropic properties of the rock. The data collected on this project are essential to develop a model for the seismic and mechanical response of the fully coupled, shallow, chemical explosions in the Barre granite. The asymmetrical shape of the damage zones, elliptical in plan view and cross section with the major axis striking parallel to the rift, suggest that the initial anisotropy of the rock controls the damage and possibly the seismic observations in both the near and far field. The extensive documentation of the geophysical and mechanical properties of the granite, as a function of orientation with respect to the rift, will be integral in modeling the seismic response and the contribution of the source effects to the generation of shear waves.

EXPERIMENTAL STUDIES ON BARRE GRANITE

The observation that the damage zone was not axisymmetric through the working point or spherical in cross section, raises an obvious question. What controls the damage that was observed? The most obvious controlling parameter is the rift. The regions of similar damage parallel to the rift, extend further than the damage normal to the rift for both micro and macroscale damage. The initial anisotropy of the granite, especially in the near surface, plays a significant role in the distribution of damage due to each detonation.

To support the interpretation and modeling of the field observations, a suite of laboratory measurements were performed on the Barre granite. The following measurements were conducted as a function of confining pressure on oriented cores:

- Linear compressibility
- Compressional and shear wave velocities
- Confined compression to failure
- Permeability
- Complex resistivity.

CONFINED COMPRESSION TO FAILURE

The orientation of most of the fractures described in the damage analysis was parallel to the rift. In light of this, a confined compression experiment was conducted to evaluate the influence of the rift on the deformation and failure on the sample.

The test specimen was a ground right circular cylinder of Barre granite 25.4 mm in diameter and 55 in length. The specimen was tested room dry. The sample was jacketed with 0.127 thick copper foil. The ends of the sample were sealed and then the jacketed sample was subjected to 20 MPa of hydrostatic pressure to seat the jacket to the specimen.

After the jacket was inspected for leaks, the sample was instrumented for strain and velocity measurements. A typical configuration is shown in Figure 11-19. The sample was instrumented with three strain gauges to measure the axial strain parallel to the rift, the transverse strain in the plane of the rift, and the transverse strain normal to the rift.



Figure 11-19. A sample jacketed with copper showing the position of the strain gages and the transverse velocity transducers. *Transverse velocity was not measured on this test.*

The sample is then secured between a pair of PS² transducers as shown in Figure 11-20. The transducer propagates one compressional parallel to the core axis with a vibration direction parallel to the propagation direction and propagates two shear waves parallel to the core axis with vibration directions normal to the core axis; the polarizations are orthogonal. The shear wave polarizations were oriented parallel and normal to the rift.

The instrumented sample was inserted into a NER AutoLab 1500. The vessel was pressurized to 10 MPa. The granite specimen was monotonically loaded to failure while simultaneously measuring stress, strains, and compressional and shear wave velocities.



Figure 11-20. An instrumented sample assembly rests on the base plug of a NER AutoLab 1500. The jacketed sample is secured between two PS2 velocity transducers. The sample instrumentation is connected to a high pressure feed on the base plug.

Data for the confined compression experiment are shown in Figure 11-21. Stress difference is plotted as a function of strain in Figure 11-5. The axial strain data show that the sample compacted nearly linearly up to a failure stress of 279 MPa. In contrast, the radial strain deviated from linearity at a stress difference of approximately 125 MPa. The change in slope indicates that the sample is dilating. Numerous studies on the deformation of granites have shown that the non-linearity is due to the opening of microcracks parallel to the loading axis. After the initiation of dilatancy, the transverse strain normal to the rift increases more rapidly than the strain parallel to the rift. As the specimen approaches failure above 225 MPa, the strain normal to the rift increases nearly three-fold relative to that parallel to the rift. The sample failed at a stress difference of 276 MPa.

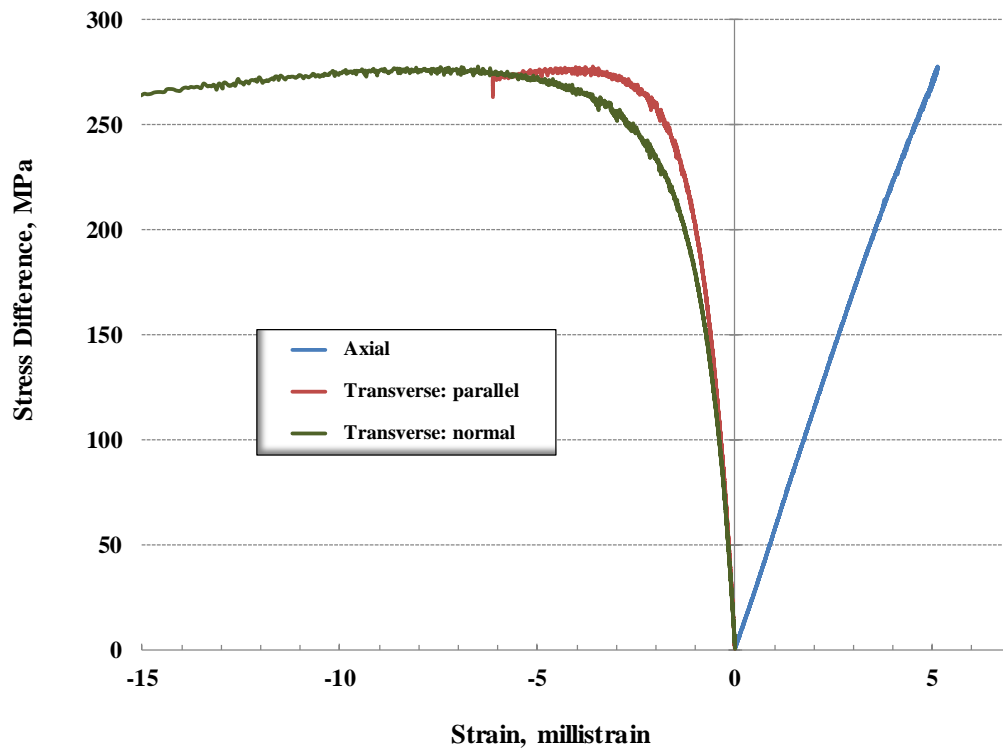


Figure 11-21. Data for a confined compression test on an oriented sample of Barre granite. *The axis of the core was in the plane of the rift. Strain gages were positioned parallel to the axis of the rift (axial), normal to the axis of rift (transverse normal), and parallel to the rift (transverse parallel). Stress difference is plotted as a function of strain. The test was performed at a confining pressure of 10 MPa.*

The shear wave velocity data for polarizations parallel and normal to the rift are shown in Fig. 11-16. The velocities for both polarizations increased with stress. At a stress difference of approximately 125 MPa, where the stress-strain behavior began to deviate from linearity, the rate of increase of velocity with stress began to decrease. At stress differences between 125 and 225 MPa, the velocities remained relatively constant or increased slightly. Above 225 MPa, the velocities began to decrease. The rate of decrease for the polarization normal to the rift exceeded that of the polarization parallel to the rift. These data are consistent with the strain observations. As penny shaped microcracks open in plane of the rift, the strain normal to the rift increases and shear waves with polarizations normal to the rift exhibit a decrease in velocity. The attenuations (Q^{-1}) were computed for each polarization using a spectral ratio technique. Q^{-1} began to increase noticeably beyond a differential stress of 225 MPa. The relative attenuation for the vibration direction normal to the rift increased two-fold compared to the attenuation parallel to the rift. These observations are also consistent with the stress strain data shown in Figure 11-22. Both the strain and acoustic data strongly suggest that microcracks preferentially develop and propagate in the plane of the rift with their flat surfaces in the plane of the rift.

The sample was removed from the sample vessel and examined. The orientation of the fracture was in the plane of the rift. As the crack density increased parallel to the rift, the cracks

coalesced and produced an instability which precipitated failure. These data re-enforce the observation that the granite failure *in situ*, especially in the high stress regimes, was influenced by the rift.

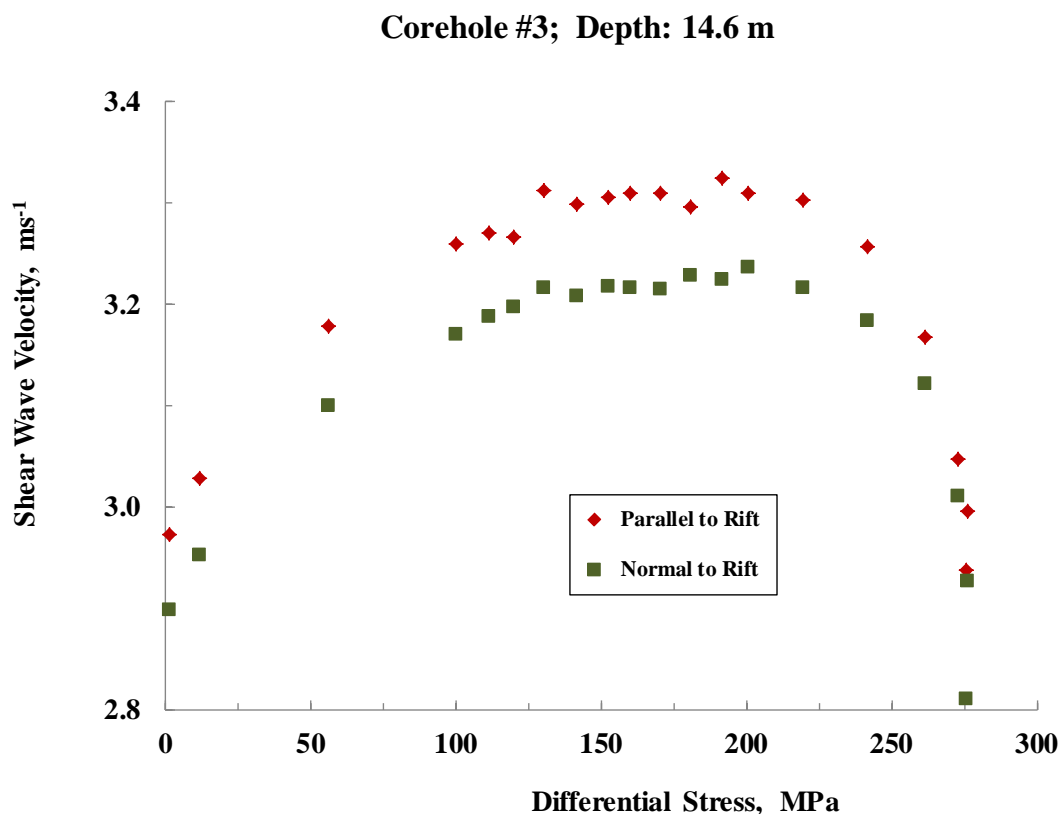


Figure 11-22. Polarized shear wave velocities are plotted as a function of differential stress for the confined compression experiment shown in Figure 11-4. *Propagation is parallel to the rift with shear vibration directions parallel and normal to the rift.*

ELASTIC ANISOTROPY

The next step is to quantify the influence of the rift on the elastic properties of the Barre granite. As the results of the confined compression test indicate, a preferred orientation of penny shaped microcracks strongly influences the properties of the granite. The seismic velocities and static moduli are strongly influenced by the length, aspect ratio, and density of microcracks (O'Connell and Budiansky, 1974). Therefore as pressure increases and cracks close, the bulk modulus and seismic wave velocities will increase. Since the Barre granite is anisotropic, the measurement of elastic properties must take into account the orientation of the rift.

The elastic properties were quantified using linear compressibility measurements with simultaneous compressional and shear wave velocities on oriented cores. The data reported here are on the intact sections of core. Earlier data on the anisotropy of granite suggest that they can be characterized as transversely isotropic (Lo et al., 1986). Pursuing this approach, a

synthesis of the elastic analysis will be outlined. In the most general case the stress strain relationship for an anisotropic material can be written as

$$\sigma_{ij} = C_{ijkl} \epsilon_{kl}$$

where σ_{ij} is stress, C_{ijkl} are the stiffness coefficients, and ϵ_{kl} is the strain; σ_{ij} and ϵ_{kl} are second rank tensors; C_{ijkl} is a fourth rank tensor. There can be up to 21 elastic coefficients for anisotropic rock. However, if the granite is considered as transversely isotropic, the number to elastic coefficients reduces to five. For this class, the axis to symmetry is normal to the rift and the properties in the plane of the rift are independent of orientation. Dealing with the full tensor notation is cumbersome. Consequently, a matrix notation is commonly adopted (Nye, 1957). In this case we can rewrite the expression as

$$\sigma_i = C_{ij} \epsilon_j \quad i, j = 1, 2, 3, \dots, 6$$

In this representation, C_{ij} are not the stiffness coefficients and do not transform as a second rank tensor.

A schematic diagram of the coordinate system with respect to the rift is shown in Figure 11-23. The 3 axis is normal to the rift the 1 and 2 axes are in the plane of the rift.

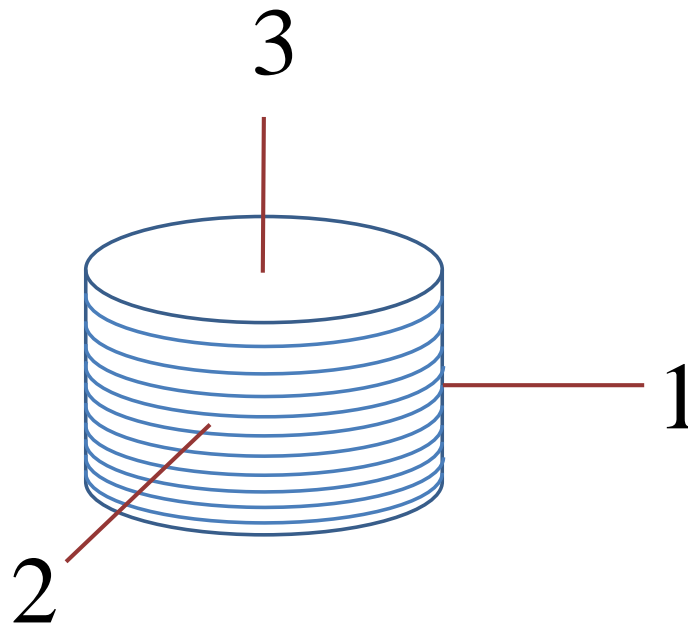


Figure 11-23. Reference coordinate system for a transversely isotropic rock.

To determine the five elastic constants, compressional and shear wave velocities (and/or stress-strain cycles) are measured on oriented cores. Figure 11-24 shows a schematic of elastic waves propagating parallel to the axis of symmetry, the 3 axis. V_{p33} is a compressional wave propagating normal to layering with a vibration direction parallel to the propagation direction. V_{s31} is a shear wave propagating in the 3 direction with a polarization in the parallel to the 1

axis. V_{S32} is a shear wave propagating parallel to the **3** axis with its polarization parallel to the **2** axis. Similar designations can be set up for each of the other propagation directions.

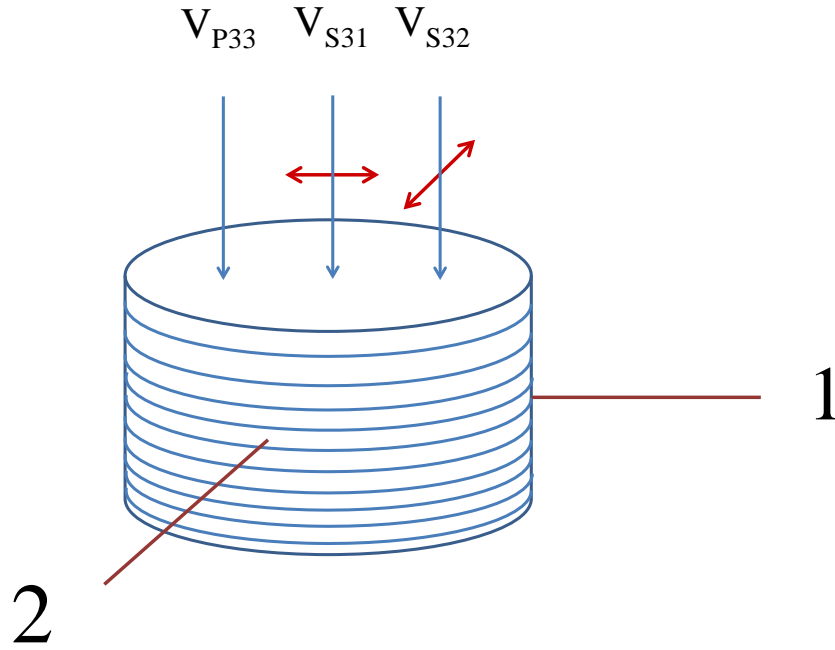


Figure 11-24. Schematic for one compressional and two polarized shear waves propagating parallel to the 3 axis in a transversely isotropic rock.

To calculate elastic constants, five (5) independent velocity measurements or static measurements are necessary. Compressional and shear waves propagating parallel to the **1** and **3** axes provide four independent values. However one additional off-axis measurement is required. The simplest measurement is a P wave propagating 45° to the rift. Using those velocity measurements, the elastic C_{ij} 's are calculated. The relation between the C_{ij} 's and velocities are listed below. A more complete discussion of the analysis is presented in Lo et al., (1986).

$$C_{11} = \rho V_{P11}^2 \quad (1)$$

$$C_{12} = C_{11} - 2\rho V_{SH1}^2 \quad (2)$$

$$C_{33} = \rho V_{P33}^2 \quad (3)$$

$$C_{44} = \rho V_{S3}^2 \quad (4)$$

and

$$C_{13} = -C_{44} + \sqrt{4\rho^2 V_{P45}^4 - 2\rho V_{P45}^2 (C_{11} + C_{33} + 2C_{44}) + (C_{11} + C_{44})(C_{33} + C_{44})} \quad (5)$$

where C_{11} , C_{12} , C_{13} , C_{33} , and C_{44} are the stiffnesses, ρ is the density of the rock, and V_{P11} , V_{P45} , V_{P33} , V_{SH1} , and V_{S3} are P and S wave velocities measured in different directions.

Most geoscientists do not think in terms of stiffness coefficients; they are more comfortable with Young's modulus and Poisson's ratio. For a transversely isotropic rock, there are two (2) Young's moduli and three (3) Poisson's ratios as shown in Figure 11-25. One Young's modulus, E_{33} , is computed parallel to the **3** axis (normal to the rift) and a second Young's modulus, E_{11} , is computed parallel to the rift, in the plane of the **1** and **2** axes. In addition, there are three independent Poisson's ratios. For example, ν_{13} is the Poisson's ratio for a greatest principal stress and strain parallel to the **1** axis and the transverse strain parallel to the **3** axis. Similarly, ν_{31} is the Poisson's ratio is the ratio of the strains parallel to the **3** and **1** axes as a result of a stress applied in the **3** direction.

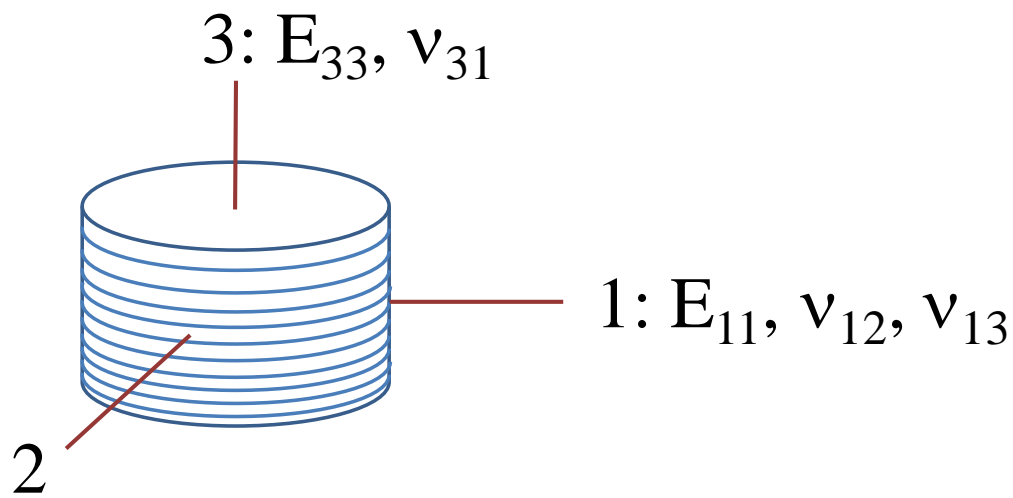


Figure 11-25. The two Young's moduli and three Poisson's ratios computed from the stiffness coefficients are shown with respect to layering in a transversely isotropic rock.

From the elastic stiffnesses, the dynamic bulk modulus, two dynamic Young's moduli, and three dynamic Poisson's ratios were computed. Using the notation of King (1969), the more intuitive elastic constants are computed from the stiffnesses and the determinate of coefficients, **D** (Nye, 1957).

$$E_v = \frac{D}{c_{11}^2 - c_{12}^2} \quad (6)$$

$$E_h = \frac{D}{c_{11}c_{33} - c_{13}^2} \quad (7)$$

$$\nu_1 = \frac{c_{12}c_{33} - c_{13}^2}{c_{11}c_{33} - c_{13}^2} \quad (8)$$

$$v_2 = \frac{c_{13}(c_{11}-c_{12})}{c_{11}c_{33}-c_{13}^2} \quad (9)$$

$$v_3 = \frac{c_{13}}{(c_{11}+c_{12})} \quad (10)$$

$$K = \frac{c_{33}(c_{11}+c_{12})-2c_{13}^2}{c_{11}+2c_{33}+c_{12}-4c_{13}} \quad (11)$$

E_v (E_{11}) is the dynamic Young's modulus perpendicular to the rift, E_h (E_{33}) is the dynamic Young's modulus parallel to the rift. v_1 is a dynamic Poisson's ratio for loading parallel to the rift with the transverse strain measured normal to the rift. v_2 is a dynamic Poisson's ratio for compression normal to the rift and transverse strain measured in the plane of the rift. Similarly, the dynamic Poisson's ratio, v_3 , is for compression parallel to the rift with transverse strain in the plane of the rift.

ELASTIC MEASUREMENTS: STATIC AND DYNAMIC

Velocity measurements were carried out on oriented granite cores to compute the elastic constants of a transversely isotropic rock. It is important to understand that the measurements must to be made on accurately oriented samples so that the elastic coefficients are correct. By measuring the elastic moduli with respect to the rift in the sample, these data can be more appropriately introduced into the wave propagation models that take into account anisotropy.

Three samples were prepared with core axes normal to the rift, parallel to the rift, and at 45° to the rift. The samples were jacketed in copper and instrumented for strain and velocity measurements. A typical configuration is shown in Figure 11-19. Three strain gauges are applied to the copper jacket, one to measure strain normal to the loading axis and two gauges to measure strain parallel to the core axis. NER PS² velocity transducers are secured to the sample. One pair of transducers measure the compressional and two shear wave velocities normal to the loading axis. The sample is then secured between a pair of PS² transducers as shown in Figure 11-20. Each velocity transducer propagates three waves. For the transducer pair secured at the ends of the sample, one compressional wave propagates parallel to the core axis with a vibration direction parallel to the propagation direction. There are two polarized shear wave crystals in each transducer. These propagate shear waves parallel to the core axis with vibration directions transverse to the core axis; the polarizations are orthogonal.

The sample assembly is then placed in a base plug for an NER AutoLab 1500 test frame where it rests directly on a force cell. The strain gauges, the force cell, and the ultrasonic transducers are connected on the base plug and then the entire assembly is inserted into a triaxial test chamber for testing. The system was pressurized. Velocity and strain data were collected simultaneously as a function of pressure.

The velocities are plotted as a function of pressure in Figure 11-26. All the velocities increase with increasing confining pressure. The compressional velocities propagated parallel to the rift were consistently greater than those propagated normal to the rift. At a pressure of 1.0 MPa, the velocity parallel to the rift is 27% greater than waves propagating normal to the rift. At a pressure of 70 MPa, the difference decreases to 5.5%. The compressional wave velocity measured on the specimen oriented at 45° to the rift was consistently greater than the velocity propagated normal to the rift and less than the velocity propagated parallel to the rift. The shear

wave velocities measured in the plane of the rift were consistently greater than those propagated normal to the rift. At a pressure of 1.0 MPa, the shear velocity propagating in the rift with its vibration direction in the rift is 11% greater than waves propagating normal to the rift. At a pressure of 70 MPa, the difference decreases to 3.8%.

The decrease in anisotropy with increasing pressure is attributable to the closing of microcracks (Walsh, 1965; O'Connell and Budiansky, 1974). In this case, the oriented array of cracks in the rift close preferentially with pressure. At 70 MPa, the cracks have not completely closed; presumably at pressures approaching 200 MPa the anisotropy will be vanishingly small (Brace, 1963)

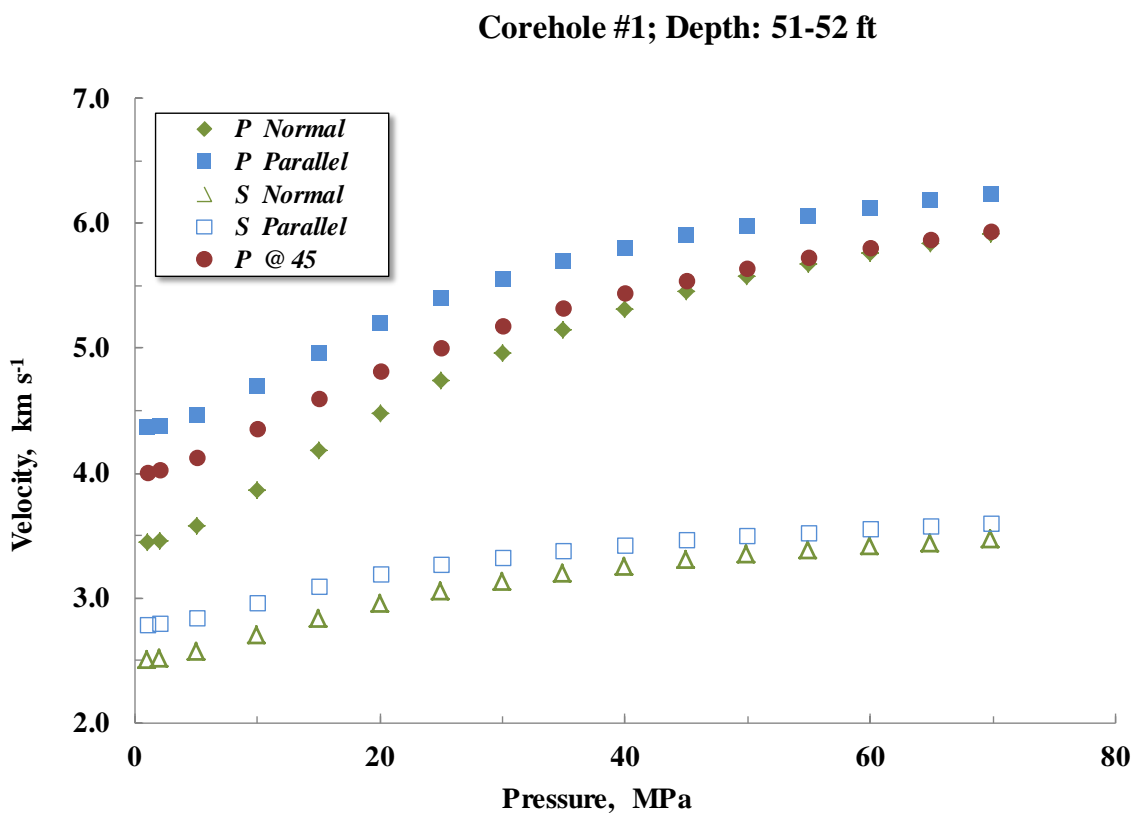


Figure 11-26. Compressional and shear wave velocities are plotted as a function of pressure. Three oriented samples were tested to obtain these data. *P* waves were propagated normal, parallel and at 45° to the rift in Barre granite. Shear waves were propagated (a.) normal to the rift with a vibration direction in the plane of the rift and (b.) parallel to the rift with a vibration direction normal to the rift.

Using the velocity data and Equations 1, 2, 3, 4, and 5 above, the elastic stiffnesses were computed. These data are shown as a function of pressure in Figure 11-27. All the stiffness coefficients increase with pressure.

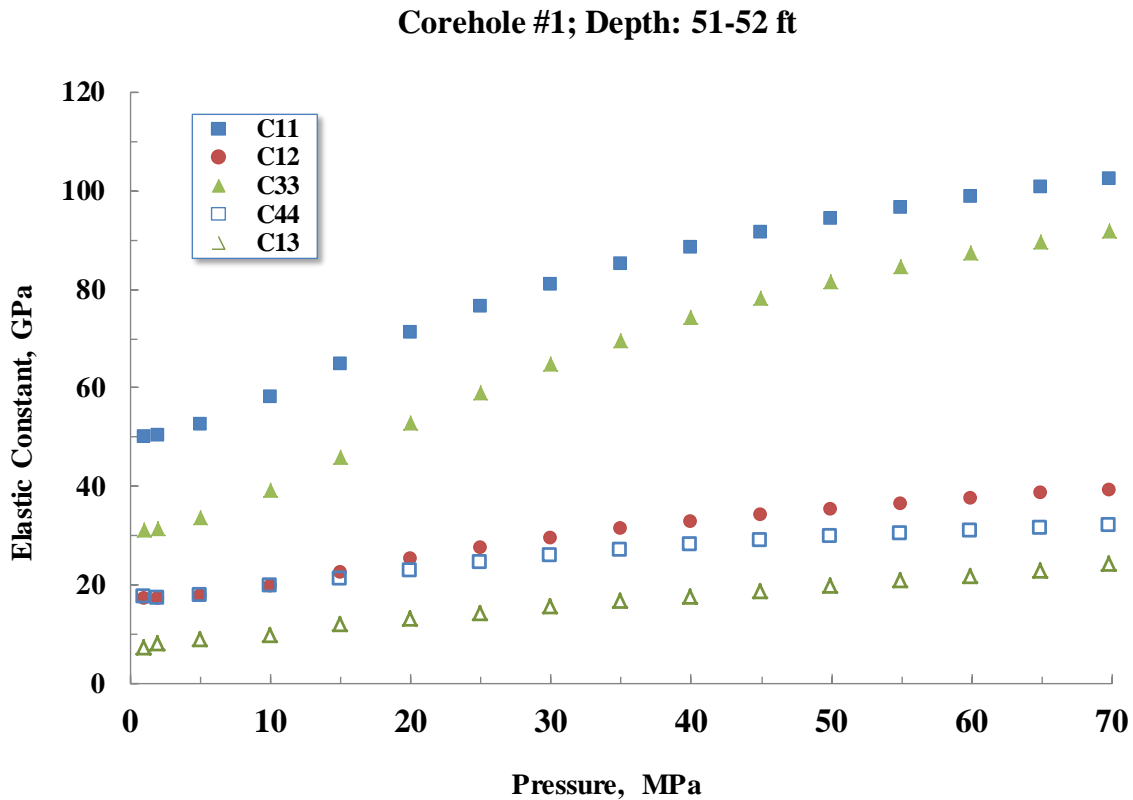


Figure 11-27. Five elastic stiffnesses for a transversely isotropic sample of Barre granite are plotted as a function of pressure. *These coefficients were computed using the velocity data presented in Figure 11-26.*

Three elastic constants computed from the stiffnesses' Young's moduli and bulk modulus, are shown in Figure 11-28. The Young's moduli increase with increasing confining pressure. The elastic modulus in the plane of the rift is greater than that measured normal than that normal to the rift. At higher pressures the Young's moduli for each orientation asymptotically approach the same value at approximately 84 GPa. The bulk modulus increases with increasing pressure and approaches a value of 52 GPa at pressure of 70 MPa.

The computed Poisson's ratios are shown in Figure 11-29. These data exhibit weak pressure dependence. The Poisson's ratio ν_1 is increases from 0.31 to 0.34 as the pressure is increased to 70 MPa. The Poisson's ratios ν_2 and ν_3 are 0.11 and 0.16 at low pressure and asymptotically approach 0.17 at a pressure of 70 MPa.

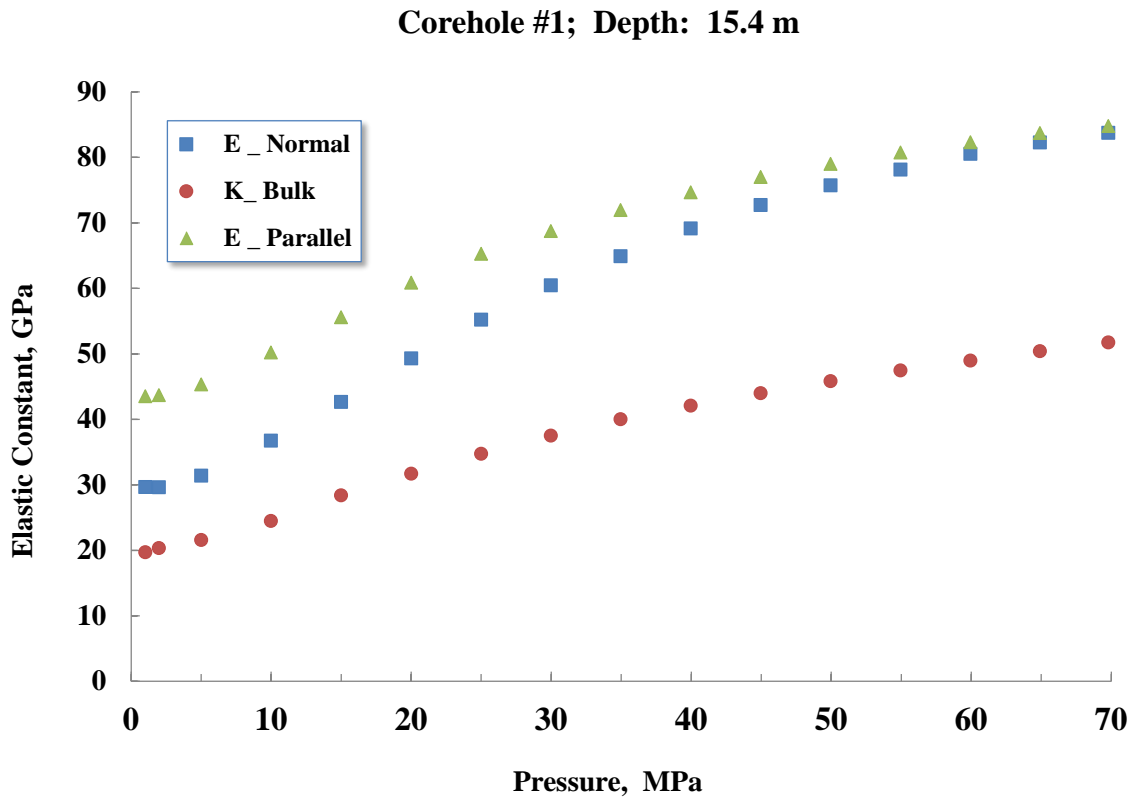


Figure 11-28. Young's moduli parallel and normal to the rift and the bulk modulus are plotted as a function of pressure. *These values were computed from the stiffnesses presented in Figure 11-27.*

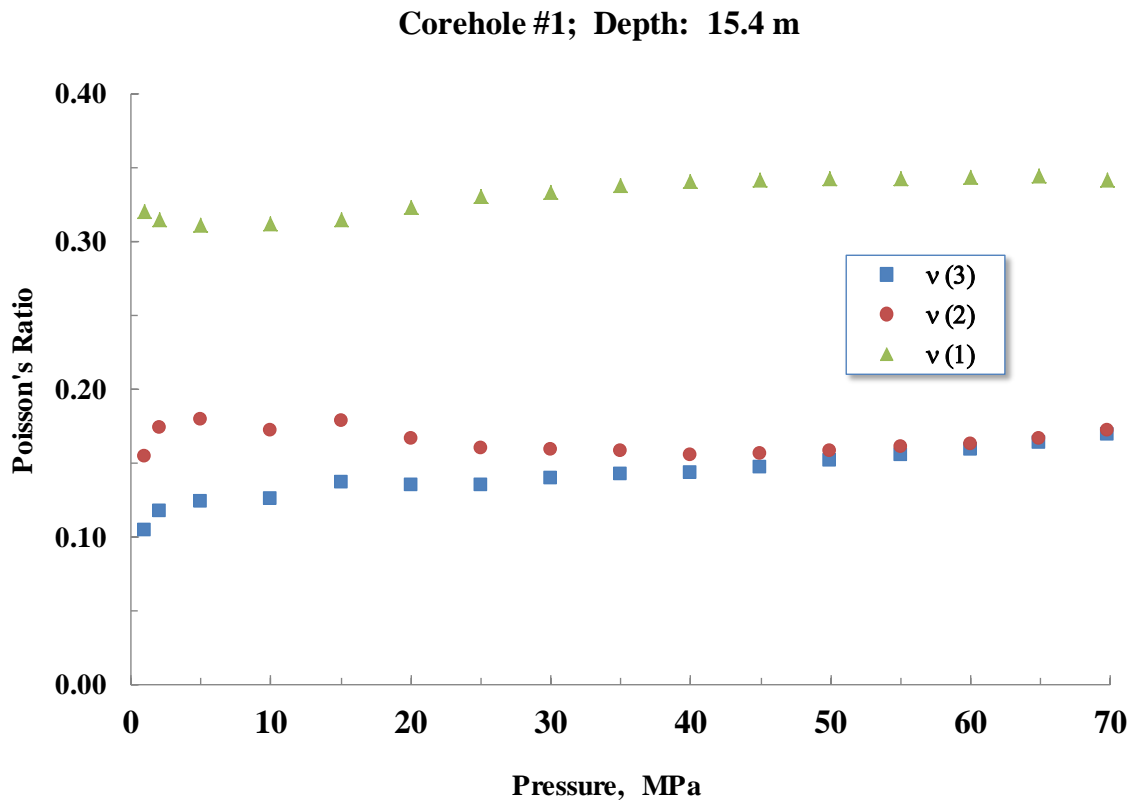


Figure 11-29. Poisson's ratios for the transversely isotropic Barre granite are plotted as a function of pressure. v_1 is the Poisson's ratio for the compression parallel to the rift and the transverse strain normal to the rift. v_2 is the Poisson's ratio for compression normal to the rift and transverse strain measured in the plane of the rift. v_3 is the Poisson's ratio for compression parallel to the rift and transverse strain measured in the plane of the rift.

LINEAR COMPRESSIBILITY

A specimen from preshot CH #1 at a depth of 15.7 m is shown in Figure 11-30. This specimen was jacketed and instrumented with strain gages for compressibility measurements. The setup procedure is the same as for the velocity anisotropy measurements.

Three strain gages were attached to the specimens used for the velocity anisotropy measurements to measure the linear compressibilities. One gage monitored the strains normal to the rift (parallel to Axis 3 in Figure 11-23). A second gage was oriented parallel to the rift and the third gage parallel to the rift and perpendicular to the hardway (in the 1-2 plane as shown in Figure 11-23). These data are shown in Figure 11-31. Two pressurization cycles were conducted. The first cycle shows pronounced hysteresis; subsequent cycles continue to load and unload over the same path with less hysteresis. This behavior is characteristic of most data collected on rocks during hydrostatic loading. Strains for each orientation are nonlinear; at pressures below 30 MPa, the effect is most pronounced. At this pressure, strains measured perpendicular to the rift were as much as a factor of two greater than measured parallel to the rift. This observation is consistent with the changes in compressional and shear wave velocity as a function of pressure.

The bulk modulus was computed from linear compressibility data. The bulk moduli for the second upload cycle are shown as a function of pressure in Figure 11-32. The dynamic bulk moduli presented in Figure 11-28 are shown for reference. The bulk moduli increase with pressure, but the static moduli are consistently lower than the dynamic moduli computed from the acoustic data. This effect has been discussed in Martin and Haupt (1994).



Figure 11-30. A Barre granite core that has been partitioned every 5 degrees in order to determine the fast and slow direction. *This specimen was jacketed and instrumented for linear compressibility measurements.*

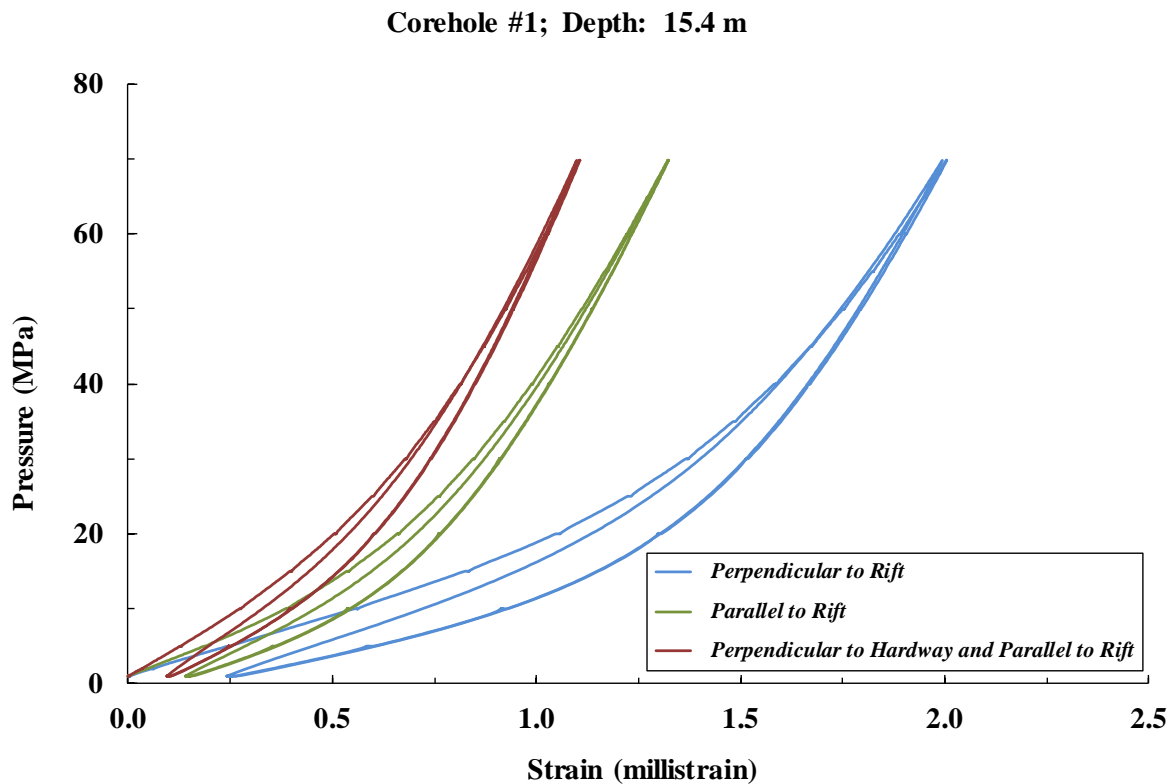


Figure 11-31. Strains are measured in the principal strain directions for a sample of Barre granite. *Gages were positioned perpendicular to the rift, parallel to the rift, and parallel to the rift – perpendicular to the hardway. Pressure is plotted as a function of strain. Two cycles were performed to a pressure of 70 MPa.*

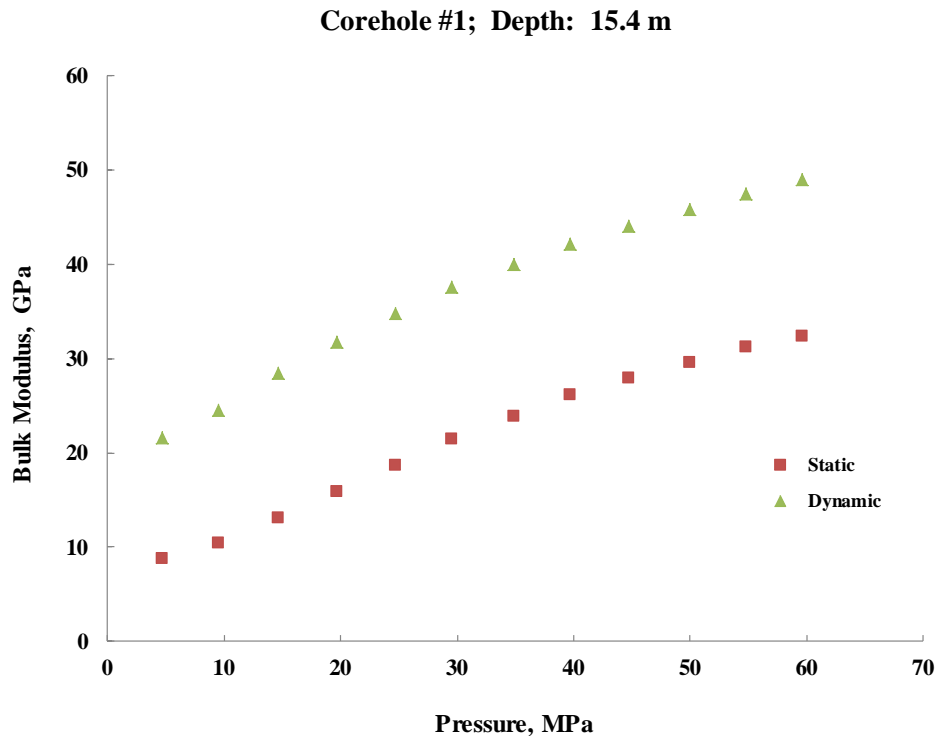


Figure 11-32. The static bulk moduli computed from the linear compressibility data presented in Figure 11-31 is plotted as a function of confining pressure. *The dynamic moduli shown in Figure 11-28 are shown for reference.*

All of the measurements described above were conducted in a room-dry condition because the tests at the Barre quarry were above the water table. In many cases, the tests in granites and other rocks are conducted below the water table. These data can still be used to compute the effects of saturation on velocity using the Biot-Gassmann method. This technique is described in Chapter 9. For completeness, however, it is also important to know how the permeability varies in the rock mass.

Velocity, permeability, and electrical resistivity, are sensitive to the pore structure of the rock. Since we are dealing with a range of stress regimes with varying boundary conditions, the changes in pore structure, and particularly increases in crack density, can be related to damage. By analyzing the damage to the core as a function of range, the continuous variation of the rheology due to the explosion can be determined.

PERMEABILITY

An extensive number of permeability measurements have been conducted on the specimens summarized above. The technique employed to measure low permeability rocks is well established at New England Research. We employ a general transient method. The basic configuration for transient testing is shown in Figure 11-33. The basic configuration is most suitable for permeabilities in the range of 10 D to 0.5 D. For lower permeabilities we implement a coreholder where the downstream volume with integral pressure transducer is contained within the downstream endcap. Employing downstream volumes on the order of

1 cm³, these coreholders are appropriate for measurements of permeability in the range 10 nD to 50 D.

In both configurations, to measure permeability AutoLab controls the pore pressure at one end of the sample (referred to as the upstream end) while the other end of the sample is attached to a fixed volume filled with pore fluid. The pressure is monitored at both the upstream and downstream ends of the sample. Starting with the system in equilibrium and then perturbing the pressure at the upstream end of the sample, the response at the downstream end of the sample is measured to measure the permeability.

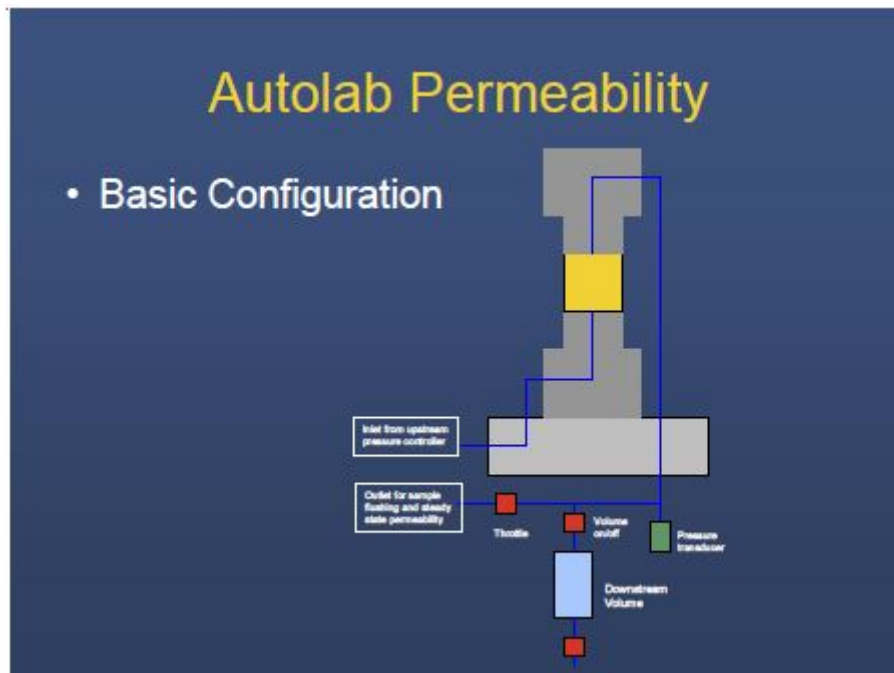


Figure 11-33. Schematic diagram of a typical AutoLab permeability system.

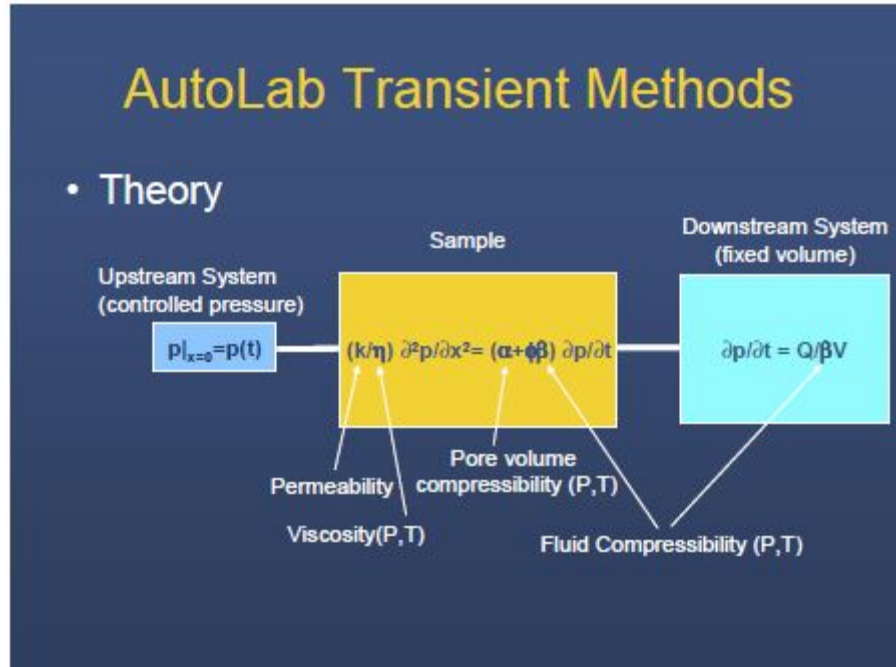


Figure 11-34. Diagram illustrating the physical model used to model transient permeability data

The transfer function describing the relationship between the perturbation in pressure at the upstream end of the sample and the response measured at the downstream end of the sample is a function of the length (L), cross-sectional area (A), permeability (k), and specific storage (S) of the sample, the viscosity (η) and compressibility (β) of the fluid, and the volume (V) in communication with the bottom of the sample (Figure 11-34).

In the absence of specific storage of the sample, or equivalently if the storage capacity ($S \cdot L \cdot A$) of the sample is small compared to the storage capacity of the downstream reservoir ($\phi \cdot g \cdot V$), the solution simplifies considerably to that of the familiar RC low-pass filter (as an electrical analogy). In this limiting case, the measurement of permeability is relatively straightforward using accepted analytical solutions.

For the case where storage is significant, the analysis becomes more difficult.

While analytical solutions to the re-equilibration process are available in a number of forms, in this general case there is no closed-form expression to compute permeability from the equilibration process. It is also important to understand that the equilibration process is a strong function of the ratio k/S , and thus in many cases it is difficult to accurately determine k and S individually. The strong dependence on k/S creates a situation where an error in the determination of one parameter (i.e. specific storage) will lead to an error in the determination of the other (i.e. permeability). AutoLab processing is designed to assist the user in quantifying the uncertainties which are a function of the sample dimensions and the choice of transient employed.

Specimens of Barre granite were saturated with water and jacketed with Viton tubing. The jacketed specimen was secured between titanium endcaps and inserted into a pressure vessel. The confining pressure was raised to 7.5 MPa and the pore pressure was raised to 5.0 MPa.

After the pore pressure equilibrated, transient permeability measurements were initiated. The confining pressure was increased to 30 MPa in a stepwise fashion. Permeability measurements were made at 5 MPa increments.

The results of typical experiments are shown in Figure 11-35. Permeability is plotted as a function of effective pressure for two cores from the same interval; on one core the permeability is measured parallel to the rift and on the other the permeability is measured normal to the rift. The permeability decreases with increasing pressure for both orientations. Permeability measured parallel to the rift was significantly greater than the values collected normal to the rift at low pressures. At pressures of 20 MPa and above the effect of orientation is minimal. The decrease in permeability for both orientations is attributable to the closure of microcracks.

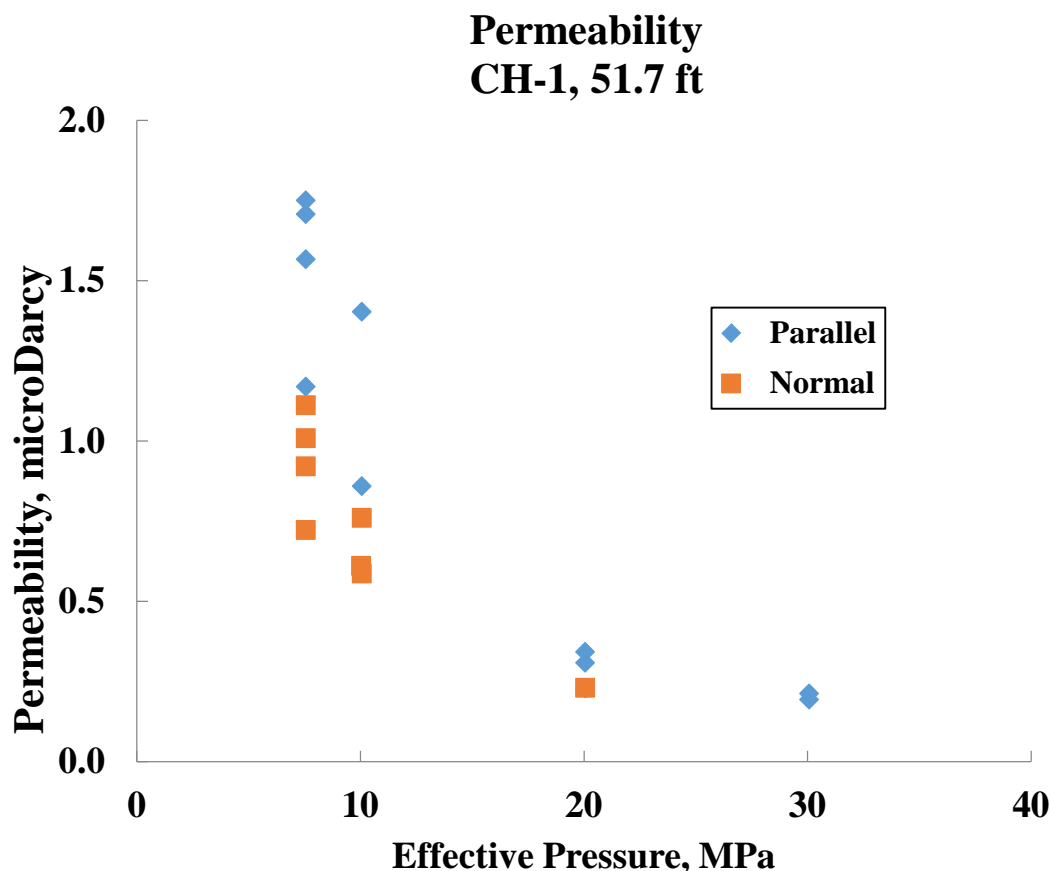


Figure 11-35. Permeability is shown as a function of effective pressure for two oriented specimens from the same depth. *One core is oriented parallel to the rift and the second is oriented normal to the rift.*

RESISTIVITY

NER's AutoLab systems and software are designed for both two electrode and true four electrode resistivity measurements as a function of frequency, stress, and temperature. A computer controlled function generator provides the input to a circuit involving a switchable reference resistor in series with the sample. An optional voltage to current converter allows a controlled current drive to be used, which improves low frequency performance and simplifies

data acquisition. Two matched FET input amplifiers measure the voltage across the reference resistor and the sample. The circuit is housed in the Zmeter interface box. The signals from these amplifiers are recorded by a digital oscilloscope. The amplitude ratio and phase shift between the two signals is used to measure the complex electrical impedance of the sample. Integral computer control of the function generator and oscilloscope allows for automated sweeps through user defined frequency ranges in a single capture. AutoLab processing software allows for corrections to be applied for slight changes in pore fluid temperature (which affects pore fluid conductivity) and for the effects of parasitic impedances which result from the cabling and electronics. Typical system configuration allows for measurements to be performed at frequencies from 0.02 Hz to 100 kHz.

The resistivity coreholder components consist of two silver electrical contacts embedded in the face of each end cap. The end caps are made of a non-conducting material such as alumina or plastic. One end cap contains the contacts for the negative current (I-) and negative voltage (V-) electrodes. This end cap also contains the pore pressure inlet port. The other end cap is electrically isolated from the apparatus and contains the contacts for the positive current (I+) and positive voltage (V+) electrodes. For systems with flow-through capability, the down-stream end cap contains an electrically isolated pore pressure outlet port. All attachments to this electrically isolated end cap must also be fully isolated electrically (including electrical conduction paths through the pore fluid itself). For example, the downstream tubing used in dual permeability and resistivity measurements must be electrically isolated from the rest of the apparatus.

To perform a resistivity experiment, electrodes must be carefully aligned on either end of the sample. The electrodes touch the voltage and current contacts and the sample. Standard electrode materials consist of porous silver membrane filters.

A suite of resistivity measurements were carried out on both pre-shot and post-shot cores to assess the damage to the core. The samples were first saturated with a weak brine and inserted into a Viton jacket. The measurement electrodes were prepared as described above and secured to the jacketed sample. The electrical resistance of the saturating fluid is measured and entered into the data file for the sample. The sample assembly was then inserted into a pressure vessel and the pore pressure lines attached. The confining pressure is increased to 5.0 MPa and the pore pressure to 2.5 MPa. The pore pressure was held constant throughout the test. After the pore pressure equilibrated, transient permeability measurements were initiated. The confining pressure was increased to 50 MPa in a stepwise fashion. Resistivity measurements were made at 5 MPa increments.

The data for two cores are shown in Figure 11-36. The axis of one core is oriented parallel to the rift and the second normal to the rift. Formation factor is plotted as a function of confining pressure. Formation factor is defined as the measured sample resistivity divided by the resistivity of the saturating fluid. With increasing confining pressure the formation factor increased. This suggests that closing microcracks force brine out of the pore space causing the resistivity to increase. The resistivity results also exhibit the same magnitude of anisotropy observed for the linear compressibility, velocity, elastic constants, and permeability data. These data indicate the observed anisotropy at all pressures is controlled by the preferred orientation of microcracks defining the rift and the closure of these microcracks is responsible for pressure dependence of these properties.

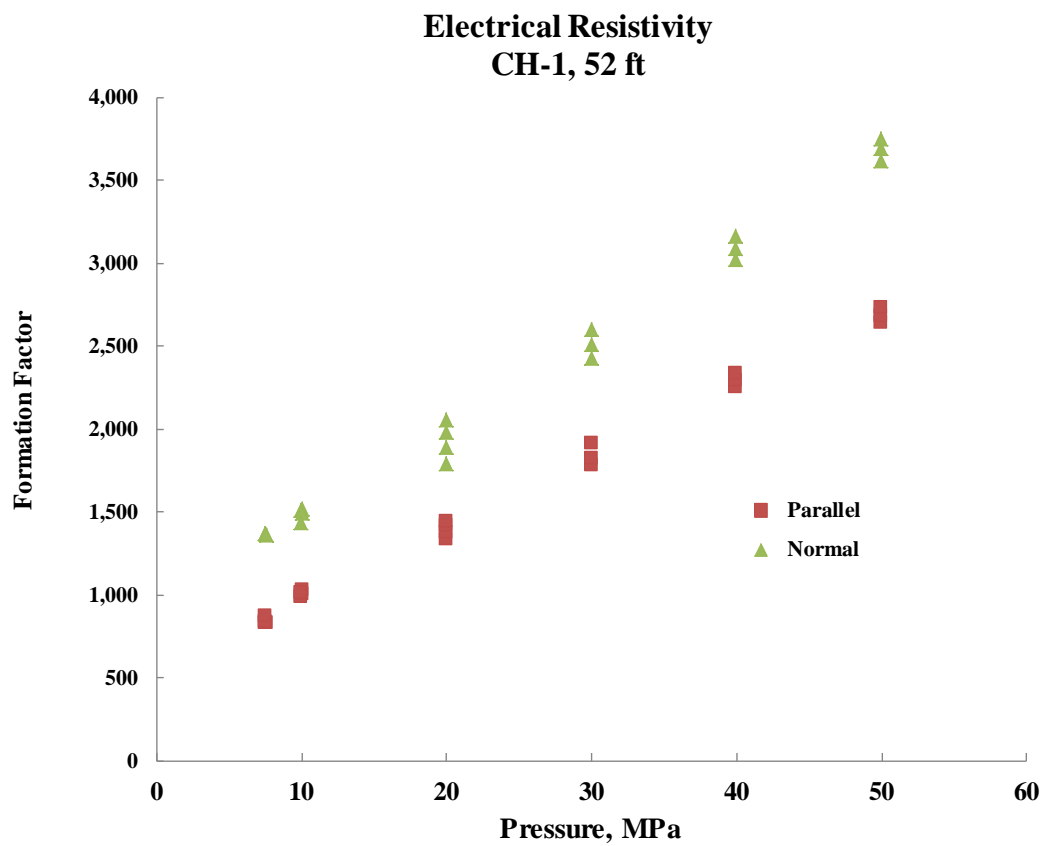


Figure 11-36. Formation factor is shown as a function of effective pressure for two oriented specimens from the same depth. *One core is oriented parallel to the rift and the second is oriented normal to the rift.*

REFERENCES

- Aki, K. and P.G. Richards (2002), Quantitative seismology, University Science Books, Sausalito, CA.
- Aki, K., M. Bouchon, and P. Reasenber (1974), Seismic source function for an underground nuclear explosion, *Bull. Seism. Soc. Am.*, **64**, pp. 131-148.
- Andrews, D. J. (1986), Objective determination of source parameters and similarity of earthquakes of different size, *Geophysical Monograph*, **37**, pp. 259-267.
- ANSI (1983), Estimating airblast characteristics for single point explosions in Air, with a guide to evaluation of atmospheric propagation and effects, *Acoustical Society of America Standards*, ANSI/ASA S2.20-1983 (R 2011).
- Ashby, M. F. and C. G. Sammis (1990), The damage mechanics of brittle solids in compressions, *Pure Appl. Geophys.* **133**, pp. 489-521.
- Ben-Zion, Y. and J.-P. Ampuero (2009), Seismic radiation from regions sustaining material damage, *Geophys. J. Int.*, **178**, pp. 1351-1356, doi:10.1111/j.1365-246X.2009.04285.x.
- Boatwright J, J. Fletcher, and T. Fumal (1991), A general inversion scheme for source, site, and propagation characteristics using multiply recorded sets of moderate-sized earthquakes, *Bull. Seism. Soc. Am.*, **81**, pp. 1754-1782.
- Bonner, J. L., D. Russell, and R. E. Reinke (2013), Modeling surface waves from above ground and underground explosions in alluvium and limestone, *Bull. Seism. Soc. Am.*, **103**, pp. 2953-2970.
- Brace, W. F. (1963), An extension of Griffith theory of fracture to rocks, *J. Geophys. Res.*, **65**, RM-35-83, 103.
- Brunish, W. M., C. R. Bradley, E. Rougier, H. J. Patton, D. Coblenz, D. W. Steedman, A. J. Sussman, and E. E. Knight (2011), Source physics experiment: Research in support of verification and nonproliferation, in Proceedings of the 2011 Monitoring Research Review: Ground-Based Nuclear Explosion Monitoring Technologies, 13-15 September 2011, Tucson, AZ, pp. 49-58.
- Butkovich, T.R. (1971), Influence of Water in Rocks on Effects of Underground Explosions, *Journ. Geoph. Res.*, **76**, 8, pp. 1993-2011.
- Bykovtsev, A. S. (2007), Mathematical description of the explosion source with a system of cracks, *Abs. Seism. Res. Letts.*, Vol **78**, No. 2, p. 221.
- Castro, R., J. Anderson, and S. Singh (1990), Site response, attenuation, and source spectra of S waves along the Guerrero, Mexico subduction zone, *Bull. Seism. Soc. Am.*, **80**, pp. 1481-1503.
- Denny, M. D., P. G. Goldstein, K. Mayeda, and W. R. Walter (1997), Seismic results from DOE's Non-Proliferation Experiment: A comparison of chemical and nuclear explosions, In *Monitoring a Comprehensive Test Ban Treaty*, edited by E. S. Husebye and A. M. Dainty, Kluwer Academic Publishers, pp. 355-364.

- Denny, M. D. and L.R. Johnson (1991), The explosion seismic source function: models and scaling laws reviewed, In *Explosion Source Phenomenology*, *Am. Geophys. Monograph*, **65**, pp. 1-24.
- Doll, W. (1984), Kinetics of crack tip craze zone before and during fracture, *Polym. Eng. Sci.*, **24**, p. 798.
- Doolan, B. (1996), The Geology of Vermont, *Rocks and Minerals Magazine*, Vol. 71, No. 4, pp. 218-225.
- Eisler, J. D. and F. Chilton (1964), Spalling of the earth's surface by underground nuclear explosions. *J. Geophys. Res.*, **69**, pp. 5285-5293.
- Ford, S. R. and W. R. Walter (2013), An explosion model comparison with insights from the source physics experiments, *Bull. Seism. Soc. Amer.*, 103 (6), doi: 10.1785/0120130035.
- Foxall, B. R., R. Reinke, C. Snelson, D. Seastrand, R. Marrs, O. R. Walton, and A.L. Ramirez (2008), The HUMBLE REDWOOD Seismic/acoustic coupling experiments, *Abs. Seism. Res. Letts.*, **79**.
- Foxall, B., R. Marrs, E. Lenox, R. Reinke, D. Seastrand, J. Bonner, K. Mayeda, and C. Snelson (2010), The HUMBLE REDWOOD seismic/acoustic coupling experiments: Joint inversion for yield using seismic, acoustic, and crater data, *Abs. Seism. Res. Letts.*, **81**, p. 315.
- Fuis, G. S., J. M. Murphy, D. A. Okaya, R. W. Clayton, P. M. Davis, K. Thygesen, S. A. Baher, T. Ryberg, M. L. Benthien, G. Simila, J. T. Perron, A. K. Yong, L. Reusser, W. J. Lutter, G. Kaip, M. D. Fort, I. Asudeh, R. Sell, J. R. Vanschaack, E. E. Criley, R. Kaderabek, W. M. Kohler, and N. H. Magnuski (2001), Report for borehole explosion data acquired in the 1999 Los Angeles Region Seismic Experiment (LARSE II), Southern California: Part I, Description of the survey, United States Geological Survey Open-File Report, 01-408.
- Gassmann, F. (1951), Uber die poroser Medien, *Veir. der Natur. Gesellschaft Zurich*, **96**, pp. 1-23.
- Gross, S. P., J. Fineberg, M. Marder, W. D. McCormick, and H. L. Swinney (1993), Acoustic emissions from rapidly moving cracks, *Phys. Rev. Lett.*, **71**, 3162-3165, DOI:10.1103/PhysRevLett.71.3162.
- Gupta, I. N., T. R. Zhang, and R.A. Wagner (1997), Low frequency Lg from NTS and Kazakh nuclear explosions-observations and interpretation, *Bull. Seism. Soc. Am.*, **87**, pp. 1115-1125.
- Hartzell, S. (1992), Site response estimation from earthquake data, *Bull. Seism. Soc. Am.*, **82**, pp. 2308-2327.
- Haskell, N. A. (1967), Analytic approximation for the elastic radiation from a confined underground explosion, *J. Geophys. Res.*, **72**, 10, pp. 2583-2587.
- Heard, H. C. and F. J. Ackerman (1967), *Prediction of cavity radius from underground nuclear explosions*, UCRL-50324, Lawrence Radiation Laboratory, Livermore, CA.

- Herrmann, R. H. (2002), An overview of synthetic seismogram computation, In *Computer Programs in Seismology, Version 3.30*.
- Herrmann, R. B. (2010), Computer Programs in Seismology, St. Louis University, St. Louis, MO.
- King, M. S. (1969), Static and dynamic moduli of rocks under pressure, Somerton, W. H., Ed., *Rock mechanics: Theory and practice; Proceedings, 11th Sympos. on Rock Mechanics*, Univ of Calif., Berkeley, CA, pp. 329-351.
- Knopoff, L. and M. J. Randall (1970), The compensated linear-vector dipole: A possible mechanism for deep earthquakes, *J. Geophys. Res.* **75**, pp. 4957-4963.
- Kohler, W. and G. Fuis (1992), Empirical dependence of seismic ground velocity on the weight of the explosives, shotpoint site condition, and recording distance for seismic refraction data, *Bull. Seism. Soc. Am.*, **82**, pp. 2032-2044.
- Lay, T. and X. Xie (2007), Near-field wave propagation contributions to S wave excitation for underground nuclear explosions, *Seism. Res. Letts.* **78**, p. 240
- Leidig, M., J. L. Bonner, T. Rath, and D. Murray (2010), Quantification of ground vibration differences from well-confined single-hole explosions with variable velocity of detonation, *Int. J. Rock Mech. Min. Sci.*, **47**, pp. 42-49.
- Lo, Tien-when, Karl B. Coyner, and M. Nafi Toksoz (1986), Experimental determination of the elastic anisotropy of Berea sandstone, Chicopee shale, and the Chelmsford granite, *Geophysics*, Vol. **51** (1), pp. 164-171.
- Lorenz, R. (1981), *Noise abatement investigation for the Bloodsworth Island Target Range: Description of the test program and New Long Range Airblast Overpressure Prediction Method*, AD-A-22292/6, Naval Surface Weapons Center, Silver Springs, MD.
- Martin, R., P. Boyd, A. Stroujkova, M. Leidig, J. Lewkowicz, and J. Bonner (2011a), The physical basis of Lg generation by explosion sources, *Proceedings of 2011 Monitoring Research Review: Ground-Based Nuclear Explosion Monitoring Techniques*, pp. 483-494.
- Martin, R., P. Boyd, A. Stroujkova, M. Leidig, J. Lewkowicz, and J. Bonner (2012), Anisotropy of the Barre granite in the vicinity of NEDE, *Proceedings of 2012 Monitoring Research Review: Ground-Based Nuclear Explosion Monitoring Techniques*, September 18-20, 2012, Albuquerque, NM, LA-UR-12-24325, pp. 428-440.
- Martin, R., P. Boyd, A. Stroujkova, M. Leidig, J. Lewkowicz, and J. Bonner (2011b), Correlating Near-Source Rock Damage from Single-Hole Explosions to Seismic Waves, *Proceedings of the 2011 Monitoring Research Review: Ground-Based Nuclear Explosion Monitoring Technologies*, LA-UR-11-04823, pp. 484-494.
- Martin, R. J. and R. W. Haupt (1994), Static and Dynamic Elastic Moduli in Granite: The Effect of Strain Amplitude, In *Rock Mechanics Models and Measurements: Challenges from Industry: Proceedings of the 1st North American Rock Mechanics Symposium*, 1-3 June 1994, Austin, TX, ed. P. P. Nelson and S. E. Laubach, Rotterdam: Balkema, pp. 473-480.
- Masse, R. P. (1981), Review of seismic source models for underground nuclear explosions, *Bull. Seism. Soc. Am.*, **71**, pp. 1249-1268.

- Mavko, G., T. Mukerji, and J. Dvorkin (2009), *The Rock Physics Handbook*, Second Edition, Cambridge University Press, Cambridge, MA.
- Medearis, K. (1979), Dynamic characteristics of ground motion due to blasting, *Bull. Seism. Soc. Am.*, **69**, pp. 627-639.
- Melosh, H. J. (1979), Acoustic Fluidization: A New Geologic Process. *J. Geophys. Res.*, **84**, pp. 7513-7520.
- Mueller, R. A. and J. R. Murphy (1971), Seismic characteristics of underground nuclear detonations, Part I, Seismic spectrum scaling, *Bull. Seism. Soc. Am.*, **61**, pp. 1675-1692.
- Mueller, R.A. (1969), Seismic energy efficiency of underground nuclear detonations, *Bull. Seism. Soc. Am.*, **59**, pp. 2311-2323.
- Murphy, J. R. and H. K. Shah. (1988), An analysis of the effects of site geology on the characteristics of near-field Rayleigh waves, *Bull. Seism. Soc. Am.*, **78**, pp. 64-82.
- Murphy, J. R. (1981), Near-field Rayleigh waves from surface explosions, *Bull. Seism. Soc. Am.*, **71**, 223-248.
- Murphy, J. R., T. J. Bennett, and B.W. Barker (2011), An analysis of the seismic source characteristics of explosions in low-coupling dry porous media, *Proceedings of 2011 Monitoring Research Review: Ground-Based Nuclear Explosion Monitoring*, pp. 524-534.
- Myers, S. C., W. R. Walter, K. Mayeda, and L. Glenn (1999), Observations in support of Rg scattering as a source for explosion S waves: regional and local recordings of the 1997 Kazakhstan depth of burial experiment, *Bull. Seism. Soc. Am.*, **89**, pp. 544-549.
- Nasseri, M. H. B. and B. Mohanty (2008), Fracture toughness anisotropy in granitic rocks, *International Journal of Rock Mechanics and Mining Sciences*, **45**, pp. 167-193.
- Nur, A., G. Mavko, J. Dvorkin and D. Gal (1995), Critical porosity: the key to relating physical properties to porosity in rocks, In *Proc. 65th Ann. Int. Meeting Soc. Expl. Geophys.*, Vol. **878**, Tulsa, OK: Society of Explorational Geophysicists.
- Nye, J. R. (1957), *Physical properties of crystals: Their representation by tensors and matrices*, Oxford University Press, Oxford, UK.
- O'Connell, R. and B. Budiansky (1974), Seismic velocities and in dry and saturated cracked solids, *J. Geophys. Res.*, **70**, pp. 5649-5656.
- Olsen, K. H. and A. L. Peratt (1994), Free-field ground motion for the non-proliferation experiment: preliminary comparisons with nearby nuclear events, in *Proc. Symp. on the Non-Proliferation Experiments (NPE): Results and Implications for Test Ban Treaties*, M. D. Denny (Editor), CONF-9404100, Department of Energy, pp. 283-297.
- Patton, H. J. (2012a), *Have the Effects of Material Damage Been Detected in Rg Waveforms Recorded on SPE-1 and -2?*, LA-UR-12-22068, Los Alamos National Laboratory, Los Alamos, NM.
- Patton, H. J. (2012b), Modeling M_s -yield scaling of Nevada Test Site nuclear explosions for constraints on volumetric moment due to source medium damage, *Bull. Seism. Soc. Am.*, **102**, pp. 1371-1387.

- Patton, H. J. and S. R. Taylor (1995), Analysis of *Lg* spectral ratios from NTS explosions: implications for the source mechanism of spall and the generation of *Lg* waves, *Bull. Seism. Soc. Am.*, **85**, pp. 220-236.
- Patton, H. J. and S. R. Taylor (2008), The apparent explosion moment: Inferences of volumetric moment due to source medium damage by underground nuclear explosions, *J. Geophys. Res.*, **116**, B03310, doi:10.1029/2010JB007937.
- Patton, H. J. and S. R. Taylor (2011), The apparent explosion moment: Inferences of volumetric moment due to source medium damage by underground nuclear explosions, *J. Geophys. Res.*, **116**, B03310, doi:10.1029/2010JB007937.
- Patton, H. J. and S. R. Taylor (1995), Analysis of *Lg* Spectral Ratios from NTS Explosions: Implications for the Source Mechanism of Spall and the Generation of *Lg* Waves, *Bull. Seism. Soc. Am.*, **85**, 220 - 236.
- Patton, H. J. and S. R. Taylor, (2011), The apparent explosion moment: Inferences of volumetric moment due to source medium damage by underground nuclear explosions, *J. Geophys. Res.* 116: B03310, doi:10.1029/2010JB007937.
- Patton, H., J. Bonner, and I. Gupta, (2005), *Rg* Excitation by Underground Explosions: Insights from Source Modeling the 1997 Kazakhstan Depth of Burial Experiments, *Geophys. J. Int.*, doi:10.1111/j.1365-246X.2005.02752.x.
- Perkins, B. and W. F. Jackson (1964), Handbook for prediction of air blast focusing, *BRL Report 1240*.
- Perret, W. R. and R. C. Bass (1975), *Free-field ground motion induced by underground explosions*, SAND74-0252, Sandia National Laboratory, Albuquerque, NM.
- Richter, D. A. (1987), Barre granite quarries, Barre, Vermont, Geological Society of America Centennial Field Guide, Northeastern Section.
- Rodean, H. C. (1971), Nuclear-Explosion Seismology, U. S. Atomic Energy Commission, TID-25572.
- Saikia, C. K., A. Kafka, S. C. Gnewuch, and J. W. McTigue (1990), Velocity and intrinsic Q structure of the shallow crust in Southeastern New England from *Rg* wave dispersion, *J. Geophys. Res.*, **95**, pp. 8527-8541.
- Sammis, C. (2003), Scaling laws for secondary seismic radiation generated by fracture damage in Proceedings of the 25th Seismic Research Review, LA-UR-03-6029, Vol. **1**, pp. 450-455.
- Sammis, C. G. (2002), Generation of High-Frequency *P* and *S* Wave Energy by Rock Fracture During a Buried Explosion: Its Effect on *P/S* Discriminants at Low Magnitude, *Proceedings of the 24th Seismic Research Review – Nuclear Explosion Monitoring: Innovation and Integration*, Sept. 17-19, Ponte Verde Beach, FL, pp. 542-551.
- Sammis, C. G. (2011), Effect of the burn rate on the spatial extent of fracture damage in an underground explosion, *Proceedings of the 2011 Monitoring Research Review on Nuclear Monitoring Technologies*, Tucson, AZ.

- Sharpe, J.A. (1942), The production of elastic waves by explosion pressures, I. Theory and empirical field observations, *Geophysics*, **7**, pp. 144-154.
- Shishkin N. (2007), Seismic efficiency of a contact explosion and a high-velocity impact, *Journal of Applied Mechanics and Technical Physics*, **48**, 2, pp. 145-152.
- Short, N. (1966), Effects of Shock Pressures from a Nuclear Explosion on Mechanical and Optical Properties of Granodiorite, *J. Geophys. Res.*, **71**, pp. 1195-1215.
- Sokolova, I. N. (2008), Investigation of dynamic parameters of seismic records of initial and repeated explosions, (*in Russian*), *NNC RK Bulletin*, **33**(1), pp. 68-73.
- Stein, S. and M. Wyssession (2003), An Introduction to Seismology, Earthquakes, and Earth Structure, Blackwell Publishing, Malden, MA.
- Stevens, J. L., G. E. Baker, H. Xu, T. J. Bennett, N. Rimer, and S. M. Day (2003a), The Physical Basis of *L_g* Generation by Explosion Sources, *Proceedings of the 25th Annual Seismic Research Review on Nuclear Monitoring Technologies*, Tucson, AZ.
- Stevens, J. L., N. Rimer, H. Xu, G. E. Baker, S. M. Day (2003b), Near-field and Regional Modeling of Explosions at the Degelen Test Site, SAIC-02/2050, SAIC, San Diego, CA.
- Stroujkova, A. J. (2010), Moment tensors from explosions in Barre Granite, *Proceedings of the 2010 Monitoring Research Review*.
- Stroujkova, A., J. Bonner, and T. Rath (2013), Effect of Fractures on Seismic Amplitudes from Explosions, *Bull. Seism. Soc. Amer.*, **103**, pp. 580-587, doi:10.1785/0120120082.
- Stroujkova, A., J. L. Bonner, M. Leidig, P. Boyd, and R. J. Martin (2012), Shear Waves from Explosions in Granite Revisited: Lessons Learned from the New England Damage Experiment, *Bull. Seism. Soc. Amer.*, **102**, pp. 1913-1926, doi:10.1785/0120110204.
- Stroujkova, A., M. Leidig, M. Carnevale, and T. Rath (submitted 2013), Effects of Water Saturation on Explosion Seismic Coupling in Intact and Fractured Granite, submitted to *Bull. Seism. Soc. Am.*, Dec. 2013.
- Stump, B., D. C. Pearson, and R. E. Reinke (1999), Source Comparisons between Nuclear and Chemical Explosions Detonated at Rainier Mesa, Nevada Test Site, *Bull Seism. Soc. Am.*, **89**, pp. 409-422.
- Stump, B. and L. Johnson (1977), The determination of source properties by the linear inversion of seismograms, *Bull. Seis. Soc. Am.*, Vol. **67**, No. 6, pp. 1489-1502.
- Townsend, M. L., B. Prothro, and C. Obi (2012), Geology of the source physics experiment site climax stock Nevada national security site, DOE/NV/25946-1448.
- Vortman, L. J. (1965), Air-blast suppression as a function of explosive-charge burial depth, *J. Acou. Soc. Am.*, **14**, pp. 229-239.
- Walsh, J. B. (1965), The effect of cracks on the compressibility of rock, *J. Geophys. Res.*, **70**(2), pp. 381-389, doi:10.1029/JZ070i002p00381.
- Walter, W. and J. Brune (1993), Spectra of seismic radiation from a tensile crack, *J. Geophys. Res.* **98**, pp. 4449-4459.

- Xie, X. and T. Lay (1994), The excitation of Lg waves by explosions: a finite-difference investigation, *Bull. Seism. Soc. Am.*, **84**, pp. 324-342.
- Yang, X. (1997), Mining explosion and collapse source characterization and modeling with near-source seismic data, Ph.D. Thesis, Southern Methodist University, Dallas, TX.
- Yang, X., and Bonner, J. (2009), Characteristics of chemical explosive sources from time-dependent moment tensors, *Bull. Seis. Soc. Am.*, Vol. **99**, pp. 36-51, doi:10.1785/0120080243.

LIST OF SYMBOLS, ABBREVIATIONS, AND ACRONYMS

AFRL	Air Force Research Laboratory
ANFO	Ammonium Nitrate Fuel Oil
BP	Black powder
CLVD	Compensated linear-vector dipole
Comp B	Composition B
FD	Fracture Decouple
HANFO	Heavy ANFO (ANFO/Emulsion Mix)
NEDE	New England Damage Experiment
NEDE1	New England Damage Experiment Phase I
NEDE2	New England Damage Experiment Phase II
NER	New England Research, Inc.
SDOB	Scaled Depth of Burial
SNR	Signal-to-Noise Ratio
VOD	Velocity of Detonation
WITS	Weston Inexpensive Timing System
WGC	Weston Geophysical Corp.

DISTRIBUTION LIST

DTIC/OCF	
8725 John J. Kingman Rd, Suite 0944	
Ft Belvoir, VA 22060-6218	1 cy
AFRL/RVIL	
Kirtland AFB, NM 87117-5776	2 cys
Official Record Copy	
AFRL/RVBYE/Robert Raistrick	1 cy

This page is intentionally left blank.